Universitat Autònoma de Barcelona

PH. D. THESIS

APPLICATION OF CMOS-MEMS INTEGRATED RESONATORS TO RF COMMUNICATION SYSTEMS

Joan Lluís López Méndez
2009

Memòria presentada per optar al
Grau de Doctor en Enginyeria Electrònica
per la Universitat Autònoma de Barcelona.
Directora: Núria Barniol Beumala

La Dra. Núria Barniol Beumala, Catedràtica d'Electrònica del Departament d'Enginyeria Electrònica de la Universitat Autònoma de Barcelona,

CERTIFICA

que la memòria "Application of CMOS-MEMS integrated resonators to RF communication systems" que presenta Joan Lluís López Méndez per optar al grau de Doctor en Enginyeria Electrònica, ha estat realitzada sota la seva direcció.

Bellaterra, juliol de 2009

Dra. Núria Barniol Beumala

A la llum que guia
les meves passes:
Gisela

We shall not cease from exploration
And the end of all our exploring
Will be to arrive where we started
And know the place for the first time.

T.S. Eliot

AGRAÏMENTS

"It was the best of times, it was the worst of times, it was the age of wisdom, it wasthe age of foolishness…". Amb aquesta frase Dickens començava 'Història de dos ciutats' aquesta mateixa frase va servir a T. Newman i R.F.W. Pease per superar el repte del Dr Feynman: escriure l'equivalent de la enciclopèdia britànica en el cap d'una agulla. La tesi que tens a les mans és la meva petita (i humil) contribució al fantàstic món dels MEMS.

Una tesi no és únicament feina de l'autor: es sustenta en la feina del conjunt de la comunitat científica i en els treballs previs d'aquells que van ser pioners. Tanmateix també representa un sacrifici important per tots aquells que envolten a l'investigador. Per tots ells espero que hagi valgut la pena i espero ser capaç de recompensar-los degudament.

Em considero afortunat d'haver començar la meva vida professional al departament d'enginyeria electrònica de la UAB en el que entre tots em veu fer sentir com a casa per tots aquells moments (i anys) gràcies de tot cor.

També tinc un agraïment especial als membres del grup ECAS: a en Gabriel, a l'Arantxa, a en Joan i en Gonzalo per totes les converses, professionals o no. Especialment a en Francesc per les tasques administratives i els moments que vam compartir a Tres Cantos. També a l'Eloi per haver fet part de les mesures de la tesi. A en Jaume i en Jordi per marcar el camí a seguir i especialment a la Núria per la seva paciència i comprensió.

Agraeixo també la feina feta per la Marta Duch i Marta Gerbolés del IMB-CNM, en el post-processat dels xips.

Finalment agrair la paciència (infinita) de la Gisela, així com el suport de les nostres famílies (pares, mares, avis,...), durant el llarg procés d'escriptura de la tesi.

Joan Lluís López
Guadalajara, 2009

SUMMARY

MEMS devices demonstrated a wide range of sensing and actuation applications. These mechanical elements present nowadays extension to the RF world as key elements for highly reconfigurable systems, frequency references and signal processors.

This thesis focuses on some of the applications of MEMS devices in the RF domain: frequency references for oscillators, filters and mixers. The resonators presented in this thesis are completely fabricated in commercial CMOS technologies to take profit of monolithic MEMS and complementary circuitry integration and low cost fabrication inherent of these technologies.

Several kinds of MEMS resonators (clamped-clamped beams, free-free beams and double ended tuning forks) were designed and fabricated to evaluate their performance according to different properties. Two different CMOS technologies, from two different foundries and also different technological node (0.35um and 0.18um) were successfully used to validate the monolithic fabrication approach on future CMOS technologies. The resonance frequencies of these resonators are located on the HF and VHF range. All these devices, based on flexural beams, show superior Q than integrated LC tanks and are also tunable. Moreover, their size is significatively lower than the one of the aforementioned LC tanks. The CMOS-MEMS resonators reported in this thesis show a Qxf value in the range between 1GHz and 10GHz in air and these values are further improved in vacuum up to 100GHz, higher than any other reported resonator based on CMOS technology.

Filtering and mixing applications were also studied. The goal in these applications was to define a flat band-pass combining different resonators. A prototype of parallel filter was measured using two CC-beams and a monolithic CMOS differential amplifier. The filter shows a flat bandpass up to 200kHz in air at a center frequency of 21.66MHz. Filtering with a single resonator was also demostrated with a DETF. A mixer based on a 22MHz CC-beam resonator was able to up and downconvert a signal from/to 1GHz.

Monolithic oscillators with MEMS elements as frequency references have shown oscillation with a reduced applied DC voltage (<5V) thanks to the reduction of the gap. The DETF based oscillator shows good phase noise performance of -87dBc/Hz@10kHz and -98.7dBc/Hz@100kHz better than previously reported monolithic oscillators whereas operating at a lower DC voltage.

RESUM EN CATALÀ

Els dispositius MEMS han demostrat la seva utilitat en un gran ventall d'aplicacions de sensat i actuació. L'extensió al domini de RF d'aquests elements mecànics són ara una de les peces clau per sistemes altament reconfigurables referències de freqüència i processadors de senyals.

Aquesta tesi es centra en algunes de les aplicacions dels dispositius MEMS en el domini de RF: referències de freqüència per oscil·ladors, filtres i mescladors. Els resonadors que es presenten en aquesta tesi s'han fabricat completament en tecnologies CMOS comercials per aprofitar la integració de MEMS i circuiteria complementària i el baix cost de fabricació d'aquestes tecnologies.

Diferents tipus de ressonadors MEMS s'han dissenyat i fabricat a fi d'avaluar les seves prestacions en diferents propietats. La validesa de la tècnica emprada per fabricar els MEMS en tecnologies CMOS futures s'ha demostrat fabricant i testant amb èxit resonadors MEMS en dos tecnologies diferents: de diferents fàbriques i nodes tecnològics (0.35um i 0.18um). La freqüència de ressonància d'aquests dispositius mecànics es troben a les bandes de HF i VHF. Tots aquests dispositius basats en bigues flexurals, presenten un major factor de qualitat Q que els tancs LC integrats i són a més a més sintonizables en freqüència, amb una mida inferior a la dels citats tancs LC. Els ressonadors MEMS-CMOS descrita a la tesi presenten un valor de Qxf en el rang entre 1GHz i els 10GHz mesurats a l'aire. Aquests valors es milloren mesurant al buit arribant als 100GHz, majors a qualsevol altre ressonador basat en tecnologia CMOS.

Les aplicacions de mesclat i filtrat de senyals també s'estudien. Dins d'aquestes aplicacions, la meta és definir una banda passant plana combinant diferents ressonadors. El prototipus d'un filtre paral·lel basat en ponts i un amplificador diferencial CMOS monolític presenta una banda passant plana de 200kHz a una freqüència central de 21.66MHz quan es mesura a l'aire. També es demostra el filtrat emprant un únic ressonador del tipus *tuning fork*. Com a mesclador, és destacable la possibilitat de convertir a alta i baixa senyals de 1GHz amb un ressonador de 22MHz

Com a oscil·ladors monolítics, es mostra un oscil·lador operatiu per tensions DC baixes (<5V), gràcies a la reducció del gap del ressonador. L'oscil·lador basat en un *tuning fork* aconsegueix valors de soroll de fase de -87dBc/Hz@10kHz i -98.7dBc/Hz@100kHz, millor que altres oscil·ladors CMOS monolític reportats.

1 INTRODUCTION 19

1.1 MEMS IN RF OVERVIEW AND RESEARCH MOTIVATION 19
1.1.1 MARKET PERSPECTIVE FOR RF MEMS 22
1.1.2 RF-MEMS APPLICATIONS ON A RF-FRONT-END 24
1.2 FABRICATION TECHNOLOGIES 28
1.2.1 SYSTEM IN PACKAGE 29
1.2.2 SYSTEM ON CHIP 30
1.2.3 PACKAGING 34
1.3 RESEARCH FRAMEWORK OF THE THESIS 36
1.3.1 NANOSYS (TIC2003-07237-C03-02) 37
1.3.2 MEMSPORT (TEC2006-03698/MIC) 37
1.4 THESIS: OBJECTIVES AND OUTLINE 37

2 MEMS RESONATORS CHARACTERISTICS AND APPLICATION IN RF SYSTEMS 43

2.1 WORKING PRINCIPLE 43
2.1.1 ELECTROSTATIC EXCITATION 43
2.1.2 EQUATION OF RESONATOR MOVEMENT 46
2.1.3 SPRING SOFTENING 47
2.1.4 PULL-IN AND COLLAPSING VOLTAGE 48
2.1.5 CAPACITIVE READOUT 50
2.1.6 RLC ELECTRICAL EQUIVALENT MODEL 51
2.2 KEY PARAMETERS OF MEMS FOR RF APPLICATIONS 52
2.2.1 RESONANCE FREQUENCY 52
2.2.2 QUALITY FACTOR 52
2.2.3 FREQUENCY TUNING 53
2.2.4 MOTIONAL RESISTANCE 54
2.2.5 NON-LINEAR RESONANT BEHAVIOR 54
2.3 MEMS RESONATORS APPLICATIONS IN A RF FRONT-END 56
2.3.1 FREQUENCY REFERENCES 56
2.3.2 FILTERING 62
2.3.3 FILTERING-MIXING (“MIXLING”) 66
2.3.4 STATE OF THE ART 68
2.3.5 CONCLUSIONS 73

3 CMOS-MEMS FABRICATION 79

3.1 CMOS-MEMS FABRICATION PROCESSES: 79

3.2 CMOS Technologies Overview **80**
3.3 Spacer Technique **82**
3.4 Technology Comparison **85**
3.5 Further Considerations **86**
3.6 Downscaling Proof Of Concept: UMC 0.18um CC-Beams Resonators **93**
3.6.1 HF Resonator 94
3.6.2 VHF Resonator 98
3.6.3 Conclusions 99

4 MEMS RESONATORS **103**

4.1 Clamped-Clamped Beams **103**
4.1.1 Linearity considerations for clamped-clamped beams 103
4.1.2 Clamped-clamped beams dimensioning 106
4.1.3 24 MHz Clamped- Clamped Beams 107
4.1.4 48 MHz Clamped-Clamped Beam 115
4.2 Free-Free Beams **117**
4.2.1 24mhz Free-Free Beam 118
4.2.2 Third-Mode 48MHz Free-Free Beam Resonator 122
4.3 Double-Ended Tuning Forks **127**
4.3.1 DETF d1u COUPLED 128
4.3.2 24MHz DETF 130
4.4 Conclusions **135**

5 FILTERING, MIXING AND OSCILLATOR APPLICATIONS **141**

5.1 Parallel Filter **141**
5.1.1 Single resonators measurement 143
5.1.2 Combined resonator response: filtering 146
5.2 Single Resonator Filter **151**
5.3 Single Resonator Mixing **153**
5.3.1 HF CC-BEAM Resonator 153
5.3.2 VHF Double-Ended Tuning Fork Filter-Mixer 155
5.3.3 VHF CC-Beam Resonator 159
5.4 Parallel Mixing **160**
5.5 Oscillator: **162**
5.5.1 s=100nm Clamped-Clamped Beam Resonator Oscillator 162
5.5.2 DETF Oscillator 165
5.6 Conclusions **167**
5.6.1 Filters 168

5.6.2 MIXERS 169
5.6.3 OSCILLATORS 170

6 CONCLUSIONS 173

MEMS RESONATORS 173
MEMS RF SIGNAL PROCESSORS 174
CMOS-MEMS OSCILLATORS 175
FINAL CONCLUSIONS 175
REFERENCES 175
PUBLICATION LIST 176
JOURNALS 176
CONFERENCES 176

ANNEX 1: MEMS DESIGN EQUATIONS 179

FLEXURAL MODES IN BEAMS 179
CLAMPED-CLAMPED BEAMS 180
FREE-FREE BEAMS 183
DOUBLE-ENDED TUNING FORKS (DETF) 186

ANNEX2: MEMS CHARACTERIZATION EQUIPMENT AND TECHNIQUES 191

MEASUREMENT TEST SETUP 191
MEASUREMENT TECHNIQUES 192
DIRECT S21 MEASUREMENTS 192
MIXING MEASUREMENTS 193
Q MEASUREMENT TECHNIQUES 194
MOTIONAL RESISTANCE EXTRACTION 194
ADVANCED MEASUREMENT TECHNIQUES 195
CALIBRATION 195
ADS FITTING 195
TERMINATION 198

ANNEX 3: RUN DESCRIPTION 201

AMS RUN 1 201
UMC RUN 202
AMS RUN 2 203

1 Introduction

MEMS is an acronym of MicroElectroMechanical Systems, however there are more denominations for the same kind of devices, as Micromachines (in Japan) or the European MST (Micro System Technology or even Microsystems). As the proper name indicates, MEMS are simply electrically actuated or sensed mechanical devices with microscale dimensions.

The earliest reference of the power of miniaturization, which is also considered as one of the most enlightening visions on MEMS topic, was provided by Dr. Feynmann in a conference given in the annual meeting of the American Physics Society in 1959 ("There's plenty of room at the bottom"), which was later reprinted in the Journal of MEMS in [1]. Only 6 years later (in 1965), the very first MEMS work was published: the resonant gate transistor [2]. Unfortunately, due to technical problems, and lack of the appropriate techniques for MEMS fabrication, MEMS technology did not take off in that moment. It was in the early 1990, that several commercial MEMS products became available in mass market applications: ink-jet printers heads [3] and airbag accelerometers [4, 5]. Nowadays applications of MEMS are widespread and include sensing: pressure [6] and gyroscopes [5]; digital light processors (DLP) [7]; memories [8]; chemical and biological applications [9, 10] as well as actuators as microphones [11]. The great advantage of miniaturization provided by MEMS is driving the research and application of these devices in RF applications.

1.1 MEMS in RF Overview and Research Motivation

Considering the benefits obtained in better performance or reduction of fabrication costs by the use of MEMS in other areas, it was only a matter of time that manufacturers and researchers tried to apply these devices in the RF world. Moreover, the increasing number of wireless protocols and the search for more compact, less power-hungry and higher performance communication systems become one of the most important driver in consumer electronics research [12]. *Figure 1.1* shows a diagram of the wireless services present (or on the road) on cellular handsets.

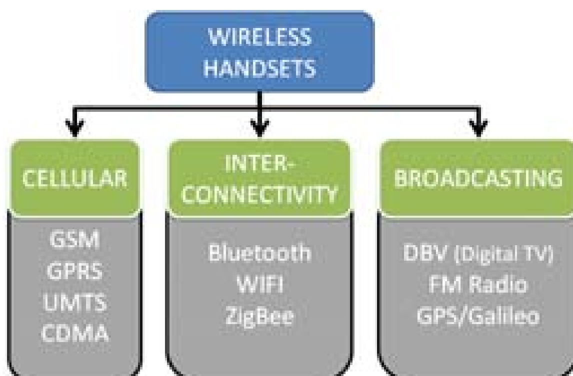

Figure 1.1: Wireless handsets services. Some of the most relevant wireless protocols are shown.

With this high amount of protocols and services, the challenge is to integrate all of these in a cellular handset maintaining its size and reduced power consumption. The goal is to design a single reconfigurable RF radio capable to deal with all these protocols and services. The current bottleneck in miniaturization of these portable systems is situated in the off-chip passives (in concrete in filters and resonators) rather than in the integrated circuits, as can be observed in *Figure 1.2:(a)*. In this figure, (b) and (c) shows the evolution from 1998 to 2004 of a RF chip. The 1998 chip is a GSM power amplifier (the BGY241 from Philips), whereas the 2004 chip is a quad-band transmitter module (BGY504 also from Philips). It can be observed that the second module offers more performance in a reduced place, thanks to the integration of passives in chips (shown with arrows), with the PASSI technology process [13] [14]. This example shows the important trends on RF technology, and is in this miniaturization, and performance improvement, MEMS are expected to provide an added value on both fields. As an example of these achievements we want to mention the case of MEMS-based oscillators, as the ones recently commercialized from Discera [15]. This company, among others mentioned in next sections, has achieved a fully MEMS oscillator which reduces size and power consumption compared with traditional quartz crystal oscillators (see *Figure 1.3* in which a comparison between both approaches is shown).

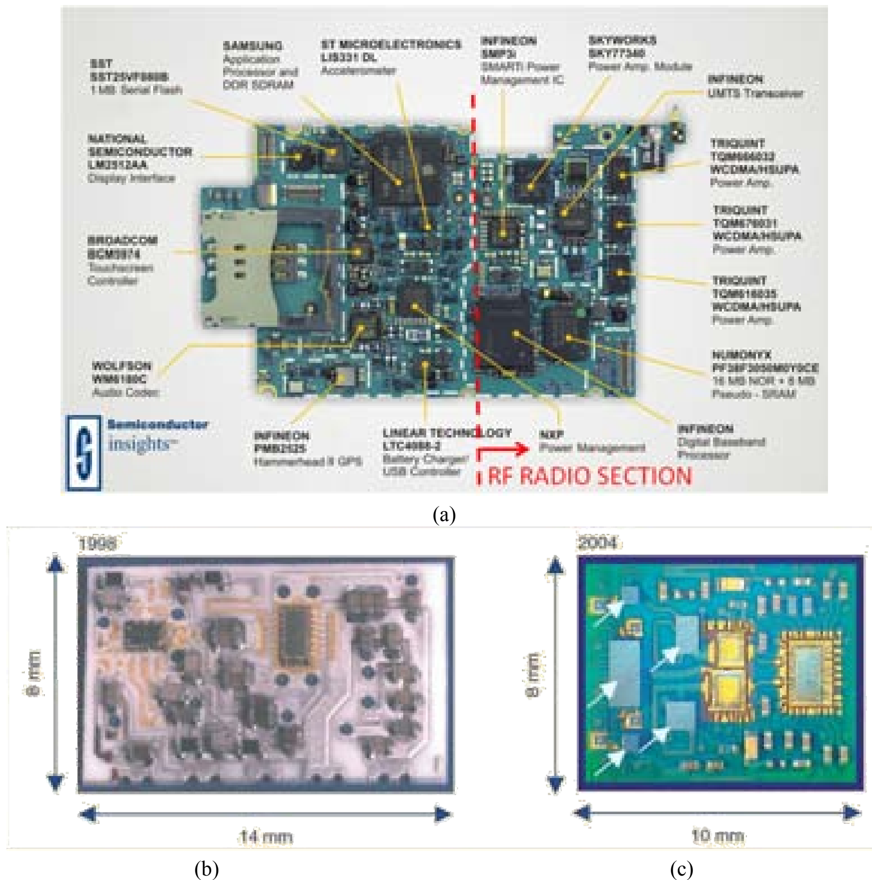

(b) (c)

Figure 1.2: (a) Photograph of a iPhone mobile phone circuitry, RF radio section is highlighted.. (b) Image of a decapsulated GSM commercial power amplifier (BGY241 from Philips), 1998 and (c) Image of an evolved RF transmitter (BGY504) with increased performance and functionality on reduced size, 2004. (b) and (c) images are from [16].

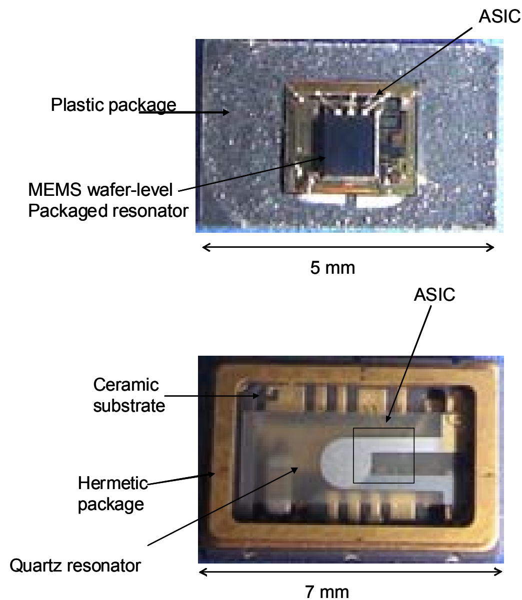

Figure 1.3: Comparison between the size of a MEMS-based oscillator and quartz crystal resonator. (from Discera web page)

The MEMS devices being used for RF applications are simply called RF-MEMS. Under this label, a wide range of devices for different applications (including basically switches, oscillators, filters and mixers) can be found. These RF mechanical devices can be divided in: RF switches, tunable capacitors, high-Q inductors and MEMS resonators (*Figure 1.4*).

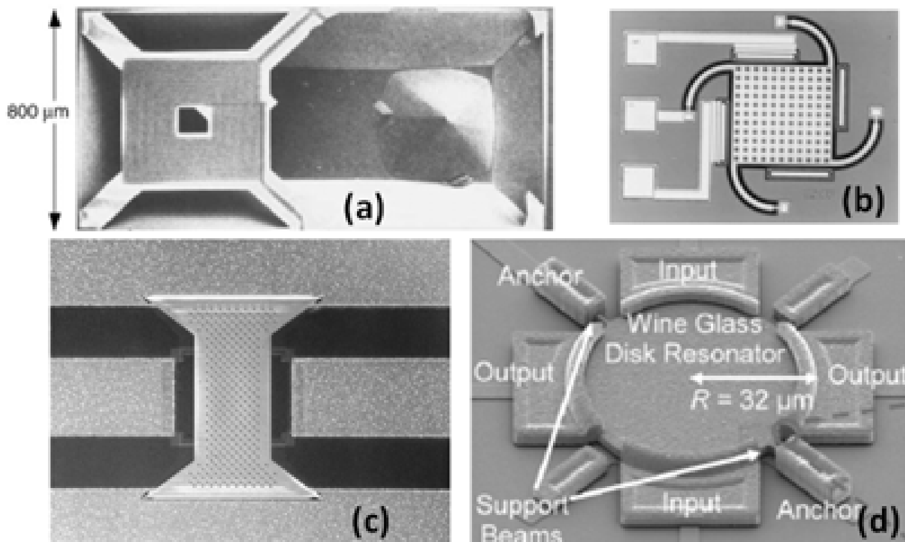

Figure 1.4: Several examples of RF MEMS: a) Suspended inductor [17], (b) DC tunable capacitor [18], (c) RF MEMS switch [19] and (d) MEMS resonator [20]

It is interesting to note, however, that although high-Q inductors are considered RF-MEMS, they are not movable mechanical parts (they do not present displacement) but take advantage of microfabrication techniques for the building of the inductors.

1.1.1 MARKET PERSPECTIVE FOR RF MEMS

It is evident that the wireless market has become one of the most important drivers in consumer electronics. Starting from GSM mobile phone to wireless technologies like WI-FI, Bluetooth and RF-ID, wireless became an important pie in which every company wants its part, and so MEMS designers and manufacturers. Moreover, the use of MEMS is claimed to bring enhancements on RF systems and provide new applications nowadays unpractical by using traditional circuit approaches. Among the most successful MEMS devices (and the first ones to be commercialized) are Bulk Acoustic Wave (BAW) filters and duplexers. The BAW filters are the most mature MEMS devices, however, the roadmap of these devices include cost reduction, increase of performance and integration with CMOS IC, the same challenges to be faced by other MEMS devices (as switches and resonators). For further information see the predictions of the International Technology Roadmap of Semiconductors [21].

Figure 1.5 shows a roadmap of the commercialization of RF-MEMS components from 2002 to 2006 on this roadmap several updates must be highlighted. Only a few of these companies have already reached the commercialization release of their products, like the aforementioned tunable capacitor technology form Philips and included in BGY504. especially relevant is the reference oscillator market. MEMS-based reference oscillators are supposed to help reducing the size of overall RF systems, once that quartz reduction reached a kind of saturation [22]. However, even though forecasts prediction set the start of serial production on 2006, by the hand of Discera, this and other companies have recently started to publish preliminary commercial products datasheets. These delays in the commercialization, can allow purely CMOS high performance oscillators [23, 24] to steal part of the market coveted for MEMS devices.

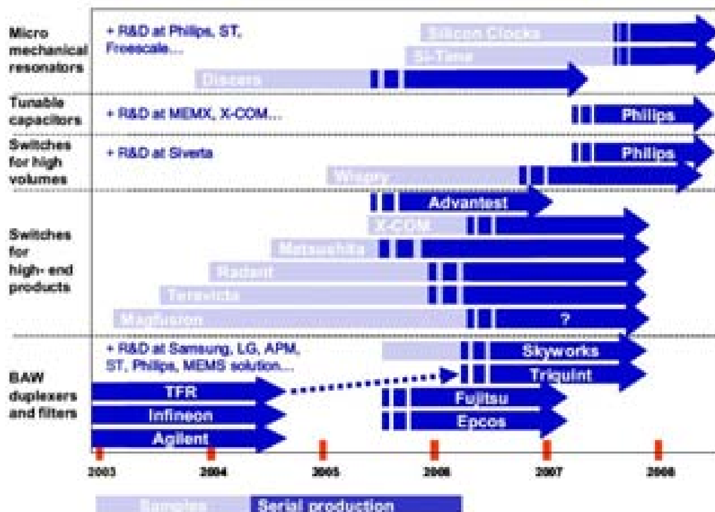

Figure 1.5: Roadmap from 2003 to 2008 of RF MEMS market, extracted from [25]

Figure 1.6 shows a forecast of the evolution of RF market from 2004 to 2009 divided in different applications.

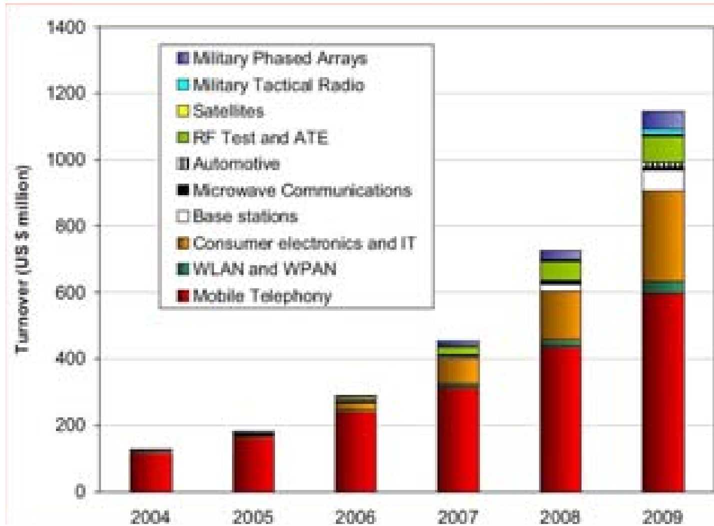

Figure 1.6: Forecast of evolution of RF MEMS market, from [25].

It can be observed in *Figure 1.6* that the highest part of the RF-MEMS market is placed on the mobile telephony, although there is a very important increase in consumer electronics expected beyond 2006.

Another interesting graphic is the one shown in *Figure 1.7*, which shows the estimated public investment on MEMS research per target application on different geographic areas: Europe, USA and Asia on 2004.

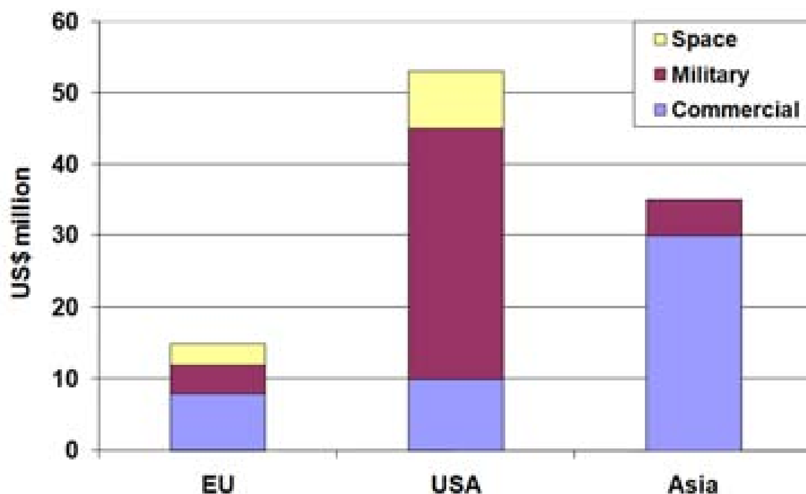

Figure 1.7: Estimated distribution of the public funding for RF MEMS research for geographic area and market in 2004, adapted from [26].

It is significant the big amount of funding in MEMS technologies on USA and Asia, when compared to Europe. Moreover, the target application is quite different in each area: whereas in USA most of the investment was focused on military and space applications, Asia's effort is focused on commercial applications and in Europe it is significant the ratio of the total funding dedicated to space applications.

1.1.2 RF-MEMS Applications on a RF-Front-end

With the successful applications of MEMS in other application markets, and with wireless electronics on the bull's eye of MEMS industry, the question is: how MEMS can improve wireless radios?

Even though this question was partially answered in terms of reconfigurability of RF front-ends using MEMS switches, some of the potential of MEMS resonators has not yet been described. In particular, these resonators show performance exceeding the obtained using integrated passive LC tank-resonators, especially in terms of the quality factor, Q of the inductor, therefore allowing highly frequency selective devices.

Considering the classical RF receiver architectures, they can be divided into: (super) hetherodyne, low-IF and zero-IF [27]. Every RF receiver works in a similar way: the RF signal received in the antenna is filtered to consider only the application interest band, attenuating all other interferers. The filtered signal is then amplified by the low-noise amplifier and then down-converted in frequency (baseband frequency) for signal processing. It is in this down-conversion where the main difference between the aforementioned architectures exists. In zero-IF receivers, the radio signal is directly down-converted to the baseband signal (nearly DC), on low-IF the down-conversion is located at low frequency. These two architectures have a single down-conversion stage, whereas hetherodyne receivers use two (or more) down-conversion stages. One of the most important problems for the RF receivers is the image frequency, because any non-desired signal at this frequency will be down-converted at the same frequency than the desired channel. Every architecture presents different alternatives to alleviate this effect [28]. Zero-IF receiver presents difficulties due to the circuitry flicker noise. For this reason, only the low-IF and the hetherodyne solutions will be considered., To sum up, the superhetherodyne architecture allows to relax the circuit elements requirements as the topology relies on high-Q passives (and therefore not integrable), whereas on the low-IF architecture the image rejection is performed by using two different channels for mixing. For this integration reason, the low-IF architecture is the more widely used for monolithic integration of RF receivers. Considering the integration of MEMS devices in the previous discussion, the hetherodyne scheme shows no clear disadvantages when compared to zero-IF, as MEMS resonators are expected to have the high Q required for this architecture.

Figure 1.8(a) shows the classic super-hetherodyne front-end receiver, with all the MEMS-replaceable functions shaded (i.e. switch, filter, mixer and oscillator). This architecture consists on a first stage of filtering (the channel selection filter) and amplification, followed by two additional stages of frequency down-conversion. *Figure 1.8 (b)* shows a multiband radio based on low-IF receiver architecture [29]. It can be observed an important increase in the filters and passives due to the multi-band architecture.

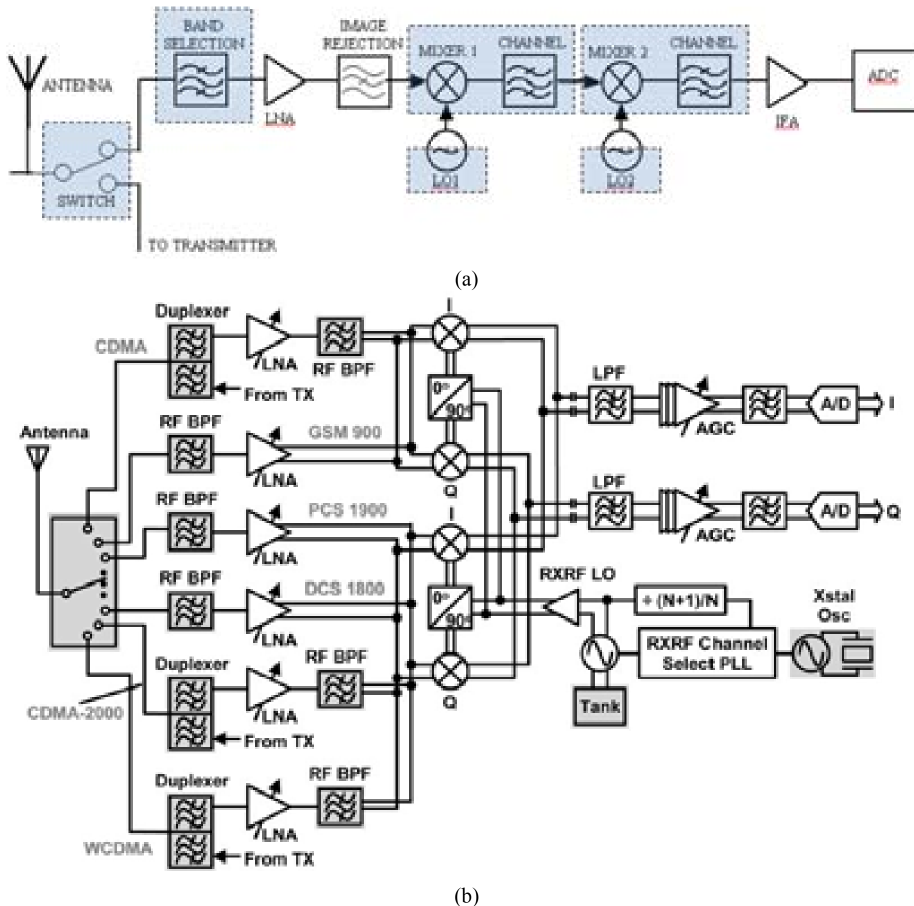

Figure 1.8: (a) Super-heterodyne RF receiver. (b) Low-IF multiband front-end receiver, from [29]. In both figures the MEMS replaceable parts are shaded.

The band selection filters require bulky off-chip elements. By using MEMS resonators, these massive elements can be substituted by tiny on-chip integrated devices. Which as observed in previous figure could be crucial for multiband devices.

To further understand the potential of MEMS resonators, we'll consider the GSM specifications using a conventional filter and a MEMS-based channel selection filtering scheme. *Figure 1.9(a)* shows a typical spectrum diagram at the antenna of the receiver. In this figure it can be observed the frequency band of interest (marked with an arrow), and other signal interferers (from other wireless protocols, for instance) present in the environment. As shown in *Figure 1.9 (b),* the other undesired signals are filtered using the pre-selection filter (which requires a low Q, Q=500). Usually the requirements of the RF protocols, GSM-1800 for example, are based on the un-filtered near-channel interferers, that are not filtered in this early stage, because they are on the frequency band of interest, *Figure 1.9(b).* An additional channel selection filtering (with Q=10000) is required. This high Q filtering is normally performed after the first down-conversion stage, alleviating the Q-frequency product requirement in RF receivers.

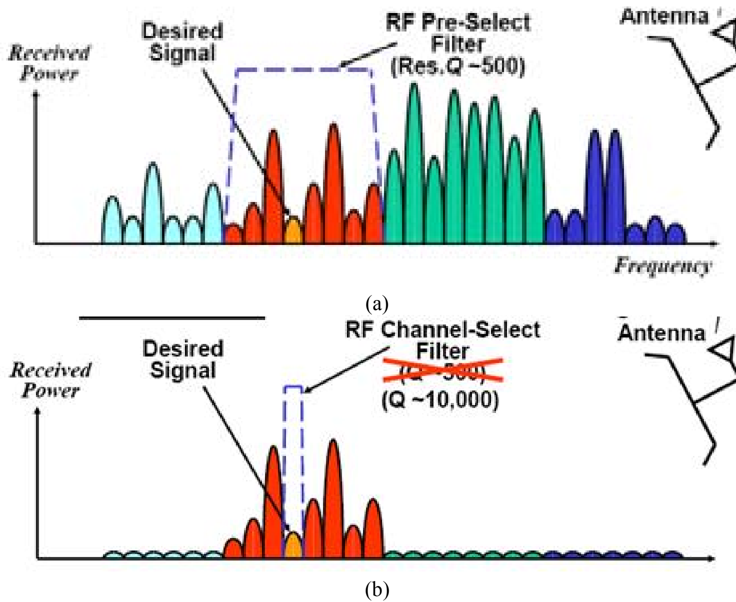

Figure 1.9: Received signal spectrum in a receiver antenna. Before (a) and after (b) the RF pre-select filter.

The direct channel selection architecture performs the channel filtering once the signal is received in the antenna. Therefore, the resulting spectrum can be observed in *Figure 1.10 (a)*. In order to be capable to select all channels, *Figure 1.10 (b*), a bank of MEMS-based filters, like the one shown in *Figure 1.10 (c)*, must be employed. Because of the micrometric size of this filter bank area is not a problem for the use of this architecture. However, the most important challenge of this topology is to provide very high Q resonators (in the order of 10000) at RF frequencies.

To further analyze the improvement in terms of phase noise requirements obtained by this receiver topology, the requirements of a receiver of the DSC-1800 (GSM-1800) wireless protocol using the conventional approach and the direct-channel selection will be compared considering the phase noise requirements of the LO oscillator for the first down-conversion stage.

The phase noise requirements are constrained by in-band interferers; in particular, the standard sets the blocking signals at 600kHz, 1.6MHz and 3MHz away than the desired signal frequency. This signal with -99dBm power must be detected with a 2% Bit Error Rate (BER) under the power blocking signals depicted in *Figure 1.11*.

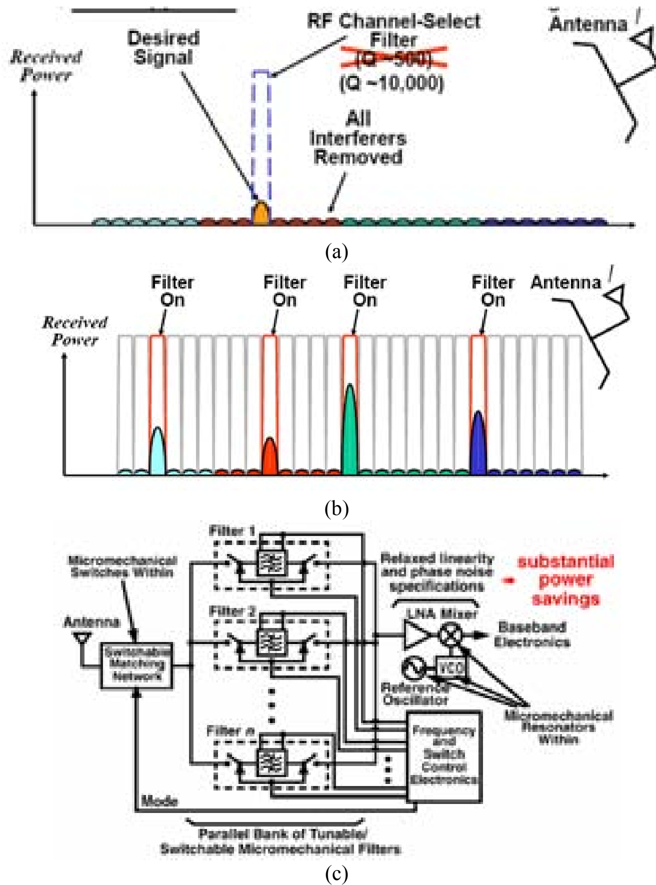

(c)

Figure 1.10: Direct RF filtering scheme. (a) Received signal spectrum after direct RF channel selection. (b) Bank filter selection spectrum and (c) Schematic diagram of a MEMS filter bank receiver [30].

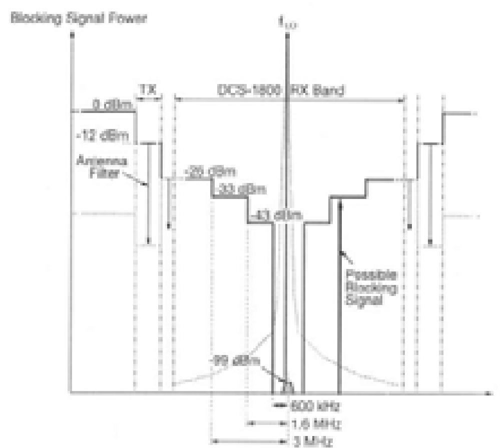

Figure 1.11: Blocking signals diagram for GSM-1800, from [28].

From these requirements the local oscillator phase noise for a conventional receiver (Low-IF, zero-IF and superhetherodyne) can be found, as shown in *Table 1.1*. Reader is referred to [28] for a extended description of the process of obtaining these values.

Table 1.1: Phase noise requirements for a DSC-1800 local oscillator using a conventional receiver topology

Freq offset	Phase noise (dBc/Hz)
600kHz	-116
1.6MHz	-126
3MHz	-133

Considering a direct channel filter architecture with 40dB stop band attenuation, the blocking signals would be attenuated accordingly, providing a 40dB relaxation on the LO phase noise requirements, as shown in *Table 1.2*.

Table 1.2: Phase noise requirements for a DSC-1800 local oscillator using a conventional receiver topology and high selectively direct channel filter

Freq offset	Phase noise (dBc/Hz)
600kHz	-76
1.6MHz	-86
3MHz	-93

This relaxation in the LO phase noise requirement, would allow extra room to reduce the power consumption of the LO and would also reduce the linearity requirements for the subsequent elements of the chain. Even though the evident benefits of the use of MEMS for selective filtering, obtaining a MEMS with the required Q at GHz frequencies can be very challenging, as it was aforementioned.

In view of the importance of the RF-MEMS for improving wireless communication systems explained in this section, and considering that further research for achieving high performance MEMS in each of the applications summarized is needed, we can state the motivation of this thesis: contribute to the study, design and fabrication of novel MEMS devices for its application in wireless communication systems. To further analyze the world of RF-MEMS and stablish the specific objectives of the thesis, a brief introduction on fabrication aspects is needed (next section).

1.2 FABRICATION TECHNOLOGIES

As it was aforementioned, MEMS succeeded in replacing classic solutions thanks to: 1) Improving performance and/or 2) Reducing fabrication costs. By adopting some of the IC manufacturing processes, the reduction of the fabrication cost per unit is inherently reduced in batch fabrication, where multiple devices are fabricated at the same time. There are, however, other factors that have to be considered. Among these factors, the most important are the integration of these mechanical structures with processing electronics and the packaging of the complete system. This section presents the different fabrication procedure and the options to integrate MEMS and circuitry.

Basically, the fabrication of MEMS devices are based on successive steps which include material deposition, material patterning and material removal, the same used in conventional integrated circuits fabrication process (*Figure 1.12*).

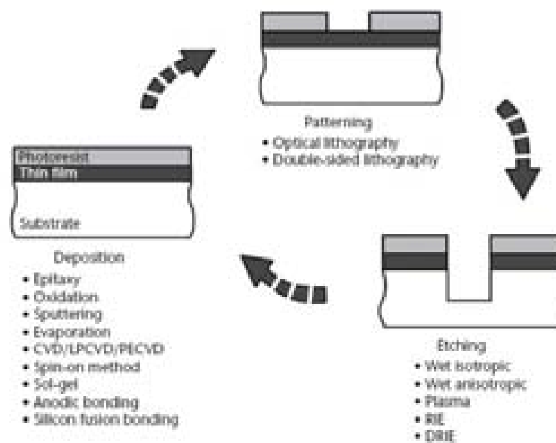

Figure 1.12: Scheme of the basic steps of microfabrication [31].

Classically, there are two basic ways to perform the micromachining process, that is the fabrication of the structure: surface and bulk micromachining (*Figure 1.13*). In surface micromachining, the removed layer is a thin layer of material, whereas bulk micromachining comprises removal of big amount of material. In most bulk micromachining the silicon wafer is the etched material.

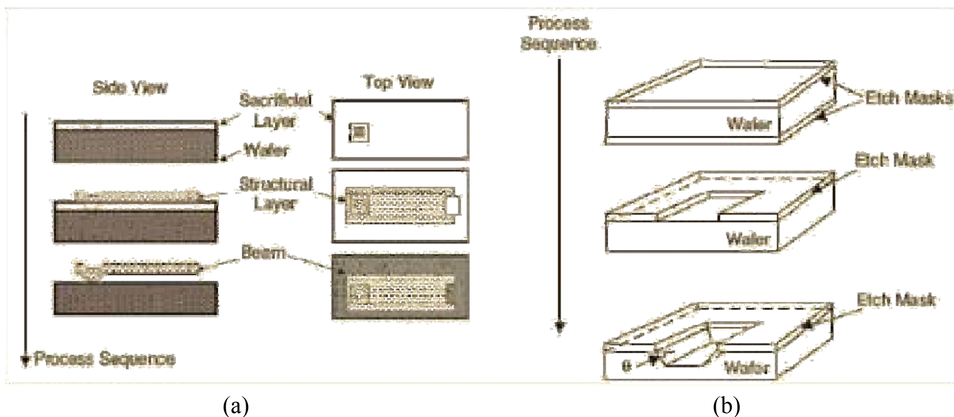

(a) (b)

Figure 1.13: (a) Surface micromachining and (b) Bulk micromachining, from [32]

Even though the great range of applications of MEMS devices, the fact that baseband signal processing is performed digitally, which historically became an important factor for cost reduction [12], makes necessary to consider the interconnection between MEMS devices and IC circuitry (usually CMOS). There are basically two concepts on integration of mechanical devices and electronics: 1) System-in-Package (SiP) and 2) System-on-chip (SoC).

1.2.1 SYSTEM IN PACKAGE

In SiP approach, the MEMS and IC have different substrates. The MEMS devices are fabricated in a dedicated process, and therefore have potentially better mechanical performance (for example thicker structures). The circuitry can be fabricated on standard IC foundries, reducing

fabrication cost and obtaining the highest electrical performance available with advanced technologies. On one hand, this modularity is positive, as it allows using state of the art technologies for both MEMS and IC components, but on the other hand the complexity is transferred to interconnection and packaging achieving at the same time bigger devices.

The interconnection between mechanical devices and electronics can be performed by means of multiple-chip wafer bonding [33], flip-chip bonding [34] or 3-D stacking of multiple chips [35] (*Figure 1.14*).

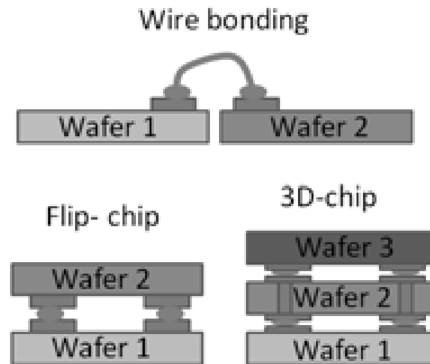

Figure 1.14: Options for wafer interconnection: wire-bonding, flip chip and 3D stacking technology

Moreover, the fact of using two different processes increases the complete cost of fabrication, and decrease fabrication yield. Furthermore, this approach presents an increase interconnection parasitic capacitor due to the big area required for the electrical connection PADs. This parasitic capacitor can be especially troublesome on high-frequency applications.

1.2.2 System on Chip

In SoC, MEMS and circuitry are placed and fabricated on the same substrate. For this reason, mechanical devices, electronic circuits (or both) must face additional constrains. On the other hand this monolithic integration offers lower cost than SiP fabrication and lower interconnection parasitics. For these reasons, this thesis will focus into monolithic integration of mechanical devices on commercial CMOS technologies. Unfortunately, SoC approach increases the complexity of the overall design and limits performance of mechanical and/or electronic devices. For integration and cost effectiveness, most widely used substrates and processes for this approach are Si wafers and CMOS IC fabrication. Considering this, the fabrication process of MEMS together with circuitry can be classified in: 1) Pre-CMOS or MEMS-first, 2) Intra-CMOS or 3) Post-CMOS or MEMS-last [36, 37].

In MEMS-first process, most of the mechanical part definition is carried out before the beginning of the front-end-of-line IC fabrication process, i.e. before transistors definition steps. Most of these MEMS processes use Silicon-on-Insulator (SOI) wafers and after the definition of the mechanical devices, the wafers are delivered to an IC foundry for CMOS fabrication. An important factor for the success of this approach is the acceptance by the IC foundry of the pre-processed wafer [38].

An example of the use of this MEMS-first approach, is the Mod- MEMS process developed by Analog Devices and the University of California, Berkeley [39], which process is shown in *Figure 1.15(a)*. This process is an evolution of the iMEMS process also from Analog Devices, that will be

explained in the Intra-CMOS processes. This SOI-MEMS process is mainly used in gyroscopes and improves material thickness and electronics complexity when compared to previous iMEMS process. An example of this process is the commercial ADIS16350 [40], able to provide a digital output signal. *Figure 1.15(b)* shows the schematic cross-section of the fabricated device and *Figure 1.15(c)* shows an optical photograph of the complete gyroscope chip fabricated using this technique.

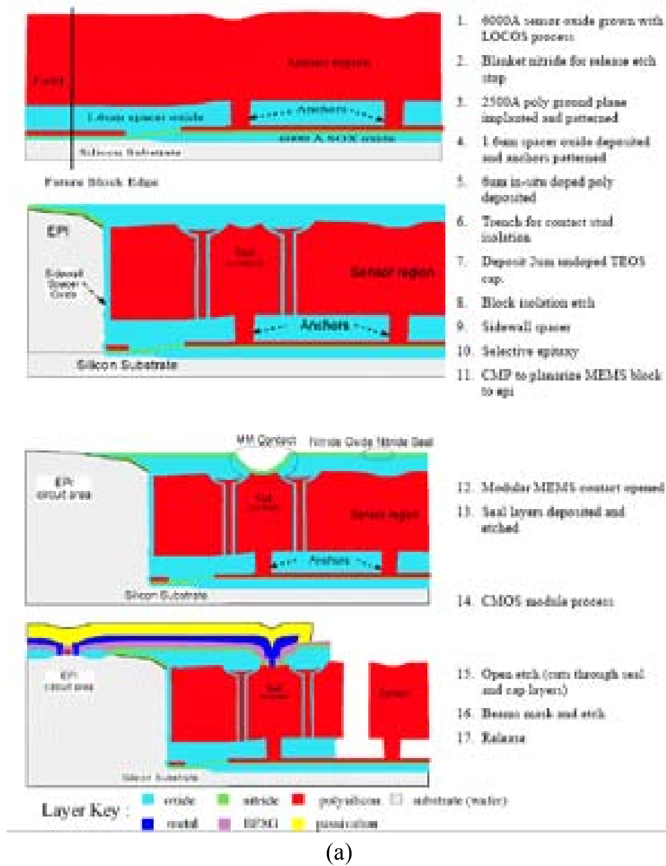

(a)

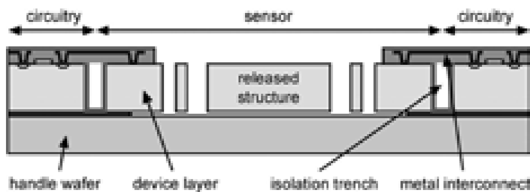

(b)

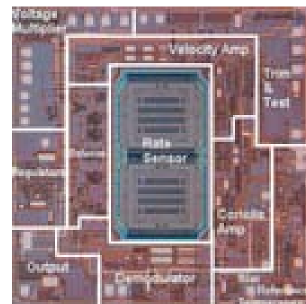

(c)

Figure 1.15: Mod-MEMS process of Analog Devices. (a) Process steps cross-section, from [39]. (b) Final cross-section, from [41]. (c) Completely processed sensor top view photograph.

Because MEMS releasing is an additional post-process step, it would be highly desiderable to release the structure in early fabrication steps to avoid post-processing. Recent works of the Mechanical Engineering dept. of Stanford University [42] allows not only the releasing of MEMS before entering the IC foundry (*Figure 1.16*), but also hermetically sealing the mechanical device, protecting it from moisture and allowing vacuum encapsulation [43].

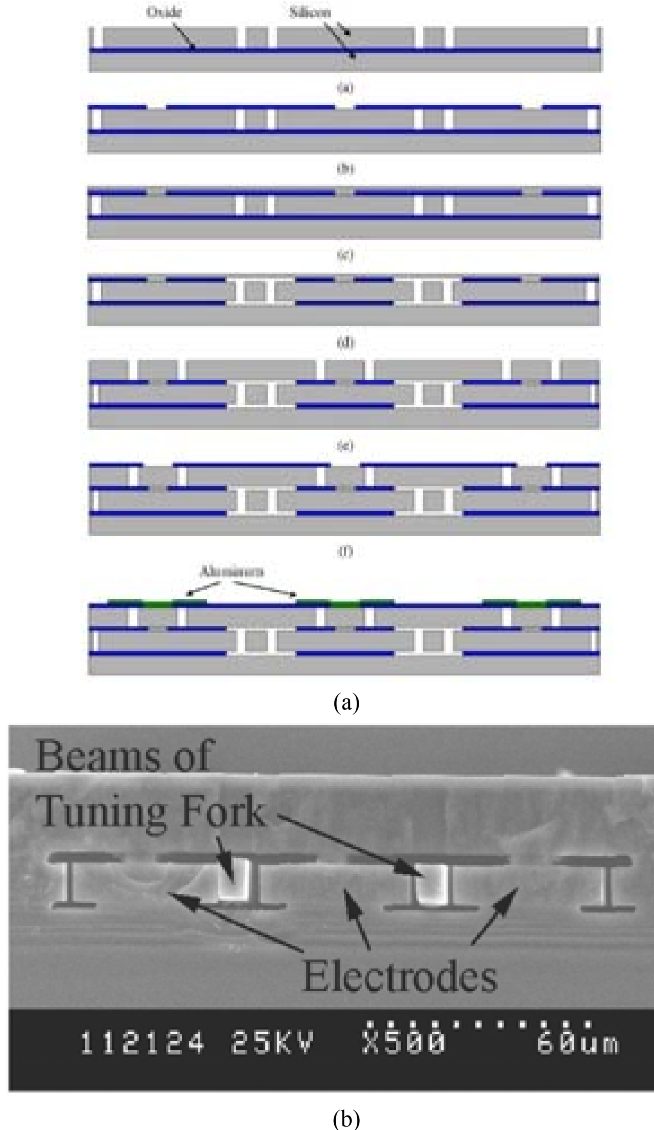

(a)

(b)

Figure 1.16: (a) SOI-MEMS fabrication process cross-section and (b) SEM cut-off cross section of the fabricated and encapsulated device. This image is from a device reported in [42] and developed with the same fabrication process.

In intra-CMOS approach a few processing steps are introduced in the standard IC process before the start of the back-end of line metallization [6], see *Figure 1.17(a)*. Another interesting process is the aforementioned iMEMS process from Analog Devices [38], shown in *Figure 1.17*

(b). However, several compromises in the IC must be taken to fabricate MEMS and circuitry using the same processes: in particular big channel length technologies (3µm in the case of Analog Devices process) are used to withstand the thermal budget imposed by the mechanical structure fabrication process. The use of these old technologies, doubtless affects the cutoff frequency of the IC circuitry. Obviously this approach cannot be followed to fabricate RF systems.

The process used in this thesis can also be considered in this category. As will be further explained in Chapter 3, the MEMS are fabricated using the interconnection layers present in the IC process to define the structure without the need of altering the CMOS standard process. This approach only requires the etching of the oxide that surrounds the movable part of the structure, performed out of foundry facilities once the CMOS process was completely finished.

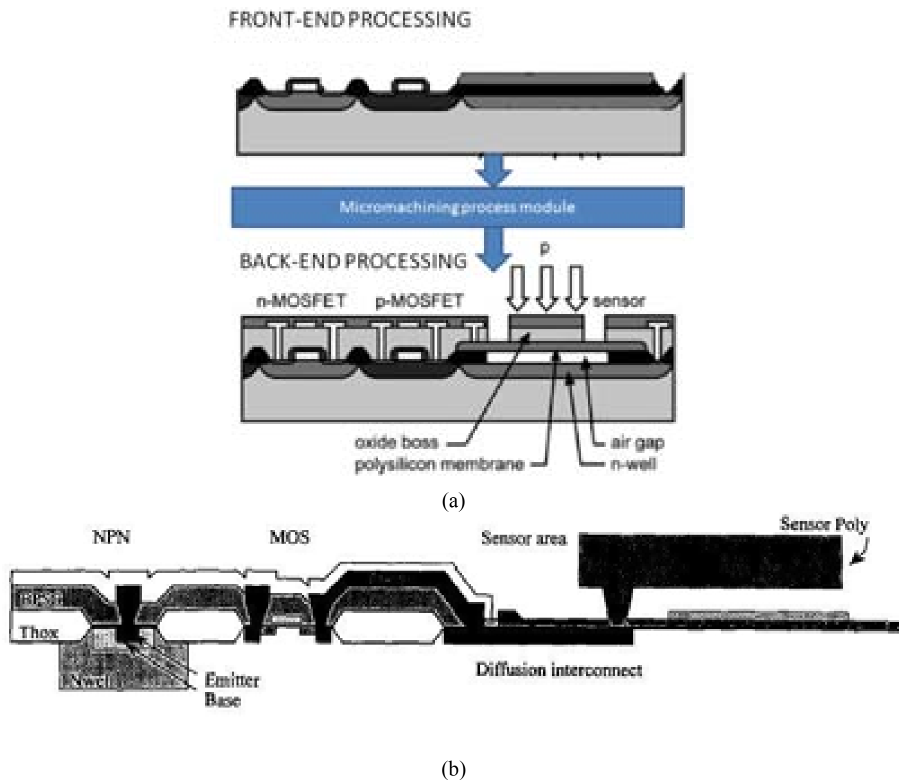

Figure 1.17: (a) Infineon (former Siemens Semiconductors), intra-CMOS pressure sensor process sequence, adapted from [6] and [41]. (b) iMEMS Analog Devices process, from [38].

In post-CMOS processes, the MEMS are fabricated in a separate process once the IC fabrication is completed. MEMS are fabricated above top metal interconnection layer. This vertical stacking makes this fabrication approach the most area-effective because no chip area is dedicated to place the mechanical devices, however this approach constrains seriously the thermal budget of MEMS process, as the fabricated electronics must remain unaffected, which becomes quite challenging for CMOS technologies below 0.35um [44, 45], compromising the modularity of this approach.

Recent advances in post-CMOS processes allowed a CMOS-MEMS oscillator on a 0.35um CMOS process with electroplated nickel and without exceeding 50ºC along the MEMS fabrication process [46] (*Figure 1.18*), therefore avoiding the thermal budget constrains of modern technological process. Another interesting post-CMOS process that avoids the thermal budget is the process developed in Carnergie Melon University, in which the metal interconnection layers of the CMOS technologies are used. The group of Dr. Fedder, developed two different processes [47], which differ between them in the use of part of the silicon wafer as a constituent part of the resonator. In the first process, the mechanical structure is defined using an oxide Reactive Ion Etching (RIE),for which top metal layer acts as a mask, a silicon DRIE (Deep RIE), and a isotropic silicon etch to finally release the structure, see *Figure 1.19(a)*. On the second process, the wafer is previously silicon etched from the backside, before starting the aforementioned microfabrication process, see *Figure 1.19(b),* and therefore part of the structure is made of silicon.

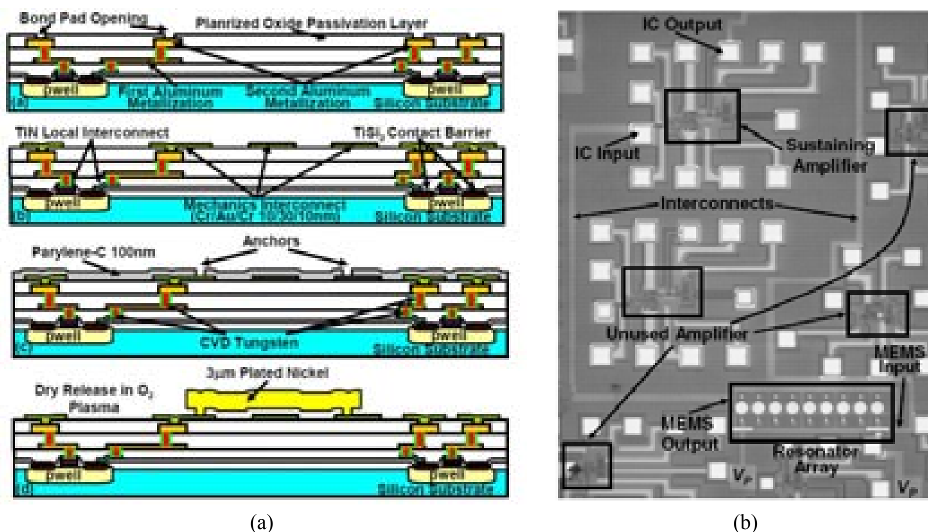

(a) (b)

Figure 1.18: (a) CMOS-compatible nickel electroplating MEMS-last process and (b) Complete fabricated chip showing MEMS resonators and oscillator circuitry. Both images are from [46] .

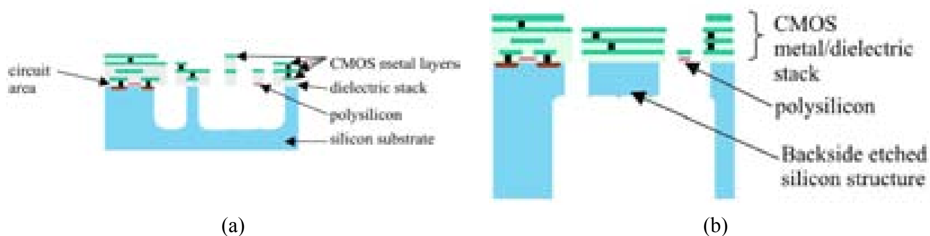

(a) (b)

Figure 1.19: Completely processed CMOS-MEMS cross-section using Carnergie Melon process. (a) Surface micromachining process and (b) bulk micromachining, form [44].

1.2.3 PACKAGING

Once MEMS resonators are fabricated, there is still an important issue: packaging [48-51]. Released MEMS devices for RF applications present movable parts that need to be protected during handling and final encapsulation against moisture and contamination. For this reason first

packaging of the device should be preferably performed at wafer level, right after the end of MEMS release. This first packaging, similar to the passivation layer in CMOS technology is called zero-level packaging. Among the main requirements of this first packaging are [32]:

1. Protection against handling and harsh environments during assembly and operation.
2. Controlled cavity environment (including vacuum conditions)
3. Good electrical performance of through shell signal paths.
4. Low temperature sealing process (subjected to thermal budget).
5. Easy integration with MEMS and IC process

This zero-level packaging can be performed by two main methods thin film sealing (*Figure 1.20-a*) and chip capping (*Figure 1.20-b*) [51]. In thin film sealing a layer of material is deposited above the un-etched MEMS device, the sacrificial layer is later removed through the unsealed etching channels[52] or by using a film permeable to the etchant [53]. On chip capping a cap of glass (or a micromachined wafer) is bonded to the MEMS substrate [54, 55].

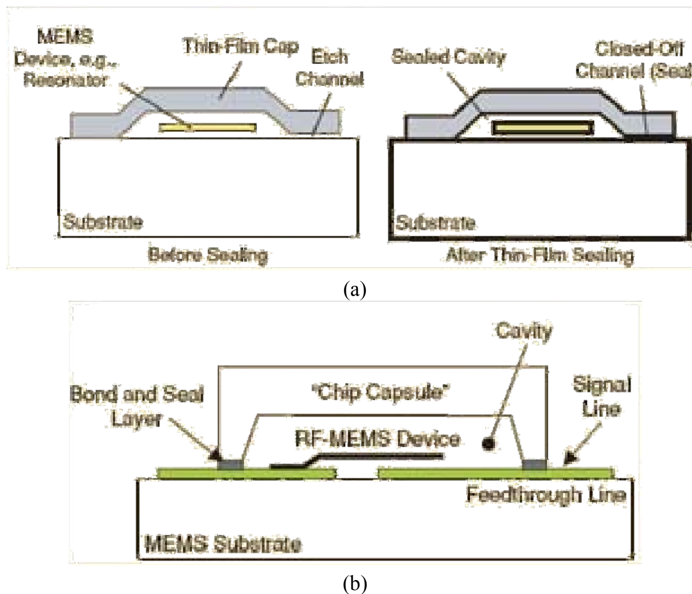

Figure 1.20: Zero-level MEMS packaging. (a) Thin film sealing and (b) Chip capping. Both figures from [32]

Once this zero-level packaging is done, the MEMS device is ready for commercial packaging (*Figure 1.21*) [49], or following the system on package approach, the packaged MEMS can be bonded to other functional substrates [56].

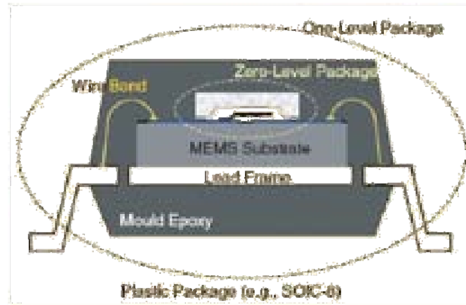

Figure 1.21: Commercially packaged MEMS, from [32]

1.3 RESEARCH FRAMEWORK OF THE THESIS

The research work presented in this thesis was carried out in the Electronics Circuits And Systems Group (ECAS) of the Universitat Autònoma de Barcelona. The main activity of the group is the development of new electronics systems based on high performance microelectronic circuits. Among the current research lines are high performance nanomechanical mass sensors, integration of MEMS resonators and IC circuits, RF-MEMS and MEMS for energy harvesting. The application scenario (which involves the whole group research lines) is a wireless sensor network node. Each node of this network is composed with an environmental energy harvester, a sensor and a wireless transmitter and receiver (*Figure 1.22*)

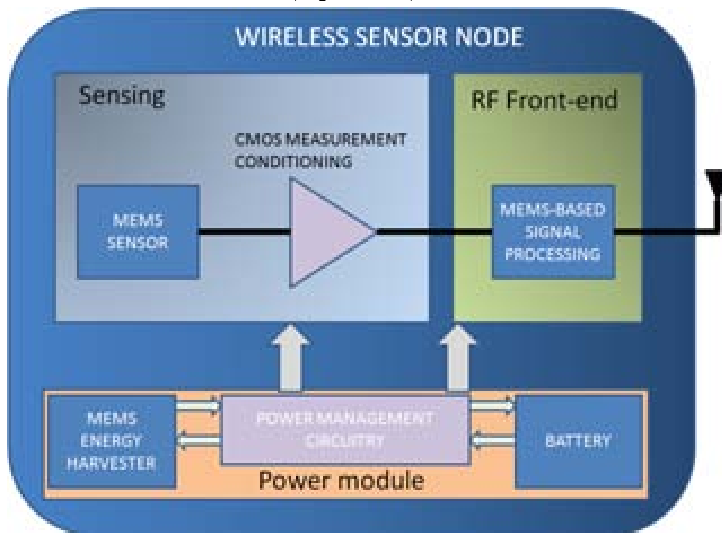

Figure 1.22: Wireless sensor node block diagram.

This research was developed mainly under two different projects: NANOSYS and MEMSPORT, both funded by MEC.

Figure 1.23 shows the timeline of these projects in which ECAS was involved. Nanomass II (IST2001-***33068),*** was an European Project dealing with the design and fabrication of nanoscaled MEMS resonators using nanotechnological approaches with integrated circuitry for high sensitivity and high spatial resolution mass detection. Althought the results achieved in this project

were not part of this thesis, part of the know-how acquired by the group researchers was fundamental for the forthcoming projects: Nanosys and Memsport, which are the core of this thesis.

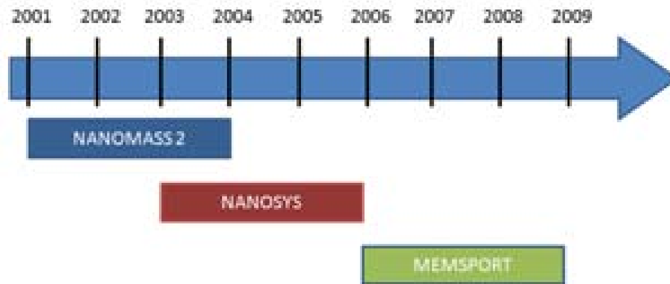

Figure 1.23: ECAS research projects timeline

1.3.1 NANOSYS (TIC2003-07237-C03-02)

This project was carried out under national research funding under the title "*Sistemas micro-nanoelectromecanicos con circuitos CMOS de bajo consumo para la transduccion y procesado de Senales en aplicaciones portable*s". The objective of this project was to develop MEMS and low power circuitry for portable applications, focusing in wireless communications and sensing. The MEMS resonators were designed using CMOS technology.

1.3.2 MEMSPORT (TEC2006-03698/MIC)

This project was carried out under national research funding under the title "*Explotación de la aplicabilidad de elementos integrados MEMS-CMOS monolíticos y heterogéneos para sistemas portátiles y autónomos de altas prestaciones (MEMSPORT)*". The objectives of this project were the development of resonant microelectromechanical elements MEMS and their CMOS associated circuitry. Among these MEMS-resonator based, there are RF building blocks like filters and oscillators, sensors and ambient energy harvesting with the purpose of providing autonomy to the power supply of the global system.

1.4 THESIS: OBJECTIVES AND OUTLINE

The main objective of this thesis is the development and study of MEMS resonators fabricated in standard CMOS technologies for RF applications. This general objective is divided in:

1. Analysis of the possibilities of including MEMS resonators in a RF frontend, obtaining the design objectives for each application and highlighting the challenges to face for a successful implementation of MEMS.

2. Study the viability of the RF-MEMS fabrication process in advanced sub-micron CMOS technologies and determine the benefits and improvement as RF devices

3. Design, fabricate and characterize different MEMS resonators fabricated in CMOS commercial technology for different RF signal processing applications (mainly filters and mixers).

The thesis has been divided in 5 chapters, without considering the first chapter (introduction), they are outlined as:

Chapter 2: Introduces the working principle of capacitively excited and transduced MEMS resonators, the main characteristics of these resonators for main RF signal processing functions and presents the state-of the art of MEMS devices for RF applications.

Chapter 3: Describes the technological process used to fabricate the devices of this thesis. A figure of merit to select the most optimal layer to fabricate MEMS resonators in CMOS technologies is introduced. It is also presented a proof of concept of MEMS fabrication in a 0.18um CMOS technology.

Chapter 4: In this chapter the results of the fabricated CMOS-MEMS resonators for frequency references and resonator building blocks are described.

Chapter 5: The results of applications of the MEMS resonator as filters, mixers and oscillators are shown in this chapter.

These final results will be compared with previous results and state-of-the art devices.

Three annexes have been included: in the first one the design equations for each reported MEMS device together with design guidelines are provided. The second annex describes briefly the experimental instrumentation available at ECAS labs, together with an explanation of the test setup employed in each kind of measurement. It briefly includes a discussion of the causes of the low power levels measured and the technique for the equivalent electrical circuit determination to model the mechanical behaviour. Finally, on annex 3 a brief description of each IC RUN carried out for this thesis can be found.

REFERENCES

[1] R. P. Feynman, "There's Plenty of Room at the Bottom," *Journal of Microelectromechanical Systems,* vol. 1, pp. 60-66, 1992 (Reprinted from a 1959 conference).

[2] H. C. Nathanson, W. E. Newell, R. A. Wickstrom, and J. R. Davis, Jr., "The resonant gate transistor," *Electron Devices, IEEE Transactions on,* vol. 14, pp. 117-133, 1967.

[3] P. Krause, E. Obermeier, and W. Wehl, "Backshooter - A New Smart Micromachined Single-chip Inkjet Printhead," in *Solid-State Sensors and Actuators, 1995 and Eurosensors IX.. Transducers '95. The 8th International Conference on*, 1995, pp. 325-328.

[4] K. H. L. Chau, S. R. Lewis, Y. Zhao, R. T. Howe, S. F. Bart, and R. G. Marcheselli, "An Integrated Force-balanced Capacitive Accelerometer For Low-G Applications," in *Solid-State Sensors and Actuators, 1995 and Eurosensors IX.. Transducers '95. The 8th International Conference on*, 1995, pp. 593-596.

[5] "Analog Devices iMEMS."

[6] T. Scheiter, H. Kapels, K. G. Oppermann, M. Steger, C. Hierold, W. M. Werner, and H. J. Timme, "Full integration of a pressure-sensor system into a standard BiCMOS process," in *EUROSENSORS XI Meeting*, Warsaw, Poland, 1997, pp. 211-214.

[7] L. J. Hornbeck, "Digital Light Processing™: A New MEMS-Based Display Technology ": Texas Instruments White Papers (Available online at: www.ti.com/dtl).

[8] P. Vettiger, G. Cross, M. Despont, U. Drechsler, U. Durig, B. Gotsmann, W. Haberle, M. A. Lantz, H. E. Rothuizen, R. Stutz, and G. K. Binnig, "The "millipede" - nanotechnology entering data storage," *Nanotechnology, IEEE Transactions on,* vol. 1, pp. 39-55, 2002.

[9] R. Bashir, "BioMEMS: state-of-the-art in detection, opportunities and prospects," *Advanced Drug Delivery Reviews,* vol. 56, pp. 1565-1586, 2004.

[10] P. S. Waggoner and H. G. Craighead, "Micro- and nanomechanical sensors for environmental, chemical, and biological detection," *Lab Chip,* vol. 7, pp. 1238–1255, 2007.

[11] Akustica, "AKU1126 Product Brief " *Available on-line at* http://www.akustica.com.

[12] A. A. Abidi, "RF CMOS comes of age," *Solid-State Circuits, IEEE Journal of,* vol. 39, pp. 549-561, 2004.

[13] A. de Graauw, C. Copetti, and W. Weekamp, "A new thin film passive integration technology for miniaturisation of mobile phone front end modules: integration of a dual-band power amplifier, switch and diplexer for GSM," in *Microwave Symposium Digest., 2000 IEEE MTT-S International*, 2000, pp. 1925-1928 vol.3.

[14] T. Rijks, P. G. Steeneken, J. T. M. van Beek, M. J. E. Ulenaers, A. Jourdain, H. A. C. Tilmans, J. De Coster, and R. Puers, "Microelectromechanical tunable capacitors for reconfigurable RF architectures," *Journal of Micromechanics and Microengineering,* vol. 16, pp. 601-611, Mar 2006.

[15] Discera, http://www.discera.com.

[16] H. J. De Los Santos, G. Fischer, H. A. C. Tilmans, and J. T. M. van Beek, "RF MEMS for ubiquitous wireless connectivity. Part II. Application," *Microwave Magazine, IEEE,* vol. 5, pp. 50-65, 2004.

[17] J. Y. C. Chang, A. A. Abidi, and M. Gaitan, "Large suspended inductors on silicon and their use in a 2-μm CMOS RF amplifier," *Electron Device Letters, IEEE,* vol. 14, p. 246, 1993.

[18] A. Dec and K. Suyama, "Microwave MEMS-based voltage-controlled oscillators," *Microwave Theory and Techniques, IEEE Transactions on,* vol. 48, p. 1943, 2000.

[19] Z. J. Yao, S. Chen, S. Eshelman, D. Denniston, and C. Goldsmith, "Micromachined low-loss microwave switches," *Microelectromechanical Systems, Journal of,* vol. 8, pp. 129-134, 1999.

[20] Y.-W. Lin, S. Lee, S.-S. Li, Y. Xie, Z. Ren, and C. T. C. Nguyen, "Series-resonant VHF micromechanical resonator reference oscillators," *Solid-State Circuits, IEEE Journal of,* vol. 39, pp. 2477-2491, 2004.

[21] "International Technology Roadmap for Semiconductors: Radio Frequency and Analog/Mixed-Signal Technologies for Wireless Communications," 2007.

[22] W.-T. Hsu, "Resonator miniaturization for oscillators," in *Frequency Control Symposium, 2008 IEEE International*, 2008, pp. 392-395.

[23] M. S. McCorquodale, "Self-referenced, trimmed and compensated RF CMOS harmonic oscillators as monolithic frequency generators," in *Frequency Control Symposium, 2008 IEEE International*, 2008, pp. 408-413.

[24] M. S. McCorquodale, J. D. O'Day, S. M. Pernia, G. A. Carichner, S. Kubba, and R. B. Brown, "A Monolithic and Self-Referenced RF LC Clock Generator Compliant With USB 2.0," *Solid-State Circuits, IEEE Journal of,* vol. 42, pp. 385-399, 2007.

[25] J. Bouchaud, B. Knoblich, and H. Wicht, "Will RF MEMS live up their promise?," in *Microwave Conference, 2006. 36th European*, 2006, pp. 1076-1079.

[26] J. Bouchaud and H. Wicht, "RF MEMS: status of the industry and roadmaps," in *Radio Frequency integrated Circuits (RFIC) Symposium, 2005. Digest of Papers. 2005 IEEE*, 2005, pp. 379-384.

[27] B. Razavi, *RF microelectronics*. Upper Saddle River, NJ: Prentice Hall, 1998.

[28] J. Janssens and M. Steyaert, *CMOS CELLULAR RECEIVER FRONT-ENDS: From Specification to Realization*: Kluwer Academic Publishers, 2002.

[29] C. T. C. Nguyen, "MEMS technology for timing and frequency control," *Ultrasonics, Ferroelectrics and Frequency Control, IEEE Transactions on,* vol. 54, pp. 251-270, 2007.

[30] C. T. C. Nguyen, "Micromechanical Resonators for Miniaturized Low-Power Wireless Communications, Keynote in 11th International Conference on Wireless Communications (Wireless'99), Calgary, Canada," 1999.

[31] N. Maluf and K. Williams, *Introduction to microelectromechanical systems engineering*, 2nd ed. Boston: Artech House, 2004.

[32] H. J. De Los Santos, G. Fischer, H. A. C. Tilmans, and J. T. M. van Beek, "RF MEMS for ubiquitous wireless connectivity. Part I. Fabrication," *Microwave Magazine, IEEE,* vol. 5, pp. 36-49, 2004.

[33] A.-C. Wong, Y. Xie, and C. T. C. Nguyen, "A Bonded-Micro-Platform Technology for Modular Merging of RF MEMS and Transistor Circuits," in *11th Int. Conf. on Solid-State Sensors & Actuators (Transducers'01)*, Munich, Germany, 2001, pp. 992-995.

[34] A. P. De Silva and H. G. Hughes, "The package integration of RF-MEMS switch and control IC for wireless applications," *Advanced Packaging, IEEE Transactions on [see also Components, Packaging and Manufacturing Technology, Part B: Advanced Packaging, IEEE Transactions on],* vol. 26, p. 255, 2003.

[35] E. Beyne, "The rise of the 3rd dimension for system intergration," in *Interconnect Technology Conference, 2006 International*, 2006, pp. 1-5.

[36] H. Baltes, O. Brand, A. Hierlemann, D. Lange, and C. Hagleitner, "CMOS MEMS - present and future," in *Micro Electro Mechanical Systems, 2002. The Fifteenth IEEE International Conference on*, 2002, pp. 459-466.

[37] H. Baltes, O. Brand, G. K. Fedder, C. Hierold, G. Korvink, and O. Tabata, *CMOS-MEMS*. Weinheim ; [Great Britain]: Wiley-VCH, 2005.

[38] S. Lewis, S. Alie, T. Brosnihan, C. Core, T. Core, R. Howe, J. Geen, D. Hollocher, M. Judy, J. Memishian, K. Nunan, R. Paine, S. Sherman, B. Tsang, and B. Wachtmann, "Integrated sensor and electronics processing for >10^8 "iMEMS" inertial measurement unit components," in *Electron Devices Meeting, 2003. IEDM '03 Technical Digest. IEEE International*, 2003, pp. 39.1.1-39.1.4.

[39] J. Yasaitis, M. Judy, T. Brosnihan, P. Garone, N. Pokrovskiy, D. Sniderman, S. Limb, R. Howe, B. Boser, M. Palaniapan, X. S. Jiang, and S. Bhave, "A modular process for integrating thick polysilicon MEMS devices with sub-micron CMOS," *Micromachining and Microfabrication Process Technology Viii,* vol. 4979, pp. 145-154, 2003.

[40] AnalogDevices, "ADIS16350, Tri-Axis Inertial Sensor Datasheet," 2007.

[41] O. Brand, "Microsensor Integration Into Systems-on-Chip," *Proceedings of the IEEE,* vol. 94, pp. 1160-1176, 2006.

[42] V. T. Park, R. N. Candler, H. J. Li, J. Cho, H. Li, T. W. Kenny, A. Partridge, G. Yama, and M. Lutz, "Wafer scale encapsulation of MEMS devices," *Advances in Electronic Packaging 2003, Vol 1,* pp. 209-212, 2003.

[43] R. N. Candler, M. A. Hopcroft, B. Kim, W. T. Park, R. Melamud, M. Agarwal, G. Yama, A. Partridge, M. Lutz, and T. W. Kenny, "Long-term and accelerated life testing of a novel single-wafer vacuum encapsulation for MEMS resonators," *Journal of Microelectromechanical Systems,* vol. 15, pp. 1446-1456, 2006.

[44] G. K. Fedder, R. T. Howe, L. Tsu-Jae King, and E. P. Quevy, "Technologies for Cofabricating MEMS and Electronics," *Proceedings of the IEEE,* vol. 96, pp. 306-322, 2008.

[45] H. Takeuchi, A. Wung, S. Xin, R. T. Howe, and K. Tsu-Jae, "Thermal budget limits of quarter-micrometer foundry CMOS for post-processing MEMS devices," *Electron Devices, IEEE Transactions on,* vol. 52, pp. 2081-2086, 2005.

[46] W.-L. Huang, Z. Ren, Y.-W. Lin, H.-Y. Chen, J. Lahann, and C. T. C. Nguyen, "Fully monolithic CMOS nickel micromechanical resonator oscillator," in *Micro Electro Mechanical Systems, 2008. MEMS 2008. IEEE 21st International Conference on*, 2008, pp. 10-13.

[47] X. Huikai, L. Erdmann, Z. Xu, K. J. Gabriel, and G. K. Fedder, "Post-CMOS processing for high-aspect-ratio integrated silicon microstructures," *Microelectromechanical Systems, Journal of,* vol. 11, pp. 93-101, 2002.

[48] B. Kim, M. Hopcroft, C. Jha, R. Melamud, S. Chandorkar, M. Agarwal, K. L. Chen, W. T. Park, R. Candler, G. Yama, A. Partridge, M. Lutz, and T. W. Kenny, "Using MEMS to Build the Device and the Package," in *Solid-State Sensors, Actuators and Microsystems Conference, 2007. TRANSDUCERS 2007. International*, 2007, pp. 331-334.

[49] A. Jourdain, K. Vaesen, J. M. Scheer, J. W. Weekamp, J. T. M. van Beek, and H. A. C. Tilmans, "From zero- to second-level packaging of RF-MEMS devices," in *Micro Electro Mechanical Systems, 2005. MEMS 2005. 18th IEEE International Conference on*, 2005, pp. 36-39.

[50] W.-T. Hsu, "Low Cost Packages for MEMS Oscillators," in *Electronic Manufacturing Technology Symposium, 2007. IEMT '07. 32nd IEEE/CPMT International*, 2007, pp. 273-277.

[51] H. A. C. Tilmans, W. D. Raedt, and B. Eric, "MEMS for wireless communications: from RF-MEMS components to RF-MEMS-SiP," *Journal of Micromechanics and Microengineering,* vol. 13, p. S139, 2003.

[52] R. Legtenberg and H. A. C. Tilmans, "ELECTROSTATICALLY DRIVEN VACUUM-ENCAPSULATED POLYSILICON RESONATORS .1. DESIGN AND FABRICATION," *Sensors and Actuators a-Physical,* vol. 45, pp. 57-66, Oct 1994.

[53] G. J. A. M. Verheijden, G. E. J. Koops, K. L. Phan, and J. T. M. van Beek, "Wafer level encapsulation technology for MEMS devices using an HF-permeable PECVD SIOC capping layer," in *Micro Electro Mechanical Systems, 2008. MEMS 2008. IEEE 21st International Conference on*, 2008, pp. 798-801.

[54] H. A. C. Tilmans, M. D. J. Van de Peer, and E. Beyne, "The indent reflow sealing (IRS) technique - A method for the fabrication of sealed cavities for MEMS devices," *Journal of Microelectromechanical Systems,* vol. 9, pp. 206-217, Jun 2000.

[55] Y. Oya, A. Okubora, M. Van Spengen, P. Soussan, S. Stoukatch, X. Rottenberg, P. Ratchev, H. Tilmans, W. De Raedt, E. Beyne, P. De Moor, I. De Wolf, K. Baert, and ieee, "A reliable and compact polymer-based package for capacitive RF-MEMS switches," in *50th IEEE International Electron Devices Meeting*, San Francisco, CA, 2004, pp. 31-34.

[56] G. J. Carchon, A. Jourdain, O. Vendier, J. Schoebel, and H. A. C. Tilmans, "Integration of 0/1-level packaged RF-MEMS devices on MCM-D at millimeter-wave frequencies," *Ieee Transactions on Advanced Packaging,* vol. 30, pp. 369-376, Aug 2007.

2 MEMS RESONATORS CHARACTERISTICS AND APPLICATION IN RF SYSTEMS

In this chapter the working principle of MEMS resonators with electrostatic actuation and capacitive detection is explained. The application of these resonators to perform the required functions of a RF front-end is explored and resonator requirements for each function are given. A review of the state of the art of RF-MEMS is also provided and the different solutions adopted to overcome the challenges are discussed.

2.1 WORKING PRINCIPLE

The operation principle of the MEMS resonators is explained in this section. The electrostatic excitation mechanism and capacitive detection method used allows the direct use of these resonators in purely electrical environment, as both input and output signals are electrical. In fact, the resonator can be directly modeled using an electrical model whose electrical parameters are directly related to physical parameters, as will be shown. Among the different excitation and readout techniques [1, 2], electrostatic excitation and capacitive detection offers a direct electrical signal processing, which is preferred to replace electrical components in the RF front-end, a low power consumption, making them potentially suitable for battery operated devices, and ease of fabrication and compatibilization in a standard CMOS technology [3].

2.1.1 ELECTROSTATIC EXCITATION

The mechanical structures used along this work are mainly composed on a vibrating part (the resonator) and two fixed electrodes (the excitation electrode and the readout electrode), as depicted in *Figure 2.1*.This configuration, also known as two port has the advantage of presenting reduced parasitic when compared to one electrode (or one port). In this topology, a time-varying signal (V_{in}) is applied to the excitation electrode whereas the resonator is biased at a fixed DC voltage. These signals generate a force (F_x) on the resonator at the same frequency of the V_{in} signal. This F_x provokes the displacement of the resonators if the applied AC signal has a frequency near to the natural resonance frequency of the mechanical structure, which it is determined by its physical dimensions. The movement of the resonator changes the value of the existing capacitor between resonator and read-out electrode, this variation of the capacitor generates a current in this electrode. *Figure 2.1* shows the applied signal configuration for a general beam-type two-port MEMS resonator with in-plane or lateral vibration. The two-port terminology is used following the same terminology used by Clark et al. [4] who considers as ports only the electrodes and not the structure. Important physical dimensions are shown: beam width (W), beam length (L), beam thickness (h), distance from the beam to the substrate, electrode length (L_c) and distance between the beam and the electrodes, also named gap (s).

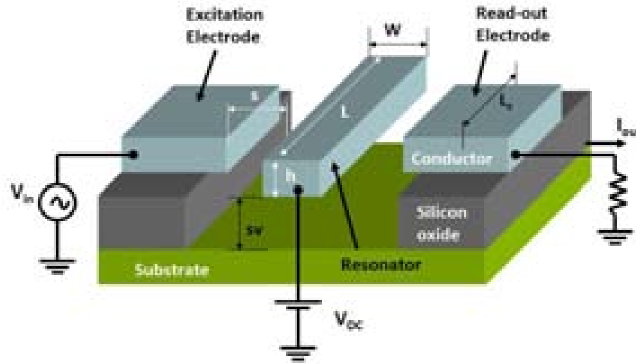

Figure 2.1: Typical two-port device with the applied signals for electrostatic excitation and capacitive transduction. The movement of the resonator is performed in the same plane than the electrodes (in-plane or lateral vibration)

It can be observed that there are two capacitors present between the excitation electrode and the resonator beam (C_E) and another one between the resonator and read-out driver (C_R) (*Figure 2.2*). These capacitors can be expressed (for small resonator beam deflection) using parallel plate capacitors:

$$C_E = \frac{\varepsilon \cdot A}{(s+x)} \tag{2.1}$$

$$C_R = \frac{\varepsilon \cdot A}{(s-x)} \tag{2.2}$$

Where ε is the electrical permittivity of the medium, A is the coupling area between the resonator and the electrodes ($A = L_c \cdot h$) and x is the displacement of the resonator.

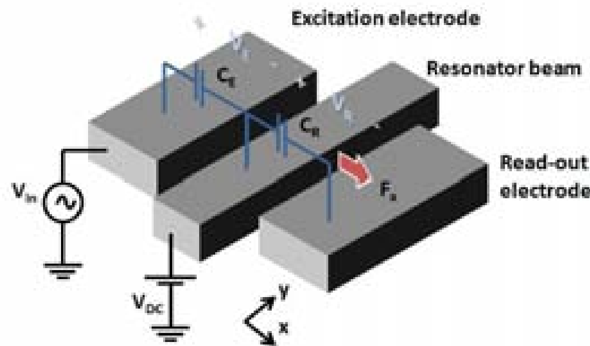

Figure 2.2: Two-port resonator with capacitors between resonator and excitation drivers shown

Voltages shown in *Figure 2.2* V_E and V_R are the voltage differences between excitation electrode and resonator beam and between the resonator beam and the read-out electrode, respectively. For the applied signals in *Figure 2.2*, these voltage differences are:

$$V_E = V_i - V_{DC} \tag{2.3}$$

$$V_R = V_{DC} \quad (2.4)$$

Note that on equation (2.4), the voltage at read-out driver is assumed to be much smaller than V_{DC}.

The exerted force to the resonator beam can be calculated as the variation in time of the energy stored in the C_E and C_R capacitors, which is $E=1/2\cdot C\cdot V^2$ for each capacitor, giving expression (2.5) .

$$F_x = -\frac{\partial E}{\partial x} = -\frac{\partial}{\partial x}\left(\frac{1}{2}\cdot C_E\cdot V_E{}^2 + \frac{1}{2}\cdot C_R\cdot V_R{}^2\right) \quad (2.5)$$

Because the applied voltages are position-independent, equation (2.5) leads to:

$$F_x = -\frac{\partial E}{\partial x} = -\frac{1}{2}\cdot\left(\frac{\partial C_E}{\partial x}\cdot V_E{}^2 + \frac{\partial C_R}{\partial x}\cdot V_R{}^2\right) \quad (2.6)$$

For small displacements (x<<s) variation of capacitances can be simplified, considering only the two first terms of the Taylor expansion:

$$\frac{\partial C_E}{\partial x} = -\frac{\varepsilon\cdot A}{s^2}\cdot\left(1-2\cdot\frac{x}{s}\right) = -\frac{C_0}{s}\cdot\left(1-2\cdot\frac{x}{s}\right) \quad (2.7)$$

$$\frac{\partial C_R}{\partial x} = \frac{\varepsilon\cdot A}{s^2}\cdot\left(1+2\cdot\frac{x}{s}\right) = \frac{C_0}{s}\cdot\left(1+2\cdot\frac{x}{s}\right) \quad (2.8)$$

Where $C_0 = \varepsilon\cdot A/s$, is the value of the capacitor without beam displacement. Finally substituting (2.3), (2.4), (2.7) and (2.8) into (2.6), the expression of the applied force can be obtained:

$$F_x = \frac{1}{2}V_i^2\frac{C_0}{s} - V_i\cdot V_{DC}\cdot\frac{C_0}{s} - x\cdot\frac{C_0}{s^2}\cdot\left[V_i^2 - 2\cdot V_i\cdot V_{DC} + 2\cdot V_{DC}{}^2\right] \quad (2.9)$$

Considering an input sinusoidal input: $V_i=A_{AC}\cdot\sin(\omega\cdot t)$, Expression (2.9) can be written as (2.10)

$$\begin{aligned} F_x = {} & \frac{1}{2}\cdot\frac{C_0}{s}\cdot A_{AC}^2\cdot\sin^2(\omega\cdot t) - A_{AC}\cdot V_{DC}\cdot\frac{C_0}{s}\sin\ (\omega\cdot t) - \\ & -x\cdot\frac{C_0}{s^2}\cdot\left[A_{AC}^2\cdot\sin^2(\omega\cdot t) - 2\cdot A_{AC}\cdot V_{DC}\cdot\sin\ (\omega\cdot t) + 2\cdot V_{DC}{}^2\right] \end{aligned} \quad (2.10)$$

Because $\sin^2(\omega\cdot t)=1/2\cdot(1-\cos(2\cdot\omega\cdot t)$, the applied force is expressed as (2.11):

$$\begin{aligned} F_x = {} & \frac{1}{4}\cdot\frac{C_0}{s}\cdot A_{AC}^2 - A_{AC}\cdot V_{DC}\cdot\frac{C_0}{s}\sin\ (\omega\cdot t) - \frac{1}{4}\cdot\frac{C_0}{s}\cdot A_{AC}^2\cdot\cos(2\cdot\omega\cdot t) - \\ & -x\cdot\frac{C_0}{s^2}\cdot\left[\frac{1}{2}\cdot A_{AC}^2 - \frac{1}{2}\cdot A_{AC}^2\cdot\cos(2\cdot\omega\cdot t) - 2\cdot A_{AC}\cdot V_{DC}\cdot\sin\ (\omega\cdot t) + 2\cdot V_{DC}{}^2\right] \end{aligned} \quad (2.11)$$

The exerted force (considering very small displacement, i.e. $x\approx 0$) has three components: (a) a DC component (proportional to $A_{AC}{}^2$) which deflects the beam, (b) a component of frequency equal to the input signal (depending on $V_{DC}\cdot A_{AC}$) and (c) another at twice the V_i frequency (proportional to $A_{AC}{}^2$). Note that a DC voltage is required to actuate the beam at the same frequency than the input signal.

A useful parameter is the electromechanical coupling factor (η_e) [5], defined considering only the input frequency term and small displacements ($x \approx 0$). This coefficient describes the ratio between the applied excitation force and the input signal applied, and is defined as (2.12):

$$\eta_e = \frac{F_x}{V_i} = \frac{\varepsilon \cdot A}{s^2} \cdot V_{DC} \tag{2.12}$$

2.1.2 Equation Of Resonator Movement

This section describes the equation of motion that transforms the applied force into resonator displacement. The MEMS movement can be modelled using a simple mass-spring-dash system excited by a harmonic force (*Figure 2.3*):

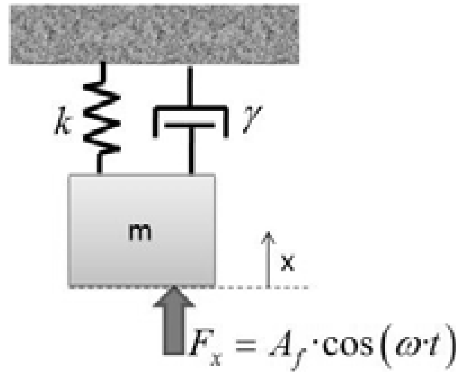

Figure 2.3: Simplified resonator model

The resonator responds to this applied force with a displacement that is mainly dominated by the forced harmonic oscillation movement equation:

$$m \cdot \frac{\partial^2 x}{\partial t^2} + \gamma \cdot \frac{\partial x}{\partial t} + k \cdot x = A_f \cdot \cos(\omega \cdot t) \tag{2.13}$$

Where *m* is resonator mass, γ is the damping coefficient, *k* is the elastic constant and A_f is the magnitude of the applied sinusoidal force. If we define the natural resonance frequency (ω_0) and the quality factor (*Q*) as:

$$\omega_0 \equiv \sqrt{\frac{k}{m}} \tag{2.14}$$

$$Q \equiv \frac{\omega_0 \cdot m}{\gamma} = \frac{\sqrt{k \cdot m}}{\gamma} \tag{2.15}$$

Expressions (2.14) and (2.15) give useful information about some of the constrains of MEMS devices. In order to obtain high *Q* values: high *k* (i.e. stiff devices), high *m* (i.e. big devices and therefore of low frequency) and low damping are needed, whereas for high frequency devices high stiffness and low mass are required. Due to these constrains one of the figures of merit for MEMS resonators is the Q-frequency product, which must be the highest possible.

Solving (2.13), the amplitude of vibration is:

$$|x| = \frac{A_f / m}{\sqrt{\left(\omega^2 - \omega_0^2\right)^2 + \left(\omega \cdot \omega_0 / Q\right)^2}} \tag{2.16}$$

This equation presents a maximum displacement (*Figure 2.4*) when the applied external force has a frequency near to the natural resonance frequency, in this situation (2.16) can be simplified to (2.17).

$$k \cdot |x| = Q \cdot F \tag{2.17}$$

Due to the high frequency selectivity of these devices, it is assumed that the applied force is effectively transformed into resonator motion only near the natural resonance frequency of the mechanical structure.

As we can see from the above expressions, the three main parameters for the harmonic oscillation are resonance frequency (ω_o), mass (m), elastic constant (k) and quality factor (Q). A detailed explanation and the definition of these parameters as a function of the dimensional parameters of flexural beams can be found in *Annex 1*.

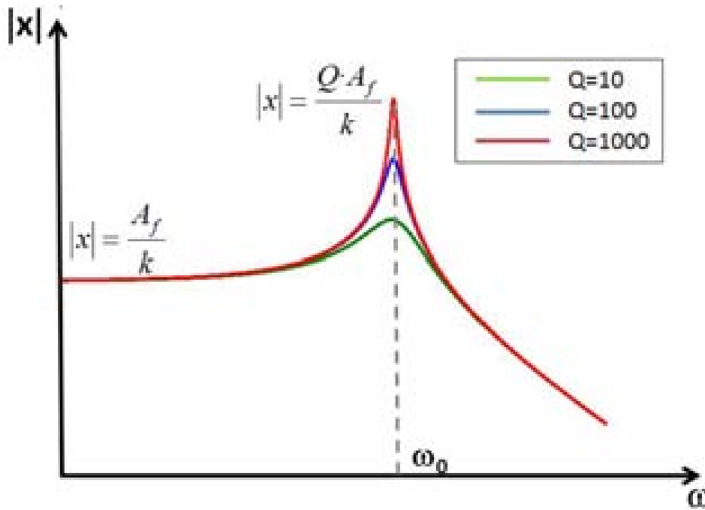

Figure 2.4: Plot of resonator displacement vs. frequency for different Q values.

2.1.3 SPRING SOFTENING

It can be observed that in equation (2.10), there is a component of the applied force proportional to the resonator displacement x due to electrostatic excitation. This component can be assimilated to an electrical stiffness k_e that can be defined as:

$$k_e(t) = \frac{\partial F_x}{\partial x} \tag{2.18}$$

The electrical stiffness expression (2.19) is found considering the applied force expression of equation (2.10).

$$k_e(t) = -\frac{C_0}{s^2} \cdot \left[\frac{1}{2} \cdot A_{AC}^2 - \frac{1}{2} \cdot A_{AC}^2 \cdot \cos(2 \cdot \omega \cdot t) - 2 \cdot A_{AC} \cdot V_{DC} \cdot \sin\ (\omega \cdot t) + 2 \cdot V_{DC}{}^2 \right] \tag{2.19}$$

As it can be observed, the elastic constant presents a dependence with the time due to the sinusoidal input signal. Considering the mean values of the voltage components, the elastic constant expression is reduced to:

$$k_e = -\frac{C_0}{s^2} \cdot \left[\frac{1}{2} \cdot A_{AC}^2 + 2 \cdot V_{DC}{}^2 \right] \tag{2.20}$$

Because V_{DC} is usually much greater than A_{AC}, this AC term is often neglected.

Considering the electric contribution to the effective elastic constant (k_{eff}), this can be written as (2.21):

$$k_{eff} = k - |k_e| \tag{2.21}$$

The resonance frequency of the electrostatically transduced resonator is then (2.22):

$$f_{RES} = \frac{1}{2 \cdot \pi} \sqrt{\frac{k_{eff}}{m}} = \frac{1}{2 \cdot \pi} \cdot \sqrt{\frac{k}{m}} \cdot \sqrt{1 - \frac{|k_e|}{k}} = f_0 \cdot \sqrt{1 - \frac{|k_e|}{k}} \tag{2.22}$$

It can be then observed that the resonance frequency is modified by the equivalent elastic constant. Substituting the electrical elastic constant (2.20), considering $V_{DC} >> A_{AC}$ the resonance frequency is (2.23):

$$f_{RES} = f_0 \cdot \sqrt{1 - \frac{|k_e|}{k}} = f_0 \cdot \sqrt{1 - \frac{1}{k} \cdot \frac{C_0}{s^2} \cdot 2 \cdot V_{DC}{}^2} \approx f_0 \cdot \left(1 - \frac{1}{k} \cdot \frac{C_0}{s^2} \cdot V_{DC}{}^2 \right) \tag{2.23}$$

Equation (2.23) states that the resonance frequency is altered by the V_{DC} applied to the resonator, reducing the natural frequency. This effect is known as spring softening [6], because this electric elastic constant reduces the effective stiffness.

2.1.4 PULL-IN AND COLLAPSING VOLTAGE

Another important effect that must be taken into consideration when using in-plane resonators with electrostatic excitation is the sticking of the resonator to the electrode (which is known as lateral pull-in) or to the substrate (vertical collapse).

Vertical collapse can be produced either by the technological process (specially during the release of the structure) or by the application of external forces (acceleration or electrostatic attraction) [7]. By biasing the necessary DC voltage for the actuation of the device, the resonator is affected by a vertical electrostatic attraction to the substrate. The maximum applicable voltage to the resonator for preventing vertical sticking of the movable structure for a clamped-clamped beam is (2.24) [7]:

$$V_{col} = \sqrt{11.9 \cdot \frac{E \cdot sv^3 \cdot h^3}{\varepsilon \cdot L^4}} \tag{2.24}$$

Where sv is the vertical distance to the substrate and h is the resonator thickness, as shown in *Figure 2.1*.

A similar effect is also observed in lateral displacement. The total energy of the resonator-driver system is the sum of the energy stored in the capacitors (E_{cap}) and the elastic recovery energy ($E_{elastic}$):

$$E_{total} = E_{cap} + E_{elastic} \tag{2.25}$$

Following the same development used in *section 1.1.1,* expression (2.25) is derived to find the total force of the system.

$$F_{tot} = \frac{\partial E_{tot}}{\partial x} \tag{2.26}$$

In two-port resonators, the energy stored in the capacitors and the elastic recovering can be expressed like (2.27) and (2.28), respectively, considering $V_E^2 \approx V_R^2 \approx V_{DC}^2$:

$$E_{cap} = -\frac{1}{2} \cdot \varepsilon \cdot A \cdot V_{DC}^2 \cdot \left(\frac{1}{s-x} + \frac{1}{s+x} \right) \tag{2.27}$$

$$E_{elastic} = k \cdot x \tag{2.28}$$

And the complete expression of the force is (2.29).

$$F_{total} = \frac{1}{2} \cdot \varepsilon \cdot A \cdot V_{DC}^2 \cdot \left(\frac{1}{(s-x)^2} - \frac{1}{(s+x)^2} \right) + k \cdot x \tag{2.29}$$

In equilibrium F_{total}=0. Figure 2.5 shows the plot of the electric and elastic (mechanical) forces of a clamped-clamped beam with W=500nm, L=13.2µm, which resonance frequency is located around 24MHz. The electric force is plotted under different DC biasing conditions: at DC voltage at twice, equal and half of the pull-in voltage (V_{PI}).

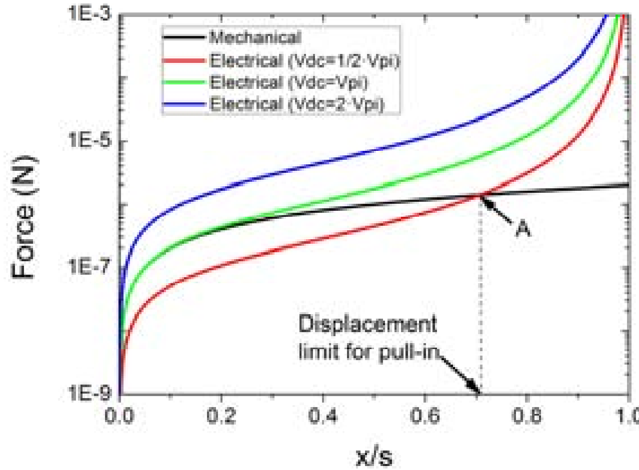

Figure 2.5: Electric and mechanical forces for a clamped-clamped beam with W=500nm and L=13.2µm. The electrical forces are calculated for different V_{DC} values.

It can be observed that in normal operation, the mechanical elastic force is bigger than the electrostatic elastic one and therefore the resonator displaces until the F_{cap}=$F_{elastic}$ condition is reached. For the two-port resonator x=0 is the stable equilibrium point. It can be observed in the figure that for displacements higher than point A, the electrical force is bigger than the mechanical one. In this scenario, the resonator would be attracted to the electrode until it collapses. To find the maximum applicable voltage, the stability condition $\partial F_{tot} / \partial x < 0$ [8] can be used. For

simplicity, stability is computed at x=0 equilibrium point. The obtained limit voltage (snap-in voltage) is (2.30) [9]:

$$V_{pi}^{two-port} = \sqrt{k \cdot s^3 / (2 \cdot \varepsilon \cdot A)} \quad (2.30)$$

If the resonator is biased at a higher voltage than V_{pi}, any perturbation would provoke the snap-in of the device. Note, however, that even though the applied voltage is less than the pull-in voltage, if the displacement is bigger than the unstable equilibrium point, the resonator would also collapse. An interesting effect can be obtained considering total force expression at the equilibrium point (x=0): in this point the electrostatic force is cancelled, and therefore the resonator does not bend to any electrode, independently of the value of V_{DC}. If $x \neq 0$ (i.e. any kind of external force is applied) and consequently the symmetry of the energy stored in the capacitors is broken, the resonator can collapse to an electrode once $V_{DC} > V_{pi}$. Note ,therefore that for a completely symmetric device and with no more external signals than the DC voltage applied to the resonator, the resonator is not affected by the lateral collapse.

It is also interesting to calculate the pull-in voltage for a one-port resonator. In that case, the energy stored in the capacitor is (2.31):

$$E_{cap} = -\frac{1}{2} \cdot \varepsilon \cdot A \cdot V_{DC}^2 \cdot \frac{1}{s - x} \quad (2.31)$$

Following the aforementioned process, the equilibrium point for a one-port device is found at $x = 1/3 \cdot s$, and therefore the pull-in voltage for the one-port resonators is (2.32):

$$V_{pi}^{one-port} = \sqrt{8 \cdot k \cdot s^3 / (27 \cdot \varepsilon \cdot A)} \quad (2.32)$$

It can be observed that comparing (2.32) and (2.30), $V_{pi}^{two\text{-}port}$ is greater than $V_{pi}^{one\text{-}port}$, concretely, 1.3 times, providing slight increase of robustness against pull-in.

2.1.5 CAPACITIVE READOUT

The movement of the resonator causes the C_E capacitor to change its value, and therefore induces a current in the output electrode, that is calculated as:

$$I_o = \frac{\partial (V_R \cdot C_R)}{\partial t} = C_R \cdot \frac{\partial V_R}{\partial t} + V_R \cdot \frac{\partial C_R}{\partial t} = V_{DC} \cdot \frac{\partial C_R}{\partial x} \cdot \frac{\partial x}{\partial t} = V_{DC} \cdot \frac{\varepsilon \cdot A}{s^2} \cdot \frac{\partial x}{\partial t} \quad (2.33)$$

The time derivative of V_R vanishes because V_{DC} is not time-dependent. It is worth to mention that a DC voltage has to be applied in order to sense the current. A similar electromechanical transducing coupling coefficient to η_e can be defined for the read-out coupling (η_r):

$$\eta_r = \frac{I_o}{\partial x / \partial t} = \frac{\varepsilon \cdot A}{s^2} \cdot V_{DC} \quad (2.34)$$

This read-out coefficient states the relation between the output current and the displacement of the beam. This readout coupling has the same value as the excitation coupling factor, then $\eta_e = \eta_r = \eta$ and combining equations: (2.33), (2.17) and (2.9), the global conversion from input signal to output signal (considering $x \approx 0$) is obtained:

$$I_o = \eta^2 \cdot \frac{Q}{k} \cdot \frac{\partial V_i}{\partial t} \quad (2.35)$$

Note that this equation is only valid for small displacements and for input signal frequencies near the natural oscillation frequency of the resonator. This output current is inversely proportional to the resonator stiffness, and therefore stiff resonators present a lower output current .

2.1.6 RLC ELECTRICAL EQUIVALENT MODEL

A useful way to model the behaviour of a MEMS resonator is using a simple RLC electric equivalent circuit (*Figure 2.6*), which is valid for linear resonators (i.e.small input signals and consequently small vibration amplitudes). Although more general models where implemented in Spice [10] and Verilog-A [11] to account for effects like resonator non-linearities, this simple $RLC//C_p$ is enough to provide a high-level perspective of most important techniques involving MEMS resonators [12].

Considering the motion equation (2.13) and substituting $\partial x/\partial t = I_0/\eta$, equation (2.34), (2.13) is written as :

$$m \cdot \frac{d}{dt}\left(\frac{I_0}{\eta}\right) + \frac{\gamma}{\eta} \cdot I_0 + \frac{k}{\eta} \cdot \int I_0 \cdot dt = F(t) \tag{2.36}$$

The applied force *F(t)* can be expressed as a function of the applied voltage V_i, following equation (2.12), (2.36) becomes:

$$m \cdot \frac{d}{dt}\left(\frac{I_0}{\eta}\right) + \frac{\gamma}{\eta} \cdot I_0 + \frac{k}{\eta} \cdot \int I_0 \cdot dt = \eta \cdot Vi \tag{2.37}$$

$$\frac{m}{\eta^2} \cdot \frac{dI_0}{dt} + \frac{\gamma}{\eta^2} \cdot I_0 + \frac{k}{\eta^2} \cdot \int I_0 \cdot dt = Vi \tag{2.38}$$

Note that this equation is the one that would be obtained from a RLC circuit by doing:

$$R_m = \frac{\gamma}{\eta^2} = \frac{\sqrt{k \cdot m}}{Q \cdot \eta^2} = \frac{1}{Q} \cdot \frac{k \cdot s^4}{\varepsilon^2 \cdot \omega_0 \cdot A^2 \cdot V_{DC}^2} \tag{2.39}$$

$$C_m = \frac{\eta^2}{k} = \frac{1}{k} \cdot \frac{\varepsilon^2 \cdot A^2}{s^4} \cdot V_{DC}^2 \tag{2.40}$$

$$L_m = \frac{m}{\eta^2} = \frac{m \cdot s^4}{\varepsilon^2 \cdot A^2 \cdot V_{DC}^2} \tag{2.41}$$

Figure 2.6(a) shows the resonator equivalent circuit. At resonance frequency, ($\omega = \sqrt{1/L_m C_m}$), L_m and C_m cancels and the branch is reduced to the motional resistance R_m, which accounts for resonator energy losses. In addition to the motional current (I_o) that comes from the resonance of the device, there is a feedthrough parasitic current from the input to output electrode (named I_p) that it is incorporated into the electrical equivalent model using a parasitic capacitor (C_p), as it is shown in *Figure 2.6(b)*. On two-port devices, this parasitic current should be zero, however, there is an amount of signal feedthrough between the electrodes with different origins: part of the energy is transferred through the air due to the bending of the electrical field between the electrodes named fringing field [10], and another part is transferred through the substrate [13] parasitic capacitors.

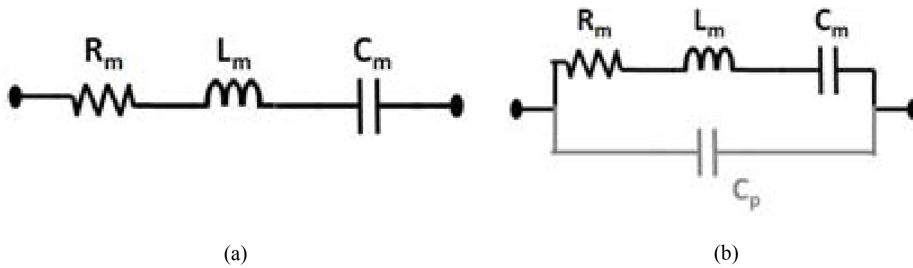

(a) (b)

Figure 2.6: (a) Simple RLC model for a MEMS resonator. (b) Modified model considering also the parasitic current at resonator output

2.2 KEY PARAMETERS OF MEMS FOR RF APPLICATIONS

The most important performance parameters of the MEMS resonators for RF applications are: resonance frequency (f_0), parallel parasitic capacitor (C_p), motional resistor (R_m), quality factor (Q), and frequency tuning (FT).

2.2.1 RESONANCE FREQUENCY

On MEMS resonators, the natural oscillation frequency (f_0) is determined by the physical dimensions of the device, its shape, the vibration mode and the mechanical properties of the material in which the resonator is made of [10, 14, 15]. Moreover, MEMS resonator frequency has to be dimensioned according to its function in the RF front-end, and consequently the resonance frequency can range from the kHz to the GHz, obviously, not all resonator shapes are applicable at any resonance frequency [16]. Expressions of the resonance frequency for the MEMS used in this thesis are given in Annex 1. Resonance frequencies of the devices described in this thesis are located in the higher section of the HF range (around 24MHz) and the lower VHF region (around 48MHz). All the used resonators have lateral flexural resonance modes, this resonance mode was chosen mainly due to the relatively low resonance frequency used Moreover, for the lateral flexural mode resonators of this thesis, the resonance frequency is determined by lateral (CAD definable) dimensions, which is a very important property for the integration of MEMS resonators [14].

2.2.2 QUALITY FACTOR

The quality factor (Q) of a resonator, introduced on section 2.1.2 and defined in terms of damping coefficient (2.15), is a measurement of the energy losses of the resonator, as defined in (2.42) [17].

$$Q = 2\cdot\pi\cdot\frac{\text{Energy stored per cycle}}{\text{Energy dissipated per cycle}} \tag{2.42}$$

It could also be observed in *Figure 2.4* how the increase of Q narrowed the frequency response and increased the height of the peak, making the resonator more frequency selective. The loss mechanisms of MEMS resonators immersed in a fluid include fluid related losses (air-damping and air-squeezing), acoustic vibration transmitted through the anchors [18], surface effects in thin resonators [19] and thermoelastic damping (TED) [20], as shown in (2.43).

$$\frac{1}{Q_{total}} = \frac{1}{Q_{Air-damping}} + \frac{1}{Q_{Air-squeezing}} + \frac{1}{Q_{Anchor}} + \frac{1}{Q_{Surface}} + \frac{1}{Q_{TED}} \tag{2.43}$$

The first two terms are related to the damping due to the movement of a device in a viscous environment. The third term states the energy of the resonator transferred to the rest of the fixed structure (anchors) and the two last terms take into account internal losses of energy, related to the material. The dominant losses when the resonator is measured in air are air-damping and air-squeezing, whereas when the resonator is measured in vacuum, the other loss components are the dominant ones, being these known as intrinsic losses. The second important contribution for the energy losses on flexural beams is the loss of movement through the anchors, these losses depend on the contact surface, and can be minimized by different techniques: one of them is using a dynamically balanced resonator topology, so that the moment of inertia is cancelled at the supports [21], another one is using using the nodes (zero displacement points) of the resonator to place the anchors [22] and the last one is to use λ/4 length supports, by using this specific length the energy lost through the supports is returned to the resonator[23].

Figure 2.7 [11] shows the experimental measurement of the quality factor Q as a function of the pressure for a metal cantilever. It can be observed that for pressure under 1mbar, Q is independent of the pressure and, consequently, is limited by the resonator intrinsic losses.

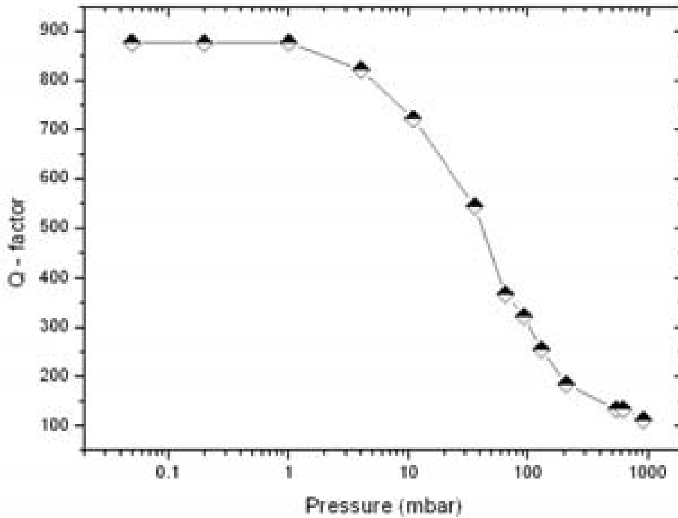

Figure 2.7: Experimental measurement of Quality factor vs. pressure. For pressures under 1mbar quality factor is limited by intrinsic losses. Extracted from [11]

Due to the difficulty to determine resonator losses, the quality factor is mainly an empirical value, and therefore is obtained from the experimental curves, following the Q extraction techniques explained in Annex 2.

2.2.3 FREQUENCY TUNING

As stated in equation (2.23), the resonance frequency of the MEMS can be adjusted with V_{DC} values. Expression (2.23) also allows the definition of the frequency tuning of the resonator (*FT*) as the relative variation of the resonance frequency to changes in the applied DC voltage. Therefore *FT* can be defined as:

$$FT = \frac{1}{f_0} \cdot \frac{\partial f_{RES}}{\partial V_{DC}^2} = -\frac{\varepsilon \cdot A}{s^3} \cdot \frac{1}{k} \tag{2.44}$$

It can be observed a strong dependence of this frequency tuning with the gap between the resonator and excitation/read-out drivers (2.44). Although this tunability can be useful to provide tunable RF elements and compensate fabrication process variations, it is counterproductive for the use of MEMS resonators as frequency references, because of the frequency variations due to the DC voltage drifts [24].

2.2.4 MOTIONAL RESISTANCE

This parameter is one of the most important for RF applications. Depending on the function of the MEMS device in the RF front-end a 50Ω impedance matching is required (for example when the MEMS resonator is the first component after the antenna). Moreover, a low R_m value is mandatory to obtain low-power oscillators [25]. This low R_m is reached for: low k value, big coupling area, a tiny gap and a high DC voltage. However, there are some observations to be made: the minimum gap is limited by fabrication process, big structures (with bigger coupling area) are more prone to collapse and usually present a lower frequency, furthermore, on portable devices, the use of a high DC voltage requires an extra voltage supply or additional circuitry to raise the DC voltage. For these reasons, typical motional resistance values obtained with MEMS resonators using CMOS fabrication process (in which layers used to fabricate resonators are usually thin) is in the MΩ range. This big motional resistance is the reason of the big losses found on the resonator measurements, carried out with 50Ω impedance instruments, see Annex 2. In this annex, an explanation of the techniques used to obtain the motional resistance from experimental data is also provided.

2.2.5 NON-LINEAR RESONANT BEHAVIOR

Previous analyses of the resonator movement (*Section 2.1*) were based on small movement of the resonator and a linear behavior. However, the resonator can show a non-linear restoring force that modifies (2.13) [26], when the resonator shows large displacements:

$$m \cdot \frac{\partial^2 x}{\partial t^2} + \gamma \cdot \frac{\partial x}{\partial t} + k \cdot x + k_2 \cdot x^2 + k_3 \cdot x^3 = A_f \cdot \cos(\omega \cdot t) \tag{2.45}$$

Where k_2 and k_3 are the non-linear terms of the spring constant. On capacitively transduced resonators, the elastic constants present two kinds of contributions: electric and mechanic (2.46)-(2.48).

$$k = k_m + k_e \tag{2.46}$$

$$k_2 = k_{m2} + k_{e2} \tag{2.47}$$

$$k_3 = k_{m3} + k_{e3} \tag{2.48}$$

Where the sub-index "m" is for mechanical contribution and "e" sub-index is for electric elastic constant. These resonators can show two kinds of non-linear behavior: mechanical non-linearity and capacitive non-linearity [26]. Mechanical elastic constants depend on the geometry of the resonator and are reported in *Annex 1*, whereas the linear term of the electrical elastic constants (k) is expressed like (2.20), and the second order terms are found in (2.49) and (2.50), obtained from the series expansion of the capacitor expressions:

$$k_{e2} = \frac{\partial^2 F_x}{\partial x^2} = \frac{3}{2 \cdot s} \cdot k_e \tag{2.49}$$

$$k_{e3} = \frac{\partial^3 F_x}{\partial x^3} = \frac{2}{s^2} \cdot k_e \tag{2.50}$$

When resonator displacement is large enough, the resonance peak is bended to the left or to the right depending on the kind of dominant non-linear effect. When the mechanical non-linearity is dominant, usually for low applied signals values, the resonance response moves to the right (named spring hardening) whereas for high applied DC signals, electrical non-linearity dominant, the resonance is bended to the left (spring softening) (*Figure 2.8-a*). Note that this later effect was already described in *Section 1.1.3*, and was due to the linear term of the electric elastic constant (k_e), whereas now up to the third non-linear term of this elastic constant is considered.

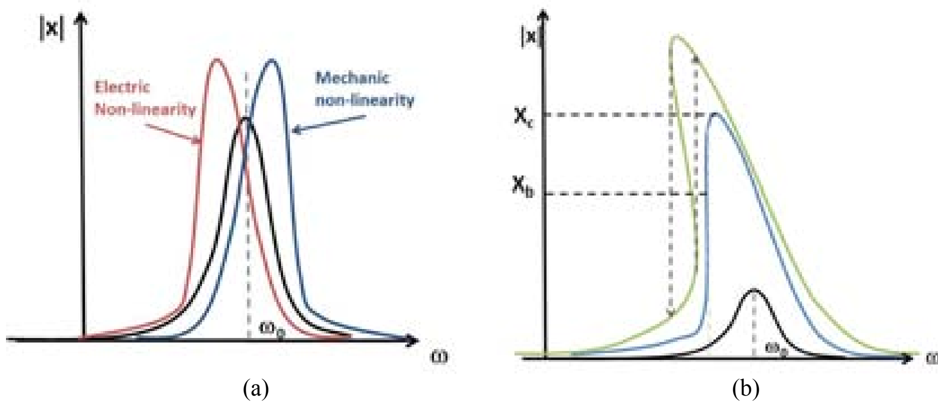

(a) (b)

Figure 2.8: (a) Displacement of the MEMS resonator. Black line shows the linear response, whereas red and blue lines shows non linear behavior due to electric and mechanic non-linearities, respectively.
(b) Peak bending due to resonator non-linear response. The black line shows a linear resonator response. The blue line shows the shape of the resonance before entering the hysteresis region, which is shown on the green curve.

For large displacements, the equation of movement can even become bi-evaluated (*Figure 2.8-b*). This non-linear behavior degrades the performance of a resonator as a filter or mixer (e.g. affecting the third order intermodulation point IIP3) and the performance of the resonator as a frequency reference provoking instabilities of the oscillation and therefore degrading the phase noise [27].

It is useful to determine the displacement limit, known as bifurcation point, before the resonator enters in hysteresis.

The bifurcation point (X_b) has the expression (2.51) [26]:

$$X_b = \sqrt{\frac{\omega_0}{\sqrt{3} \cdot Q \cdot |\kappa|}} \tag{2.51}$$

Where ω_0 is the angular natural resonance frequency of the device with linear behavior, and κ can be witten as:

$$\kappa = \left(\frac{3 \cdot k_3}{8 \cdot k} - \frac{5 \cdot k_2^2}{12 \cdot k^2} \right) \cdot \omega_0 \qquad (2.52)$$

The resonance frequency considering non-linearities can be expressed as (2.53):

$$\omega_{0non-linear} = \omega_0 + \kappa X_0^2 \qquad (2.53)$$

As it can be observed, however, the displacement obtained on the resonator is higher than the value given by equation (2.51), the displacement of the resonator under these condition is named critical displacement (X_c) and is related with the bifurcation point:

$$X_c = \frac{2}{\sqrt{3}} \cdot X_b \qquad (2.54)$$

Observing (2.17) and (2.9) a relationship between the resonator displacement and the applied signals is shown. Therefore, the displacement limit is translated to a limit of the applicable signals for the linear operation of the resonator. Moreover, this limit of the resonator displacement sets the maximum stored energy of the device, which is (2.55) [26]:

$$E_m = \frac{1}{2} \cdot k \cdot X_c^2 \qquad (2.55)$$

As a case study, the linearity of a clamped-clamped beam will be analyzed on Chapter 4, where the key elements to obtain a highly linear resonator will be highlighted.

2.3 MEMS Resonators Applications In A RF Front-End

In this section the requirements of MEMS devices for different functions on a RF front-end are discussed. Among the applications studied are: frequency references, filtering and frequency mixing. State of the art resonators for each application will be also provided at the end of this section.

2.3.1 Frequency References

The equivalent electrical model of MEMS resonators (see *Figure 2.6*) is the same used in quartz-crystal resonators, and therefore direct replacement of quartz crystals with MEMS resonator oscillators is a quite straightforward application. The advantage of the use of MEMS devices is to replace the relatively bulky off-chip crystal with a micro scale on-chip resonator. *Figure 2.9* shows the evolution in terms of size reduction of quartz-crystal resonators and MEMS. The later shows an important size reduction and a continuous size decrease whereas the reduction of quartz resonators seems to saturate.

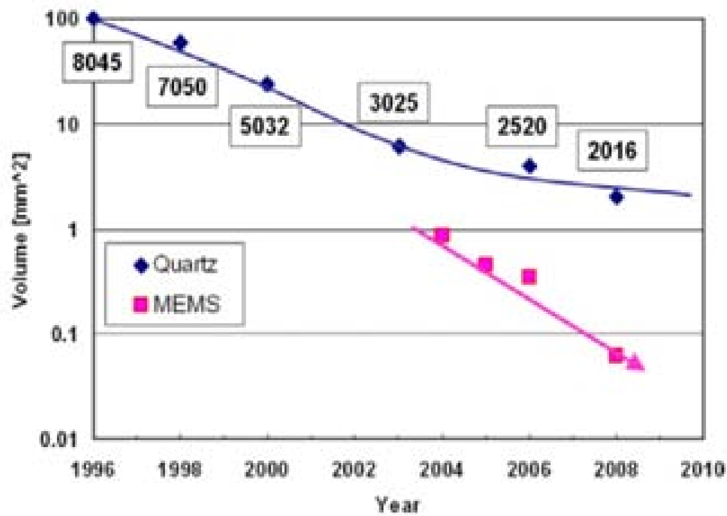

Figure 2.9: Evolution of the miniaturization in frequency references (quartz and MEMS), from [28].

However, when these micro devices are used as frequency references new problems, mainly concerning the miniaturization of the resonator (process variation effects and package miniaturization) arise [28].

Different performance parameters are defined for oscillators: frequency tolerance (that is set by the fabrication process of the resonator), frequency stability (that can be measured in an oscillator in terms of jitter in time domain or phase noise in frequency domain), ageing (also known as long term stability), temperature and voltage drifts and total power consumption.

Considering the resonator alone, key performance parameters are: motional resistance, parasitic parallel capacitor, quality factor (*Q*), resonator linearity and frequency stability versus external conditions (like temperature, biasing, etc). As it will be shown the performance at resonator level are translated to the aforementioned oscillator performance characteristics.

According to the Barkhausen criteria (oscillation criteria for positive feedback systems), a system (like the one shown in *Figure 2.10-a*) oscillates when H(s)=1. Usually a frequency selective network is added to the feedback branch (see *Figure 2.10-b*) in order to tune the output oscillator signal to a very specific frequency, set by this network. When an RLC//Cp resonator is used, the oscillation criteria (Barkhausen's criteria) can be applied as follows (see *Figure 2.10-c*) [30]: where an active circuit is used to provide a negative resistor that compensates the losses of the resonator. If a single transistor resonator is considered, like a Pierce oscillator (*Figure 2.11*), this transistor has to provide enough negative resistance to cancel the losses of the resonator (R_m). By analyzing this simple oscillator, the requirements of low R_m and low C_p will be clearly explained.

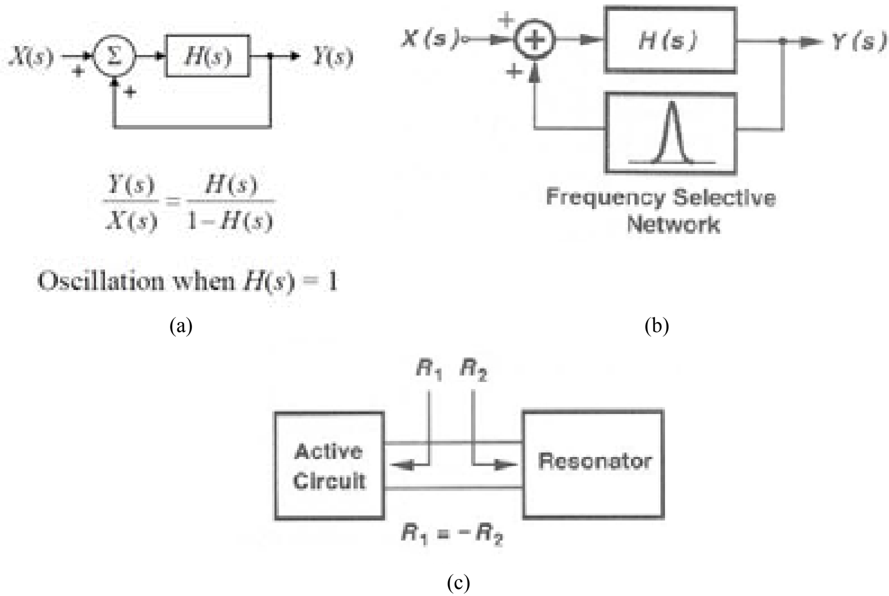

(c)

Figure 2.10:a) Two-port model of the feedback circuit to implement an oscillator. b) Oscillator with an added LC tank for frequency stabilization. c) One-port model of the circuit to implement an oscillator

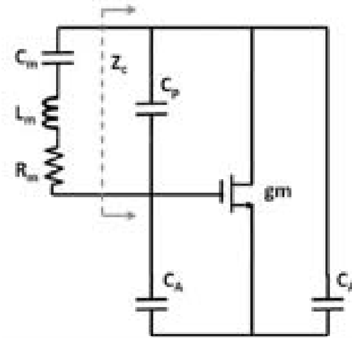

Figure 2.11: Pierce oscillator with the RLC//C_p resonator

For this circuit, the expressions of the real and imaginary part of the equivalent circuit impedance, together with the parasitic shunt capacitance are [25]:

$$\mathrm{Re}(Z_c) = -\frac{g_m \cdot C_A{}^2}{\left(g_m \cdot C_p\right)^2 + C_A{}^2 \cdot \omega_0{}^2 \cdot \left(C_A + 2 \cdot C_p\right)^2} \tag{2.56}$$

$$\mathrm{Im}(Z_c) = -\frac{g_m{}^2 \cdot C_p + 2 \cdot \omega_0{}^2 \cdot C_A{}^2 \cdot \left(C_A + 2 \cdot C_p\right)}{\omega_0 \cdot \left[\left(g_m \cdot C_p\right)^2 + \omega_0{}^2 \cdot C_A{}^2 \cdot \left(C_A + 2 \cdot C_p\right)^2\right]} \tag{2.57}$$

The main requirement for the oscillation is that $\mathrm{Re}(Z_c)+R_m<0$, whereas the imaginary part (2.57) is responsible of the deviation of the obtained signal frequency due to the circuit, which is known as frequency pulling (p) and is defined like (2.58). This parameter is related to the imaginary part of Zc as shown in (2.59).

$$p \equiv \frac{\omega_{osc} - \omega_o}{\omega_o} \tag{2.58}$$

$$-\operatorname{Im}(Z_c) = \frac{2}{\omega_0 \cdot C_m} \cdot \frac{\omega_{osc} - \omega_0}{\omega_0} = \frac{2 \cdot p}{\omega_0 \cdot C_m} \tag{2.59}$$

In these expressions ω_{osc} is the frequency of the signal at the output of the oscillator and ω_0 is the natural frequency of the resonator. Rearranging (2.59), the following expression is found:

$$p = -\frac{1}{2} \cdot \operatorname{Im}(Z_c) \cdot C_m \cdot \omega_0 \tag{2.60}$$

From (2.60), to obtain a low p (so that oscillator does not affect the natural resonance frequency of the resonator) a low motional capacitor (C_m) and a low resonance frequency are preferred. To analyze the effect of the parasitic capacitance (C_p) and the motional resistance (R_m), equations (2.55) and (2.56) will be plotted for different C_p values as a function of the g_m of the transistor, with C_A=500aF.

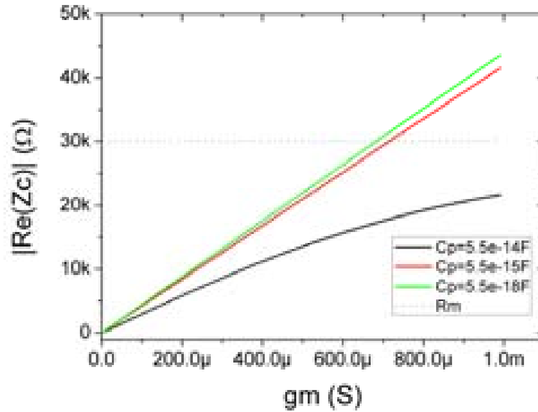

Figure 2.12: Plot of the real part of the circuit impedance as function of transistor transconductance g_m. Oscillation is possible for $|\operatorname{Re}(Zc)|>R_m$

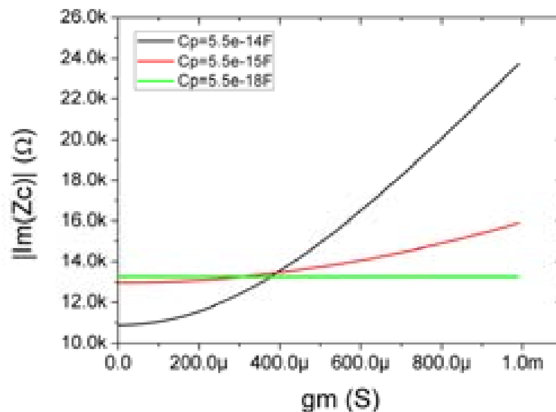

Figure 2.13: Imaginary part of the circuit impedance as function of transistor transconductance g_m

On *Figure 2.12*, only the oscillator presenting a real part higher than the motional resistor R_m oscillates. It can be observed that for low R_m values the required g_m is lower. It is also worth to notice that parasitic shunt capacitor C_p can even make the circuit not to oscillate. The oscillator begins to oscillate if g_m>680µA/V and C_p=5.5aF. *Figure 2.13* shows that the imaginary part of Z_c (and therefore p) is higher for higher C_p value resonators. From this calculus, it can be deduced that low motional resistance is required for oscillation whereas a low C_p is required for low frequency pulling, and therefore resonator controlled oscillation. Moreover, a low R_m allows reducing the g_m of the transistor and therefore, reduces power consumption.

Once the oscillator is able to perform its function, i.e. oscillate, an important performance parameter of an oscillator, especially in RF systems is its phase noise [29]. According to Leeson's model [30], the phase noise at f_m frequency offset from the carrier of an oscillator can be expressed like:

$$L\{f_m\} = \frac{2 \cdot k \cdot T \cdot F}{P_o} \cdot \left[1 + \left(\frac{f_o}{2 \cdot Q \cdot f_m} \right)^2 \right] \tag{2.61}$$

Where k is Boltzman's constant, T is the temperature; F the noise factor of the oscillator, P_o is the output power of the oscillator, f_0 the carrier frequency (oscillation frequency) and Q the quality factor of the resonator. This simple model shows (see *Figure 2.14*) two different regions: a) far from the carrier (high f_m), the spectrum is flat and its value is mainly determined by the noise factor and the output power thus will be basically the thermal noise of the amplifier stage and b) for frequencies near the carrier, the phase noise presents a $1/f_m^2$ slope (i.e. -20dB/dec) and its value is dependent on Q factor. In order to obtain a low phase noise, output power, and quality factor should be as high as possible. Unfortunately, the increase of both Q and P_o could provoke the apparition of $1/f_m^3$ phase noise due to an increase of resonator non-linearity [27]. The limit of P_o is set by the maximum energy that can be stored in the resonator, and consequently by the linearity of the resonator.

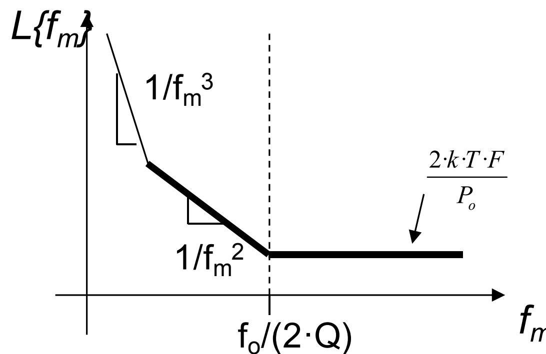

Figure 2.14: Phase noise shape. Bold line represents the leeson equation prediction; $1/f^3$ region is also shown.

Because of the impact of C_p, C_m and the quality factor Q on the oscillator performance, a figure of merit for resonators can be defined as [28]:

$$M = \frac{Q}{C_p / C_m} \tag{2.62}$$

Even though the requirement for high Q (i.e. low R_m) and low C_p was explained above, the inpact of C_p/C_m coeffient was not mentioned. For this reason, several electrical simulations (magnitude and phase) of the $RLC//C_p$ equivalent model are shown in *Figure 2.15*

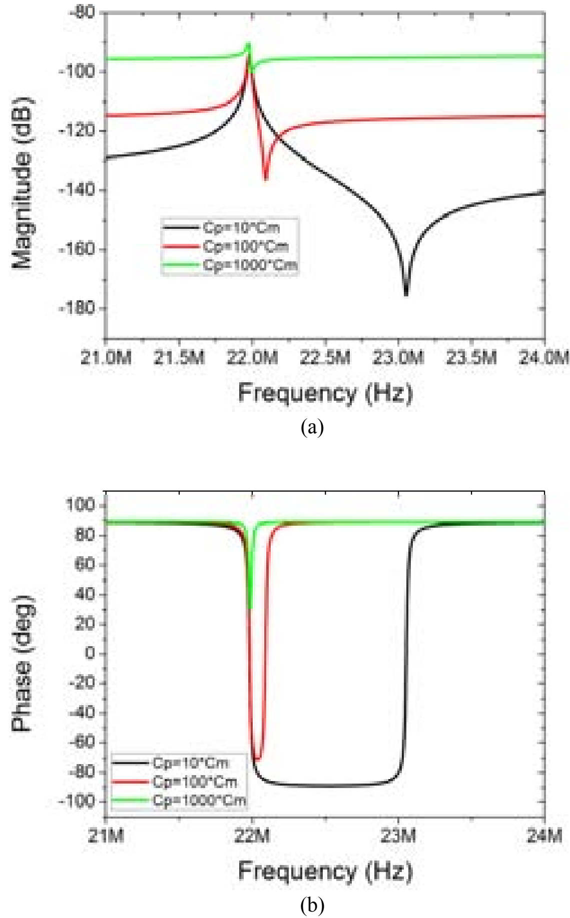

(a)

(b)

Figure 2.15: (a) Magnitude and (b) Phase electrical simulations of the $RLC//C_p$ model considering different values for C_p/C_m coefficient.

In these plots it can be observed the importance of obtaining a low C_p/C_m: when $C_p=10\cdot C_m$, the resonance peak is not altered by the parasitic capacitor, and the phase shift reaches 180 degrees. For highest values of this coefficient, the phase shift is reduced and the resonance is reduced and altered by the proximity of the antiresonance peak.

The equivalent RLC model described on section 1.1.6, allows us to translate the M figure of merit in mechanical resonator requirements. Substituting (2.40) into (2.62) and arranging the expression, equation (2.63) is found.

$$M = \frac{Q}{C_p \cdot k} \cdot \left(\frac{\varepsilon \cdot A}{s^2} \cdot V_{DC} \right)^2 \tag{2.63}$$

For maximizing this figure of merit, Q, coupling area (A), and the applied V_{DC} have to be the highest possible, whereas the parasitic capacitor (C_p), the elastic constant (k) and the electrode to resonator gap (s) must be minimized. Note however the stronger dependence on the gap (4th power dependence) compared with the others. As a figure to the reader, M value for macroscopic quartz crystal resonator is of 57818, whereas for MEMS resonator, the highest reported value is of 234 [31]. Even though this value is lower when compared to macroscopic quartz crystals, when these crystals are miniaturized, the M value is importantly reduced [32]. Another important performance characteristic that has to be also considered is the thermal stability and long and short-term stability. On thermal stability several studies were published, including some techniques in order to improve this performance parameter [33, 34]. Although this performance is very important and some work among this issue recently started inside the research group [35], it will not be object of the analysis of this thesis, which is more focused on resonator topologies. Moreover, the structures without vacuum-encapsulation are prone to moisture contamination that can modify the performance. In fact, the MEMS resonators+oscillator were used as ultra-sensitive mass sensors as their first application [36].

Frequency tuning requires a further discussion. Although this frequency tunability can be used to trim the resonance frequency to mitigate process variations, a high amount of tunability is counterproductive when drift on the DC bias voltage is considered. The resonator with the highest tunability in this thesis, the 24MHz clamped-clamped beam shows a FT=1090ppm/V^2. Assuming a drift in the DC voltage of the 10%, the frequency variation of the resonator will be of 5.5kHz, less than the 0.03%.

To summarize, a resonator for frequency reference has to accomplish: low R_m and C_p, to comply with the oscillation criteria, high Q and high power handling, for phase noise performance, and high stability, for which vacuum encapsulation is needed.

2.3.2 FILTERING

MEMS devices are frequency selective, especially when they have high Q values, and therefore are able to filter signals. The shape and characteristics of the filter varies depending on the function of this element in the RF front-end. As it can be observed in *Figure 1.8*, most of the filters are band-pass, and therefore an appropriate bandwidth according to the RF protocol has to be designed. To obtain a filter, a flat band-pass has to be created, for doing so; there are several techniques that will be briefly explained in this section. Due to the high Q of the MEMS resonators, termination resistors have to be added at the input and output of the filters to provide a more flat pass-band [37]. An important property of these filters is their tunability, which allows slight bandwidth center tuning of the filter.

2.3.2.1 Parallel Filtering

In this architecture, the output signals of two or more resonators are combined [38]. The resonators, with slightly different resonance frequencies, are modelled using the RLC//C_p model shown in *Figure 2.6* and simulated using Agilent Advanced Design System (ADS) electrical simulator (*Figure 2.16*). In practical implementations, the resonators are identical and the difference between resonance frequency is obtained by DC voltage tuning (applying different DC values in each resonator).

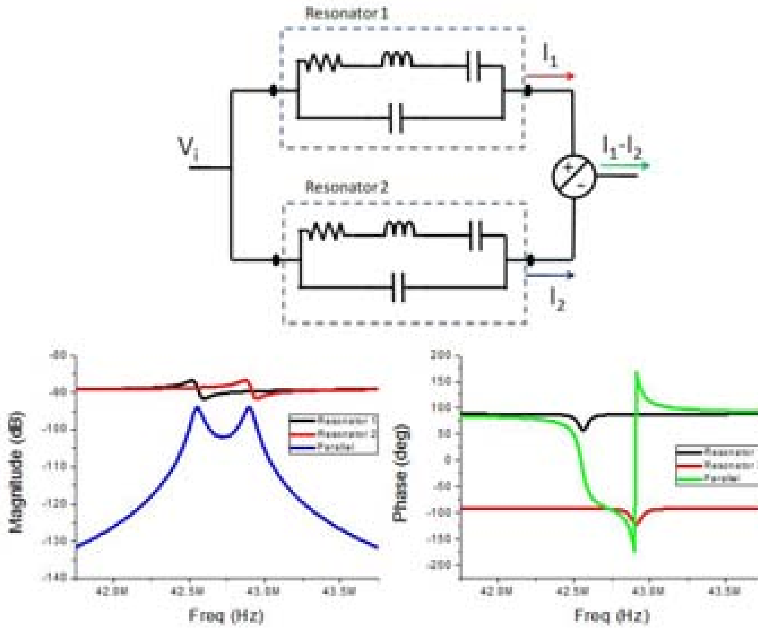

Figure 2.16: Parallel filtering with MEMS resonators. R_m=5MΩ, C_m= 1.25aF, C_p=0.1fF. L_m value is calculated in terms of the resonance frequency of each device. Note that the combined phase response shows an abrupt phase change due to a change of scale.

This output current subtraction can be performed using two different methods: direct current addition, in which the input of one of the resonators is previously inverted [38] or differential amplification [39]. An interesting effect observed in these simulations is the cancelation of the parasitic feedthrough current when the outputs of both resonators are combined, and therefore does not affect the resonance response.

2.3.2.2 Coupled resonators

Another method to create the bandpass, is to couple identical resonators (with the same applied DC voltage) by means of electrical [40] or mechanical [41] coupling. In both techniques the frequency response of the resonant element is modified introducing an additional resonance mode by means of a coupling element.

In the case of the electrical coupling, the resonance frequency is usually altered by a coupling capacitor. *Figure 2.17* shows ADS simulation of two identical coupled resonators with capacive coupling. Termination resistors (R_Q) are used to reduce the resonators Q and flatten the passband. Considering a second order filter like the one shown in *Figure 2.17*, one of the magnitude peaks is placed in the natural resonance frequency of the resonator whereas the other will be placed at [40]:

$$f_1 = f_0 \sqrt{\frac{1 + \pi \cdot f_0 \cdot C_{coup} \cdot R \cdot Q}{\pi \cdot f_0 \cdot C_{coup} \cdot R \cdot Q}} \qquad (2.64)$$

It can be then observed that the bandwidth of this kind of filters can also be tuned by changing the applied DC voltage (which changes f_0 and R) or changing the C_{coup}, for example using a variable capacitor.

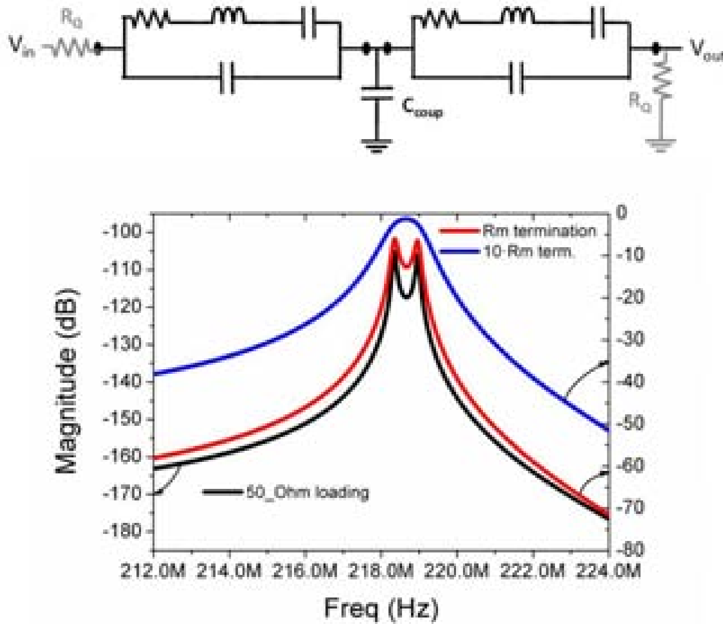

Figure 2.17: Coupled resonators with electrical capacitive coupling. The resistors in gray are the termination resistors parametrized as a function of R_m. R_m=100kΩ, C_m= 1.25aF, C_p=0.1fF. L_m value is calculated in terms of the resonance frequency of each device.

On the mechanical coupling, the resonators are connected by means of a mechanical beam. With this coupling an additional resonance mode close to the natural resonance is created [41], providing a frequency response similar to the shown in *Figure 2.17*. In mechanically coupled resonators, the bandwidth is basically set by the stiffness of the coupling element (i.e. its dimensions) and the location of the coupling along the resonator, and therefore are not bandwidth tunable.

2.3.2.3 Single resonator filter

Filtering can also be performed using a stand-alone resonator, as shown in [42]. The main idea is to use a device that has two close modes of resonance. For this kind of resonators, the electrical equivalent model is like the one shown in *Figure 2.18(a)*, where each RLC branch models each resonance mode. A similar response to the *Figure 2.16*, can be obtained if the two resonant modes are out of phase, which is modeled using a phase inverter or a transformer, as shown in *Figure 2.18(b)*.

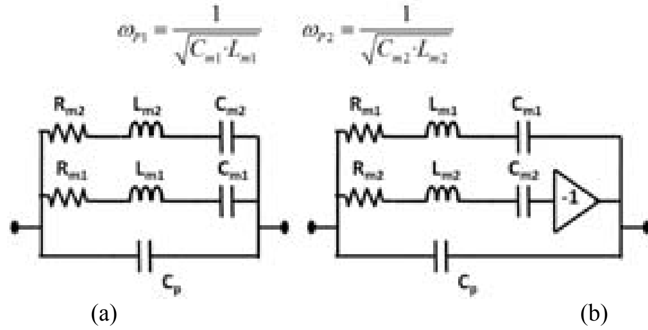

Figure 2.18: (a) Two mode resonator electrical model and (b) Two mode resonator model with off-phase resonance modes .

As it is shown in the equivalent electrical model simulations of *Figure 2.19,* the resonator with off-phase resonance modes behaves like a band-pass filter if $\omega_{p2}>\omega_{p1}$. It is remarkable that this functionality is achieved using a single resonator, instead of coupling different resonators.

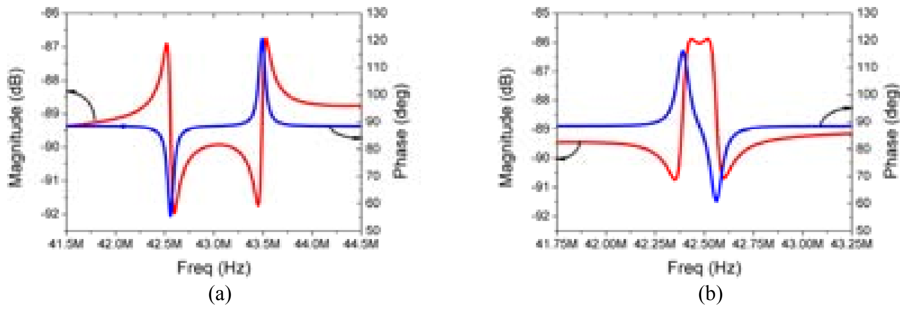

Figure 2.19: Frequency response for a out-of-phase 2-mode resonator. (a) $\omega_{P1}<\omega_{P2}$ and (b) $\omega_{P1}>\omega_{P2}$

2.3.2.4 Resonator requirements for filtering

The requirements for MEMS resonators as filters depend on the function of the filter, i.e. where it is located on the RF chain. For example, if a RF filter is designed considering a direct channel selection topology [14], a high resonance frequency (corresponding to a channel of an RF protocol) is required. Additionally, because it is the nearest device to the antenna, a nearly 50Ω series motional resistance for proper impedance matching is also necessary. The need of low impedance is translated to a requirement of high *Q*. Unfortunately, high *Q* resonator have a very narrow resonance peak, which makes difficult to define wide band-pass filters. For broadening the pass-band, coupling of several resonators and termination resistances are required [43]. These high frequency resonators, also suffer more seriously the effect of parasitic capacitor. On filtering, parasitic capacitor plays an important role in the performance of the filter, as it sets the stop-band rejection. Operating at high frequencies, parallel parasitic impedance presents low value and therefore an important amount of input signal is feed-through directly at the output, increasing the stop-band signal.

IF filters (with characteristic center frequencies of tens of MHz) do not suffer so much as RF filters on these aforementioned issues. First of all, considering the monolithic integration of MEMS filters on the on-chip receiver greatly alleviates the requirement of a 50Ω motional

resistance. Moreover, lower frequency resonators usually have higher coupling area and higher *Q* than their higher frequency counterparts, and consequently lower motional resistance.

2.3.3 FILTERING-MIXING ("MIXLING")

MEMS resonators are capable to perform mixing between signals [67]. Depending on where the mixing operation (product between two signals) takes place, there are two different mechanisms: "force-mixing" [44] or "current-mixing" [45]. On both mixing types, the signals are applied to the resonator like in *Figure 2.20,* where the RF signal is applied in the excitation electrode and the LO signal (plus the DC voltage) is connected to the resonator. The applied force to the resonator is (2.65):

$$F_x = \frac{\partial E}{\partial x} = \frac{1}{2}\cdot\left(\frac{\partial C_E}{\partial x}\cdot\left(V_i - V_{DC} - V_{LO}\right)^2 + \frac{\partial C_R}{\partial x}\cdot\left(V_{DC} + V_{LO}\right)^2\right) \tag{2.65}$$

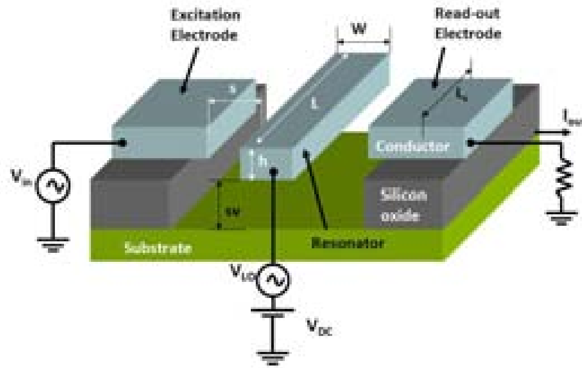

Figure 2.20: Applied signal for mixing applications

Expanding the different terms of equation (2.65), the applied force becomes (2.66):

$$\begin{aligned} F_x = {} & V_{DC}^2\cdot\frac{1}{2}\left(\frac{\partial C_E}{\partial x}+\frac{\partial C_R}{\partial x}\right) - V_i\cdot V_{DC}\cdot\frac{\partial C_E}{\partial x} + V_{LO}\cdot V_{DC}\cdot\left(\frac{\partial C_E}{\partial x}+\frac{\partial C_R}{\partial x}\right) - \\ & - V_i\cdot V_{LO}\cdot\frac{\partial C_E}{\partial x} + \frac{1}{2}\cdot\frac{\partial C_E}{\partial x}\cdot V_i^2 + V_{LO}^2\,\frac{1}{2}\left(\frac{\partial C_E}{\partial x}+\frac{\partial C_R}{\partial x}\right) \end{aligned} \tag{2.66}$$

Where the interesting frequency terms are the second and fourth, that correspond to the current and force mixing components, respectively. Note that the term $V_i\cdot V_{LO}$ is already performing the mixing and therefore the frequency of this force is at $f=f_i \pm f_{LO}$, . The $V_i\cdot V_{DC}$, with $f=f_i$ component is the same that was found on section 2.1.1 and represents an amplitude modulation functionality [45]. The selection of one or other kind of mixing depends on the applied signal frequencies. As it was aforementioned, the MEMS resonator moves only for forces whose frequency is near to the natural resonance frequency (f_0) of the resonator, whereas all other force components do not produce movement, and are filtered. Therefore, for force mixing f_i and f_{LO} must be chosen so that $f_i+f_{LO}=f_0$ or $f_i-f_{LO}=f_0$, depending if up or down conversion is desired. For current-mixing, input frequency complies $f_i=f_0$. Considering only the force frequency components for each kind of mixing, equation (2.66), can be divided into (2.67) and (2.68):

$$F_x^{force-m} = V_i \cdot V_{LO} \cdot \frac{\partial C_E}{\partial x} \tag{2.67}$$

$$F_x^{current-m} = V_i \cdot V_{DC} \cdot \frac{\partial C_E}{\partial x} \tag{2.68}$$

Where “force-m” and “current-m” superscripts, depict the force and current mixing, respectively. And therefore, the displacement associated to these forces are:

$$x_{force-m} = \frac{Q}{k} V_i \cdot V_{LO} \cdot \frac{\partial C_E}{\partial x} \tag{2.69}$$

$$x_{current-m} = \frac{Q}{k} V_i \cdot V_{DC} \cdot \frac{\partial C_E}{\partial x} \tag{2.70}$$

The general output current expression for the resonator shown in *Figure 2.20* is:

$$\begin{aligned} I_o &= C_R \cdot \frac{\partial \left(V_{DC} + V_{LO} \right)}{\partial t} + \left(V_{DC} + V_{LO} \right) \cdot \frac{\partial C_R}{\partial t} = \\ &= C_R \cdot \frac{\partial V_{LO}}{\partial t} + V_{LO} \cdot \frac{\partial C_R}{\partial x} \cdot \frac{\partial x}{\partial t} + V_{DC} \cdot \frac{\partial C_R}{\partial x} \cdot \frac{\partial x}{\partial t} \end{aligned} \tag{2.71}$$

The second term is the used in current-mixing and the third is the one used in force-mixing. And therefore the output current expression are (2.72) and (2.73):

$$I_o^{force-m} = V_{DC} \cdot \frac{\partial C_R}{\partial x} \cdot \frac{\partial C_E}{\partial x} \cdot \frac{Q}{k} \cdot \left(V_{LO} \cdot \frac{\partial \left(V_i \right)}{\partial t} + V_i \cdot \frac{\partial \left(V_{LO} \right)}{\partial t} \right) \tag{2.72}$$

$$I_o^{current-m} = V_{DC} \cdot \frac{\partial C_R}{\partial x} \cdot \frac{\partial C_E}{\partial x} \cdot \frac{Q}{k} \cdot V_{LO} \cdot \frac{\partial V_i}{\partial t} \tag{2.73}$$

It can be observed that current has similar expressions, although the force-mixing presents an additional term that increases the amount of the output current. Although the final output current have more or less the same magnitude, the displacement of the MEMS in current-mixing operation is greater than the one using force-mixing as it can be observed comparing (2.69) and (2.70), in fact it is the same as in the usual operation of the resonator, and therefore limits the linearity of the mixer, which is expected to be greater on force-mixing resonators.

Thanks to the linear dependence of V_{DC} term, shown for both mixing mechanisms, the mixer-filter can be disconnected when V_{DC}=0V is applied. This property can be used to directly select the appropriate filter bank branch without the use of switches [46], enhancing the capabilities for MEMS use in RF-applications.

Note that the input and output signal frequencies are different, so that the feedthrough parasitic signal is outside of the desired output frequency band, and therefore does not affect the resonance measurement. In fact the electrical equivalent model is reduced only to the RLC branch. This allows the electrical measurement of the resonance without the undesired interference of the parasitic feedthrough capacitor.

An important property of MEMS as mixers is that the output signal is filtered by the resonator frequency response, and therefore the mixer-filter can be designed to have a determined band-pass. Due to the similarity or functions with the filters, the resonator requirements for mixing are the same aforementioned for filtering.

2.3.4 STATE OF THE ART

In this section some of the most relevant works on the use of MEMS resonators in the previously described functionalities will be presented. Special focus will be taken on the proposed solutions to overcome the different challenges involving the use of MEMS resonators as frequency references, filters and mixers.

2.3.4.1 Frequency reference

In this section stand-alone resonators (*Table 2.1*) and resonators together with oscillators which use MEMS resonators (*Table 2.2*) will be shown. As it can be observed, different resonator topologies are used for different resonance frequency ranges from the HF (3MHz to 30MHz) to UHF (30MHz to 3GHz). *Table 2.1* shows some experimental results of the reported resonators. Most of these resonators are reviewed in [14], which also contains additional information of these devices. In *Table 2.1* only the information reported in the original works is provided.

It can be observed that these resonators present very different resonance frequencies from the lower 8.5MHz for a clamped-clamped beam from [41] to the highest 1.210GHz obtained in the third oscillation mode of a hollow disk resonator [56]. On the selected resonators, big values of Q can be observed, however they seem to require vacuum encapsulation [57-60] to obtain these results, except for square resonator array [51] and disk-shaped [48, 50, 52, 53] resonators which present values of Q>1000 even in air. Additional techniques like λ/4 anchors where adopted to decrease the losses and therefore increase *Q* value on most resonators. Most of the shown resonators, but [55] are fabricated by special MEMS processing, and even piezoelectric materials are used in [53]. Only two of the resonators in *Table 2.1* presents a DC actuation voltage compatible with CMOS technology (less than 5V) [49] and [53], this later does not require a DC voltage as it is made with a piezoelectric material. Another factor which affects the use of the MEMS resonators is the value of the motional resistance; again the piezoelectric resonator shows the best result (only 84Ω). Among the most interesting techniques to reduce the motional resistance is the coupling of different resonators to increase the overall coupling area [51] and the use of a solid-gap [54], which moreover protects the gap from moisture contamination. The last considered performance parameter is the temperature drift of the resonance frequency (Δf_T), the usual reported values are on the tens of ppm/ºC, higher than the usual 5ppm/ºC of temperature compensated oscillators based on quartz resonators (TO501) [61], the stiff-compensated resonator [34] is able to improve this drift and obtain a less than 1ppm/ºC.

Table 2.1: State of the art MEMS resonators characteristics

Res.	Ref.	f_{RES} (MHz)	V_{DC} (V)	Δf_T (ppm/ºC)	*Q* *Air/vacuum*	R_m (kΩ)	Technology
CC-Beam							
Bannon, 2000	[41]	8.50	10	NR	50/ 8000	NR	Flexural mode beam, polysilicon microfabrication
Wang, 2000	[23]	54.2	35	16.7[a]	-/840	8.67	Flexural mode beam, polysilicon microfabrication
	[23]	71.8	28	NR	-/300	NR	
Verd, 2006	[47]	59.6[d]	80[d]	NR	40/-	NR	AMS CMOS technology, M4 layer flexural beam.
Teva, 2008	[15]	290	14	NR	-/2836	NR	AMS, Poly1, mixing, on-chip amplif. Flexural beam.
Hsu, 2002	[34]	9.96	8	0.24	-/4000	NR	Stiffness Temperature comp.
FF-Beam							
Wang, 200	[23]	30	22	-12[b]	-/8110	31.1	Flexural mode beam, polysilicon microfabrication, λ/4 torsional support beams
	[23]	90	76	NR	-/7000	167	
W-G Disk *Abdelmoneum, 2003*	[48]	73.4	7	NR	8600/ 98000	26@18V[b]/ 2.7@16V	Polysilicon microfabrication, wine-glass mode
Bulk anular ring							
Teva, 2008	[15]	1046	10[d]	NR	400/-	NR	CMOS AMS, Poly1, bulk acoustic mode
Li, 2004	[49]	24.4	2.5	NR	-/67519	13.1	Polysilicon microfabrication,
	[49]	1210[c]	8[c]	NR	14603[c]	NR	Mixing meas.
Cont-M Disk[c]							
Wang, 2004	[50]	152	6	NR	9816/ 12289	480[b]	Mixing meas. Polysilicon microfabrication. Radial contour mode
	[50]	274	30.5	NR	7500/ 8950	17.2[b]	
	[50]	1160	10.5	NR	2655/ 2689	2440	
Square res array *Demirci, 2006*	[51]	63.4	30[d]/40	-10	1900/ 12400	5.10	Polysilicon microfabrication, flexural mode
SOI Disk *Pourkamali, 2004*	[52]	149	15[d]/17	-26	25900/ 45742	91.2[d]/ 43.3	Single crystal silicon fabrication
Lat. Piezo Ring *Piazza, 2005*	[53]	472		-25	2900/-	0.084	Piezo, AIN
s-g disk res *Lin, 2005*	[54]	61	8	NR	-/ 25300	1.51	solid gap
SiFR *Lo, 2007*	[55]	8.04	46	NR	-/ 3589	NR	Post-processed CMOS

[a]Value for a resonator at 4.2MHz
[b]Value for a resonator at 53.6MHz
[c]Mixing measurement
NR: Not Reported

Some resonators like the ones presented in previous table were used as frequency references for oscillators. In *Table 2.2* some performance parameters of integrated oscillators are presented together with the characteristics of a commercial oscillator based on a quartz crystal resonator: TO501 [61], listed for comparison purposes.

Table 2.2: MEMS-based oscillators characteristics

Res.	***Ref.***	f_{RES} **(MHz)**	V_{DC} **(V)**	***Q***	R_m **(kΩ)**	***M***	***L*** **(dBc/Hz)**		I_{cc}/V_{cc} (μA/V)	***Comments***
							1kHz	100kHz		
Cantilever (Flexural)	[11]	6.3	45	108	29.3E3	NR	-55.6	-91.6	5.2E3 /3.3	AMS monolithic, Metal
Cantilever[a] (Flexural)	[11]	6.3	17	880	34.9E3	NR	-68.5	-95	5.2E3 /3.3	AMS monolithic, Metal
CC-Beam (Flexural)	[11]	15.36	70	156	15.4E3	NR	-53.1	-98.1	5.2E3 /3.3	AMS monolithic, Metal
CC-Beam[a] (Flexural)	[11]	15.36	30	918	11.9E3	NR	-69.1	-98	5.2E3 /3.3	AMS monolithic, Metal
CC-Beam (Mattila)[a] (Flexural)	[5]	14.3	100	1500	1000	0.71	-105	NR		Silicon microfabrication. Discrete amplifier, compensation loop
CC-Beam[a] (Flexural)	[31]	9.34	8	3100	8.79	151	-82	-116	236/3.3	Polysilicon micromachining, TSMC integrated oscillator, wire-bonded
CC-Beam 2 (wide)[a] (Flexural)	[31]	8.61	15	1036	0.340	234	-80	-120	236/3.3	
Wine-glass Dsk[a] (Wine-Glass)	[31]	61.2	12	48000	1.5	54.6	-110	-132	236/3.3	
Wine-glass array[a] (9 resonators)	[63]	61.2	7	119500	2.56	NR	-120	-136	117/3.3	Polysilicon micromachining, TSMC integrated oscillator, wire-bonded
Wine-glass array[a]	[64]	10.9	5	1092	5.80	NR	-80	-95	350/3.3	TSCM integrated + CMOS comp nickel resonator
Square BAW[a] (Bulk)	[62]	12.9	20	100000	0.5	41.1	-130	-147	12/3 (oscil.) 15/3 (buffer)	Silicon microfabrication. Bonded AMS 0.35um CMOS
TO501	[61]	30.0	3.3				-135	-145	2E3/3.3	TO501 Datasheet

[a] Measurements in vacuum

The most relevant parameter and which is more directly related to resonator performance is the close to carrier phase noise. The best phase noise on the table is obtained with the commercial resonator [61], followed by the BAW resonator [62], but using V_{DC}=20V. The only CMOS compatible DC voltage resonator is [64], which moreover is fabricated using a CMOS compatible MEMS fabrication process in which the MEMS is built above the fully processed CMOS wafer, however, it presents a 55dBc/Hz higher phase noise than [61] at 1kHz. The utility of arraying several resonators can be observed when comparing the wine-glass disk and the wine-glass disk array oscillators reported in [63]: even though the *Q* of the arrayed frequency reference is reduced when compared to the single version, its phase noise is lower than the single resonator version.

As it was aforementioned in *Chapter 1*, frequency references are a key segment of RF applications of MEMS, for this reason some start-up companies have begun very recently to sell this kind of frequency references. The first one with a full set of devices up to 220MHz based on MEMS solutions is SiTime, located in California. The manufacturing process includes Deep Reactive Ion Etching (DRIE) in a standard CMOS fab. Quality factors around 80000 are achieved with resonators oscillating in plane. The complete packaged oscillator is a combination of the sealed resonator and a CMOS driver IC which provides electronic frequency compensation for temperature variations and has a PLL for determine the output frequency. One of the prototypes from SiTime is the SiT0100 which has the following characteristics: die size of 0.8mmx0.6mmx0.15mm, resonance frequency 5.1MHz @ Q=80000, 0.15ppm/25 years aging and -115dBc/Hz phase noise at 10 kHz offset. The penalty for these resonators is the higher power consumption compared with quartz crystal to decrease phase noise [65].

Another start-up, Discera [66] founded by C.T.Nguyen and also located in California, starts selling last year (2008), some oscillators solutions based on its PureSilicon Resonator™ technology with different properties and frequencies up to 150MHz. The sealed resonator is bonded to an IC circuit and plastic-packaged together for the final device. Equally that SiTime, a PLL is in charge of providing the final output frequency. The devices achieve a 10ppm frequency deviations, a lower value than the the required performance from the market (in the range between 50ppm to 100ppm). The main problem is the need for temperature compensation (normally achieved via digital circuitry) which degrades the phase noise performance.

Silicon Clocks [67], founded by R.T.Howe and E.Quevy as an start up company from U.California-Berkeley, has developed a low temperature silicon-germanium process (patented as CMEMS™, from Standard CMOS + MEMS) from which they are capable to integrate over standard CMOS integrated circuit its MEMS resonator, achieving a 3D silicon manufacturing capabilities. Unfortunately the data sheets are not available from the web page of the company, but they claim to have resonators (32 kHz to 150 MHz) and the J-Series™ of PLL IP which generates clock outputs from 100 MHz to 700 MHz with ultra-low phase jitter less than 1 ps RMS, providing a low-cost alternative to expensive SAW oscillators.

Mobius Microsystems [68] is also selling monolithic CMOS dies up to 100 MHz for replacing the quartz crystal based on low noise very high frequency harmonic LC oscilators fabricated using RF CMOS technologies. Mobius Microsystems was established in April 2004, founded by Michael S. McCorquodale, following his PhD research work at the University of Michigan, Ann Arbor. The technology developed is called CMOS harmonic Oscillator (CHO), and is not based on MEMS resonators. In this approach the required output frequency is produced programming the required division ratio, instead of using frequency multiplication by means of a PLL. Following this technology researchers from this company has presented new advances on their technology extending the frequency range till 480 MHz and achieving low phase noise performances {McCorquodale, 2008 #256}. The key innovation from this company is the analog control circuit that compensates for process, voltage and temperature variations the oscillating frequency.

Ecliptek corporation http [69], is also selling silicon oscilators products up to 125 MHz from last year (EMO family); this EMO family are silicon oscillator products where the CMOS output frequency is primarily controlled by an internal MEMS resonator. At the heart of EMO oscillators is a vibrating MEMS mechanical resonator 100 times smaller than its consumer grade quartz competitor which allows ultra-miniature packaging without sacrificing performance.

2.3.4.2 Filter

Different published MEMS resonators for filtering application are shown in *Table 2.3*. The performance parameters compared are the central frequency of the filter (f_c), the 3dB attenuation bandwidth (BW_{3dB}), the pass-band ripple, the shape factor at 20dB (SF_{20dB}), which is defined as the $BW\text{-}_{20dB}/BW\text{-}_{3dB}$, and the stop-band rejection (*SB rej.*) [14].

Table 2.3: State of the art MEMS filters

Resonator	*Ref.*	f_c *(MHz)*	BW_{3dB} *(kHz)*	*Ripple (dB)*	SF_{20dB}	*SB Rej. (dB)*	*Comments*
Tuning fork	[70]	2.29	8.24	2.7	1.64	22	Single resonator
CC-Beam mechanical coupling	[41]	7.8	18	1.5	2.31	35	
CC-Beam electrical coupling	[40]	0.810	0.54	N.R.	2.9	28	Off-chip amplif.
CC-Res.+nanowire	[71]	17.9	120	0.3	NR	6	
Coupled disk	[43]	163	98.5	0.5	2.85	27.6	
Bridged CC-beam	[56]	9	20	NR	1.95	51	
Array composite filter	[72]	68.1	190	NR	NR	25	

It can be observed that most filters present a quite low bandwidth, which cannot be directly used in nowadays RF protocols, with bandwidths above 200kHz (GSM)., but demonstrates the possibility to obtain low bandwidths on high frequency MEMS-based filters, something impossible in conventional filters. The most interesting techniques for filtering are the mechanical coupling of several resonators [43, 71, 72]. Using multiple resonators at the same frequency increase the overall coupling area (therefore reducing the motional resistance and consequently reduce the insertion losses) whereas the coupling makes all the resonators to oscillate at the same frequency, consequently minimizing fabrication mismatches. The tuning fork of [70] presented a filter which only uses a single resonator instead of the coupled resonator approach of the other filters in the table.

2.3.4.3 Mixers

Another important function that MEMS resonators are capable to perform is the down and up conversion frequency for RF systems. Nearly all the devices are reported as down-conversion mixers, and therefore the input electrode is the RF port, the resonator acts as the LO port and the readout electrode is the IF port. *Table 2.4* shows the most important resonator characteristics of MEMS resonators acting like filter-mixers. The selected characteristics are: conversion loss (*CL*), applied V_{DC} and P_{LO}, f_{RES}, isolation between ports ($I_{LO\text{-}IF}$, $I_{LO\text{-}RF}$, $I_{RF\text{-}IF}$) and the highest down-converted input frequency (f_{RF}). Among the different MEMS topologies there are cantilevers, clamped-clamped beams, mechanically coupled clamped-clamped beams, coupled ring resonators and single (and coupled) double-ended tuning forks (DETF).

Table 2.4: State of the art for MEMS-mixers

Resonator	Ref..	*CL* (dB)	P_{LO}(dBm)/ /V_{DC}(V))	f_{RES}(MHz))	*Isolation* (dB) $I_{LO-IF}/I_{LO-RF}/I_{RF-IL}$	f_{RF} (MHz)	Comments
Cantilever	[39]	49.5	13.5/10	0.435	- / - /-	3200	CMOS stack, off-chip amplif.
CC-beam	[45]	75	5/14	22.5	58 / - / 82	1000	On-chip amplif. AIR meas.
Coupled CC-Beams	[73]	72/13*	15/11	37	39/29.4/44	242	Off-chip buffered meas.
Coupled rings res.	[74]	83.5	18/3	423		438	
DETF	[75]	48	0/40	0.743	36/48	10	Off-chip amplif.
Coupled DETF	[75]	54		0.66	56/68	10	Off-chip amplif.
Coupled DETF	[76]	45	0/7	1.3	30 / 38 / -	400	
Coupled DETF (AM modulation)	[76]	15	Not required/7	1.3		500	

As it can be observed from the resonators of *Table 2.4*, MEMS mixlers show high conversion losses, mainly due to the impedance mismatch between the measurement instrumentation and the high-impedance resonator, as it is shown in [73], where a correction of this effect is applied. The highest input RF signal able to be downconverted is up to 3.2GHz of [39], fabricated using a CMOS technology + DRIE to define the structures.

2.3.5 CONCLUSIONS

In this chapter the working principle of MEMS resonators in different RF applications have been presented, highlighting the most relevant design parameters for each application. The state of the art resonators shown in previous section are expected to provide some practical insight in the value of the different parameters and show the potential of MEMS resonators in RF systems. These resonators will be used in next chapters to compare and discuss the obtained results. *Table 2.5* shows a summary of the most important parameters for the applications discussed.

Table 2.5: Summary of performance requirements for each RF application

Performance parameters	Frequency reference	Filter	Mixer	Comments
Resonance frequency	HF or VHF	HF or VHF	HF or VHF	Depends on application
Frequency tuning	Moderate	High	High	Desired as high as possible in filter and mixer
Quality factor	Very high	Very high or moderate	Very high or moderate	Q requirement must be relaxed for wide band-pass filters
Motional resistance	Very low	Very low or moderate	Very low or moderate	R_m requirement can be relaxed in a monolithic receiver
Feed-through capacitor	Very low	Very low	Low	In general C_p must be reduced to the minimum although in mixing applications can be neglected
Linearity	Very high	Very high	High	Linearity affects $1/f^3$ phase noise on oscillators and IIP3 on filters-mixers

REFERENCES

[1] H. A. C. Tilmans, D. J. Ijntema, and J. H. J. Fluitman, "Single element excitation and detection of (micro-)mechanical resonators," in *Solid-State Sensors and Actuators, 1991. Digest of Technical Papers, TRANSDUCERS '91., 1991 International Conference on*, 1991, pp. 533-537.

[2] G. Stemme, "Resonant silicon sensors," *Journal of Micromechanics and Microengineering,* vol. 1, p. 113, 1991.

[3] N. Maluf and K. Williams, *Introduction to microelectromechanical systems engineering*, 2nd ed. Boston: Artech House, 2004.

[4] J. R. Clark, W. T. Hsu, and C. T. C. Nguyen, "High-Q VHF micromechanical contour-mode disk resonator," in *Technical Digest, IEEE Int. Electron Devices Meeting*, San Francisco, California, 2000, pp. 493-496.

[5] T. Mattila, O. Jaakkola, J. Kiihamäki, J. Karttunen, T. Lamminmäki, P. Rantakari, A. Oja, H. Seppä, H. Kattelus, and I. Tittonen, "14 MHz micromechanical oscillator," *Sensors and Actuators A: Physical,* vol. 97-98, pp. 497-502, 2002.

[6] H. C. Nathanson, W. E. Newell, R. A. Wickstrom, and J. R. Davis, Jr., "The resonant gate transistor," *Electron Devices, IEEE Transactions on,* vol. 14, pp. 117-133, 1967.

[7] T. Niels, S. Tonny, J. Henri, L. Rob, and E. Miko, "Stiction in surface micromachining," *Journal of Micromechanics and Microengineering,* p. 385, 1996.

[8] M. Bao, *Analysis and Design Principles of MEMS Devices*: Elsevier, 2005.

[9] V. Kaajakari, "MEMS Tutorial: Pull-in voltage in electrostatic microactuators (available in http://www.kaajakari.net)."

[10] J. Teva, "Integration of CMOS-MEMS resonators for radiofrequency applications in the VHF and UHF bands." vol. Ph.D Bellaterra: Universitat Autònoma de Barcelona, 2007.

[11] J. Verd, "Monolithic CMOS-MEMS Resonant Beams for Ultrasensitive Mass Detection." vol. Ph.D Bellaterra: Universitat Autònoma de Barcelona, 2008.

[12] T. Mattila, J. Kiihamäki, T. Lamminmäki, O. Jaakkola, P. Rantakari, A. Oja, H. Seppa, H. Kattelus, and I. Tittonen, "A 12MHz Micromechanical Bulk Acoustic Mode Oscillator," *Sensors and Actuators A: Physical,* vol. 101, pp. 1-9, 2002.

[13] K. Tanaka, R. Kihara, A. Sánchez-Amores, J. Montserrat, and J. Esteve, "Parasitic Effect on Silicon MEMS Resonator Model Parameters," *Microelectronic Engineering,* vol. 84, pp. 1363-1368, 2007.

[14] C. T. C. Nguyen, "MEMS technology for timing and frequency control," *Ultrasonics, Ferroelectrics and Frequency Control, IEEE Transactions on,* vol. 54, pp. 251-270, 2007.

[15] J. Teva, G. Abadal, A. Uranga, J. Verd, F. Torres, J. L. Lopez, J. Esteve, F. Perez-Murano, and N. Barniol, "From VHF to UHF CMOS-MEMS monolithically integrated resonators," in *Micro Electro Mechanical Systems, 2008. MEMS 2008. IEEE 21st International Conference on*, 2008, pp. 82-85.

[16] J. Teva, G. Abadal, A. Uranga, J. Verd, F. Torres, J. L. Lopez, J. Esteve, F. Perez-Murano, and N. Barniol, "VHF CMOS-MEMS resonator monolithically integrated in a standard 0.35um CMOS technology," in *Micro Electro Mechanical Systems, 2007. MEMS. IEEE 20th International Conference on*, 2007, pp. 779-782.

[17] B. Razavi, "A study of phase noise in CMOS oscillators," *Solid-State Circuits, IEEE Journal of,* vol. 31, pp. 331-343, 1996.

[18] H. Hosaka, K. Itao, and S. Kuroda, "Damping characteristics of beam-shaped micro-oscillators," *Sensors and Actuators A: Physical,* vol. 49, pp. 87-95, 1995.

[19] J. Yang, T. Ono, and M. Esashi, "Surface effects and high quality factors in ultrathin single-crystal silicon cantilevers," *Applied Physics Letters,* vol. 77, pp. 3860-3862, 2000.

[20] V. T. Srikar and S. D. Senturia, "Thermoelastic damping in fine-grained polysilicon flexural beam resonators," *Microelectromechanical Systems, Journal of,* vol. 11, pp. 499-504, 2002.

[21] S. P. Beeby, G. Ensell, and N. M. White, "Microengineered silicon double-ended tuning fork resonators," *Engineering Science and Education Journal,* vol. 9, pp. 265-271, 2000.

[22] W. T. Hsu, J. R. Clark, and C. T. C. Nguyen, "Q-Optimized lateral free-free beam micromechanical resonators," in *Transducers '01: Eurosensors Xv, Digest of Technical Papers, Vols 1 and 2*, Berlin, 2001, pp. 1110-1113.

[23] K. Wang, A.-C. Wong, and C. T. C. Nguyen, "VHF free-free beam high-Q micromechanical resonators," *Microelectromechanical Systems, Journal of,* vol. 9, pp. 347-360, 2000.

[24] M. Agarwal, K. K. Park, M. Hopcroft, S. Chandorkar, R. N. Candler, B. Kim, R. Melamud, G. Yama, B. Murmann, and T. W. Kenny, "Effects of Mechanical Vibrations and Bias Voltage Noise on Phase Noise of MEMS Resonator Based Oscillators," in *Micro Electro Mechanical Systems, 2006. MEMS 2006 Istanbul. 19th IEEE International Conference on*, 2006, pp. 154-157.

[25] E. A. Vittoz, M. G. R. Degrauwe, and S. Bitz, "High-performance crystal oscillator circuits: theory and application," *Solid-State Circuits, IEEE Journal of,* vol. 23, pp. 774-783, 1988.

[26] V. Kaajakari, T. Mattila, A. Oja, and H. Seppa, "Nonlinear limits for single-crystal silicon microresonators," *Microelectromechanical Systems, Journal of,* vol. 13, pp. 715-724, 2004.

[27] L. Seungbae and C. T. C. Nguyen, "Influence of automatic level control on micromechanical resonator oscillator phase noise," in *Frequency control symposium and pda exhibition jointly with the 17th european frequency and time forum, 2003. proceedings of the 2003 ieee international*, 2003, pp. 341-349.

[28] W.-T. Hsu, "Resonator miniaturization for oscillators," in *Frequency Control Symposium, 2008 IEEE International*, 2008, pp. 392-395.

[29] B. Razavi, *RF microelectronics*. Upper Saddle River, NJ: Prentice Hall, 1998.

[30] D. B. Leeson, "A simple model of feedback oscillator noise spectrum," *Proceedings of the IEEE,* vol. 54, pp. 329-330, 1966.
[31] Y.-W. Lin, S. Lee, S.-S. Li, Y. Xie, Z. Ren, and C. T. C. Nguyen, "Series-resonant VHF micromechanical resonator reference oscillators," *Solid-State Circuits, IEEE Journal of,* vol. 39, pp. 2477-2491, 2004.
[32] F. P. Stratton, D. T. Chang, D. J. Kirby, R. J. Joyce, H. Tsung-Yuan, R. L. Kubena, and Y. Yook-Kong, "A MEMS-based quartz resonator technology for GHz applications," in *Frequency Control Symposium and Exposition, 2004. Proceedings of the 2004 IEEE International*, 2004, pp. 27-34.
[33] W.-T. Hsu, J. R. Clark, and C. T. C. Nguyen, "Mechanically temperature-compensated flexural-mode micromechanical resonators," in *Electron Devices Meeting, 2000. IEDM Technical Digest. International*, 2000, pp. 399-402.
[34] W. T. Hsu and C. T. C. Nguyen, "Stiffness-compensated temperature-insensitive micromechanical resonators," in *Micro Electro Mechanical Systems, 2002. The Fifteenth IEEE International Conference on*, 2002, pp. 731-734.
[35] M. Sansa, "Caracterització d'Oscil·ladors Basats en CMOS-M/NEMS i la Seva Aplicació com a Sensors de Massa." vol. Projecte Final de Carrera: Universitat Autònoma de Barcelona, 2008.
[36] J. Verd, A. Uranga, G. Abadal, J. L. Teva, F. Torres, J. L. Lopez, E. Perez-Murano, J. Esteve, and N. Barniol, "Monolithic CMOS MEMS Oscillator Circuit for Sensing in the Attogram Range," *Electron Device Letters, IEEE,* vol. 29, pp. 146-148, 2008.
[37] A. T. Alastalo and V. Kaajakari, "Systematic design approach for capacitively coupled microelectromechanical filters," *Ultrasonics, Ferroelectrics and Frequency Control, IEEE Transactions on,* vol. 53, pp. 1662-1670, 2006.
[38] L. Lin, C. T. C. Nguyen, R. T. Howe, and A. P. Pisano, "Microelectromechanical filters for signal processing," in *Micro Electro Mechanical Systems, 1992, MEMS '92, Proceedings. An Investigation of Micro Structures, Sensors, Actuators, Machines and Robot. IEEE*, 1992, pp. 226-231.
[39] F. Chen, J. Brotz, U. Arslan, C.-C. Lo, T. Mukherjee, and G. K. Fedder, "CMOS-MEMS resonant RF mixer-filters," in *Micro Electro Mechanical Systems, 2005. MEMS 2005. 18th IEEE International Conference on*, 2005, pp. 24-27.
[40] S. Pourkamali and F. Ayazi, "Electrically coupled MEMS bandpass filters - Part 1: With coupling element," *Sensors and Actuators a-Physical,* vol. 122, pp. 307-316, Aug 2005.
[41] F. D. Bannon, J. R. Clark, and C. T. C. Nguyen, "High-Q HF microelectromechanical filters," *Solid-State Circuits, IEEE Journal of,* vol. 35, pp. 512-526, 2000.
[42] Y. Jize, A. A. Seshia, K. L. Phan, and J. T. M. van Beek, "Internal electrical phase inversion for FF-beam resonator arrays and tuning fork filters," in *Micro Electro Mechanical Systems, 2008. MEMS 2008. IEEE 21st International Conference on*, 2008, pp. 1028-1031.
[43] S.-S. Li, Y.-W. Lin, Z. Ren, and C. T. C. Nguyen, "An MSI Micromechanical Differential Disk-Array Filter," in *Solid-State Sensors, Actuators and Microsystems Conference, 2007. TRANSDUCERS 2007. International*, 2007, pp. 307-311.
[44] J. L. Lopez, J. Teva, A. Uranga, F. Torres, J. Verd, G. Abadal, N. Barniol, J. Esteve, and F. Perez-Murano, "Mixing in a 220MHz CMOS-MEMS," in *Circuits and Systems, 2007. ISCAS 2007. IEEE International Symposium on*, 2007, pp. 2630-2633.
[45] A. Uranga, J. Verd, J. L. Lopez, J. Teva, G. Abadal, F. Torres, J. Esteve, F. Perez-Murano, and N. Barniol, "Fully integrated MIXLER based on VHF CMOS-MEMS clamped-clamped beam resonator," *Electronics Letters,* vol. 43, pp. 452-454, 2007.
[46] C. T. C. Nguyen, "Vibrating RF MEMS Technology: Fuel for an Integrated Micromechanical Circuit Revolution?," in *Int. Conf. on Solid-State Sensors & Actuators (Transducers'05)*, Seoul, Korea, 2005, pp. 243-246.
[47] J. Verd, A. Uranga, J. Teva, J. L. Lopez, F. Torres, J. Esteve, G. Abadal, F. Perez-Murano, and N. Barniol, "Integrated CMOS-MEMS with on-chip readout electronics for high-frequency applications," *Electron Device Letters, IEEE,* vol. 27, pp. 495-497, 2006.

[48] M. A. Abdelmoneum, M. U. Demirci, and C. T. C. Nguyen, "Stemless wine-glass-mode disk micromechanical resonators," in *Micro Electro Mechanical Systems, 2003. MEMS-03 Kyoto. IEEE The Sixteenth Annual International Conference on*, 2003, pp. 698-701.
[49] S.-S. Li, Y.-W. Lin, Y. Xie, and C. T. C. Nguyen, "Micromechanical "Hollow-Disk" Ring Resonators," in *Int. IEEE Micro Electro Mechanical Systems Conference (MEMS)*, Maastricht, 2004, pp. 821-824.
[50] J. Wang, Z. Ren, and C. T. C. Nguyen, "1.156-GHz self-aligned vibrating micromechanical disk resonator," *Ultrasonics, Ferroelectrics and Frequency Control, IEEE Transactions on,* vol. 51, pp. 1607-1628, 2004.
[51] M. U. Demirci and C. T. C. Nguyen, "Mechanically Corner-Coupled Square Microresonator Array for Reduced Series Motional Resistance," *Microelectromechanical Systems, Journal of,* vol. 15, pp. 1419-1436, 2006.
[52] S. Pourkamali, H. Zhili, and F. Ayazi, "VHF single crystal silicon capacitive elliptic bulk-mode disk resonators-part II: implementation and characterization," *Microelectromechanical Systems, Journal of,* vol. 13, pp. 1054-1062, 2004.
[53] G. Piazza, P. J. Stephanou, J. M. Porter, M. B. J. Wijesundara, and A. P. Pisano, "Low motional resistance ring-shaped contour-mode aluminum nitride piezoelectric micromechanical resonators for UHF applications," in *Micro Electro Mechanical Systems, 2005. MEMS 2005. 18th IEEE International Conference on*, 2005, pp. 20-23.
[54] Y.-W. Lin, S.-S. Li, Y. Xie, Z. Ren, and C. T. C. Nguyen, "Vibrating micromechanical resonators with solid dielectric capacitive transducer gaps," in *Frequency Control Symposium and Exposition, 2005. Proceedings of the 2005 IEEE International*, 2005, pp. 128-134.
[55] C. C. Lo and G. K. Fedder, "On-Chip High Quality Factor CMOS-MEMS Silicon-Fin Resonators," in *Solid-State Sensors, Actuators and Microsystems Conference, 2007. TRANSDUCERS 2007. International*, 2007, pp. 2449-2452.
[56] S.-S. Li, M. U. Demirci, Y.-W. Lin, Z. Ren, and C. T. C. Nguyen, "Bridged micromechanical filters," in *Frequency Control Symposium and Exposition, 2004. Proceedings of the 2004 IEEE International*, 2004, pp. 280-286.
[57] G. J. A. M. Verheijden, G. E. J. Koops, K. L. Phan, and J. T. M. van Beek, "Wafer level encapsulation technology for MEMS devices using an HF-permeable PECVD SIOC capping layer," in *Micro Electro Mechanical Systems, 2008. MEMS 2008. IEEE 21st International Conference on*, 2008, pp. 798-801.
[58] B. Kim, M. Hopcroft, C. Jha, R. Melamud, S. Chandorkar, M. Agarwal, K. L. Chen, W. T. Park, R. Candler, G. Yama, A. Partridge, M. Lutz, and T. W. Kenny, "Using MEMS to Build the Device and the Package," in *Solid-State Sensors, Actuators and Microsystems Conference, 2007. TRANSDUCERS 2007. International*, 2007, pp. 331-334.
[59] V. T. Park, R. N. Candler, H. J. Li, J. Cho, H. Li, T. W. Kenny, A. Partridge, G. Yama, and M. Lutz, "Wafer scale encapsulation of MEMS devices," *Advances in Electronic Packaging 2003, Vol 1,* pp. 209-212, 2003.
[60] R. Legtenberg and H. A. C. Tilmans, "ELECTROSTATICALLY DRIVEN VACUUM-ENCAPSULATED POLYSILICON RESONATORS .1. DESIGN AND FABRICATION," *Sensors and Actuators a-Physical,* vol. 45, pp. 57-66, Oct 1994.
[61] Vanlong, "TO501 Temperature Compensated Crystal Oscillator datasheet."
[62] P. Rantakari, V. Kaajakari, T. Mattila, J. Kiihamaki, A. Oja, I. Tittonen, and H. Seppa, "Low noise, low power micromechanical oscillator," in *Solid-State Sensors, Actuators and Microsystems, 2005. Digest of Technical Papers. TRANSDUCERS '05. The 13th International Conference on*, 2005, pp. 2135-2138 Vol. 2.
[63] Y.-W. Lin, S.-S. Li, Z. Ren, and C. T. C. Nguyen, "Low phase noise array-composite micromechanical wine-glass disk oscillator," in *IEEE International Electron Devices Meeting*, Washington, DC, USA, 2005, pp. 287-290.
[64] W.-L. Huang, Z. Ren, Y.-W. Lin, H.-Y. Chen, J. Lahann, and C. T. C. Nguyen, "Fully monolithic CMOS nickel micromechanical resonator oscillator," in *Micro Electro*

Mechanical Systems, 2008. MEMS 2008. IEEE 21st International Conference on, 2008, pp. 10-13.

[65] SiTime, http://www.sitime.com/.

[66] Discera, http://www.discera.com.

[67] SiliconClocks, http://www.siclocks.com/.

[68] Mobius_Microsystems, http://www.mobiusmicro.com/.

[69] Ecliptek, http://www.ecliptek.com/.

[70] J. Yan, A. A. Seshia, K. L. Phan, and J. T. M. van Beek, "Internal electrical phase inversion for FF-beam resonator arrays and tuning fork filters," in *Micro Electro Mechanical Systems, 2008. MEMS 2008. IEEE 21st International Conference on*, 2008, pp. 1028-1031.

[71] N. Arellano, E. P. Quevy, J. Provine, R. Maboudian, and R. T. Howe, "Silicon nanowire coupled micro-resonators," in *Micro Electro Mechanical Systems, 2008. MEMS 2008. IEEE 21st International Conference on*, 2008, pp. 721-724.

[72] M. U. Demirci and C. T. C. Nguyen, "A low impedance VHF micromechanical filter using coupled-array composite resonators," in *Solid-State Sensors, Actuators and Microsystems, 2005. Digest of Technical Papers. TRANSDUCERS '05. The 13th International Conference on*, 2005, pp. 2131-2134 Vol. 2.

[73] A.-C. Wong and C. T. C. Nguyen, "Micromechanical mixer-filters ("mixlers")," *Microelectromechanical Systems, Journal of,* vol. 13, pp. 100-112, 2004.

[74] S.-S. Li, Y.-W. Lin, Y. Xie, Z. Ren, and C. T. C. Nguyen, "Small percent bandwidth design of a 423-MHz notch-coupled micromechanical mixler," in *Ultrasonics Symposium, 2005 IEEE*, 2005, pp. 1295-1298.

[75] A. T. Alastalo, M. Koskenvuori, H. Seppa, and J. Dekker, "A micromechanical resonating RF mixer," in *Microwave Conference, 2004. 34th European*, 2004, pp. 1297-1300.

[76] M. Koskenvuori and I. Tittonen, "Towards Micromechanical Radio: Overtone Excitations of a Microresonator Through the Nonlinearities of the Second and Third Order," *Microelectromechanical Systems, Journal of,* vol. 17, pp. 363-369, 2008.

3 CMOS-MEMS FABRICATION

This chapter describes the CMOS-MEMS fabrication process used. A figure of merit to compare different CMOS processes is provided and used to evaluate the performance of two CMOS commercial technologies from different foundries (AMS and UMC). This chapter also includes the fabrication and measurement of a proof-of-concept prototype resonators fabricated on UMC 0.18um CMOS technology.

3.1 CMOS-MEMS FABRICATION PROCESSES:

In this and previous works from the research group [1, 2], MEMS resonators are defined in a commercial CMOS process, using the traditional layout, and a post-CMOS wet etching is used to remove the silicon oxide that surrounds the mobile structure, releasing it. The complete design and fabrication process flow is shown in *Figure 3.1*.

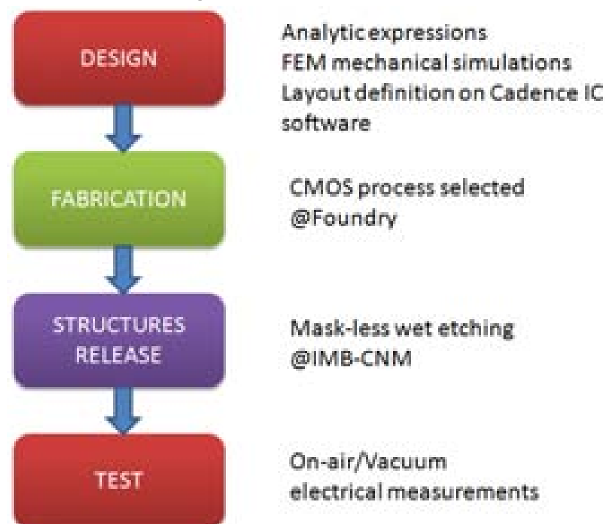

Figure 3.1: Complete MEMS design and fabrication workflow

The design stage includes several iterations with FEM mechanical simulations to obtain the target MEMS resonators. Once the design is fixed (final dimensioning of the resonators is found), the resonators are drawn in a standard IC CAD environment prior to the design delivery to the foundry. In this workflow, no modification of the CMOS process is required, even though some violations of the design rules will be needed. Like in any IC design, modifications of the layout can be necessary after the verification of the design by the foundry, to correct design mistakes. The CMOS fabrication is completely transparent to the designer, as it is entirely developed on the

standard CMOS process of the selected foundry. Moreover, the total amount of masks required in this MEMS fabrication is the same of the CMOS process selected, thanks to the smart use of the available layers in the CMOS process. To allow the etchant to reach the resonators, the passivation layer deposition above the resonator is prevented by using the PAD window layer available in the technology (*Figure 3.2*), whereas the remaining area of the chip is protected by this passivation layer. The use of this PAD window (which is usually used to allow the electrical connection to the pads) is one of the main responsible of the simplicity of the overall process. Otherwise, the passivation layer above the MEMS devices should be removed after the reception of the chips, adding more post-processing complexity and masks.

Once the dies are fabricated and delivered to the designer, the following step is release the already built resonators. The wet-etching, is carried out in the Institut de Microelectrònica de Barcelona (IMB-CNM). The etchant used is a hydrofluoric acid (HF) based solution buffered to protect metal layers, and this etching is performed at room temperature with an approximate etching rate of 200nm/min to 300nm/min [2], this etching rate depends on the presence of metal in the surroundings of the resonator, which acts as catalyst. Moreover, the etching time does not only depend on the amount of oxide to be removed but also on the physical layout of the resonator, for example low gap structures require additional time for the oxide removal. Some of these layout considerations are presented on section 3.5.

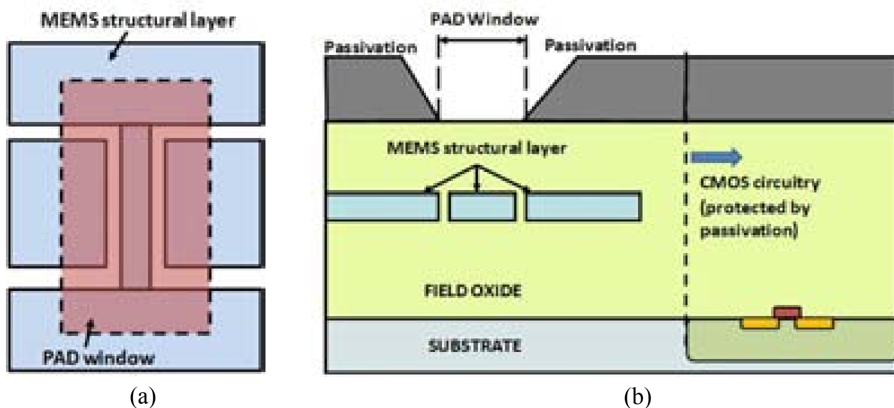

Figure 3.2: (a) Schematic layout of the MEMS resonator, structural layer and pad window is shown. (b) Schematic cross-section of the chip. Passivation layer protects the CMOS circuitry whereas the PAD window allows the etching of field oxide.

3.2 *CMOS TECHNOLOGIES OVERVIEW*

As aforementioned, the MEMS resonators have been designed using commercial CMOS technologies. The selected IC processes were: Austria Microsystems (AMS-0.35um CMOS technology) [3] and United Microelectronics Corporation (UMC-0.18um CMOS technology) [4], both available under multi-project wafer (MPW) program of Europractice [5]. *Figure 3.3* shows the schematic cross-sections of each technology.

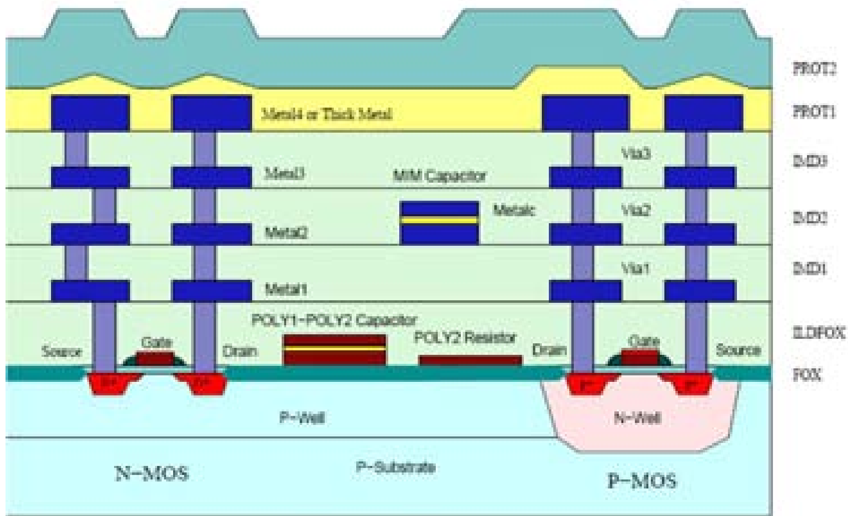

(a)

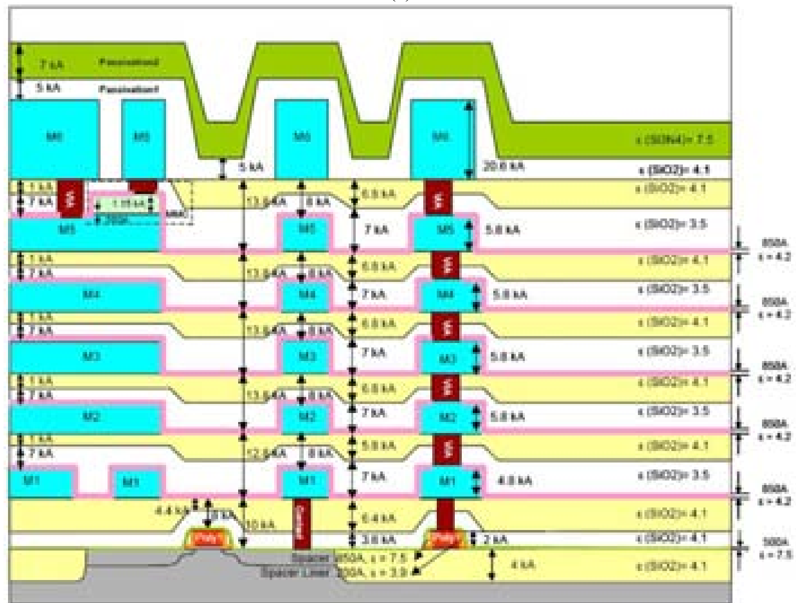

(b)

Figure 3.3: Schematic cross-sections of the CMOS technologies used. (a) AMS 0.35um Standard CMOS technology. MIM capacitor module is not available in the C35B4C3 process used. (b) UMC 0.18um Standard CMOS technology.

AMS 0.35um has 4 metal layers and 2 polysilicon layers whereas UMC has 6 metal layers and only one polysilicon layer. Both technologies have conductor-insulator-conductor capacitive modules that offer the possibility to obtain submicrometric gap resonators, as will be explained in next section. AMS has two capacitor modules one made with polysilicon layers (PIP capacitors made with poly1 and poly2) and another with metal layers (MIM capacitors made with metal2 and metalc), however only the one made on polysilicon is included in the standard AMS CMOS

process (C35B4C3) and the MIM module is offered as an option. UMC offers the metal-insulator-metal (MIM) capacitor made with M5 and MMC layers. *Table 3.1* and *Table 3.3* show the most relevant physical dimensions for each conductive layer for both technologies. The thickness values are obtained from process parameters documentations [6, 7] whereas minimum width and distances are taken from the technology topological layout rules [8, 9]. Its is worth to mention that the dimensions shown in *Table 3.1* are the typical and are subjected to process variations. Additional information of each process tolerances can be found on the aforementioned foundry documentation.

Table 3.1: AMS 0.35um CMOS process (C35B4C3) parameters of each conductive layer

Conductive layer	Thickness (nm)	Min.width (nm)	Min. distance between conductors (nm)	Height to substrate (μm)
Polysilicon 1	282	350	450	0.3
Polysilicon 2	200	800	500	0.38
Metal 1	665	500	450	1
Metal 2	640	600	500	1.5
Metalc	150	4000	800	1.52
Metal 3	640	600	600	2
Metal 4	925	600	600	3

Table 3.2: UMC 0.18um CMOS process (thick top metal) layers physical parameters

Conductive layer	Thickness (nm)	Min.width (nm)	Min. distance between conductors (nm)	Height to substrate (μm)
Polysilicon 1	200	180	240	0.4
Metal 1	480	240	240	1.4
Metal 2	580	280	280	2.68
Metal 3	580	280	280	4.06
Metal 4	580	280	280	5.44
Metal 5	580	280	280	6.82
MMC	115	600	550	7.68
Metal 6	2060	1200	1000	8.2

From previous tables, it can be observed that UMC technology presents lower distance between conductors and therefore a lower gap can be obtained, which has a very important role on the motional resistance R_m as described in chapter 2. However, using special techniques (like spacer technique) allows obtaining smaller gaps.

3.3 SPACER TECHNIQUE

The aforementioned CMOS processes allow the definition of two kinds of resonators. In the first one the drivers and resonators are fabricated in the same conductive layer, and therefore, the minimum achievable gap is determined by each technology layout rules (as stated in *Table 3.1* and *Table 3.2*). On the second one, the resonator and drivers are defined on the conductive layers of the conductor-insulator-conductor capacitor modules. *Figure 3.4* shows the typical use of these modules to fabricate capacitors. In these capacitors, a thin layer of insulator is deposited over an area of conductor 1 and then covered partially with conductor 2 layer, therefore building the capacitor.

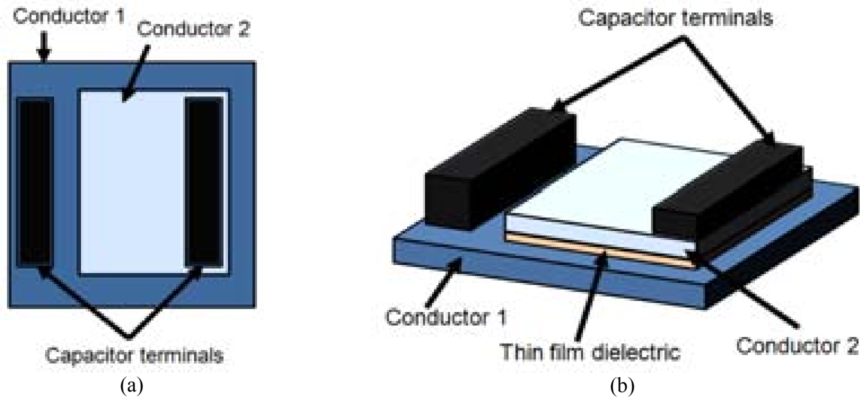

(a) (b)

Figure 3.4: (a) Layout and (b) cross-section schemes of the conductor-insulator-conductor modules used to fabricate capacitors in CMOS technologies.

In the spacer technique, one of the conductors is used to build the resonator, whereas the other conductor is employed for the excitation and readout drivers. The thin film dielectric layer (that is grown by default) is used to determine the distance between the resonator and the drivers. *Figure 3.5* shows the schematic layout (a) and the schematic 3D profile obtained for a zero distance conductor1-conductor2 layout (b).

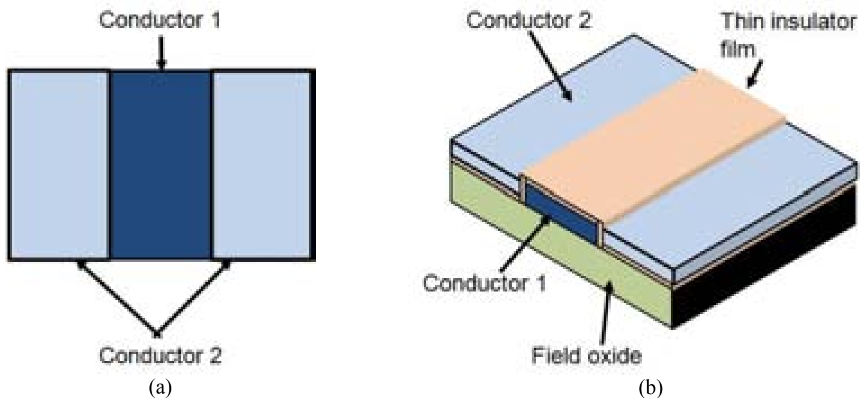

(a) (b)

Figure 3.5: Basic layout for the use of the spacer technique with zero distance drawn (a). Obtained profile for previous layout (b)

Therefore, although the drawn layout distance between conductors is zero, the obtained distance corresponds to the thickness of the thin film dielectric layer. Even though the use of two different layers would introduce problems of misalignment that could provoke overlap of the conductor 1 with conductor 2, this does not affect the functionality of the MEMS device, because layer deposition is conformal and the thin dielectric layer (which is then removed in the etching process) ensures the gap distance between the structure and drivers. *Table 3.3* shows the gap obtainable for the different technologies by using the spacer technique approach, note that this gap corresponds exactly to the thickness (and its process variations) of the thin film dielectric of each technology capacitor modules [6, 7].

Table 3.3: Minimum gap obtainable (thickness of the dielectric layer of capacitor modules) with spacer technique for AMS 0.35um and UMC 0.18um CMOS technologies

Capacitor module	Minimum gap (thin film thickness) (nm)		
	Minimum	Typical	Max
AMS PIP module	36.88	41.16	45.39
AMS MIM module	23.8	27.61	32.87
UMC MIM module		24	

A comparison between these values and the gap that can be obtained by using the same material for resonator and drivers, shows that the spacer technique allows a reduction of the gap of nearly an order of magnitude. It is worth to mention that the gap shown in *Table 3.3* is the minimum achievable, and it can be designed bigger, if required.

Another additional consideration affecting the design of these structures in MIM approach is the thickness difference between the main metal and the capacitor metal for both technologies as it can be observed in *Table 3.1* and *Table 3.2*. The difference between the thicknesses of the metals when the metal capacitor module is employed makes necessary to modify the layout scheme used for AMS polysilicon resonators. When using metal capacitors module, the mechanical structure is fabricated with the thicker metal whereas the electrodes will be drawn in the other layer, just like in the polysilicon resonators. The low thickness and the fact that the etching is accelerated around metals would make the drivers prone to bending down. The proposed layout of. *Figure 3.6* alleviates this robustness problem because the thin metal electrode is supported by the thicker metal layer. Even though in polysilicon capacitors on AMS technology it also exist difference between layer thickness, it is not so big as in the case of metal capacitors, and therefore do not suffer of electrode robustness.

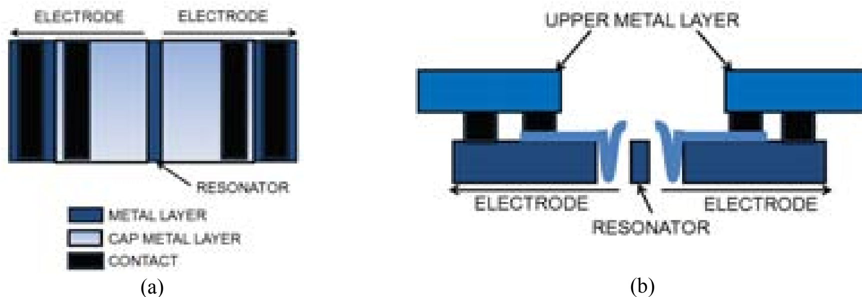

(a) (b)

Figure 3.6: Scheme of the MIM resonator proposal. (a) Layout and (b) Cross-section

The contacts connected to the METAL and CAPMETAL layers of each electrode are connected together using higher metal layers. An important topological problem is the distance between the METAL that composes the driver and the resonator. Although the minimum distance is restricted by design rules, it has to be tested the optimal distance that allows a good coverage of the coupling area with the minimum gap between the resonator and the CAPMETAL electrode.

It can be observed that because polysilicon layers in AMS technology have similar thickness values, this kind of design is not required.

It is also important to say that the use of this technique is a serious violation of the design rules, and therefore it is subjected to foundry agreement.

3.4 TECHNOLOGY COMPARISON

In order to compare both CMOS technologies and select the most appropriate layer to fabricate the MEMS resonators, a figure of merit involving some of the parameters described in chapter 2 is defined and applied to the simple clamped-clamped beam resonator [10].

$$FOM_{tec} = V_{col} \cdot FT / R_m \tag{3.1}$$

This figure of merit promotes: (1) robust resonators, those with high collapse voltage (V_{col}), equation (2.24) (2) with high frequency tuning (FT), *equation* (2.44) and (3) low motional resistance (R_m), equation (2.39). For comparison purposes, this FOM will be defined using only technology parameters: layer thickness (h), minimum electrode to resonator gap (s) and distance to substrate (sv) and structural material properties (E and ρ). The properties selected for the definition of the FOM_{tec} depend on the elastic constant (k). For a clamped-clamped beam, the analytic expression of k (see *annex 1*) allows obtaining the compact relationship of (3.2):

$$FOM_{tec} = \frac{1}{E\sqrt{\rho}} \frac{\sqrt{t^5 sv^3}}{s^7} \tag{3.2}$$

This FOM allows the MEMS designer to compare between the different available layers in any CMOS technology in order to choose the most optimal layer and even the best technology for the fabrication of MEMS resonator. Although is derived for a clamped-clamped beam resonator, similar expressions can be found for any resonator topology.

Table 3.4 shows the values of the computed FOM for the different CMOS technologies layers. The values of R_m, Frequency Tuning (FT) and V_{col} are provided to ease comparison, and are calculated considering a beam of W=1um, L=10um and the minimum allowed gap for the layer. The mechanical properties (Young modulus and mass density) considered for this calculus are: E_{metal}=77GPa, ρ_{metal}=2300Kg/m^3 (corresponding to aluminium), E_{poly}=160GPa and ρ_{poly}=2230Kg/m^3 (for polysilicon based resonators).

Table 3.4: Value of the defined figure of merit for different layers of AMS and UMC commercial CMOS technologies A Q=50 and an applied V_{DC}=5V are assumed.

	s (nm)	FOM_{tec} (3,2)	R_m (2.39)	FT (2.44)	V_{col} (V) (2.24)
AMS 0.35um					
Poly 1-Poly 1	450	2.4578E+05	79.6GΩ	3.80E-07	1.1411E+02
Poly 1- Poly 2	41	**5.6055E+12**	4.97MΩ	5.40E-04	1.1411E+02
Metal1-Metal1	450	2.6134E+07	23.8GΩ	7.89E-07	1.7445E+03
Metal2-Metal2	500	2.0866E+07	37.7GΩ	5.75E-07	3.0259E+03
Metal3-Metal3	600	8.9656E+06	78.1GΩ	3.33E-07	4.6586E+03
Metal4-Metal4	600	4.1364E+07	54.0GΩ	3.33E-07	1.4871E+04
UMC 0.18um					
Poly-Poly	240	1.3059E+07	9.08GΩ	2.50E-06	1.0493E+02
Metal1-Metal1	240	1.5612E+09	2.67GΩ	5.20E-06	1.7721E+03
Metal2-Metal2	280	2.2559E+09	4.09GΩ	3.27E-06	6.2343E+03
Metal3-Metal3	280	4.2063E+09	4.09GΩ	3.27E-06	1.1625E+04
Metal4-Metal4	280	6.5239E+09	4.09GΩ	3.27E-06	1.8030E+04
Metal5-Metal5	280	**9.1577E+09**	4.09GΩ	3.27E-06	2.5308E+04
Metal5-MMC	24	**9.1577E+16**	**410kΩ**	**3.27E-03**	2.5308E+04
Metal6-Metal6	1000	7.3558E+06	364GΩ	7.19E-08	8.2437E+04

From this table, the highest figure of merit is the one of metal5-MMC layers (MIM capacitors) on UMC technology, which moreover can reach a low motional resistance value of 410kΩ with only 5V of DC applied voltage. The second best *FOM* is for the Poly1-Poly2 layers of the AMS technology, that has a R_m of nearly 5MΩ at the same conditions. The third best FOM (the metal5-metal5 approach on UMC) presents a value three orders of magnitude lower than the second, and seven orders of magnitude lower than the best FOM. The motional resistance value for this layer and all the others is on the GΩ range. From this study, the great importance of the gap reduction is clearly highlighted. Moreover, it is demonstrated that for resonators fabricated in the same layers (polysilicon or metal), the use of a more advanced technology allows an increase of the figure of merit up to two orders of magnitude, reduces an order of magnitude the motional resistance and increases an order of magnitude the frequency tuning all thanks to the smaller distance between conductors allowed in more advanced technological nodes.

3.5 FURTHER CONSIDERATIONS

In addition to the selection of the optimum layer, there is an important consideration to take into account while designing a MEMS resonator in a CMOS technology which is the feasibility of the foundry to accept the required layout rules violations to fabricate MEMS resonators. In our CMOS-MEMS fabrication approach the following layout design rules violations are required:

a) In order to allow the etching, a pad window without metal is located above the resonator to prevent passivation deposition (see *Figure 3.2*). This simplifies the post-process as no additional masks to remove the passivation layer are required once the chip is received. The minimum dimensions for this PAD set by technology design rules from AMS is 15µmx15µm whereas for UMC is set to 5µmx5µm, according to foundry recommendations. The dimensions of this layer is set according to these minimums

b) When spacer technique is used to build resonators, the conductor 2 layer is drawn without conductor 1 underneath, which is not usually allowed in CMOS processes.

c) When deep conductor layers are used (i.e. polysilicon or lower metal layers), VIAs without metal are opened to provide a better access of the etchant in order to decrease the etching time and reduce damage to the metals, which is observed in very long etching times. This, however, is not necessary when the MEMS are fabricated in upper metal layers, and therefore has only been used on polysilicon resonators of AMS technology. *Figure 3.7* shows the cross-section of the structure with part of the above oxide removed using technology VIA layer without metals.

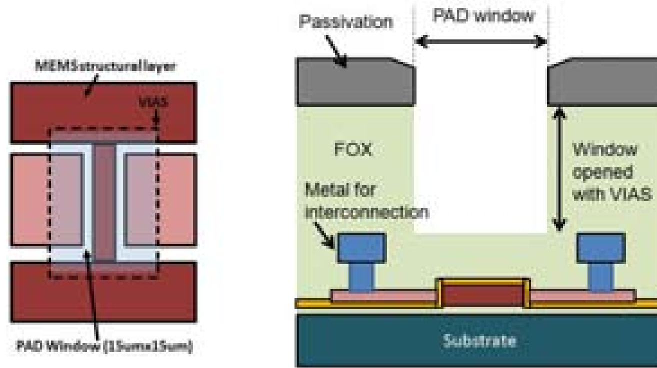

Figure 3.7: Layout and Schematic cross-section of one resonator fabricated in bottom conductive layers (poly1 and poly2) in which part of the above resonator field oxide was removed at the foundry by using VIA layers (drawn in layout).

Unfortunately, the use of VIAS without metal, has an important drawback. When the structure is released some squares of material fall to the resonator area (*Figure 3.8*).

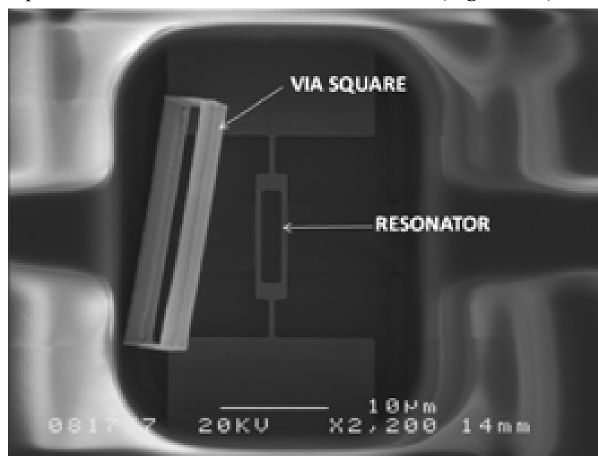

Figure 3.8: Released resonator with a fallen VIA square

These squares are only observed when VIAS are drawn and have the same dimensions than the layout drawn PAD. The origin of these squares is found on the technological process carried out to build the metal paths and the VIAS (*Figure 3.9-a*). In fact the metal layers is a three layers sandwich, composed by two layers of TiN and an aluminum filling between these aforementioned layers.

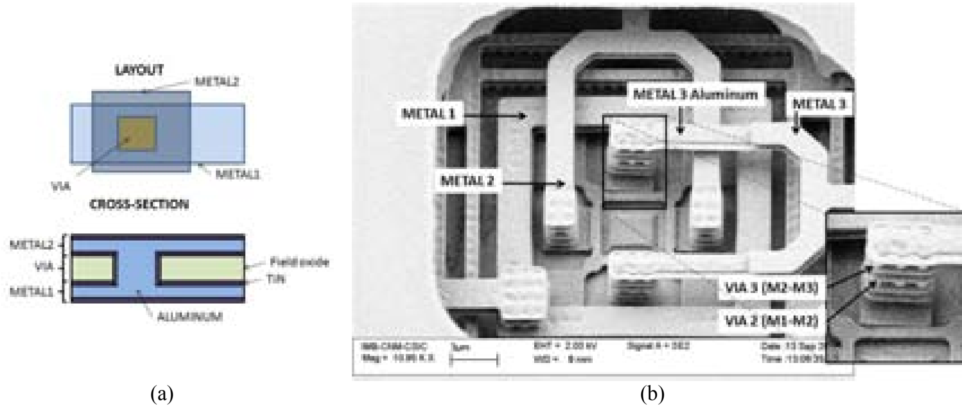

(a) (b)

Figure 3.9: (a) Layout and schematic cross-section showing the three-layer metal sandwich and interconnection between two metal layers using VIAS. (b) SEM image of a resonator with complex metal-based interconnection. The three layer metal topology and VIAS can be clearly seen.

Figure 3.9(b) shows a resonator in which the VIAS between metals can be clearly observed. In this image is shown a clear cut in the metal 3 top TiN layer caused by the drawing of a VIA 3 above the resonator. When VIAS, which are usually drawn of 15µmx15µm (like the minimum PAD opening) are drawn without metal, the squares are trapped in the field oxide, and when the oxide is removed, they can fall above the resonator, as it is observed in *Figure 3.10*. Although this material does not always fall in the resonator area, it reduces the process yield.

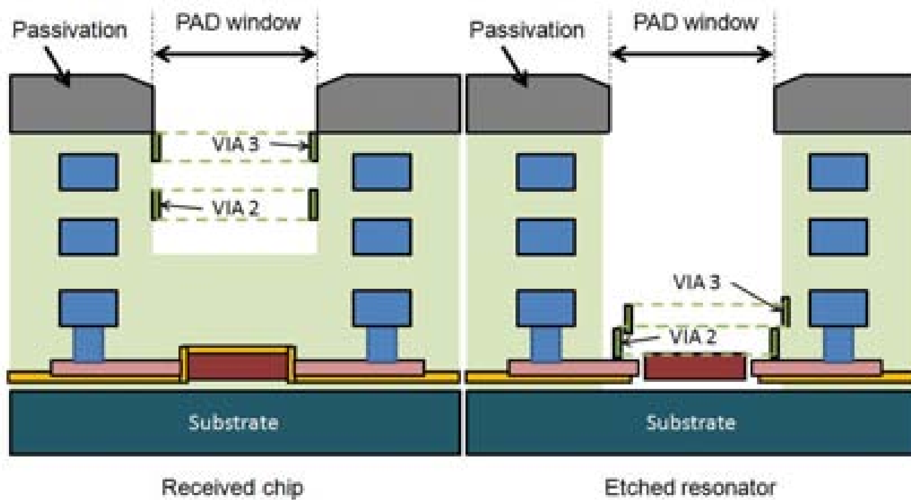

Figure 3.10: Released resonator with fallen VIA squares (Via 2 and Via 3). In the received resonator the VIA material is trapped by the surrounding oxide an can fall above the resonator once part of this oxide is removed.

To try to alleviate this problem several modifications to the basic PAD/VIA layout were tested:

a) No VIAS are drawn above the resonator. The main idea of this modification was to simply eliminate the VIA squares, and was supported by the evidence that where the

resonators are etched, the area of the removed oxide is greater than the 15µmx15µm of the drawn PAD window, as it can be observed in *Figure 3.11*.

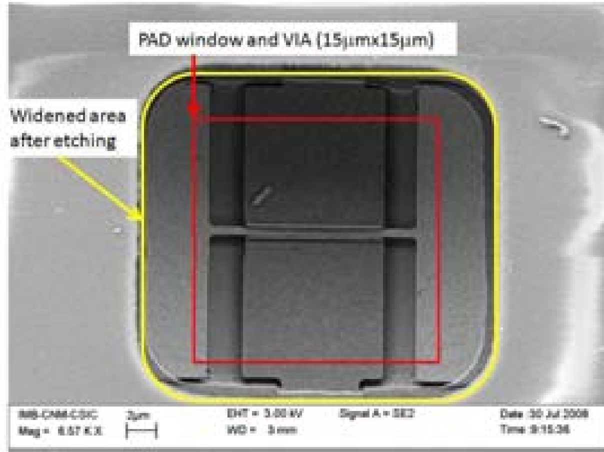

Figure 3.11: SEM image of a released resonator. It can be observed that the oxide is removed also sideways, increasing the etching area when compared to the 15µmx15µm PAD window dimensions.

Unfortunately, this option has shown no positive results. The high amount of oxide to be etched requires an increase of the etching time to a value that damages the metals, as it can be observed in *Figure 3.12*. This SEM image shows that although the etching time was high enough to seriously damage metals e. g. releasing the contacts, it can also be observed that there is still silicon oxide surrounding the resonator and preventing it to move.

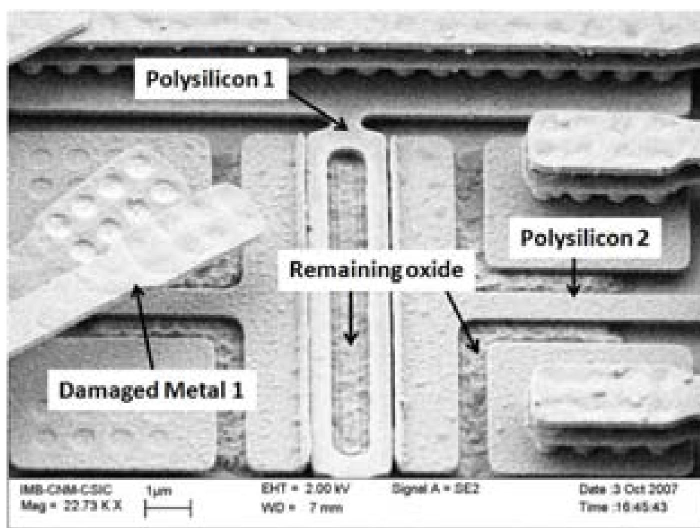

Figure 3.12: SEM image of a resonator after etching without VIAS drawn. Even though the etching time was increased, there is still oxide remaining which does not allow resonator movement. Damage on metal paths can be observed on the left side of the image.

b) VIAS are drawn bigger than the PAD window. Two approaches were studied, in the first one the VIAS are slightly bigger than the PAD window (*Figure 3.13-a*). This

approach shows an improvement in reducing the etching time, as it was expected. On the second approach the VIAS are oversized (*Figure 3.13-b*). The main objective of doing so is to fix the VIAS with the remaining oxide after the etching. Unfortunately, the results of etching shows that the VIAS square acts as an accelerant of the etching solution, as it can be observed in the optical and SEM images (*Figure 3.14*). In the latter image, the VIAS were even capable to break the passivation. The good point is that these oversized VIAS do not fall directly above the resonator.

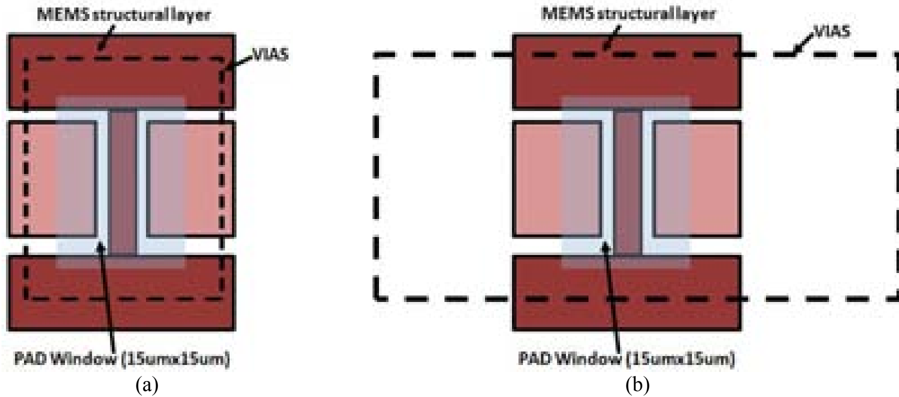

(a) (b)

Figure 3.13: Layout of the VIA greater than PAD window options. (a)Slightly greater VIA window (30µmx30µm) and (b) oversized VIA (35µmx135µm).

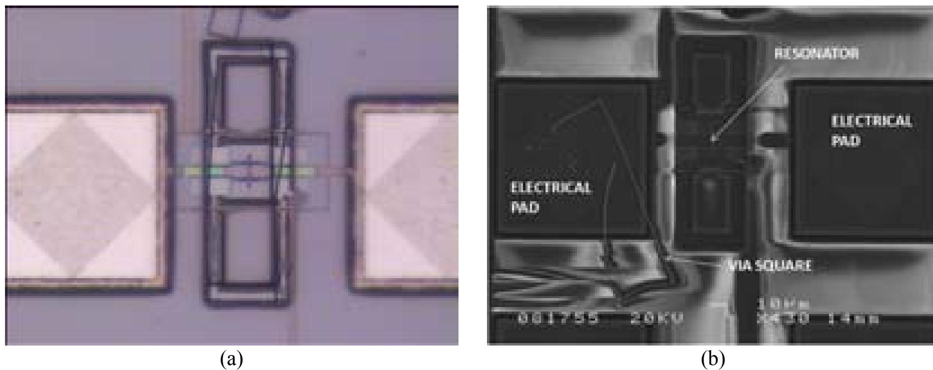

(a) (b)

Figure 3.14: Optical (a) and SEM image (b) of a resonator with oversized VIA openings.

c) The last approach is to place a metal grid above the resonator to trap the falling VIAS above the resonator (*Figure 3.15*). Figure 3.16: SEM image of a resonator protected with a metal 1 grid. The VIA square does not fall on the resonator..*Figure 3.16* shows a SEM image of the resonator where it can be observed the released VIA catched by the grid. Unfortunately these resonators were thought as test structures and were not electrically connected to PADS and therefore their functionality could not be tested.

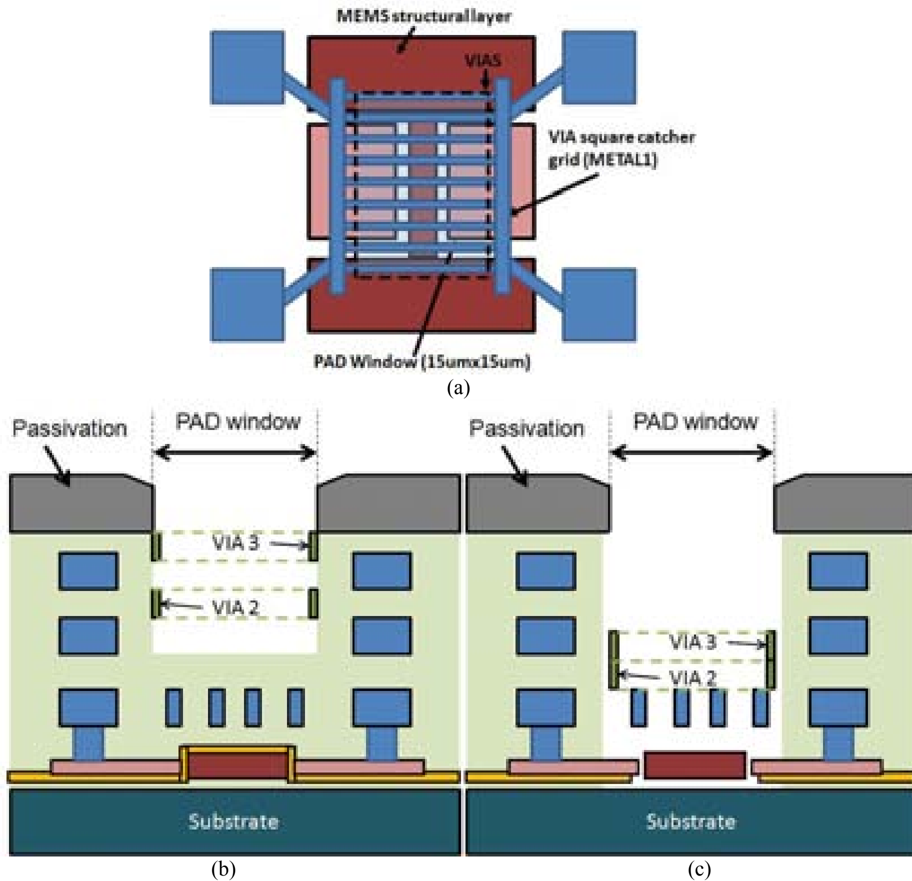

Figure 3.15: (a) Layout diagram of the MEMS resonator with the VIA grid. (b) Schematic cross-section of the resonator before the etching. (c) Resonator cross-section once etched. The VIA squares are trapped by the grid..

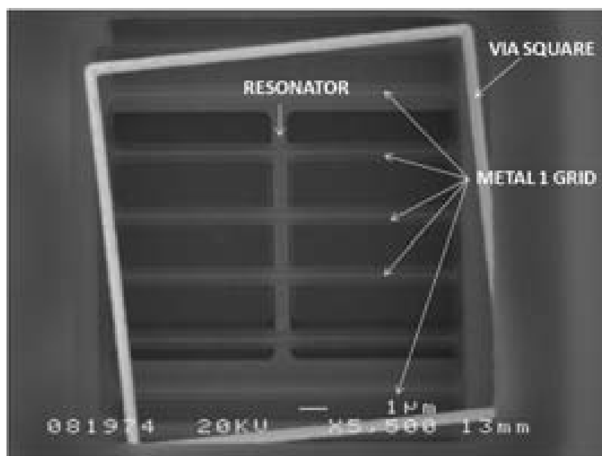

Figure 3.16: SEM image of a resonator protected with a metal 1 grid. The VIA square does not fall on the resonator..

As a conclusion about the better solution in relation to VIAS size design, we have found that the best solution is design the VIAS with a double size than the PAD definition over the resonator (solution b). We have already experimentally verified this in last AMS run (see *Annex 3*) in which almost a 100% releasing yield has been achieved for a clamped-clamped beam with *s*=100nm.

In addition to the aforementioned considerations three more items are crucial to the success of integrating MEMS resonators in CMOS technologies. The first one concerns to the robustness of the resonator and drivers to the wet etching. It is obvious to think that if the oxide underneath the resonator is removed, it is also removed in the electrodes, therefore, the use of small electrodes should be avoided.

The second one affects the layout at chip level. CMOS technologies introduce dummy metal structures to alleviate the stresses. As it was aforementioned, metal acts as an accelerant to the wet etching employed, and the oxide surrounding metal structures is removed in lower time. As a result of this, these dummy structures can be released during the wet etching an fall above a resonator, affecting its functionality. Luckily, these technologies provide a layer to prevent these dummies. *Figure 3.17* shows the effect of a long etching time in a chip in which this layer was not drawn in layout.

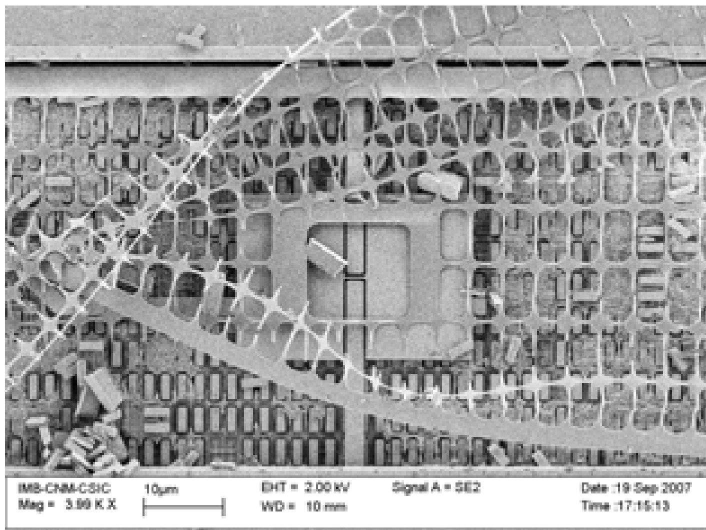

Figure 3.17: SEM image of an overetched resonator with metal dummies. The dummy structures were completely released, affecting the passivation layer and falling above the resonator area.

The last consideration deals with a technique to reduce the parasitic capacitor to the substrate due to electrical PADS. In AMS technology the PAD cell is made on a combination of all metal layers (metal 1, metal 2, metal 3 and metal 4) interconnected by VIAS. UMC technology shows more advanced functionality: by default the PADS in this technology use the first metal layer (metal 1) as a shield which is not connected, whereas the number of metal layers can be chosen by the designer. The smallest number of metal layers is therefore of two: Metal 6 for electrical interconnection and metal 1 for shielding. This shield (together with the use of top metal layers) reduces the parasitic PAD capacitor to the substrate from 1pF (AMS) to 31.36fF (UMC). *Figure 3.18* shows the cross-section of each technology PADS.

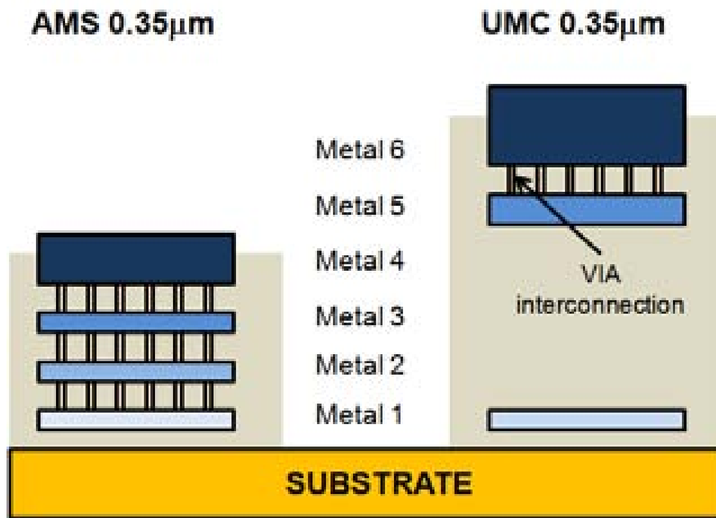

Figure 3.18: Schematic cross-section of the used PADS for each technology.

3.6 Downscaling Proof Of Concept: UMC 0.18um CC-Beams Resonators

To demonstrate the possibility of using the CMOS-MEMS fabrication previously explained to other downscaled CMOS technologies, simple resonators (CC-Beams) were fabricated on a more advanced technological node (UMC 0.18um). Although the first idea was to take advantage of the Metal5-MMC layer to obtain gaps around 24nm, foundry restrictions on design rules violation prevented us to fabricate the resonators with this layer combination. Therefore the resonators were fabricated on a M5-M5 layers combination, which has the second higher FOM value from UMC technology and the third one of

Table 3.4.

The beams resonance frequencies were located in the HF and VHF frequency ranges, and the resonator dimensions are depicted in *Table 3.5*.

Table 3.5: UMC 0.18um CMOS technology resonators using M5

	f_0 (MHz)	W (nm)	L (µm)
HF resonator	22.8	280	8.6
VHF resonator	230	280	2.7

Figure 3.19(a) shows the drawn layout of the resonator and an schematic cross-section, (b) is a SEM image of the received die, and (c and d) show the SEM image of the post-processed (released) HF and VHF resonators, respectively.

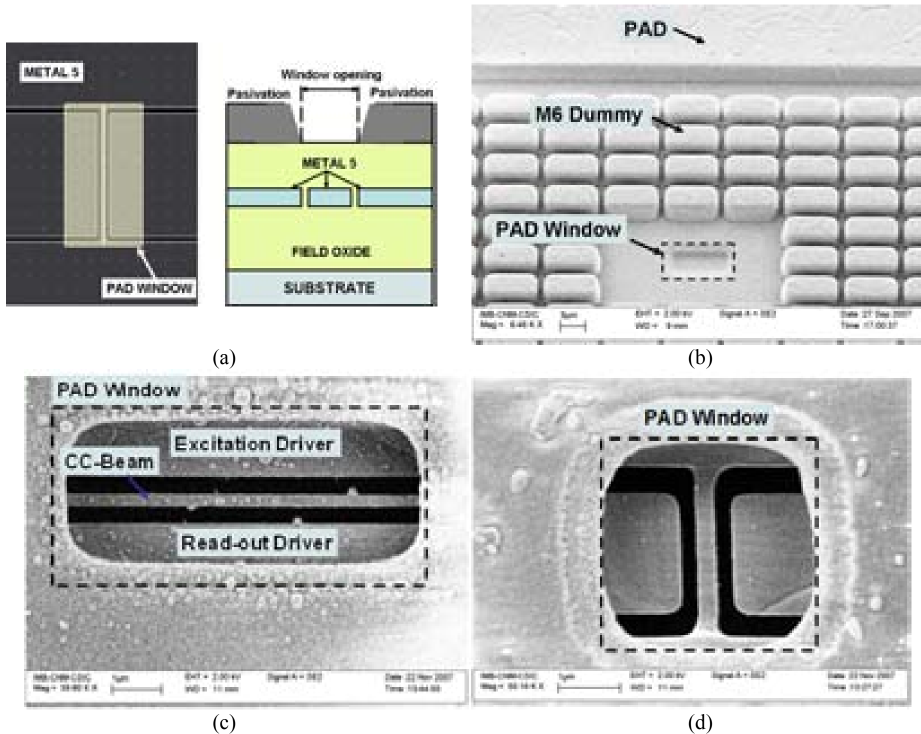

(a) (b)

(c) (d)

Figure 3.19 Different stages of the MEMS resonator. (a) Layout and schematic cross-section. (b) SEM image of the received die. (c) SEM image of the released HF resonator and (d) SEM image of the released VHF resonator.

As can be observed in *Figure 3.19(c)*, the PAD window is not enough opened to see the anchors of the clamped-clamped beam, which can be clearly observed for the smaller (and higher resonant frequency) resonator, *Figure 3.19(d).* There are differences between the obtained window opening dimensions and the drawn dimensions. We believe that the cause of this discrepancy lies in the fact that in the normal use, the passivation is removed above the electric connection pads, which are made of thick metal (2µm thick), something that it is not done in our case for the pad window located above the resonators.

On the next sections, the measurement results of the resonators fabricated in UMC 0.18µm CMOS technology are provided.

3.6.1 HF RESONATOR

Once the resonator is released, electrical characterization is performed using the measurement techniques explained in Annex 2. *Figure 3.20* shows the resonator frequency response (magnitude and phase) for different biasing voltages and an applied input power of -10dBm. From these results, a clear resonance and antiresonance peak magnitudes are obtained. A magnitude resonance peak of approximately 7 dB and a phase shift of nearly 85º for an applied DC voltage of 80V is achieved without using amplification circuitry, allowing the measurement of the quality factor, Q=42, a value higher than the obtained for similar metal resonators without on-chip circuitry resonators fabricated on AMS 0.35µm CMOS technology [11].

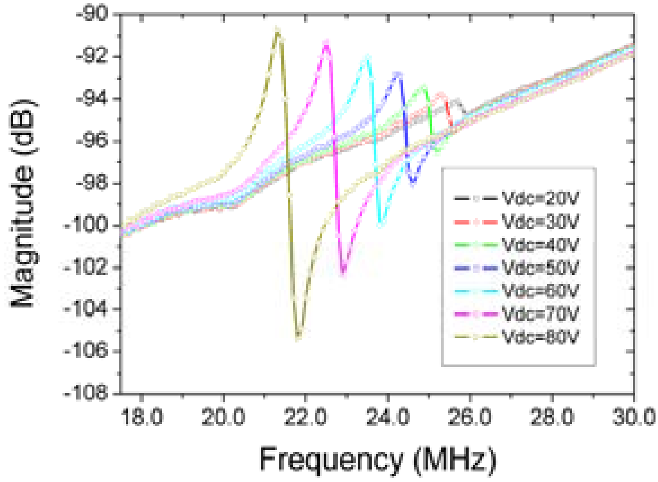

(a)

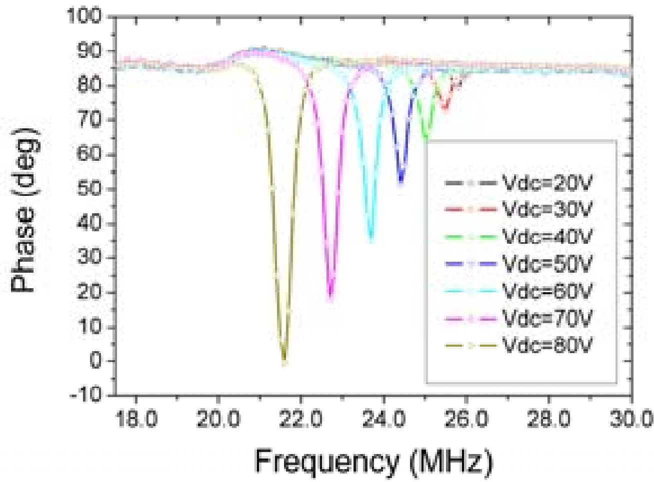

(b)

Figure 3.20: S21 measurement: magnitude (a) and phase (b) plots for different applied DC voltage. Applied input power Pi=-10dBm.

From these measurements the variation of the resonance frequency with the applied DC voltage can be analyzed. *Figure 3.21* shows the f_{RES} vs. V_{DC}^2 plot, showing a linear dependence. The natural resonance frequency of the resonator can be found by a linear fitting of the experimental data, this frequency is f_{RES}=26MHz whereas the experimental frequency tuning is of 27.84ppm/V^2.

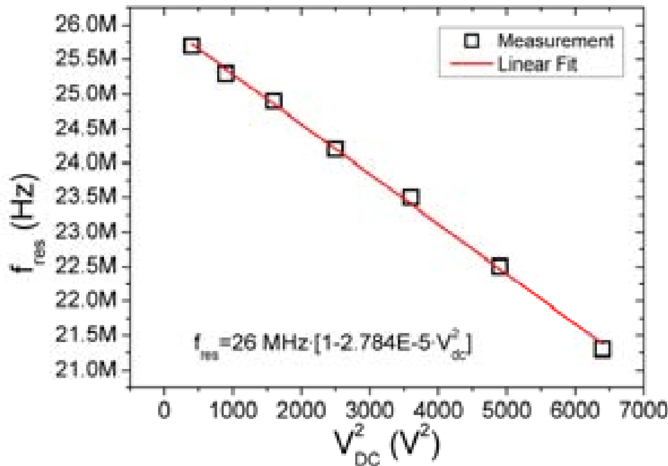

Figure 3.21: Resonance frequency (f_{res}) vs. V_{DC}^2 for the HF resonator. A linear relationship is shown.

In order to obtain the experimental motional resistance, a simple linear RLC//Cp model is used to fit the resonance curve of the resonator. To ensure measurement accuracy the test setup is calibrated up to the probe tips using a calibration substrate. The parasitic capacitor associated to the PAD is obtained from the extracted layout netlist. This capacitor presents a low value of 30fF because of using only top metal layers (M6 and M5) to define the PAD, furthermore a metal shield of M1 is located below the pad to provide better isolation to the substrate. Both adjusted and measured magnitude response are shown in *Figure 3.22*, showing good agreement between measurements and model fit. From this fitting, the motional resistance value is 3.37MΩ, nearly twice the calculated value of the motional resistance using the magnitude frequency response (*Figure 3.20*) and the equation of *Annex 3* (1.26MΩ). Note, however, that the expression of *Annex 3* does not consider the effect of the parasitic capacitor and therefore gives a lower R_m.

Mixing technique was used to eliminate the parasitic parallel resonance of the resonator. By using this technique the parasitic capacitor (parallel capacitor) effect is removed because the excitation and readout frequencies are different [12]. Moreover, this measurement is performed in a custom-made vacuum chamber to reduce the air damping and therefore obtain a Q which is mainly limited by intrinsic losses. *Figure 3.23* shows the resonator response with the mixing measurement technique (see Annex 2) and a Lorentzian fit of this response. It can be observed that antiresonance peak is completely removed as expected. The applied DC voltage was reduced to avoid non-linear operation of the device, which is more visible under vacuum conditions. The combination of the vacuum and mixing technique allows a measurement of the Q factor of 819, twenty times higher than the one previously obtained with S21 measurement performed in air.

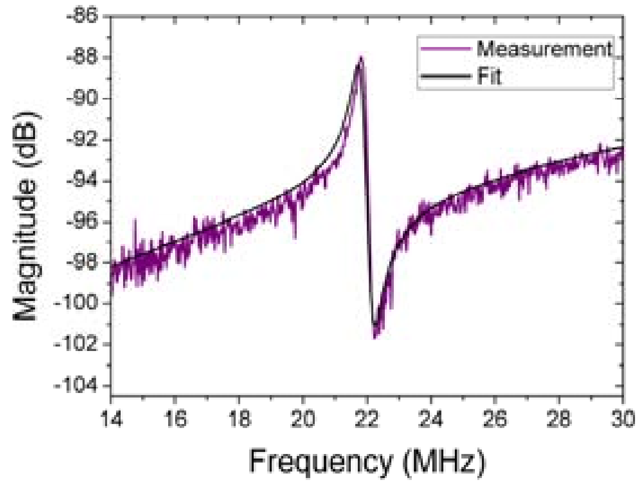

(a)

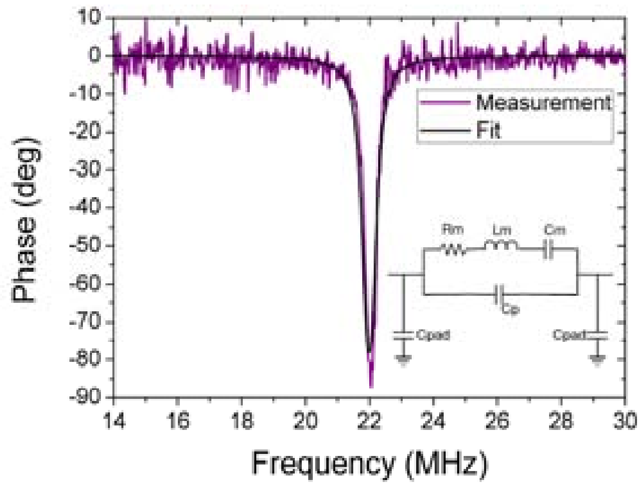

(b)

Figure 3.22: Measured and fitted frequency response for Vdc = 80 V, Pi=-10dBm: magnitude (a) and phase (b). Equivalent model values are Rm = 3.37 MΩ, Cm = 40.9 aF, Lm = 1.3 H, Cp = 1.325 fF and $Cpad$ = 31.36 fF.

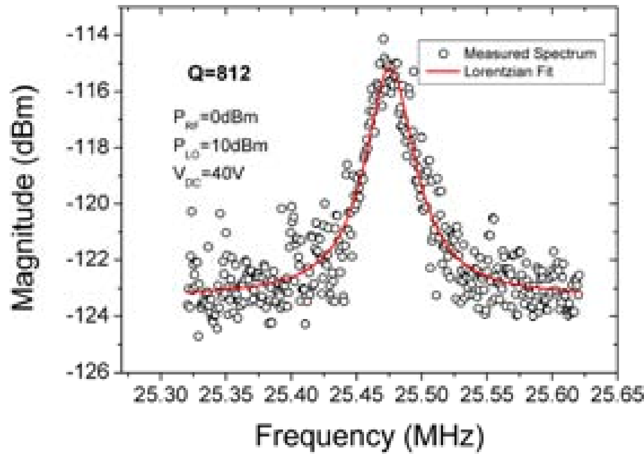

Figure 3.23: Frequency response of the resonator using mixing technique and vacuum (20µBar). Applied DC voltage is 40V, P_{LO}=10dBm, f_{LO}=15MHz, P_{RF}=0dBm and RF frequency is swept between 40.3MHz and 50.65MHz.

3.6.2 VHF RESONATOR

S21 measurements were also performed with an Agilent E8357A network analyzer to characterize the VHF range resonator. *Figure 3.24* shows S21 magnitude measurements of the resonator for 80V and 90V applied DC voltages. The resonator presents resonance around 228MHz. Due to the low peak height, the input power has to be increased (P_{in}=10dBm) to reduce noise effect on measurement. The measured response of this resonator presents several differences with the measurements of the previous resonator. Resonance peak height is smaller due to the reduced coupling area, and the increase of parasitic current inherent to higher frequency resonators (nearly 20 dB higher than for the 25MHz resonator).

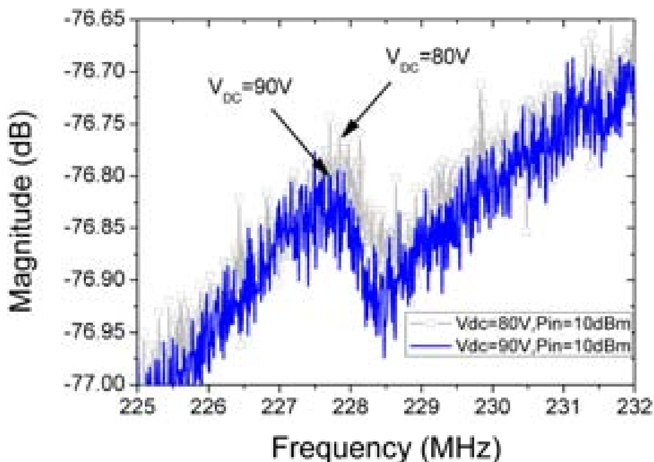

Figure 3.24: Magnitude S21 measurements of the VHF range resonator.

The absence of a 3dB resonance peak does not allow direct measurement of the quality factor. The measured response is fitted using an RLC//Cp electric model similar to the one used for the lower frequency resonator (*Figure 3.25*).

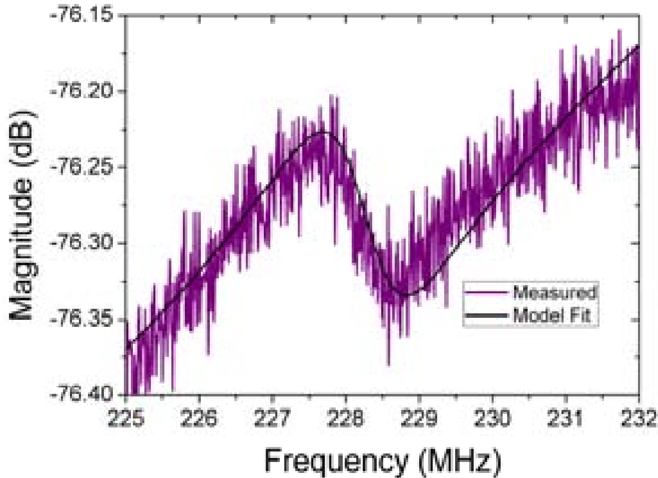

Figure 3.25: Measured and fitted frequency magnitude response for V_{DC}=80V. Equivalent model values are: R_m=35.84MΩ, C_m=0.13aF, L_m=11.71H, C_p= 1.07fF and C_{pad}=31.36fF.

The values of the fitted magnitude response present a slightly lower parasitic capacitance (small coupling dc capacitance due to the smaller CC-beam length and consequently smaller input/output drivers). Despite of this the parasitic current is higher due to the higher frequency. The motional resistance is higher than in the lower frequency resonator (a factor of 10), consequence of the smaller coupling area.

3.6.3 CONCLUSIONS

Just to provide some figures to the reader, the results of the resonators fabricated in UMC technology are compared to previous resonators reported by the research group (*Table 3.6*). The labeling of the resonator is made as follows: the first letter designates the technology (A: AMS and U: UMC), the second letter describes the material in which the resonator is made (M: Metal and P: Polysilicon), the third one designates if it is a cantilever (C) or a clamped-clamped beam (B), and the termination V is used only on measurements on vacuum conditions. Some state-of-the-art resonators are also included in the table to provide deeper comparison.

From *Table 3.6* it can be observed that metal UMC resonators show better $Q\text{x}f_{RES}$ performance than their AMS fabricated counterparts, even without amplification circuitry. The results obtained, however, by the AMS polysilicon resonators are superior, as it was expected from the *FOM* analysis, and with much lower DC voltage, due to the tiny gap obtained with spacer technique.

Table 3.6:Summary table of UMC resonator performance and some previous resonators

Resonator	s (nm)	f_{res} (MHz)	Q	V_{dc} (V)	Qxf_{res} (GHz)	Comments	Ref.
U_MB	280	24.36	43	80	1.0	Lateral mode metal CC Beam on UMC	
U_MB_V	280	24.36	812	40	19.8	Lateral mode metal CC Beam on UMC	
U_MB_2	280	228	145	80	33	Lateral mode metal CC Beam on UMC	
A_MC	600	6.33	100	60	0.6	Lateral mode metal cantilever on AMS, with on-chip amplifier	[13]
A_MC_V	600	6.33	1000	17	6.3	Lateral mode metal cantilever on AMS, with on-chip amplifier	[14]
A_MB	600	59.5	30	80	1.8	Lateral mode metal CC-beam on AMS, with on-chip amplifier	[11]
A_PB	40	192.5	300	12	57.7	Lateral mode polysilicon resonator on AMS, lateral mode with on-chip amplification	[15]
A_PB_V	40	192.5	1000	17	192	Lateral mode polysilicon resonator on AMS, with on-chip amplification	[15]
Dai' 07	3500	39.5	806	30	31.8	CMOS vertical mode metal resonator with off-chip amplification	[16]
Lo' 05	900	6.18	996[b]	20	6.2	CMOS stack lateral mode square resonator with differential on-chip amplification	[17]
Lo' 07	1450	8.04	3589[b]	46	29	CMOS stack lateral mode resonator with differential on-chip amplification	[18]
Huang'08	100	11.7	1651[b]	5	19.3	Post-CMOS compatible vertical circular resonator	[19]

When compared to other selected resonators, the 24.36MHz beam shown in this chapter has a $Q\mathrm{x}f_{res}$ value (1.9E10) on the same order of magnitude as the selected state of the art resonators [16-18], with a $Q\mathrm{x}f_{res}$ range from 6.2E9 [17] to 3.2E10 [16]. However, the presented resonators take advantage of the small gap distance (280nm). This gap will allows obtaining a motional resistance significantly lower than reported resonators [16-18] because of the strong dependence of the motional resistance with the gap. The HF resonator reported in this work would present a 674kΩ if measured on vacuum conditions, only an order of magnitude above, and presenting a simpler and cheaper post-process than the ones used in [17-19].

Although in present days AMS technology should be the preferred choice, for the building of CMOS monolithic MEMS resonators, the results of this chapter demonstrated the possibility to continue using the proposed CMOS-MEMS fabrication approach described on downscaled technologies. Moreover, whereas the maximum technological potential (in terms of minimum gap) of AMS was exploited, the UMC potential remains hidden. We hope in the future that commercial foundries would accept easily design rules violation to build MEMS once the use of these devices will begin to be generalized.

REFERENCES

[1] J. Verd, "Monolithic CMOS-MEMS Resonant Beams for Ultrasensitive Mass Detection." vol. Ph.D Bellaterra: Universitat Autònoma de Barcelona, 2008.

[2] J. Teva, "Integration of CMOS-MEMS resonators for radiofrequency applications in the VHF and UHF bands." vol. Ph.D Bellaterra: Universitat Autònoma de Barcelona, 2007.

[3] "Austria Micro Systems (AMS) 0.35um 2-poly, 4-metal standard CMOS technology."

[4] "UMC 0.18um 1-poly, 6-metal standard CMOS technology."

[5] "http://www.europractice-ic.com/prototyping.php."

[6] UMC, "0.18um Mixed-Mode and RFCMOS 1.8V/3.3V 1P6M Metal Metal Capacitor Process Interconnect Capacitance Model," 2006.

[7] AMS, "0.35um CMOS C35 Process Parameters," 2005.

[8] UMC, "0.18um Mixed-Mode and RFCMOS 1.8V/3.3V 1P6M Metal Metal Capacitor Process Topological Layout Rule," 2006.

[9] AMS, "0.35um CMOS C35 Design Rules," 2005.

[10] J. L. Lopez, J. Verd, J. Teva, G. Murillo, J. Giner, F. Torres, A. Uranga, G. Abadal, and N. Barniol, "Integration of RF-MEMS resonators on submicrometric commercial CMOS technologies," *Journal of Micromechanics and Microengineering,* vol. 19, p. 015002, 2009.

[11] J. Verd, A. Uranga, J. Teva, J. L. Lopez, F. Torres, J. Esteve, G. Abadal, F. Perez-Murano, and N. Barniol, "Integrated CMOS-MEMS with on-chip readout electronics for high-frequency applications," *Electron Device Letters, IEEE,* vol. 27, pp. 495-497, 2006.

[12] J. L. Lopez, J. Teva, A. Uranga, F. Torres, J. Verd, G. Abadal, N. Barniol, J. Esteve, and F. Perez-Murano, "Mixing in a 220MHz CMOS-MEMS," in *Circuits and Systems, 2007. ISCAS 2007. IEEE International Symposium on*, 2007, pp. 2630-2633.

[13] J. Verd, A. Uranga, G. Abadal, J. Teva, F. Torres, F. Perez-Murano, J. Fraxedas, J. Esteve, and N. Barniol, "Monolithic mass sensor fabricated using a conventional technology with attogram resolution in air conditions," *Applied Physics Letters,* vol. 91, p. 013501, 2007.

[14] J. Verd, A. Uranga, G. Abadal, J. L. Teva, F. Torres, J. L. Lopez, E. Perez-Murano, J. Esteve, and N. Barniol, "Monolithic CMOS MEMS Oscillator Circuit for Sensing in the Attogram Range," *Electron Device Letters, IEEE,* vol. 29, pp. 146-148, 2008.

[15] J. Teva, G. Abadal, A. Uranga, J. Verd, F. Torres, J. L. Lopez, J. Esteve, F. Perez-Murano, and N. Barniol, "VHF CMOS-MEMS resonator monolithically integrated in a standard 0.35um CMOS technology," in *Micro Electro Mechanical Systems, 2007. MEMS. IEEE 20th International Conference on*, 2007, pp. 779-782.

[16] C.-L. Dai, C.-H. Kuo, and M.-C. Chiang, "Microelectromechanical resonator manufactured using CMOS-MEMS technique," *Microelectronics Journal,* vol. 38, pp. 672-677, 2007.

[17] C.-C. Lo, F. Chen, and G. K. Fedder, "Integrated HF CMOS-MEMS square-frame resonators with on-chip electronics and electrothermal narrow gap mechanism," in *Solid-State Sensors, Actuators and Microsystems, 2005. Digest of Technical Papers. TRANSDUCERS '05. The 13th International Conference on*, 2005, pp. 2074-2077 Vol. 2.

[18] C. C. Lo and G. K. Fedder, "On-Chip High Quality Factor CMOS-MEMS Silicon-Fin Resonators," in *Solid-State Sensors, Actuators and Microsystems Conference, 2007. TRANSDUCERS 2007. International*, 2007, pp. 2449-2452.

[19] W.-L. Huang, Z. Ren, Y.-W. Lin, H.-Y. Chen, J. Lahann, and C. T. C. Nguyen, "Fully monolithic CMOS nickel micromechanical resonator oscillator," in *Micro Electro Mechanical Systems, 2008. MEMS 2008. IEEE 21st International Conference on*, 2008, pp. 10-13.

4 MEMS RESONATORS

In this chapter the design and experimental results of MEMS resonators are presented. The results of different resonator topologies based on flexural beams: clamped-clamped and free-free beams and double-ended tuning forks are compared, and their performance is analyzed according to the parameters described in Chapter 2.

The MEMS resonators shown in this chapter were fabricated on AMS 0.35μm CMOS commercial technology using the spacer technique with the polysilicon 1 as structural layer. These resonators, on the HF and VHF frequency ranges, are studied as frequency reference for oscillator, and are designed to have resonance frequencies of 24MHz and 48MHz. These devices were designed to replace quartz crystal as the frequency reference in a USB half and full-speed controller [1], respectively. The use of the spacer technique allows obtaining the small gaps required for low motional resistance at low DC voltages (V_{DC}<5V). In particular, the analysis of the results will be based on parameters like frequency tuning, quality factor (Q) and motional resistance. The analytic equations and the design process used for dimensioning the resonators can be found on *Annex1*. The young modulus (E) and density (ρ) values considered for the dimensioning (used on analytic expressions and FEM mechanical simulations) are 160GPa and 2230 kg/m^3, respectively, corresponding to the polysilicon structural layer selected.

4.1 *CLAMPED-CLAMPED BEAMS*

The resonators reported in this section are clamped-clamped beams fabricated with and without on-chip amplification circuitry [2, 3], when this amplification is used an easier characterization and reduction of parasitic capacitances is found.

Linearity on this resonator has been considered on design stage. Using the expressions from *Chapter 2* and considering simple clamped-clamped beams, the following section deals with the linearity study carried out in the design stage.

4.1.1 LINEARITY CONSIDERATIONS FOR CLAMPED-CLAMPED BEAMS

As stated in Chapter 2, the linearity of a MEMS resonator depends on both electrical and mechanical elastic constants contributions. The electric elastic constants (up to third order non-linearity) are (4.1)-(4.3):

$$k_e = -\frac{C_0}{s^2}\cdot\left[\frac{1}{2}\cdot A_{AC}^2 + 2\cdot V_{DC}{}^2\right] \qquad (4.1)$$

$$k_{e2} = \frac{3}{2\cdot s}\cdot k_e = -\frac{3}{2}\frac{C_0}{s^3}\cdot\left[\frac{1}{2}\cdot A_{AC}^2 + 2\cdot V_{DC}{}^2\right] \qquad (4.2)$$

$$k_{e2} = \frac{2}{s^2} \cdot k_e = -2 \cdot \frac{C_0}{s^4} \cdot \left[\frac{1}{2} \cdot A_{AC}^2 + 2 \cdot V_{DC}{}^2 \right] \tag{4.3}$$

These expressions are general for beam-like resonators. The mechanical elastic constants for clamped-clamped beams can be written as (4.4)-(4.6):

$$k_m = \frac{16 \cdot E \cdot h \cdot W^3}{L^3} \tag{4.4}$$

$$k_{m2} \approx 0 \tag{4.5}$$

$$k_{m3} = \frac{k_m}{\sqrt{2} \cdot W^2} \tag{4.6}$$

The second-order mechanical elastic constant (k_{m2}) can be neglected (i.e. approached to zero) for two port devices [4]. The combined elastic constants are then: $k=k_m+k_e$, $k_2= k_{m2}+k_{e2}$ and $k_3= k_{m3}+k_{e3}$.

As it can be observed, the electrical contribution presents a strong dependence on the electrode to resonator gap, whereas the mechanical non-linearity depends mainly on the resonator width ($k_{m3} \alpha W$). Note that if W is increased, the linear component of the linear mechanic elastic constant (k_m) grows quicker than the third-order component. For this reason wider clamped-clamped beams are expected to have a more linear behavior than narrower resonators. This can also be observed using the expression of the critical displacement (2.51), where κ for a clamped-clamped beam and neglecting the electrical non-linearities (i.e. $k=k_m$, $k_2=k_{m2}$ and $k_3=k_{m3}$) can be written as (4.7):

$$\kappa = \omega_0 \cdot \frac{3 \cdot k_3}{8 \cdot k} = \omega_0 \cdot \frac{3 \cdot k_{m3}}{8 \cdot k_m} = \omega_0 \cdot \frac{3}{8 \cdot \sqrt{2} \cdot W^2} \tag{4.7}$$

Therefore the critical displacement for a clamped-clamped beam is proportional to $W/\sqrt{Q}$ (4.8):

$$X_c \propto \frac{W}{\sqrt{Q}} \tag{4.8}$$

The higher is the critical displacement the more linear is the resonator, consequently wide resonators are more linear. Moreover, because of the stiffer resonators, the displacement is reduced for wider resonators, being these more robust to mechanical no-linearities. The first design consideration then is the width of the resonator. Although a wide resonator can increase the mechanical linearity, it also increases the resonator stiffness and consequently increases the motional resistance (see equation *4.7*). The following task is to analyze the constrains that imposes the width on the linearity and the motional resistance. For doing so, the motional resistance, equation (4.9) will be plotted as function of resonator width..

$$R_m = \frac{1}{Q} \cdot \frac{k \cdot s^4}{\varepsilon^2 \cdot \omega_0 \cdot A^2 \cdot V_{DC}^2} \tag{4.9}$$

Resonator parameters used are a length L=13.2μm, a quality factor of 100, an input AC signal of 10dBm (1V of amplitude) and V_{DC}=5V, the curves are also obtained for different gap values (s). To calculate the electrical elastic constant contribution, the length of the driver is considered to be L_c=9μm and fixing its thickness as the poly1 thickness (280nm). The minimum width available for the poly1 layer is 350nm which represents the first point of this study.

Prior to analyze the effect of the resonator width on the motional resistance it is important to verify that the resonator will not collapse for the considered voltage and applied power, using expression (2.30). *Figure 4.1* shows the plot of the pull-in voltage under these biasing conditions as a function of resonator width (W) and are plotted for different gap values (40nm, 100nm and 150nm). Note that: 1) the pull-in voltage is increased for wider resonators and 2) the influence of the gap decrease into reducing the maximum voltage that can be applied to the resonator.

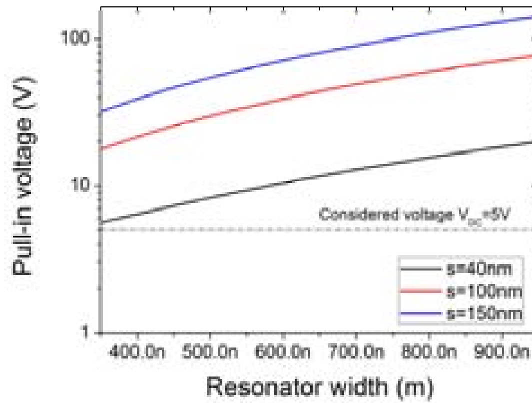

Figure 4.1: Pull-in voltage plot as a function of resonator width for the considered resonator with s=40nm, s=100nm and s=150nm. The applied voltage of 5V is below the pull-in voltage in all cases.

Once the bias point has been verified, the next step is to analyze the motional resistance as a function of the resonator width (*Figure 4.2*).

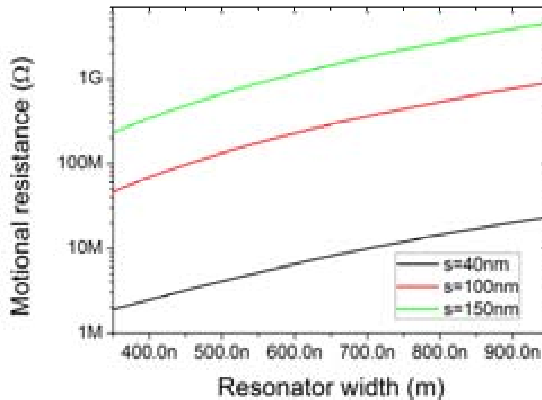

Figure 4.2. Plot of the motional resistance of the MEMS resonator as function of the resonator width for different gap values.

The increase of resonator width increases the motional resistance as result of the higher stiffness of the resonator. Therefore a compromise on the selection of the resonator width must be taken. For this reason a compromise value of W=500nm was selected. Note that according to expressions (4.9) and (4.1), the motional resistance value depends on the applied input power, however this dependence does not affect significatively the value of R_m.

Table 4.1 shows the analytic calculus of the motional resistance of a CC-beam using equation (4.9) with for different applied DC voltages (V_{DC}) and gaps (s) considering the L=13.2μm and W=0.5 μm resonator. Quality factors of 100 (for measurements in air) and 1000 (for in vacuum measurements) are assumed to perform the calculus.

Table 4.1: Calculated motional resistance under different DC voltages and gaps

	R_m					
	Q=100			Q=1000		
	s=40nm	s=100nm	s=150nm	s=40nm	s=100nm	s=150nm
V_{DC}=5V	653kΩ	21.17MΩ	105.52MΩ	65kΩ	13.2MΩ	10.55MΩ
V_{DC}= 10V	251kΩ	5.49MΩ	26.72MΩ	25kΩ	549kΩ	2.67MΩ
V_{DC} =15V	178kΩ	2.60MΩ	12.13MΩ	19kΩ	261kΩ	1.21MΩ
V_{DC} =17V	166kΩ	2.09MΩ	9.55MΩ	10kΩ	208kΩ	955kΩ

Shadowed cells show V_{DC}>V_{col} (and therefore unattainable R_m values)

To ensure a linear resonator, and robust against collapse, a gap of 100nm was selected, however, due to the high values of R_m obtained with this gap, versions of the same resonator with s=40nm were also fabricated.

4.1.2 CLAMPED-CLAMPED BEAMS DIMENSIONING

Considering these linearity concerns, the dimensions of the fabricated clamped-clamped beams are shown in *Table 4.2*. Note that to improve the linearity, the resonator is widened when compared to previous beam versions, whereas the gap is reduced to decrease the motional resistance [2].This kind of resonators were implemented and measured in different configurations and resonance frequencies of 24MHz and 48MHz.

Table 4.2: Designed clamped-clamped beam resonator dimensions

Resonance frequency	**W** (μm)	**L** (μm)	**Gap** (nm)	**Configuration**
24MHz	0.5	13.2	40	Stand-alone resonator
24MHz	0.5	13.2	100	Stand-alone resonator + on-chip amplification
48MHz	0.5	9.4	40	Stand-alone resonator

Figure 4.3 shows the layout of a CC-beam resonator on Cadence Virtuoso Layout tool. The red layer is the poly1 layer and the pink colored is the poly 2. Note that to show more clearly the mechanical structure, the PAD and the VIA layers, described in *Chapter 3*, are not drawn.

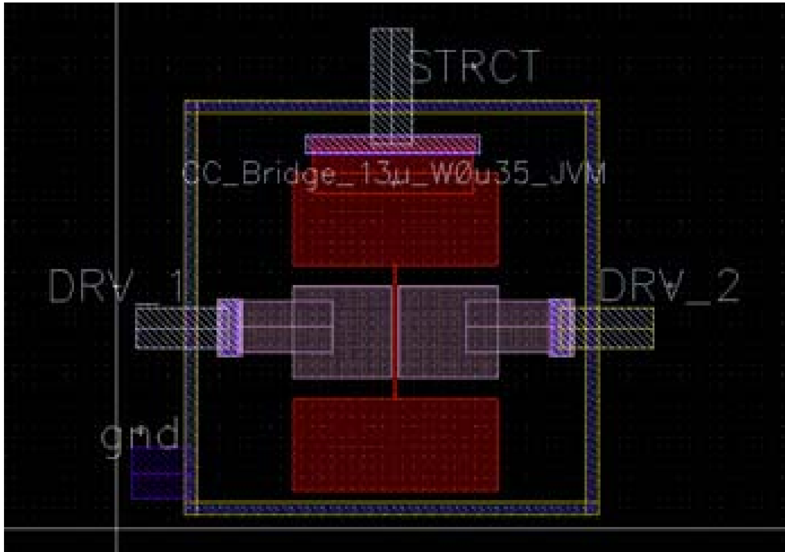

Figure 4.3: Cadence layout of a clamped-clamped beam.

Figure 4.4 shows the Coventor mechanical simulation of the lateral movement of the 24MHz and 48MHz clamped-clamped beams. The mechanical resonance frequencies of the FEM simulation are: 24.6MHz and 47.95MHz, respectively. The drivers length are dimensioned to 9µm for the 24Mhz resonator and 7µm for the 48MHz beam.

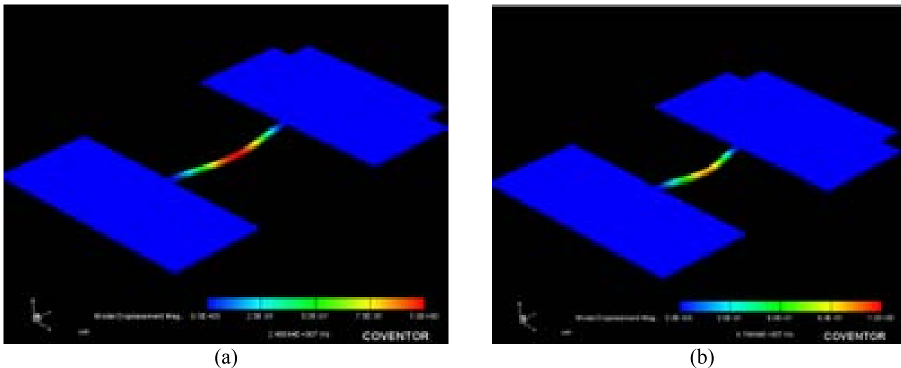

(a) (b)

Figure 4.4: Coventor simulations of the CC-beams (a) 24MHz resonator and (b) 48MHz resonator. Both correspond to the first lateral mode of resonance.

4.1.3 24 MHz Clamped- Clamped Beams

Figure 4.5 shows a SEM image of the 24MHz resonator fabricated with AMS technology and released using the post-process explained in *Chapter 3*.

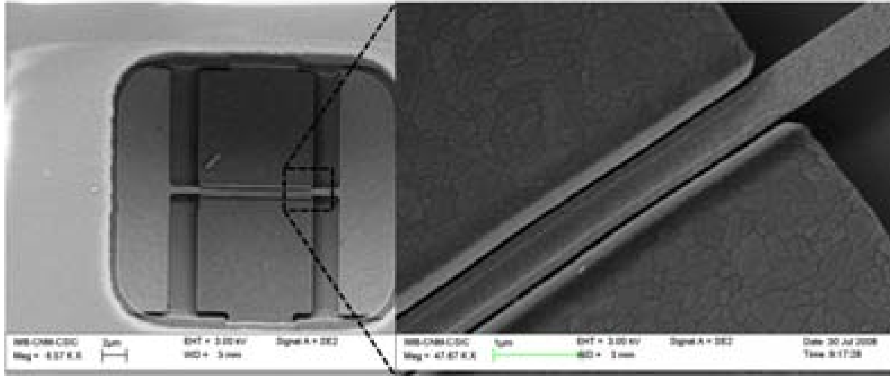
Figure 4.5: SEM images of the fabricated 24MHz resonator with *s*=40nm (general view and close view).

4.1.3.1 Stand-Alone Resonators

S21 (magnitude and phase) measurements in air were performed for different biasing conditions and input signal powers for the 24MHz clamped-clamped beam stand-alone resonators. *Figure 4.6* shows the magnitude response of the *s*=40nm and *s*=100nm MEMS resonator response, whereas *Figure 4.7* shows the phase frequency response of the same resonators. All measurements were performed for different DC voltage biasing conditions.

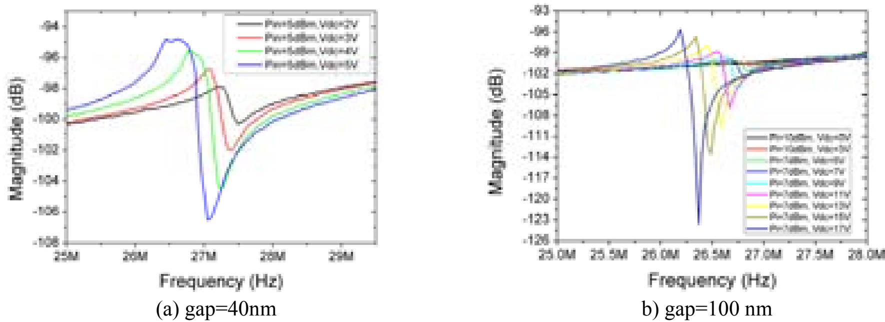

(a) gap=40nm b) gap=100 nm

Figure 4.6: Magnitude frequency response for the 24 MHz resonator under different V_{DC} applied voltages. (a) *s*=40nm resonator version, applied intput power is P_i=5dBm. (b) *s*=100nm resonator, applied input powers are of P_{in}=10dBm for V_{DC}<3V and P_i=7dBm for higher DC voltages. Note the non-linear behaviour in both cases due to a high bias voltage and AC power to excite the resonator.

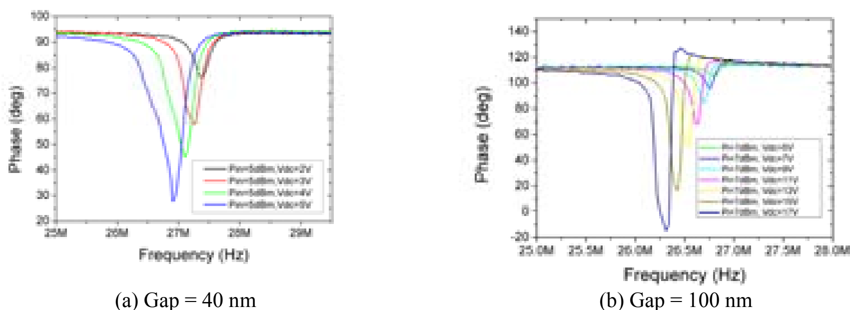

(a) Gap = 40 nm (b) Gap = 100 nm

Figure 4.7: Phase frequency response for the 24 MHz resonator for different V_{DC} voltages. (a) *s*=40nm and (b) *s*=100nm.

From magnitude measurements (*Figure 4.6*) it can be observed that the required DC voltage is lower for the 40nm gap version than for the 100nm, thanks to the impact of the gap reduction in the coupling factor. This is also evidenced in *Figure 4.8*, where the magnitude responses of both gap versions clamped-clamped beams resonators under the same DC biasing conditions (V_{DC}=5V) are plotted. Comparing *Figure 4.6* plots it is shown that the *s*=100nm resonator presents a slightly lower feedthrough level (nearly 2dB) than the *s*=40nm resonator, thanks to the higher distance between the excitation and read-out electrodes (700nm instead of 580nm). According to S21 measurements, the 40nm resonator express a more non-linear behavior (the magnitude peaks are distorted for lower DC values) than the 100nm device, as it was expected due to the dependence with the gap (further explanation below).

It is worth to mention that both resonators have big phase shifts (*Figure 4.7*), specially the 40nm resonator with more than 60 degrees shift for an applied DC voltage of only 5V.

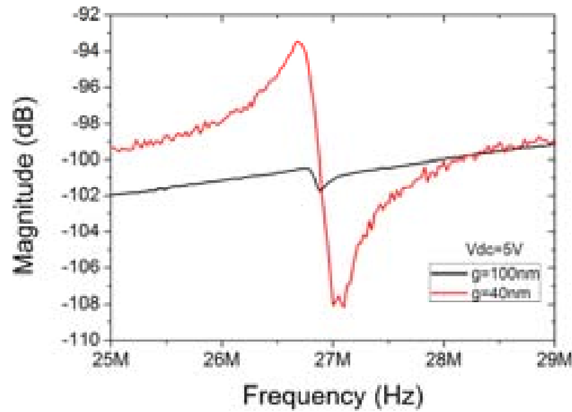

Figure 4.8: Magnitude response at V_{DC}=5 for the 40nm and 100nm versions of the 24MHz MEMS resonator. Applied input powers are of 5dBm and -10dBm for the *s*=100nm and *s*=40nm resonators, respectively.

Figure 4.9 shows the magnitude response of both gap resonators with different AC applied input powers (P_i) for fixed DC voltage values. From these measurements it is clearly shown the non-linear behavior of the resonators. For the *s*=40nm resonator, the phase measurements are the same for input applied powers of -10dBm and 0dBm, and therefore the behavior is linear. When P_i=5dBm and V_{DC}=5V the phase is distorted. Under this biasing, the magnitude curve behavior is strange: the peak is not bended to the left but it seems compressed, showing that the displacement is limited. We believe that this movement is limited by the electrodes, i.e. the resonator contacts (in a no destructive way) the electrodes. *s*=100nm shows a more usual magnitude behavior with the applied DC levels, i.e. the peak bends to lower frequencies.

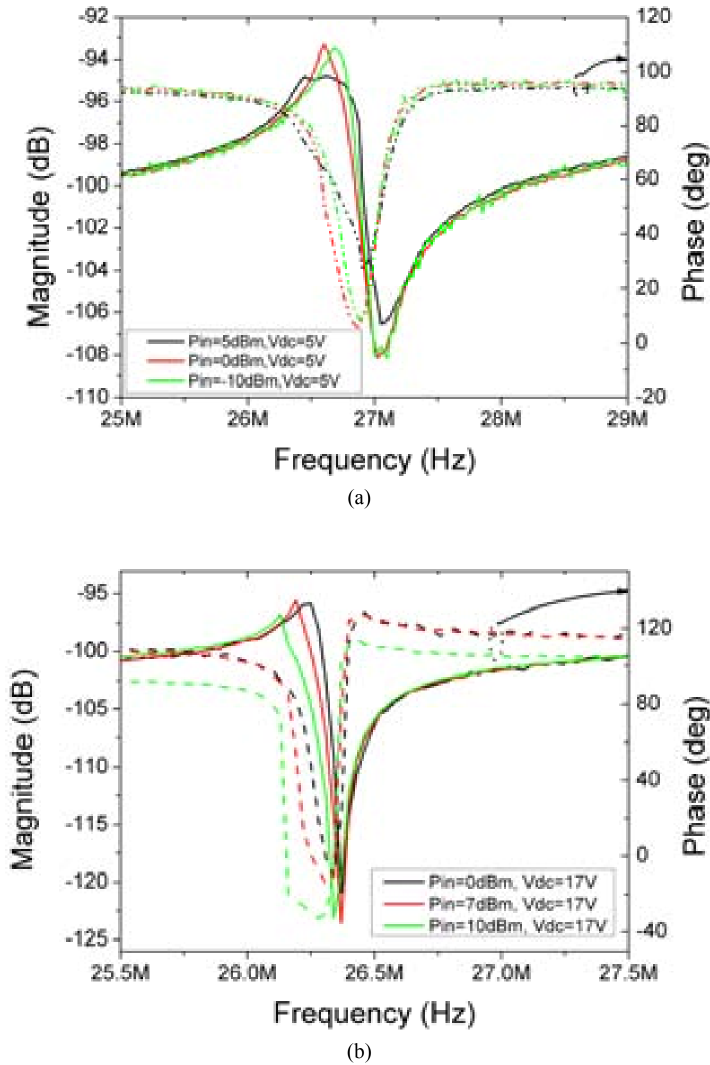

Figure 4.9: Non-linear behavior of the 24MHz clamped-clamped beam. (a) 40nm gap version (b) 100nm gap.

The magnitude characterization can also be used to determine the natural oscillation frequency of the oscillator, by linearly fitting the f_{RES} vs. V_{DC}^2 response. However, because the magnitude measurements show non-linear behavior, it is not recommended to perform this fitting to evaluate accurately the frequency tuning. However, f_{RES} vs. V_{DC}^2 relationship is used to obtain the natural resonance frequencies for both resonators, these frequencies are: 27.37MHz (s=40nm version) and 26.75MHz (s=100nm version). Both resonator version have a resonance frequency higher than the designed, and present a difference between them of the 2%. The discrepancy between measured natural resonance and the designed is nearly the 10%. This indicates that the Young modulus of the polysilicon layer is higher than the used in simulations and calculus. This difference, however,

is not important as long as the desired resonance frequency can be tuned with an applied DC voltage, remember that in order to have an output current, a DC voltage must be applied.

Another important characteristic of these resonators is the quality factor. This magnitude is measured for the device with both gap distances, using 3dB peak and phase measurement formulas that can be found in *Annex 2*. The magnitude plots used to calculate the *Q* are shown in *Figure 4.10*. It is worth to notice that in order to obtain a 3dB resonance peak, the DC voltage applied is higher in the case of the *s*=100nm resonator**.**

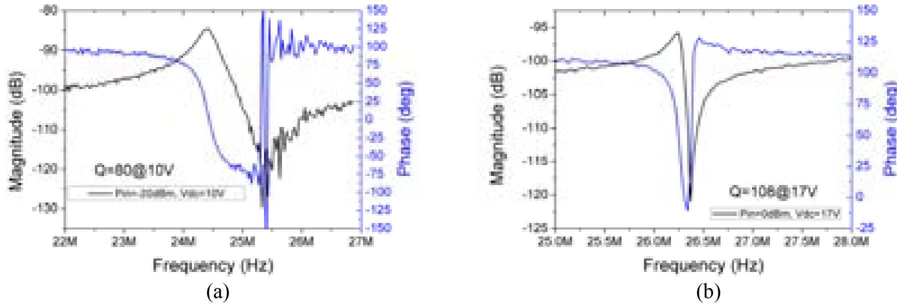

Figure 4.10: 24MHz clamped-clamped beam resonator frequency response used for the calculus of Q. (a) *s*=40nm and (b) *s*=100nm

The *Q* values obtained are of 80@V_{DC}=10V and 108@V_{DC}=17V for the *s*=40nm and *s*=100nm resonator, respectively. For comparison purposes, the quality factor obtained from phase measurements is also calculated, showing similar values than the obtained with the 3dB peak formula: for phase calculations *Q*=79 and *Q*=105, for the *s*=40nm and *s*=100nm resonators, respectively.

However, measurement of *Q* factor by direct S21 measurement in air presents two main inaccuracies: the first one is caused by the reduction of *Q* due to air damping, and the second one comes from the electrical characterization: the parasitic feedthrough capacitor can mask the resonance peak [3]. Moreover, due to the loading of the *Q* due to the output electrical pad parasitic capacitor, the measured electrical *Q* is lower than the resonator mechanical quality factor. This can be alleviated by integrating monolithic amplification circuitry on the CMOS chip [3], as will be shown in next section.

Electrical characterization presents an antiresonance peak that affects this measurement accuracy, presenting different values for different applied DC voltages. In addition to monolithic amplification, several methods were presented in order to obtain a more accurate *Q* value [5, 6]. The measurement technique used here is mixing, which is explained in detail in *Annex 2*. The main advantage of this kind of measurement is that the excitation and readout frequencies are different, so that the input signal feedthrough (the parasitic current) does not affect the output and the obtained peak does not present antiresonance. *Figure 4.11* shows the down-conversion mixing measurement results for the *s*=100nm CC-beam, measured with a Agilent E5070 network analyzer equipped with frequency offset measurement option, which allows excitation and measurement at different frequencies using the same network analyzer [7]. In this measurement, a LO signal of 5MHz is applied to the clamped-clamped resonator whereas the input signal is swept from 30MHz to 43MHz. In the figure, a Lorentzian fit is also shown to highlight the resonance peak shape.

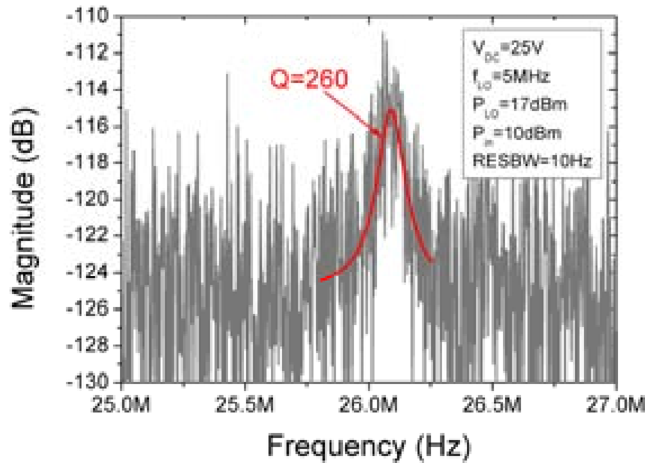

Figure 4.11: Mixing measurement for the 24MHz clamped-clamped beam with s=100nm. Applied signals are: P_i=10dBm, P_{LO}=17dBm and V_{DC}=25V. The LO signal frequency is 5MHz. RESBW is the resolution bandwidth set in the measurement instrument.

A Q of 260 is measured for this resonator using this technique, using a Lorentzian fit. The mixing was used only for resonator characterization purposes, being this the reason for the low LO frequency value. Note the high level of the signals applied which are required to perform mixing measurements without amplification, as expected when comparing the expressions developed for each excitation case in *Chapter 2*.

Experimental motional resistor can be found using an $RLC//C_p$ equivalent circuit or the direct analytic (but inaccurate) formula shown on *Annex 2*. *Figure 4.12* shows the fit of the experimental magnitude curve of the s=100nm clamped-clamped beam with the equivalent $RLC//C_p$ circuit for V_{DC}=17V.

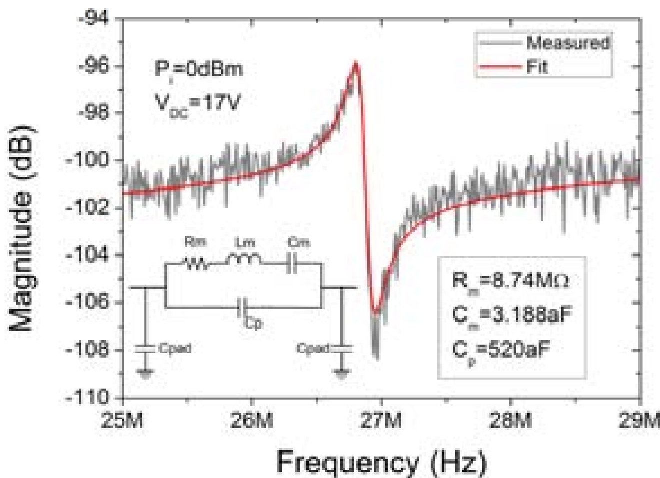

Figure 4.12: Fitting of experimental measurement data using an RLC//Cp equivalent circuit for the 100nm gap CC-beam resonator at 24MHz. Parasitic pad capacitor for AMS technology is C_{pad}=1pF.

The equivalent circuit shows a very nice fitting of the resonator response. The motional resistance is found to be 8.74MΩ, a pretty high value for the *s*=100nm. Analytic calculus of the motional resistance for this resonator is 12.17MΩ and the R_m found using the direct formula (A2.3) on the resonator response magnitude (*Figure 4.10-b*) is of 3.1MΩ, a value lower than the obtained by curve fitting but on the same order of magnitude, this underestimation is thought to be caused by the effect of the C_p parasitic capacitor not considered in this analytic expression. These R_m values are pretty high due to the low quality factor of these resonators when measured directly in air conditions, and the *s*=100nm gap.

4.1.3.2 CC-Beam+ On-Chip Amplifier:

The 24MHz CC-beam with *s*=100nm, has been also fabricated with an on-chip amplifier for ease of testing. The amplifier designed by J. Verd [3] , shows a transimpedance gain of 115dBΩ (56.2kΩ) at 27.5MHz. This amplifier alleviates the *Q* loading of the MEMS resonator and reduces the effect of the parasitic feedthrough capacitor, as it can be observed in the magnitude and phase measurement of the device (*Figure 4.13*), which presents higher magnitude and phase variations when compared to previous stand-alone resonators.

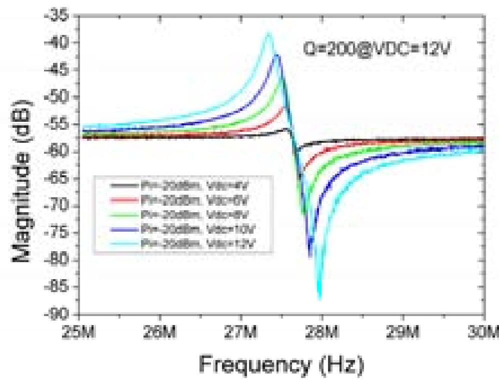

(a)

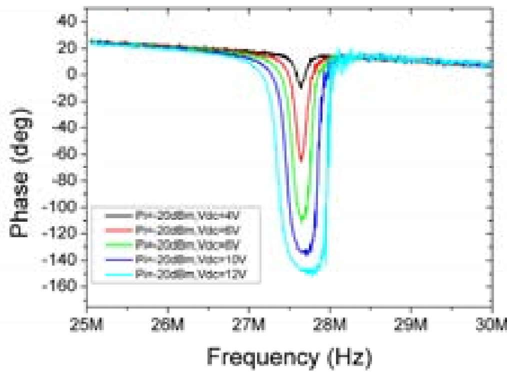

(b)

Figure 4.13: S21 measurements of the 100nm gap CC-beam with on-chip amplifier for different applied DC voltages. (a) Magnitude and (b) Phase

As it can be observed from these measurements, the peak height has been amplified when compared with the stand-alone resonator (from 5dB to 17dB), as well as the phase variation (from 110 degrees to nearly 180 degrees). The use of on-chip amplification, allows a measurement of the quality factor of 200 at V_{DC}=12V, nearly twice the value obtained in the stand-alone resonator with similar measurements (which was of 108) and it was measured with higher applied DC voltage (17V instead of 12V with amplifier). To take into account the amplification in the calculus of motional resistance, R_m expression on *Annex 2* (A2.3) can be modified as (4.9) [8].

$$A = 20 \cdot \log\left(\frac{R_{amp}}{R_m}\right) \tag{4.9}$$

Where R_{amp} is the amplifier resistance, which has a value R_{amp}=56.2kΩ for the used on-chip amplifier. Using this expression, the motional resistance of the CC-beam is R_m=7MΩ for V_{DC}=10V. Note that this value is lower than the one calculated for the stand-alone *s*=100nm clamped-clamped beam resonator, even with the reduction of the applied DC voltage. The analytic calculus of the motional resistance provides a value of 17.2MΩ considering the applied voltage of 10V and a *Q*=200, a value higher than the motional resistance value obtained from the S21 measurements, showing the inaccuracies of this expression.

Figure 4.14 shows the f_{RES} vs. V_{DC}^2 not used previously because the non linear behavior of the resonators. The obtained frequency tuning is of 71.8ppm/V^2, whereas the analytic calculus value is 577ppm/V^2, this difference can be explained due to the overestimation of the electric elastic constant due to considering that the entire beam displaces the same amount, without using the beam bending profile.

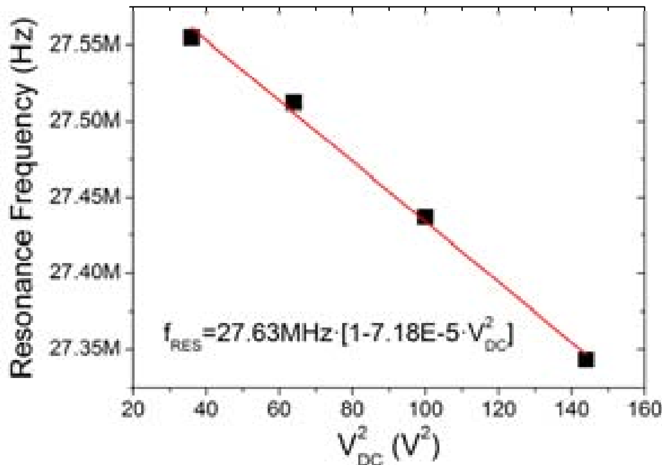

Figure 4.14: f_{RES} vs. V_{DC}^2 plot for the 24MHz CC-beam with s=100nm with monolithic amplification.

Mixing measurement is also performed in this buffered resonator to evaluate the performance of this characterization scheme (*Figure 4.15*). The measured *Q* value (230) using mixing with the resonator+amplifier configuration is slightly lower than the measured in the stand-alone resonator using the same technique (260), however, this measurement is in the same order of magnitude and presents much less noise when compared the stand-alone resonator mixing measurements. The

measured Q using mixing is only slightly greater than the obtained with direct S21 measurements (which was of Q=200, see figure 1.14), this light difference shows the ability of the on-chip amplifier to decrease parasitic measurements, when compared to conventional measurements performed on stand-alone resonators.

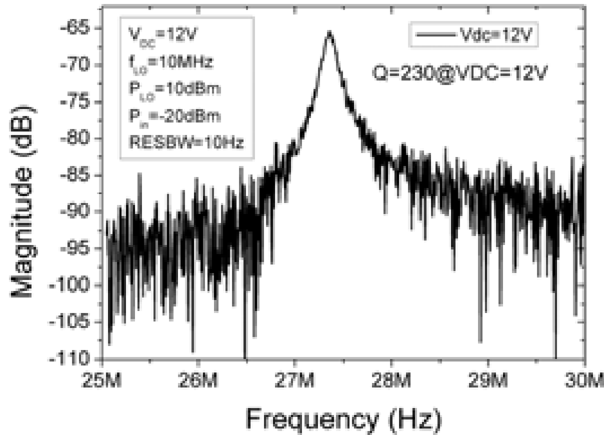

Figure 4.15: Mixing measurement for the 24MHz clamped-clamped beam with s=100nm with on-chip amplifier. Applied signals are: P_i=-20dBm, P_{LO}=10dBm and V_{DC}=12V. The LO signal is of 10MHz.

4.1.4 48 MHZ CLAMPED-CLAMPED BEAM

The 48MHz CC-beam resonator was fabricated with a gap s=40nm in the polysilicon layers of AMS technology, *Figure 4.16* shows a SEM image of the released 48MHz CC-beam. The length of the resonator was scaled (L=9.4 µm) to reach the desired resonance frequency. This reduction of the length makes necessary to reduce the length of the excitation and readout electrodes to 7µm, decreasing the coupling area. This necessary scaling of the coupling in these resonators is one of the reasons because these devices are limited to “low” frequencies [9, 10].

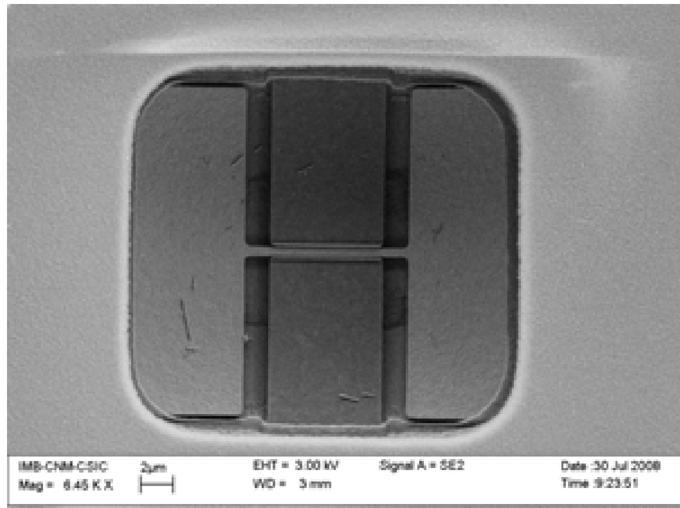

Figure 4.16: SEM image of the 48MHz CC-beam resonator.

Resonator characterization is performed in the same way than the stand-alone 24MHz clamped-clamped beams previously presented. *Figure 4.17* shows the frequency response characterization (in frequency and phase) for the fabricated device with an AC power of -5dBm, and under different DC biasing conditions.

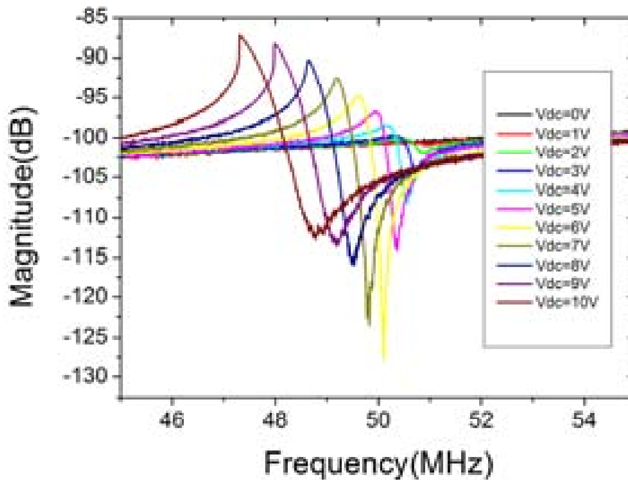

(a)

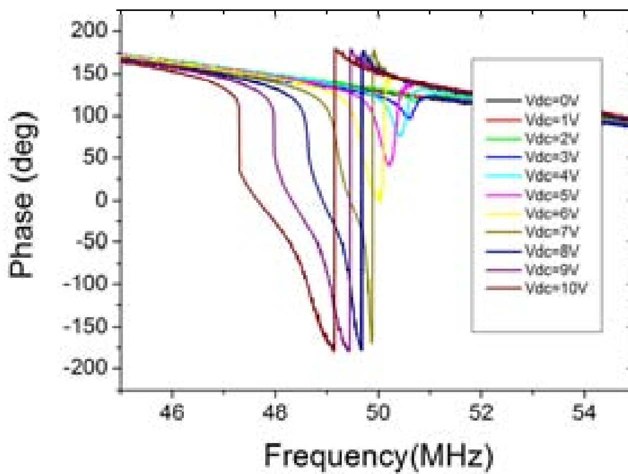

(b)

Figure 4.17: Frequency response of the 48MHz, 40nm gap CC-beam resonator for different applied DC voltages, applied input power is P_i=-5dBm. (a) Magnitude and (b) Phase.

From the previous measurements, the frequency softening (and resonator non-linearity) is clearly observed for V_{DC}>6V. Above this applied bias voltage, phase curves are also highly distorted. Quality factor calculus from the magnitude measurements are not possible for DC voltages below 6V (the linear region), because magnitude shift is lower than 3dB. Consequently, the Q is calculated using the phase curves for V_{DC}=5V. The quality factor for this resonator is

Q=76 at V_{DC}=5V, lower than the obtained for 24MHz resonators, as it could be expected. In the magnitude frequency response of this resonator it can be clearly observed the electric-dominated no-linearity for DC voltages above 8V. For these voltages both magnitude and phase show a sharp transition (vertical line) showing the hysteresis behavior described in *Chapter 2*.

The natural frequency response of the MEMS can be calculated fitting the f_{RES}vs.V_{DC}^2 relationship (*Figure 4.18*), like for the previously presented 24MHz resonators, but considering only the resonance peaks at V_{DC}<6V.

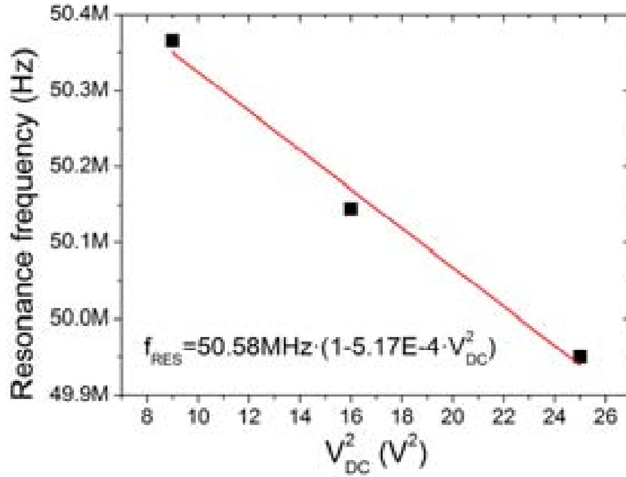

Figure 4.18: f_{RES} vs. V_{DC}^2 graph. Linear fit shows a value of the natural resonance frequency of 50.58MHz.

The measured natural resonance frequency is of 50.58MHz, a value a 5.3% higher than the one obtained with Coventor simulations. Even though the reduction of the coupling area, the narrower gap used in this resonator (s=40nm), makes the frequency tuning higher (517ppm/V^2) than the obtained for the 24MHz s=100nm CC-beam described in *Section 1.1.3.2*.

4.2 FREE-FREE BEAMS

Two different kinds of free-free beams were designed and fabricated: a first order lateral mode free-free beam with resonance frequency at 24MHz, and a third-order lateral mode free-free beam at 48MHz. These resonators were fabricated using the polysilicon layers of the AMS CMOS technology.

Table 4.3: Free-free beams dimensions

Resonance frequency	W_r (µm)	L_r (µm)	W_s (µm)	L_s (µm)	**Gap** (nm)	**Application**
24MHz	0.8	17	0.4	20	40	Resonator, high Q
48MHz (third mode)	0.8	28	0.4	14	100	Resonator, low Rm, phase shifter

The resonator dimensions were calculated using the formulas from *Annex 1* and the support dimensioning was made considering the supports like second lateral mode CC-beams and using the corresponding equations also from *Annex 1*. Due to the location of the supports, the electrodes are reduced to 7µm and 5µm for the 24MHz free-free beam and the third mode free-free beam, respectively. *Figure 4.19* shows the Cadence layout of a third resonance mode 48MHz free-free beam.

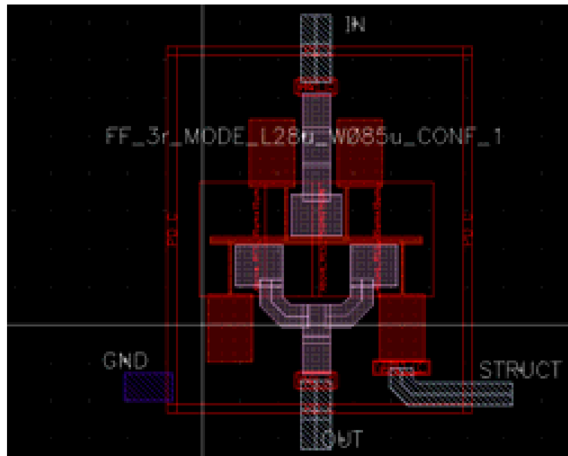

Figure 4.19: Cadence layout of the 48MHz third mode free-free beam.

Figure 4.20 shows the Coventor FEM simulations of both free-free beam resonators. In these simulations it is shown how the joints of the supports and the structures present zero lateral displacement (areas in blue). These mechanical simulations show a resonance frequency of 23.98MHz and 48.7MHz for the first mode and third mode free-free beam resonators, respectively.

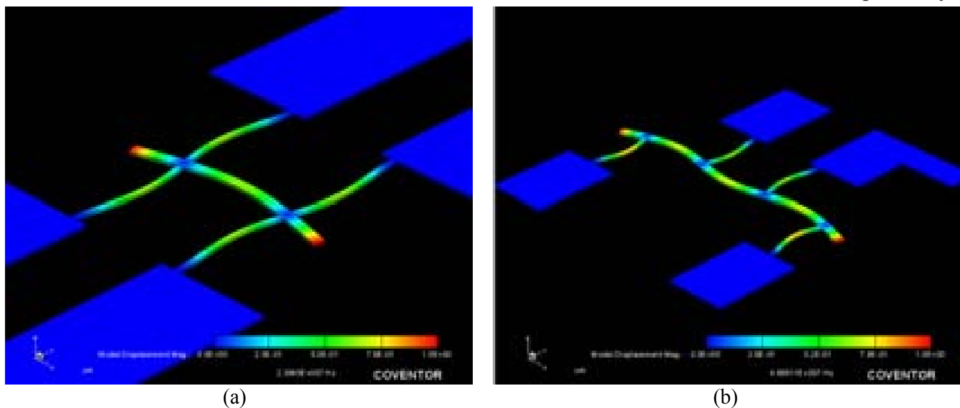

(a) (b)

Figure 4.20: FEM mechanical simulation of the designed free-free resonators. (a) First lateral mode free-free beam with resonance frequency of 24MHz and (b) Third lateral mode free-free beam with resonance frequency of 48MHz.

4.2.1 24MHZ FREE-FREE BEAM

Figure 4.21 shows the SEM image of the released 24MHz designed free-free beam with gap *s*=40nm. S21 magnitude and phase measurements were performed using a network analyzer under different applied DC voltages (*Figure 4.22*).

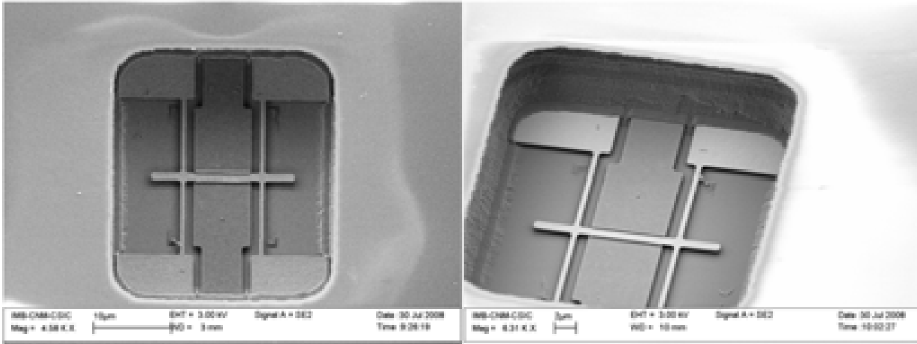

Figure 4.21: SEM images of the 24MHz free-free beam, *s*= 40 nm

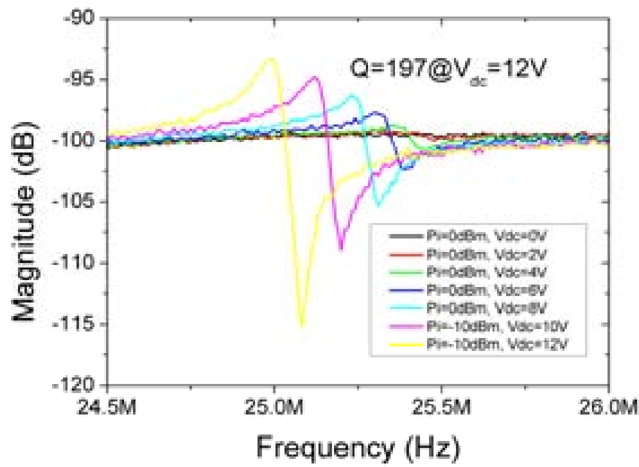

(a)

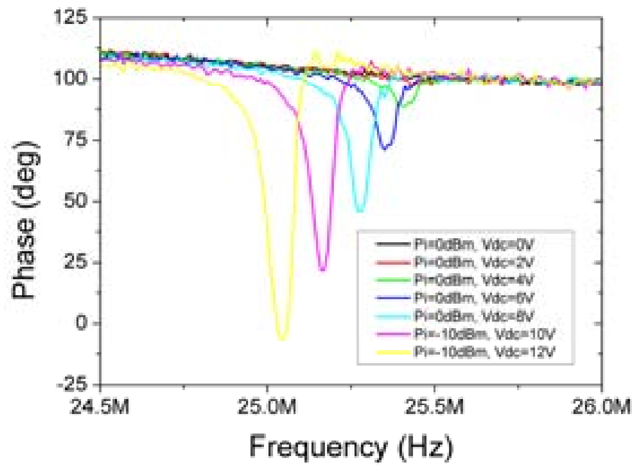

(b)

Figure 4.22: 24MHz free-free beam frequency response. (a) Magnitude and (b) Phase

From S21 measurements it can be observed that a quality factor Q=197 is measured in air from the 3dB peak for V_{DC}=12V, and a similar value is obtained using the phase curves. This value is twice the best obtained with the 24MHz clamped-clamped beam, demonstrating the higher Q of the free-free beams, as expected [11, 12].

The natural resonance frequency of the free-free beam is obtained using the linear fit of the f_{RES}vs.V_{DC}^2 relationship (*Figure 4.23*). This value is of 25.3MHz, a 6% higher than the obtained using Coventor simulations. The frequency tuning of this resonator is of 113ppm/V^2, lower than the obtained for the CC-beam with s=40nm, making this resonator more robust against DC voltage drifts. Because of this robustness, the required V_{DC} to obtain the target 24MHz resonance frequency with the free-free beam resonator is 23V, obviously higher than the required for s=40nm clamped-clamped beam, which was of 10.6V.

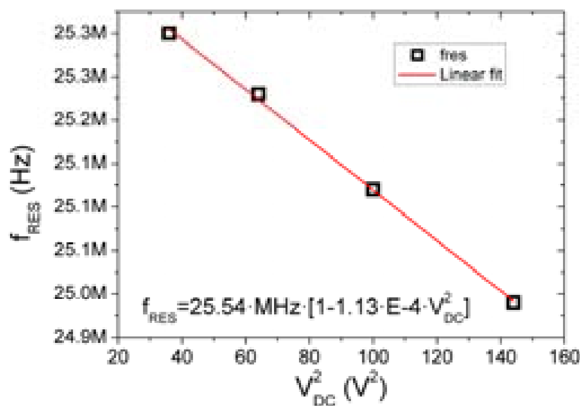

Figure 4.23:f_{RES} vs. V_{DC}^2 plot. Natural resonance frequency is 25.54MHz.

The $RLC//C_p$ model is used to fit the frequency response of the s=40nm 24MHz FF-beam. *Figure 4.24* shows the fitting curve for P_{in}=0dBm and V_{DC}=12V.

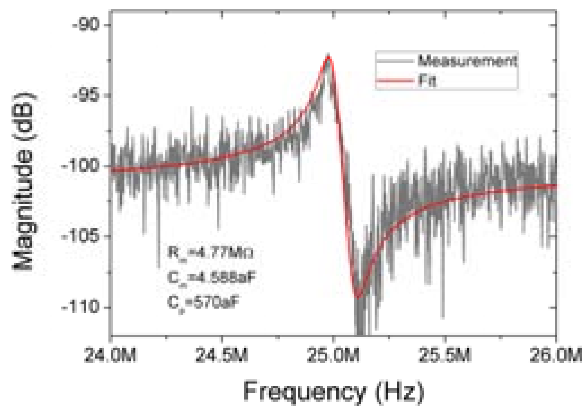

Figure 4.24:Curve fitting of the 24MHz FF-beam. Applied input power is P_i=0dBm and V_{DC}=12V.

The obtained motional resistance by curve fitting is of 4.77MΩ, whereas the value obtained from direct calculus on magnitude measurements, using (A2.3) and the k value obtained from FEM mechanical simulations, is 2.3MΩ. Comparing the RLC//Cp model of the s=40nm FF-beam with the one of the s=100nm CC-beam several observations can be made: even though the gap reduction and the increase of Q, the motional resistance of the FF-beam is only a half of the one from s=100nm CC-beam. However it is worth to mention that the applied DC voltage is lower in the FF-beam, and that the coupling area was reduced. The motional capacitor is slightly greater in the FF-beam, but on the same order of magnitude and finally, the parasitic capacitor was increased due to the reduction of the distance between electrodes. Motional resistance for free-free beams resonators, would be higher than the one for the clamped-clamped beams for the same bias voltage and gap (s=40nm). Comparing the motional resistances of both resonators using (2.39):

$$\frac{R_m^{FF-Beam}}{R_m^{CC-Beam}} = \frac{Q_{CC-Beam} \cdot A_{CC-BEAM}^2 \cdot k_{FF-Beam}}{Q_{FF-Beam} \cdot A_{FF-BEAM}^2 \cdot k_{CC-Beam}} \tag{4.10}$$

To evaluate expression (4.10), Q values are obtained from previous measurements ($Q_{CC\text{-}Beam}$=80 and $Q_{FF\text{-}Beam}$=197, the coupling areas are determined by the coupling length ($L_{cCC\text{-}Beam}$=9µm and $L_{cFF\text{-}Beam}$=7µm) and the mechanical elastic constants are calculated from Coventor FEM simulations ($k_{CC\text{-}Beam}$=38.7N/m and $k_{FF\text{-}Beam}$=90.6N/m), using these values the motional resistance for a free-free resonator is 1.6 still times higher than the clamped-clamped beam, even though the higher Q of the free-free beams, indicating the importance of the coupling area (quadratic dependence).

Figure 4.25 shows the mixing measurement of the 24MHz free-free beam with applied powers of P_i=10dBm, P_{LO}=17dBm and V_{DC}=12V, the LO frequency is fixed to 5MHz and the input signal is swept from 29MHz to 31MHz. Comparing this curve with the previously obtained for a CC-beam, it can be observed that this response shows a less noisy signal and a higher measured Q of 334.

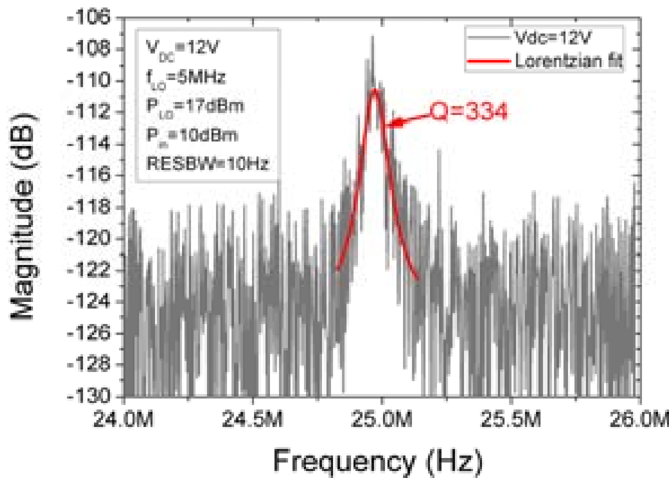

Figure 4.25: Mixing measurement for a 24MHz 40nm gap free-free beam with P_i=0dBm, P_{LO}=10dmb, and V_{DC}=12V.

4.2.2 THIRD-MODE 48MHZ FREE-FREE BEAM RESONATOR

Flexural beam-like resonators resonance frequency scale with $\alpha W/L^2$. So to increase the resonance frequency, resonator length (and therefore the coupling area) has to be reduced, this fact states a limit to the highest frequency achievable with this kind of resonators [9]. A possible solution is the use of higher modes of resonance: for a given resonance frequency, resonators working at a higher flexural mode are longer than their fundamental resonance mode counterparts, and therefore present a higher coupling area. Moreover, these devices are claimed to have a more linear behavior when compared to fundamental resonance mode resonators [13]. With this in mind, the objectives of this resonator are: obtain a high *Q* device with high linearity and largest coupling area possible. The selected resonator is a 3rd lateral mode resonator, which is dimensioned to have a 48MHz resonance frequency, being its dimensions: W_r=0.8µm and L_r=28µm, according to the equations in *Annex 1*.

The number of nodes of the beam is four, and therefore eight support beams are required. With this number of beams, the anchor losses would be specially high, consequently, we propose to reduce the number of support beams and hence obtain a potential higher Q resonator. For this reason, the CC-beam supports used are only half length, reducing the supports number (and therefore the anchor losses) from 8 to 4. These supports are dimensioned to be second-lateral mode CC-beams whose central node is attached to the nodes of the resonator (blue area in FEM simulations), the same kind of support used in the fundamental 24MHz free-free beams. Support dimensions are: W_s=0.4µm and L_s=14µm (although the drawn length is of 7µm). The schematic of the resonator is shown in *Figure 4.26.*

Note that like in the case of the first-mode free-free beams the electrode lenght is reduced by the need of the support beams, and this increases the motional resistance. Fortunately, this third-mode resonator allows the use of multiple drivers for excitation or read-out, to alleviate the increase of the motional resistance. In the resonator fabricated, the excitation is applied to one electrode, whereas the read-out is performed using two electrodes. In order to study new functionalities, two read-out electrode configurations have been fabricated, where electrodes are placed on different sides of the beam (*Figure 4.26*). The gap between the electrodes and the resonator beam is designed at *s*=100nm.

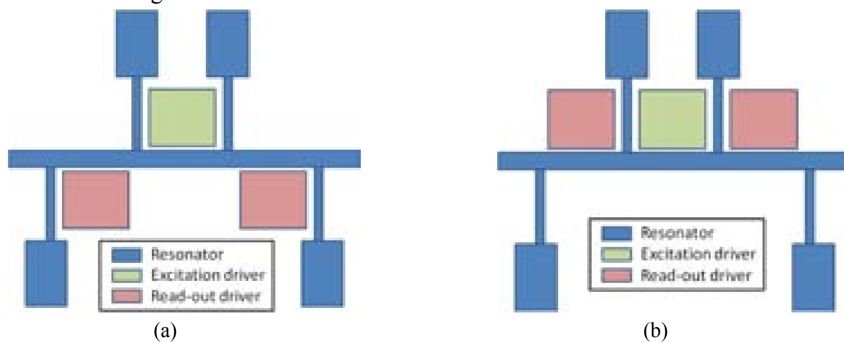

Figure 4.26: Electrode configuration for the 48MHz 3rd lateral mode free-free beam. (a) Configuration 1 and (b) Configuration 2

Even though configuration 2 allows an additional read-out electrode placed in front of the excitation electrode, this would degrade the isolation between excitation and read-out electrodes

when compared to the scheme depicted in *Figure 4.26(b)*. For this reason the total number of electrodes is set to three.

With these two electrode configurations, the motional current has different sign, as can be observed in the diagram of *Figure 4.27*. On electrode configuration 1, when the beam moves away from the excitation electrode, it also moves away from the read-out electrode, whereas on configuration 2 it moves closer. In this sense, configuration 2 is similar to the clamped-clamped beam presented in previous section, whereas on configuration 1 the feedthrough current and the motional current will present a 180º phase shift.

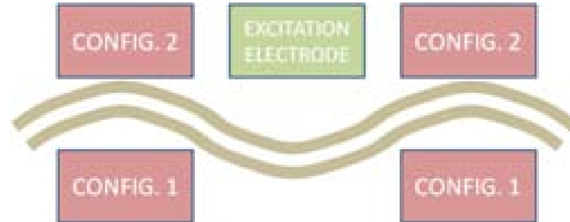

Figure 4.27: Schematic diagram of the bending profile and the location of output electrodes for the two configurations

Figure 4.28 shows the SEM image of the released third lateral mode 48MHz FF-beam resonator with electrode configuration 1. Inset shows SEM image of configuration 2.

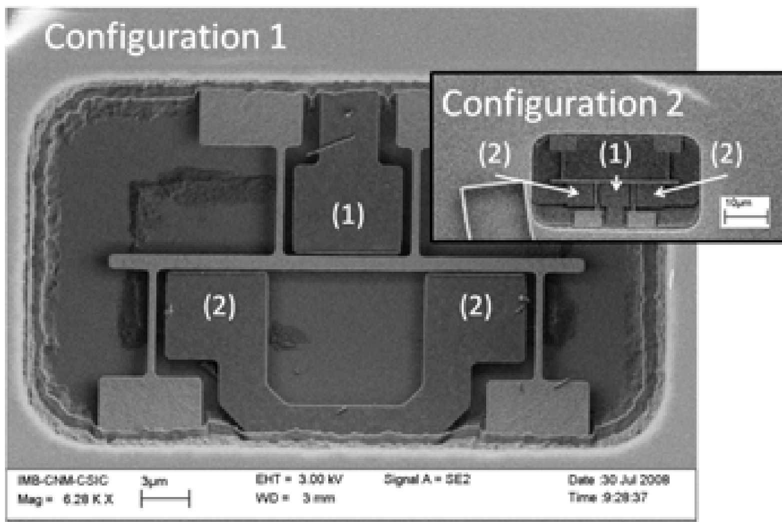

Figure 4.28: 48MHz 100nm gap third lateral mode FF-beam resonator (both electrode configurations). (1) Excitation electrode and (2) Read-out electrodes.

Figure 4.29 shows the S21 magnitude measurement for both electrode configurations. For both resonators the applied input power is set to 5dBm whereas the DC voltage is varied from 0V to 20V.

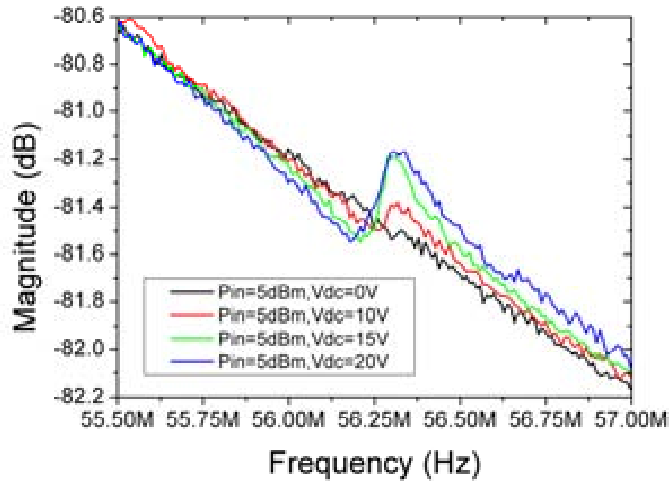

(a)

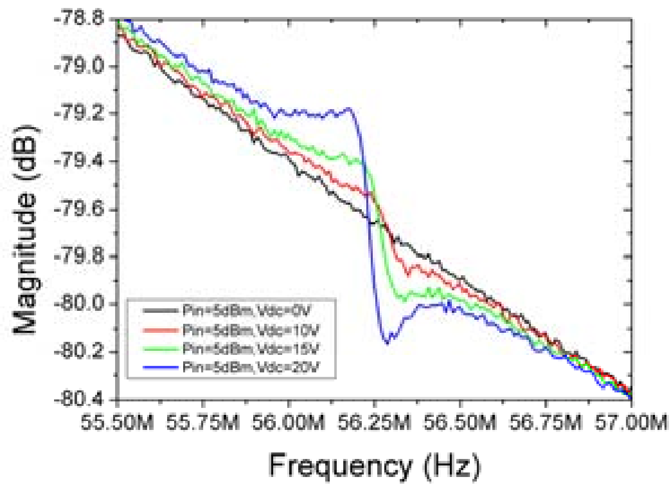

(b)

Figure 4.29: S21 magnitude measurements for the 3rd mode 100nm gap free-free beam resonator. (a) Electrode configuration 1 and (b) configuration 2.

It is observed that the magnitude peaks have different shape: configuration 1 presents the antirresonance before the resonance peak whereas configuration 2 shows the usual shape of magnitude frequency response observed in the CC-beams. This fact demonstrates the bending behavior shown in *Figure 4.27*, in which the two configurations present opposite sign phase shifts, as it can be observed in the phase measurements from *Figure 4.30*.

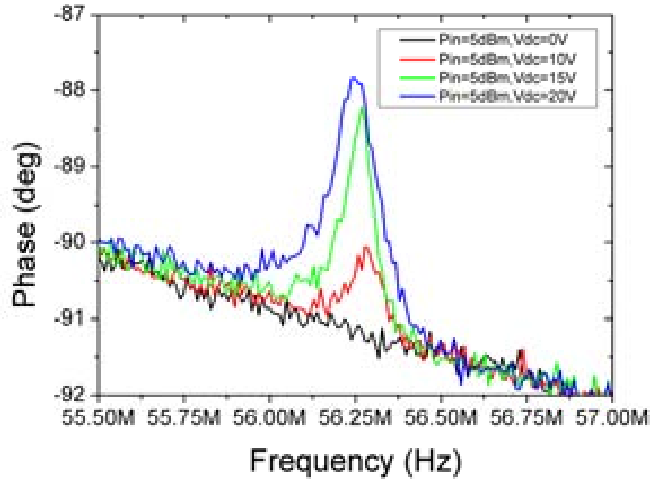

(a)

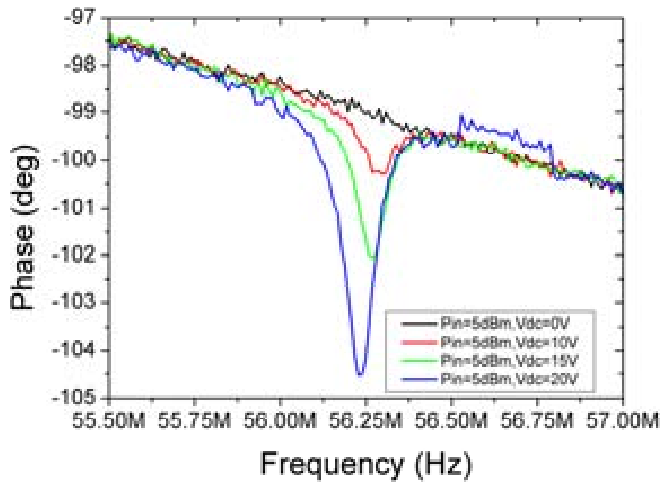

(b)

Figure 4.30: Phase frequency response of the 3rd mode 100nm gap free-free beam. (a) Electrode configuration 1 and (b) configuration 2.

On the magnitude frequency response (*Figure 4.27*) it can be observed that the feedthrough signal is a little bit lower (1.8dB) when the electrode configuration 1 is used, thanks to the different location of the read-out electrodes, note that on configuration 2 the excitation and readout electrodes are closer than with configuration 1.

Unfortunately the low coupling factor (5µm coupling electrodes and *s*=100nm) makes the signal very low, and therefore the quality factor cannot be calculated with the 3dB magnitude peak. Phase calculations give Q values at V_{DC}=20V of 11 and 18.8, for configuration 1 and configuration 2, respectively. These low quality factors, prevent us to use these resonators as frequency references. Moreover, this structure is quite big and therefore presents additional

releasing problems (sticking to the substrate or complete releasing of the resonators) which affect negatively the yield of the MEMS fabrication process.

This resonator, however, can be used for different functions rather than as frequency reference. *Figure 4.31* shows the relative magnitude and relative frequency shifts for both resonator configurations. Even though the magnitude and phase shifts are low, the behavior of this resonator for the electrode configurations shown presents two potential applications if the electrode configuration shown in *Figure 4.32* is used. Note that by combining IN+ and IN- (for example by subtracting them on a differential amplifier), a filter behavior can be obtained. The other application is a single-ended to differential signal processor as long as the phase shift between the two output signals would be of 180º.

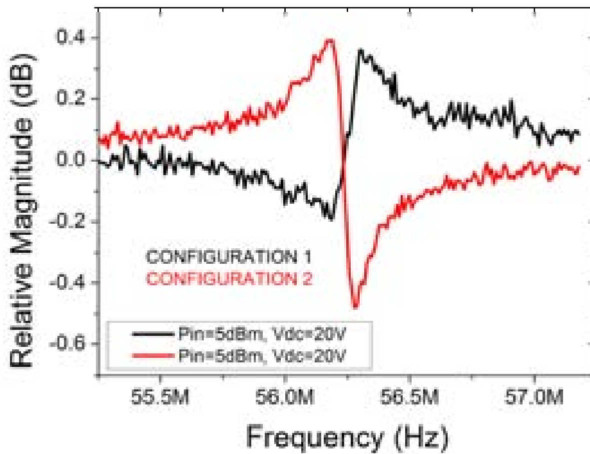

(a)

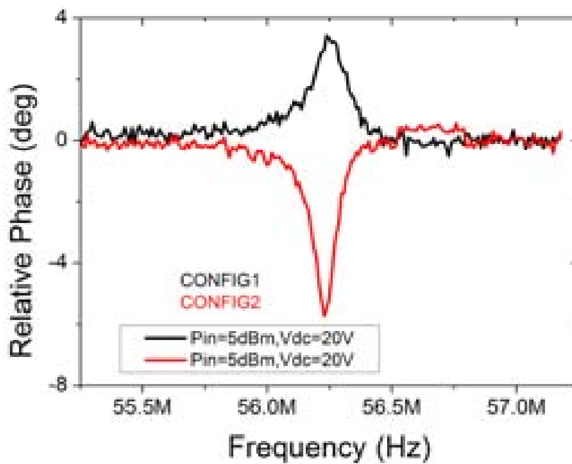

(b)

Figure 4.31: Relative frequency characteristics for both electrode configurations of the 3rd-mode free-free beam resonator. (a) Magnitude and (b) Phase.

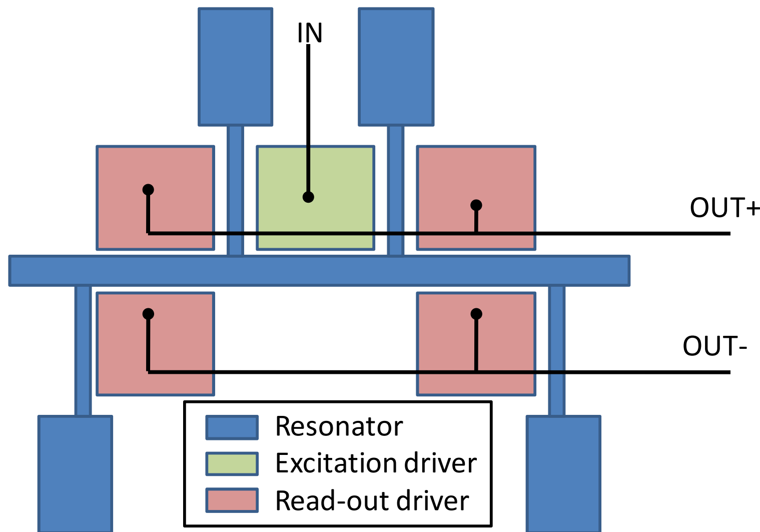

Figure 4.32: Third lateral mode free-free beam connected as a BALUN.

4.3 DOUBLE-ENDED TUNING FORKS

One of the most important properties of this kind of resonators is the presence of two near resonance modes (balanced and unbalanced) to perform filtering (see chapter 2 and 5), the double-ended tuning fork (DETF) offers interesting properties which allows its use for frequency reference applications. The first one is due to the intrinsic nature of the tuning fork topology: it allows increasing the distance between the excitation and readout electrodes (and therefore reducing C_p) without affecting the coupling (gap distance) between the electrodes and the resonant structure, as it happened with previously presented resonators. There is, however, a constrain in the maximum distance that can be reached; FEM simulation on a DETF for different distance between the two tines demonstrates that as the distance between the two tines increases, the two lateral resonance modes frequencies become closer (see also *Annex 1*) [14]. Although this can be useful for other applications like filtering it is not a desired effect for frequency references in which the sharpest frequency response is an important requirement. Fortunately, there are several techniques which can be applied to increase the frequency distance between the balanced and unbalanced resonance modes. The second advantage is obtained by using the second lateral resonance mode (balanced mode). By doing so, the two resonator beams (tines) move out of phase and cancels the moment of inertia at supports, for this reason no movement is transmitted through the anchors, reducing the losses and increasing Q. In fact tuning forks has been widely used as shape of piezoelectric resonators to be used as frequency references. *Table 4.4* shows the summary of the designed double-ended forks for frequency reference applications reported in this section.

Table 4.4: Summary of the designed DETF resonators and designed dimensions

Resonance frequency	W_r (μm)	L_r (μm)	d (μm)	W_{da} (μm)	L_s (μm)	s (nm)	Comments
40MHz	0.5	9	1	0.5	0.5	100	Two beams coupled
24MHz	0.5	12.8	1	1.5	5.3	100	

4.3.1 DETF D1U COUPLED

The primary objective of the design of this resonator is to demonstrate the reduction of the C_p by increasing to the maximum the excitation and readout electrode distance. For doing so, a DETF resonator with distance between tines of 2µm (d=1µm) was designed and fabricated to further separate the excitation and read-out drivers. Unfortunately, by separating the tines, the balanced and unbalanced resonance modes become very close, for this reason the balanced resonance mode was cancelled by adding a coupling bar between the two tines. Resonator was designed with an electrode to resonator gap of 100nm.

Figure 4.33 shows the FEM Coventor simulation of the designed resonator, obtaining a resonance frequency close to 40MHz. *Figure 4.34* shows the SEM image of the released resonator.

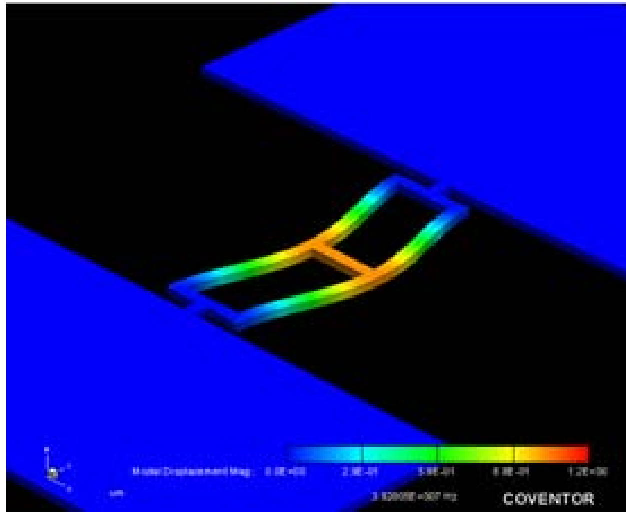

Figure 4.33: FEM Coventor simulation of the designed DETF coupled resonator. Resonance frequency is of 39.28MHz.

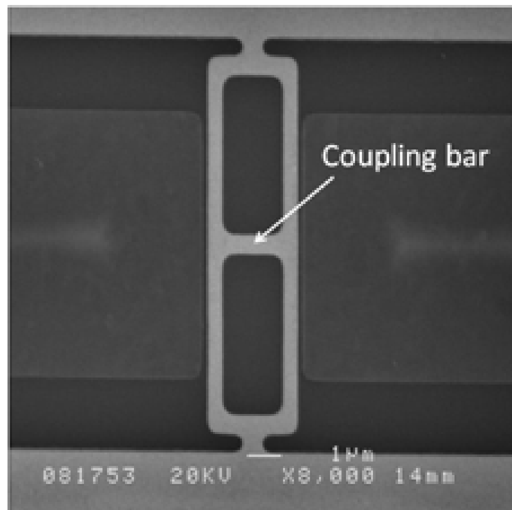

Figure 4.34: SEM image of the 100nm gap DETF with 2µm distance between tines and a coupling bar to eliminate the balanced resonance mode.

Figure 4.35 shows the magnitude and phase frequency response of the MEMS resonator measured with a network analyzer.

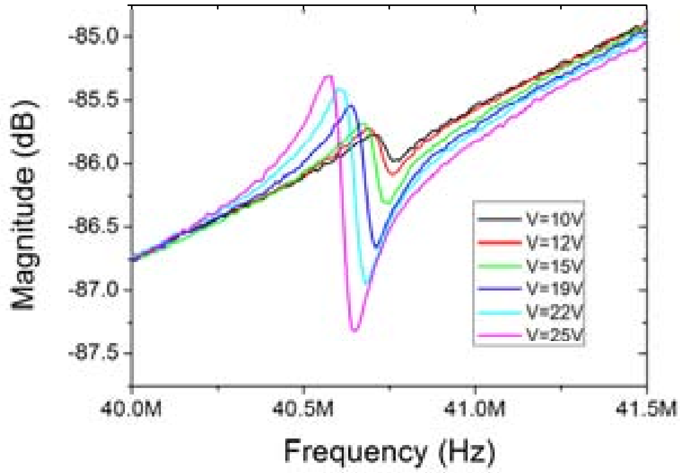

(a)

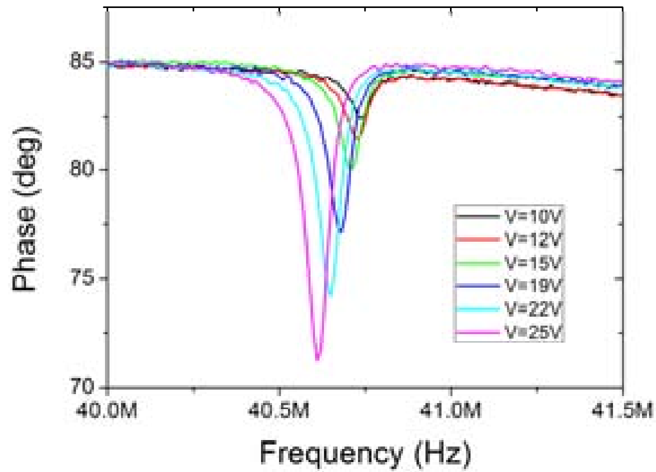

(b)

Figure 4.35: Magnitude (a) and phase (b) S21 measurement of the fabricated coupled 100nm gap DETF, *Pi* =0dBm

The low magnitude peak does not allow us to calculate the quality factor of the resonator, therefore to obtain an approximate value the Q is evaluated using the phase, which is found to be Q=49. The natural resonance frequency can be found by fitting the f_{res}vs.V_{DC}^2 plot (*Figure 4.36*)

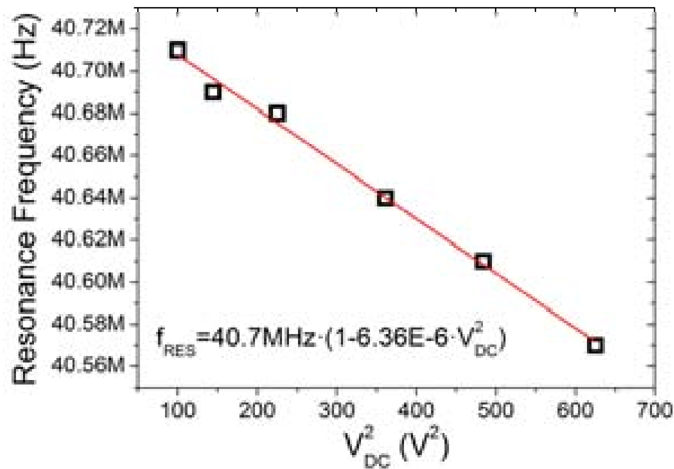

Figure 4.36: Frequency tuning of the 100nm gap DETF *d*=1um coupled resonator

The experimental natural resonance frequency is found at 40.7MHz, whereas the Coventor FEM simulation is of 39.28MHz, a variation of the 3%.

4.3.2 24MHz DETF

This resonator has been designed to present the 24MHz resonance in the second lateral mode (balanced vibration). This resonance mode is selected to increase the *Q* of the resonator. *Figure 4.37* shows the Cadence layout of this resonator.

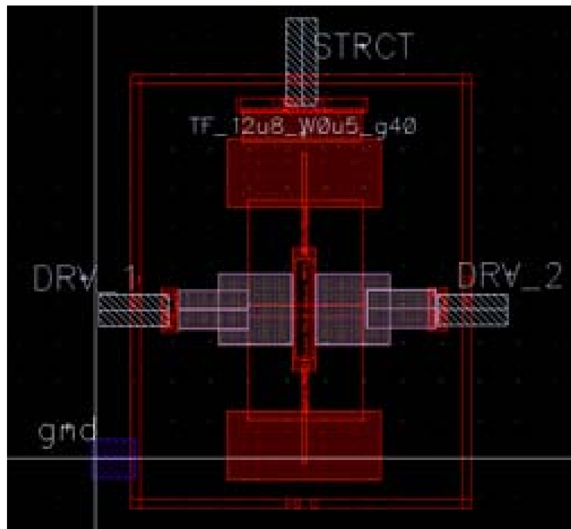

Figure 4.37: Cadence layout of the DETF resonator with l/4 supports

Moreover, to further reduce the losses to the anchors, support beams were dimensioned to have length equal to the acoustic quarter-wavelenght at resonance frequency [12]. By properly

dimensioning the support beams, the acoustic waves that are responsible of anchor losses see infinite impedance in the anchors, and therefore no energy is transmitted through the support-anchor joints. Another function of the beams is to separate the oscillation modes because the beams mass only contributes to movement (decreasing the frequency) for the unbalanced resonance mode [15], as it can be observed in the Coventor simulations (*Figure 4.38*).

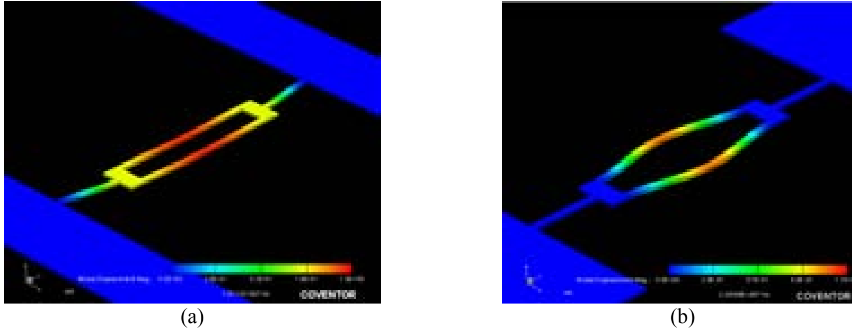

(a) (b)

Figure 4.38: FEM Coventor simulation of DETF resonator: (a) Unbalanced mode with resonance frequency at 10MHz and (b) Balanced mode with frequency at 24MHz.

Figure 4.39 shows the SEM images of the λ/4 support beam resonator once released. The driver length is of 9μm.

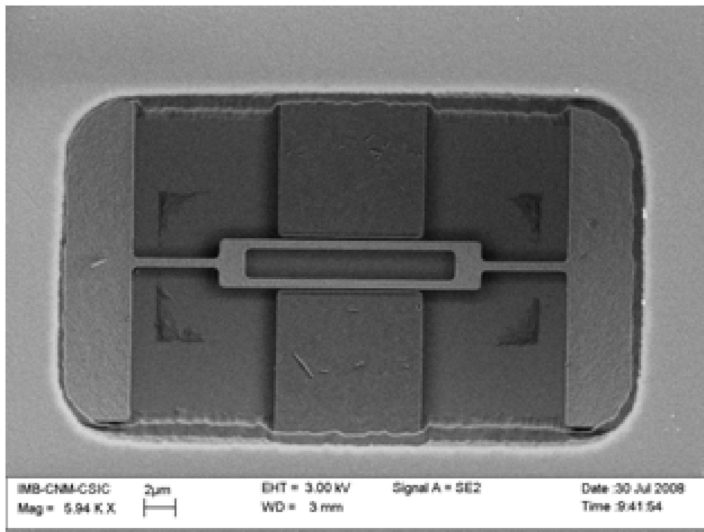

Figure 4.39: SEM image of the 24MHz λ/4 DETF with 100nm gap.

This device was integrated with an on-chip amplifier dor ease of testing. S21 measurements of this resonator are shown in *Figure 4.40*.

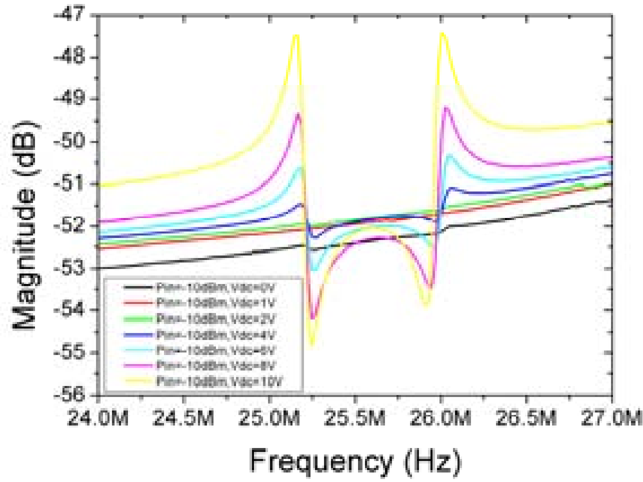

(a)

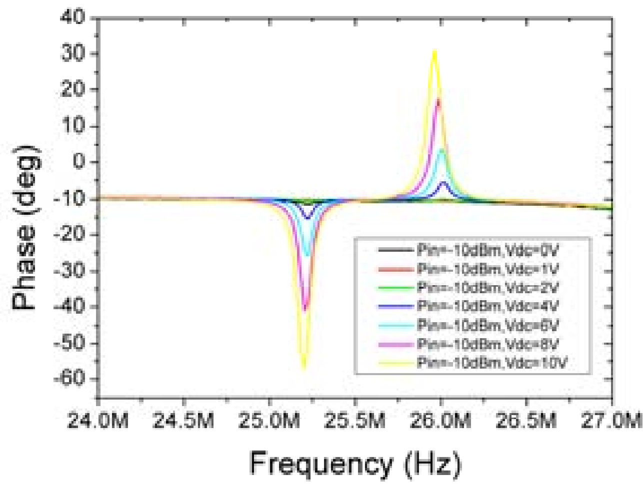

(b)

Figure 4.40: S21 measurements, magnitude (a) and phase (b) for a 24MHz 100nm gap DETF with Ls=1µm support length and on-chip amplification.

In these measurements the unbalanced (near 25MHz) and the balanced (near 26MHz) resonance modes can be observed. Whereas the unbalanced mode shows negative phase shifts (like the previously measured CC-beams), the balanced frequency mode phase shift is positive, following the behavior observed in the third-order free-free beam.The measured Q of the two modes at V_{DC}=10V are 115 and 93 for the unbalanced and balanced resonance modes respectively, these Q values are lower than the obtained for CC-beams. The frequency difference between the resonance modes is less than 1MHz instead of the nearly 14MHz difference obtained by Coventor simulations. This frequency difference is quite similar to the one that could be obtained by a resonator with distance between tines equal to 2µm (like the measured resonator) but with

negligible anchor length. Therefore it is believed that this resonator has not been completely released, and some oxide underneath the decoupling area is anchoring the structure to the substrate. This hipothesis was later corroborated by the measurements of an identical resonator but with an additional etching time of 2 minutes, where no resonance peak is observed near the balanced mode response (*Figure 4.41*).

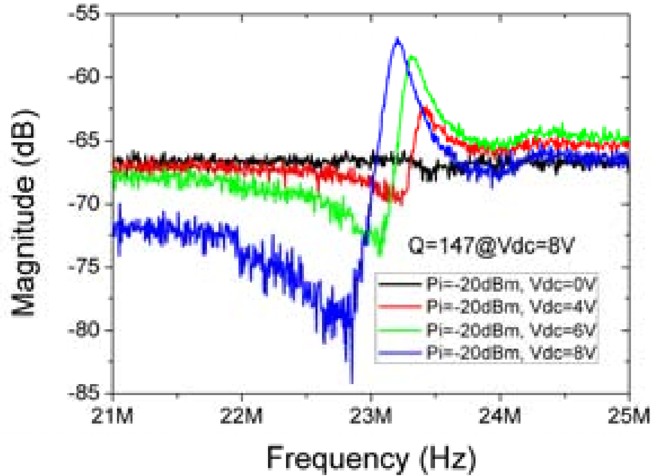

Figure 4.41: Magnitude measurement of a 100nm gap DETF with additional etching time, showing only the balanced resonance mode as expected.

The natural resonance frequency of this completely released resonator is near 23.8MHz, a 2% lower than the predicted by FEM simulations. A Q=147 is measured at V_{DC}=8V, a value higher than the obtained with the previous DETF resonator, and slightly higher than the obtained with the CC-beam resonator + amplifier with the same gap (s=100nm), at V_{DC}= 8V, which is of 111. Even though apparently this Q does not offer a very big difference it is worth to notice that has been obtained with a resonator whose resonant mode (considering not only lateral modes) is the 9th, whereas the resonance mode for the clamped-clamped beams is the 2nd. *Figure 4.42* shows the complete mechanical simulations of the 10 first resonance modes of the DETF resonator. As it can be observed, the long and narrow support beams introduce several undesired torsional modes. These support beams were designed to present $\lambda/4$ flexural dimensions at 24MHz, and therefore the support width was then constrained to allow a reasonable length beam according to the $\lambda/4$ specification (to prevent collapse of the structure) and reduce contact surface to the anchors.

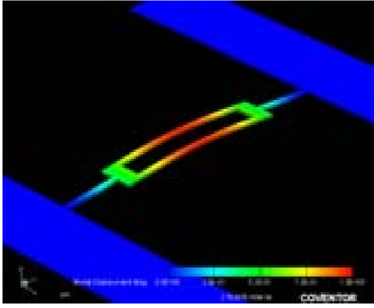

(a) f_{RES}=2.76MHz

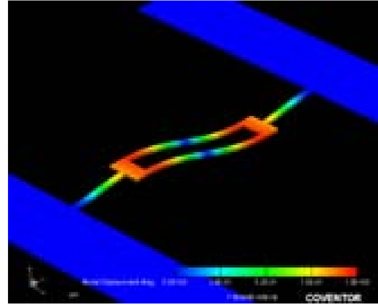

(b) f_{RES}=7.56MHz

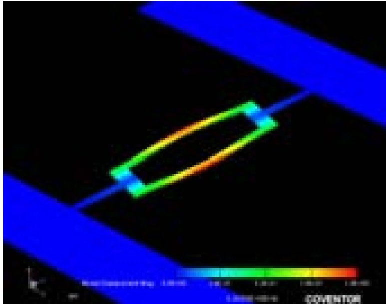

(c) f_{RES}=8.24MHz

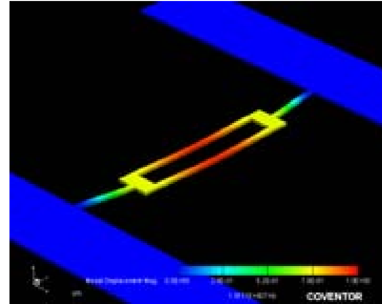

(d) f_{RES}=10.11MHz

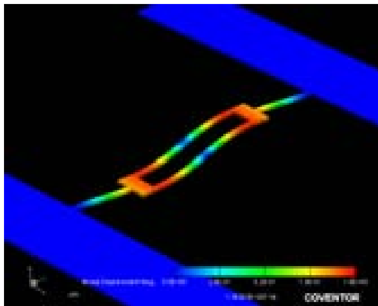

(e) f_{RES}=13.62MHz

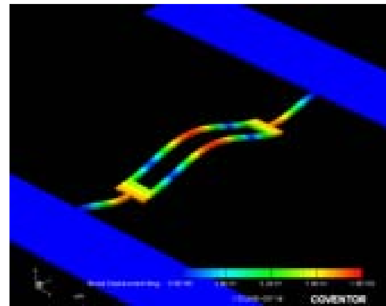

(f) f_{RES}=15.32MHz

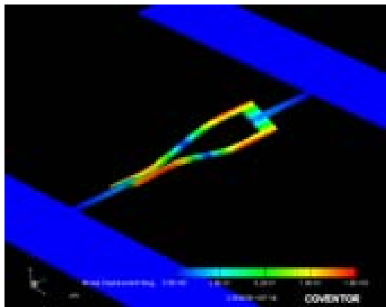

(g) f_{RES}=20.05MHz

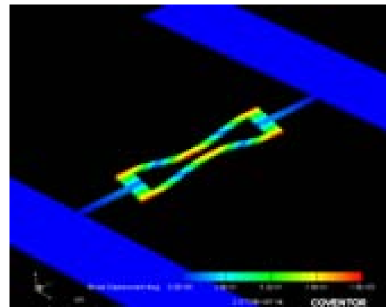

(h) f_{RES}=22.77MHz

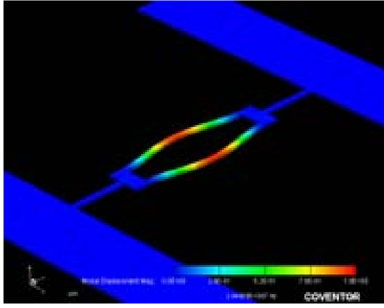

(i) f_{RES}=24.48MHz

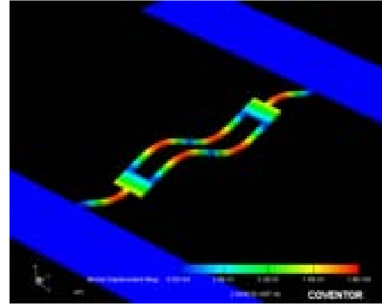

(j) f_{RES}=28.4MHz

Figure 4.42: Ten first resonance modes of the DETF resonator designed. First (unbalanced) and second (balanced) lateral resonance modes are shown on (d) and (j), respectively.

Figure 4.43 shows the f_{RES} vs. V_{DC}^2 relationship, the frequency tuning of the DETF is of 378ppm/V^2 and the natural resonance frequency is found at 23.64MHz..

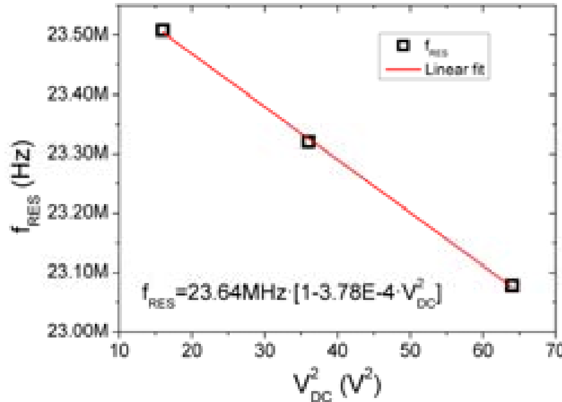

Figure 4.43: Resonance frequency vs. V_{DC}^2 for the 24MHz double-ended tuning fork with λ/4 support beams.

4.4 CONCLUSIONS

Once the different resonators fabricated have been presented and measured, this section will compare the obtained results to determine the optimum flexural resonator topology to implement frequency references for oscillators.

Table 4.5 shows some of the comparison parameters: natural resonance frequency (f_0) (measured and FEM simulated), frequency tuning (FT), resonance frequency at applied DC voltage, resonator measured quality factor (Q) and motional resistance (R_m). Theoretical values of some of these characteristics are also provided, together with the pull-in voltage. The equations used can be found in *Chapter 2* and are: pull-in voltage ($V_{pi}^{two\text{-}port}$) (2.30), motional resistance (2.39) and frequency tuning (2.44). Note that for all these expressions the mechanical elastic constant is needed. The value of this mechanic elastic constant is found using the already performed FEM simulations and using the formula (2.17), given that Coventor provides the frequency and the effective mass for each resonance mode. The effective elastic constant is calculated using the general expression for two-port devices *(4.1)*. The values of the other parameters used to calculate the motional resistance (Q and V_{DC}) are the ones shown in the table.

Several discrepancies can be observed between the analytic performances (pull-in voltage, motional resistance and frequency tuning) and the obtained by measurements. The case of the pull-in voltage is especially remarkable for the 24MHz CC-beam with s=40nm. The applied voltage was 10V for the *Q* measurement (higher than the analytic value of 7.5V) and the beam was not damaged by collapsing to the driver, even though the resonator displacement was apparently limited. However, it is worth to mention that in the development of the pull-in expression the bending of the structure was not considered, and therefore the analytic pull-in voltage is the worst case and it is over dimensioned, because it considers that the entire beam is displaced by the same amount. The analytic frequency tuning also shows an overestimation when compared to the measurements, except for the DETF, for which the experimental frequency tuning is bigger than the calculated. Again I believe that the main cause of this variation is due to the fact of considering uniform distance between the beam and the resonator when calculating the electrical elastic constant. The uniform bending profile considered also causes an underestimation of the calculated motional resistance shown in *Table 4.5*.

Table 4.5: Resonator for frequency reference performance summary

	f_0 (MHz)		FT (ppm/V^2)		f_{RES}@ V_{DC} (MHz)	V_{DC} (V)	V_{pi}	Quality factor		R_m (MΩ)		
Name	*FEM sim.*	*Meas.*	*An. (2.44)*	*Meas.*			*An.*	Q_{3dB}	Q_{phase}	*An. (2.39)*	*Formula (A2.3)*	*ADS fit*
CC- Beams												
24MHz, s=40nm	24.6	27.37	9010		24.4	10	7.45	80	79	0.163	0.85	
24MHz, s=100nm	24.6	26.75	576		26.3	17	29.45	108	104.7	1.66	3.1043	8.74
(mixing)					26.1	25		260				
24MHz, s=100nm+ amplifier	24.6	27.6	576	71.8	27.3	12	29.45	200		1.66	2.3	
(mixing)					27.37	12		230				
48MHz, s=40nm	47.95	50.9	2610	517	50	6	54.7	NM	136	0.61		
FF-Beam												
24MHz, s=40nm	23.98	25.4	2993	113	24.99	12	13	197	190	0.181	2.3065	4.77
(mixing)					24.71	12		334				
DETF												
d=1um + amplifier	24.35	23.64	306	378	23.8	8	44.6	147	NM	10.4		

The best *Q* factor measured in air for the presented resonators is obtained for the free-free beam (194 for S21 measurements) this value is twice the one measured with CC-beams. Note that integrated amplification doubles the *Q* measured as it can be observed comparing the values of the quality factor for the 24MHz s=100nm CC-beam with and without amplification. The frequency tuning capability of the free-free beam with *s*=40nm is only slightly higher than the measured in the *s*=100nm CC-beam, even though the important effect of gap reduction in this characteristic. However, this is a double-edged sword: on one hand, the limited tunability reduces the compensation range on the resonance frequency, but on the other hand it improves the robustness

of the free-free device against DC voltage drifts. Moreover, the variation between the designed and obtained natural frequency of the free-free beam is only of the 6%, whereas for the CC-beam this difference is above the 10%, consequently, compensations on the free-free beam can be more easily implemented on the design stage. As long as the frequency process variations allow to obtain a very similar frequency to the designed, *FT* has to be minimized to reduce frequency variations with DC voltage drifts, therefore FF-beams show promising results for a well-controlled fabrication process. Unfortunately, this structure reduces the effective coupling (due to the supports) and therefore the motional resistance of this resonator is higher than the obtained with the clamped-clamped beams. Moreover, this structure is larger and more prone to sticking to the substrate in the releasing process. The DETF resonator results show lower *Q* than the FF-beam, but with on chip amplification. Considering the x2 factor improvement of the quality factor due to the amplifier, the measured *Q* without amplification would be below the one of the CC-beam. Moreover, the lower length electrode length and the higher stiffness of this resonator gives a high analytic value of the motional resistance.

Table 4.6 compares the performance of the free-free resonator and cc-beam with the state of the art resonators presented in Chapter 2, for this comparison the R_m used is the motional resistance value obtained from S21 measurements and (A2.3).

From this table it can be observed that the resonance frequency of nearly all resonators, but [16, 17], have higher resonance frequency than the clamped-clamped and free-free beam resonators of this thesis. Very few of the resonators in the table were developed in a CMOS technology, only [17] and previous works from ECAS members [3, 18]. The applied DC voltages are the same range for every resonator (around 10V). The quality factors of the presented resonators 260 and 334, for the CC-beam and the FF-beam, respectively, are lower than the other resonators measured in air [17] [20] [19] [20] [17], but these resonators are not flexural. However the improvement of the quality factor expected for in vacuum measurements (a x20 factor), would result values of 5200 and 6680, and a decrease of the motional resistance to 42kΩ and 115kΩ, for the CC-beam and FF-beam respectively. With these new figures the presented resonators exceeds the *Q* of [16] [3] [18] [20] [24] and the higher frequency resonator of [21]. Moreover, the presented resonators can take advantage of monolithic integration.

Table 4.6: Comparison of presented resonators with state of the art resonators

Resonator	Reference	f_{RES} (MHz)	V_{DC} (V)	Q	R_m (kΩ)	Technology
CC-Beam						
Bannon'00	[16]	8.50	10	50	NR	
Verd'06	[3] A	59.6	80	40	NR	AMS, M4 layer
	This work A	24.4	10	80/260M	850	AMS, Poly1,s=40
FF-Beam						
Wang'00	[12]	30	22	8110	31.1	Vacuum meas.
	This work A	24.9	12	197/334M	2306	AMS, Poly1
W-G Disk						
Abdelmoneum'03	[22] A	73.4	7	8600	26@18V	
Bulk anular ring						
Teva'08	[18] A	1046	10	400	NR	AMS, Poly1
Cont-M Disk						Mixing meas.
Wang'04 c	[21]	152	6	9816	480	
Wang'04	[21]	274	30.5	7500	17.2	Mixing meas.
Wang'04	[21]	1160	10.5	2655	2440	Mixing meas.
Square res array						
Demirci'06	[23] A	63.4	30	1900	5.10	
SOI Disk						
Pourkamali'04	[19] A	149	15	25900	91.2	SOI
Lat. Piezo Ring						
Piazza'05	[20] A	472		2900	0.084	Piezo, AIN
s-g disk res						
Lin'05	[24]	61	8	25300	1.51	solid gap
SiFR						
Lo'07	[17]	8.04	46	3589	NR	CMOS

A Resonator measured at atmospheric pressure
M Obtained from mixing measurements

REFERENCES

[1] "Universal Serial Bus Specification (Revision 2.0)," 2000.

[2] J. Verd, "Monolithic CMOS-MEMS Resonant Beams for Ultrasensitive Mass Detection." vol. Ph.D Bellaterra: Universitat Autònoma de Barcelona, 2008.

[3] J. Verd, A. Uranga, J. Teva, J. L. Lopez, F. Torres, J. Esteve, G. Abadal, F. Perez-Murano, and N. Barniol, "Integrated CMOS-MEMS with on-chip readout electronics for high-frequency applications," *Electron Device Letters, IEEE,* vol. 27, pp. 495-497, 2006.

[4] L. C. Shao, M. Palaniapan, W. W. Tan, and L. Khine, "Nonlinearity in micromechanical free-free beam resonators: modeling and experimental verification," *Journal of Micromechanics and Microengineering,* p. 025017, 2008.

[5] J. L. Lopez, J. Teva, A. Uranga, F. Torres, J. Verd, G. Abadal, N. Barniol, J. Esteve, and F. Perez-Murano, "Mixing in a 220MHz CMOS-MEMS," in *Circuits and Systems, 2007. ISCAS 2007. IEEE International Symposium on*, 2007, pp. 2630-2633.

[6] A.-C. Wong and C. T. C. Nguyen, "Micromechanical mixer-filters ("mixlers")," *Microelectromechanical Systems, Journal of,* vol. 13, pp. 100-112, 2004.

[7] Agilent, "Improving Network Analyzer Measurements of Frequency-translating Devices (Application Note 1287-7)," 2000.

[8] J. Wang, X. Yuan, and C. T. C. Nguyen, "Frequency tolerance of RF micromechanical disk resonators in polysilicon and nanocrystalline diamond structural materials," in

Electron Devices Meeting, 2005. IEDM Technical Digest. IEEE International, 2005, p. 4 pp.

[9] J. L. Lopez, J. Verd, J. Teva, G. Murillo, J. Giner, F. Torres, A. Uranga, G. Abadal, and N. Barniol, "Integration of RF-MEMS resonators on submicrometric commercial CMOS technologies," *Journal of Micromechanics and Microengineering,* vol. 19, p. 015002, 2009.

[10] J. Teva, "Integration of CMOS-MEMS resonators for radiofrequency applications in the VHF and UHF bands." vol. Ph.D Bellaterra: Universitat Autònoma de Barcelona, 2007.

[11] W. T. Hsu, J. R. Clark, and C. T. C. Nguyen, "Q-Optimized lateral free-free beam micromechanical resonators," in *Transducers '01: Eurosensors Xv, Digest of Technical Papers, Vols 1 and 2*, Berlin, 2001, pp. 1110-1113.

[12] K. Wang, A.-C. Wong, and C. T. C. Nguyen, "VHF free-free beam high-Q micromechanical resonators," *Microelectromechanical Systems, Journal of,* vol. 9, pp. 347-360, 2000.

[13] M. U. Demirci and C. T. C. Nguyen, "Higher-mode free-free beam micromechanical resonators," in *Frequency control symposium and pda exhibition jointly with the 17th european frequency and time forum, 2003. proceedings of the 2003 ieee international*, 2003, pp. 810-818.

[14] J. L. Lopez, F. Torres, G. Murillo, J. Giner, J. Teva, J. Verd, A. Uranga, G. Abadal, and N. Barniol, "Double-ended tuning fork resonator in 0.35um CMOS technology for RF applications," in *Research in Microelectronics and Electronics, 2008. PRIME 2008. Ph.D.*, 2008, pp. 89-92.

[15] S. P. Beeby, G. Ensell, and N. M. White, "Microengineered silicon double-ended tuning fork resonators," *Engineering Science and Education Journal,* vol. 9, pp. 265-271, 2000.

[16] F. D. Bannon, J. R. Clark, and C. T. C. Nguyen, "High-Q HF microelectromechanical filters," *Solid-State Circuits, IEEE Journal of,* vol. 35, pp. 512-526, 2000.

[17] C. C. Lo and G. K. Fedder, "On-Chip High Quality Factor CMOS-MEMS Silicon-Fin Resonators," in *Solid-State Sensors, Actuators and Microsystems Conference, 2007. TRANSDUCERS 2007. International*, 2007, pp. 2449-2452.

[18] J. Teva, G. Abadal, A. Uranga, J. Verd, F. Torres, J. L. Lopez, J. Esteve, F. Perez-Murano, and N. Barniol, "From VHF to UHF CMOS-MEMS monolithically integrated resonators," in *Micro Electro Mechanical Systems, 2008. MEMS 2008. IEEE 21st International Conference on*, 2008, pp. 82-85.

[19] S. Pourkamali, H. Zhili, and F. Ayazi, "VHF single crystal silicon capacitive elliptic bulk-mode disk resonators-part II: implementation and characterization," *Microelectromechanical Systems, Journal of,* vol. 13, pp. 1054-1062, 2004.

[20] G. Piazza, P. J. Stephanou, J. M. Porter, M. B. J. Wijesundara, and A. P. Pisano, "Low motional resistance ring-shaped contour-mode aluminum nitride piezoelectric micromechanical resonators for UHF applications," in *Micro Electro Mechanical Systems, 2005. MEMS 2005. 18th IEEE International Conference on*, 2005, pp. 20-23.

[21] J. Wang, Z. Ren, and C. T. C. Nguyen, "1.156-GHz self-aligned vibrating micromechanical disk resonator," *Ultrasonics, Ferroelectrics and Frequency Control, IEEE Transactions on,* vol. 51, pp. 1607-1628, 2004.

[22] M. A. Abdelmoneum, M. U. Demirci, and C. T. C. Nguyen, "Stemless wine-glass-mode disk micromechanical resonators," in *Micro Electro Mechanical Systems, 2003. MEMS-03 Kyoto. IEEE The Sixteenth Annual International Conference on*, 2003, pp. 698-701.

[23] M. U. Demirci and C. T. C. Nguyen, "Mechanically Corner-Coupled Square Microresonator Array for Reduced Series Motional Resistance," *Microelectromechanical Systems, Journal of,* vol. 15, pp. 1419-1436, 2006.

[24] Y.-W. Lin, S.-S. Li, Y. Xie, Z. Ren, and C. T. C. Nguyen, "Vibrating micromechanical resonators with solid dielectric capacitive transducer gaps," in *Frequency Control Symposium and Exposition, 2005. Proceedings of the 2005 IEEE International*, 2005, pp. 128-134.

5 FILTERING, MIXING AND OSCILLATOR APPLICATIONS

The results of MEMS resonators/systems in filter, mixing and oscillator applications are presented in this chapter. The filters shown in this chapter include a parallel filter composed by two high-Q clamped-clamped beams whose output is combined with a differential amplifier, a prototype of a single resonator filter-mixer and a single resonator filter, being these two last resonators double-ended tuning forks. The performance of oscillators based on clamped-clamped beam and tuning fork resonator are compared.

5.1 PARALLEL FILTER

As stated in *Chapter 2*, the filters implemented by this technique are based on two identical MEMS resonators with slightly different resonance frequency. This difference can be set in first instance by process mismatch and can be tuned by the DC applied voltages to the resonators. Therefore, the DC biasing for each resonator must be set by different signal paths.

The proposed architecture is composed by two identical MEMS resonators whose outputs are connected an on-chip CMOS differential amplifier. *Figure 5.1(a)* shows a diagram of the MEMS+ amplifier in which the frequency spectrum at each point of the system is shown. The resonators can be biased by different DC voltage values (V_{DC1} and V_{DC2}) to control independently the resonance frequency of each resonator. This on-chip differential amplifier performs two main functions: it combines the output currents of the resonators and provides gain, therefore reducing the losses due to impedance mismatch during measurements. Thanks to this differential amplification, the parasitic feedthrough current can be eliminated because it is a common-mode signal, allowing the measurement of each resonator by its own (setting the DC voltage of the other resonator to zero), cancelling the parasitic capacitor effect, as it is shown in the $RLC//C_p$ equivalent model electrical simulation of *Figure 5.1(b)*. Parasitic capacitor cancellation allows obtaining not only a larger phase shift but also a higher magnitude peak shift, facilitating the calculus of Q with the 3dB peak formula. It can also be observed how C_p raises the signal level, affecting the R_m calculus using the (A2.3), as it is detailed in *Annex 2*.

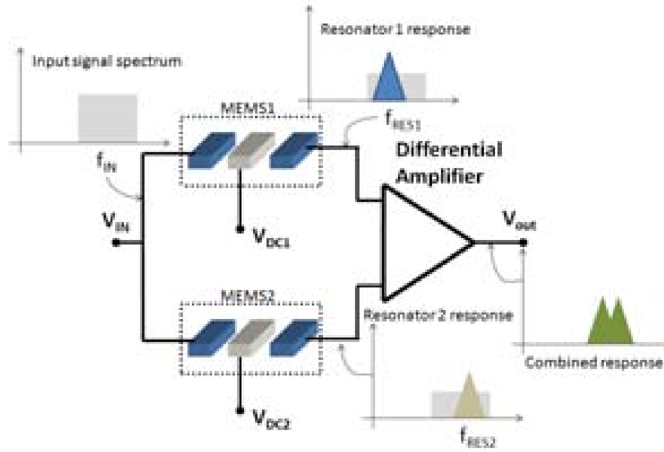

(a)

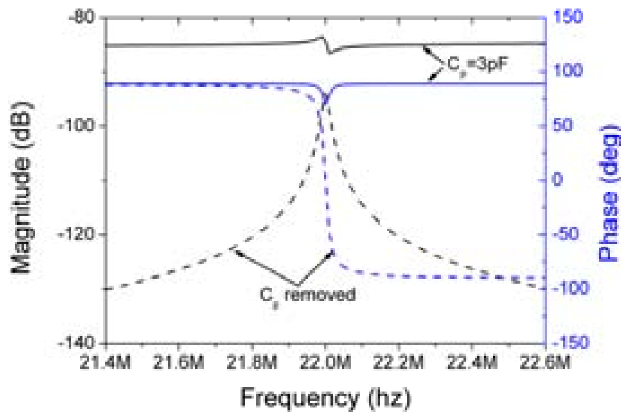

(b)

Figure 5.1: (a) Diagram of the amplification scheme. (b) ADS simulation showing parasitic capacitor cancellation RLC model parameters are: R_m=5MΩ, C_m=1.26aF and f_{RES}=22MHz.

The resonators implemented in this circuit are simple clamped-clamped beams with resonance frequencies around 22MHz. The resonators are fabricated in polysilicon 1 using spacer technique with a gap of 150nm. The dimensions of the resonator are: L=13µm and W=0.35µm and the resonator thickness (set by the technology) is t=280nm.

The on-chip differential amplifier[1] is composed by three stages: the first one is a transimpedance amplifier (one for each resonator output), which performs the initial amplification and the conversion of the resonator output current to the voltages which are the inputs of the second amplification stage, the differential amplifier itself. The single-ended output of this stage is connected to a 50Ω buffer (the third stage). *Figure 5.2* shows the complete system combining SEM images of the resonator (left side), the conceptual schematic (upper- right side) and an

[1] Designed by A. Uranga

optical photograph of the circuit including the auxiliary circuit biasing and the electrical bonding pads.

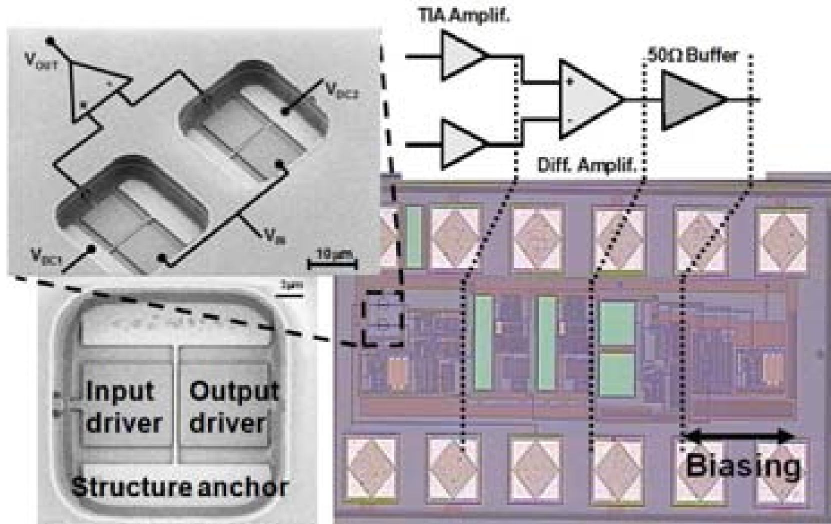

Figure 5.2: Several images of the complete CMOS-MEMS filter. It includes SEM images of the MEMS resonators (grayscale images on the left side), an optical image of the complete system and block diagram of the different stages of the amplifier.

The complete amplifier shows a differential gain of 87dB@20MHz achieved with a Common-Mode Rejection Rate *(CMRR)* of 40dB@20MHz, according to post-layout amplifier simulations.

The complete system was measured on air conditions using IC probes mounted on a manual probe table and a network analyzer. This IC die was later wire-bonded to a PCB and measured on a custom-made vacuum chamber for in-vacuum characterization.

5.1.1 SINGLE RESONATORS MEASUREMENT

In the first test each resonator is measured alone (biasing the other resonator to zero). *Figure 5.3* shows the frequency response of resonator 1 for measurements performed on air (a) and in-vacuum (b), at a low DC (and CMOS compatible) voltage of 5V.

Comparing on air and in-vacuum measurements, an important narrowing of the peak width is observed for measurements in vacuum. This narrowing is directly related to the reduction of the air damping and air squeezing, effects that increase the resonator losses. For the measurements performed at V_{DC1}=5V (and V_{DC2}=0V), the Q measured in air is of Q=227 whereas when measured in vacuum Q=4400. This increase of Q was caused by the use of vacuum to perform measurements and the cancellation of the parasitic feed-though capacitor by the differential amplification scheme.

Motional resistance values for the s=150nm polysilicon CC-beam resonator can be obtained from the previous measurements. For doing so, the amplifier gain is subtracted from the peak measurements, giving peak amplitude values of -117dB (-30.7dB-87dB) and -91.4dB (-4.4dB-87dB) for in air and in vacuum measurements, respectively. Therefore the calculated motional resistances are: R_m(AIR)=35.4MΩ and R_m(VAC)=1.77MΩ.

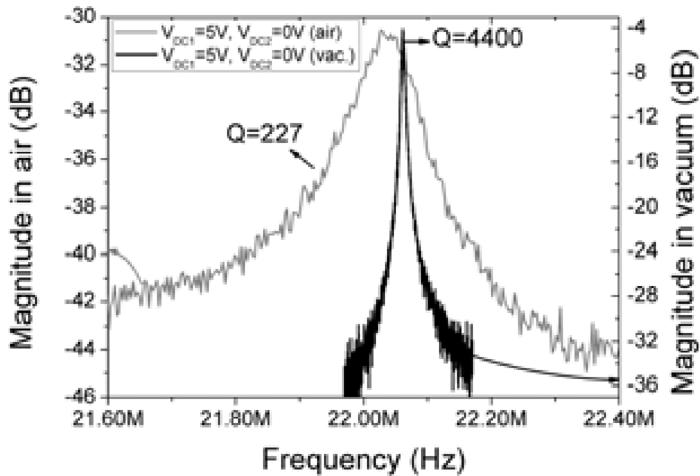

Figure 5.3: Resonator 1 magnitude frequency response at V_{DC1}=5V, V_{DC2}=0V with the differential amplification scheme. Measurements in air and in vacuum are shown.

Figure 5.4(a) shows the f_{RES} vs. V_{DC} measured in air and in-vacuum for the resonator 1. It can be observed that the tendency of the line is the same independently of the pressure conditions, as expected. *Figure 5.4(b)* shows the $f_{RES}(V_{DC})$ relationship for both MEMS resonators measured in air.

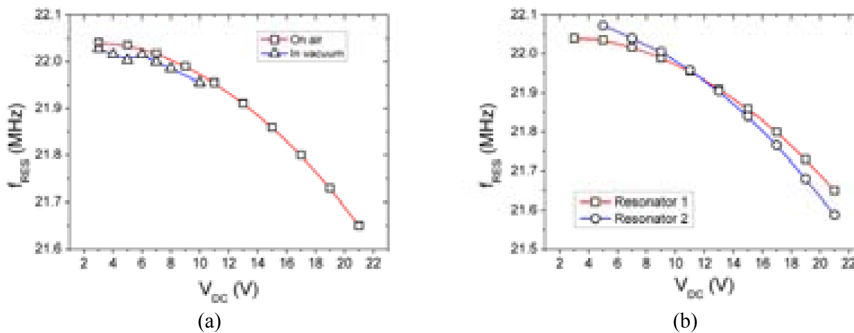

Figure 5.4: f_{RES} vs. V_{DC} relationship. (a) Resonator 1 measured on air and in vacuum mesasurements. (b) Resonator 1 and resonator 2 measurements on air conditions for applied positive DC voltages.

From *Figure 5.4*, we can see that resonance frequency decreases with the applied DC voltage in a quadratic shape, as it was expected from the spring softening of the MEMS resonator electrostatically excited, see equation (2.23), MEMS frequency tuning. The clamped-clamped beam resonators show a frequency variation of 400kHz in a voltage range of 20V, showing a frequency tuning FT=45.2ppm/V^2, lower than the obtained for the resonators presented in *Chapter 4*, due to the greater gap distance s=150nm. The analytic value of this frequency tuning for this resonator is 495ppm/V^2, again higher than the obtained experimentally. It is observed that even though resonators are placed very near, there is a small mismatch between both devices. However, the tuning range of the resonators of *Figure 5.4(b)* is greater than the difference between resonance

frequencies for each resonator, demonstrating that tuning appropriately the DC voltage, any mismatch between identical resonators can be compensated.

The frequency response of a resonator with a negative V_{DC} is also measured and compared to the response of the resonator with a positive V_{DC} of the same value (*Figure 5.5*). These measurements show that the resonator with V_{DC}<0V behaves as if the applied DC was higher (the magnitude is higher and the peak is further moved to lower frequencies, 120kHz). Because of the biasing of the input of the amplification scheme, the resonator with a negative DC voltage "sees" an effective voltage higher than when a positive voltage is applied. Bias point simulation of the circuit shows a DC voltage value of 1.17V on the input of the amplifier, being this voltage also applied to the readout electrode of the resonator, and the reason why measurement differs depending of the sign of the applied voltage.

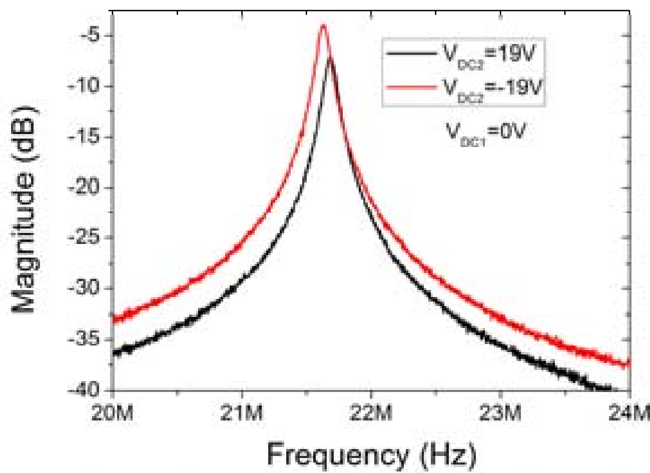

Figure 5.5: Resonator 2 frequency response for positive and negative DC voltage, V_{DC1}=0V

To further characterize the voltage dependence and frequeny matching between resonators, in *Figure 5.6* the frequency and magnitude behavior as a function of the applied V_{DC} is shown. The DC applied voltage is positive for resonator 1, R1, and positive and negative for resonator 2, R2.

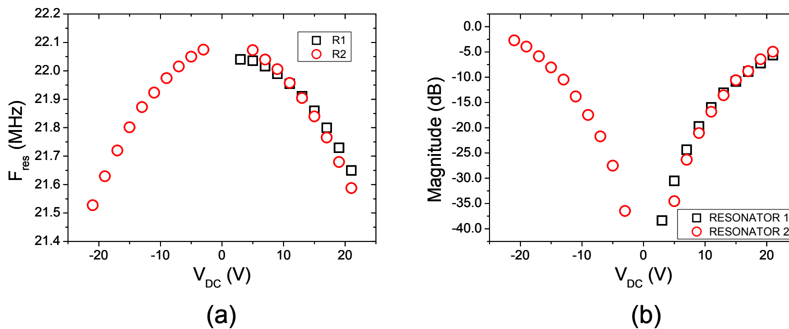

Figure 5.6: Single resonator measurement using the differential amplification scheme. (a) Resonance frequency vs. V_{DC} and (b) Magnitude vs. V_{DC}

Two effects can be observed from these figures: (1) a good matching is obtained between resonators not only in frequency (as it was already shown in *Figure 5.4-b*) but also in magnitude (which will be necessary for filtering purposes) and (2) the magnitude is increased. This later effect can be explained by means of the reduction of the motional resistance with the increase of V_{DC}, see (2.39).

Just to verify the level of reduction of the parasitic current, a mixing measurement is performed. *Figure 5.7* shows the direct S21 measurement with the differential amplification scheme and the mixing measurement also with this circuit. The measured Q is similar in both cases, therefore demonstrating the capability of this scheme to remove the parasitic current.

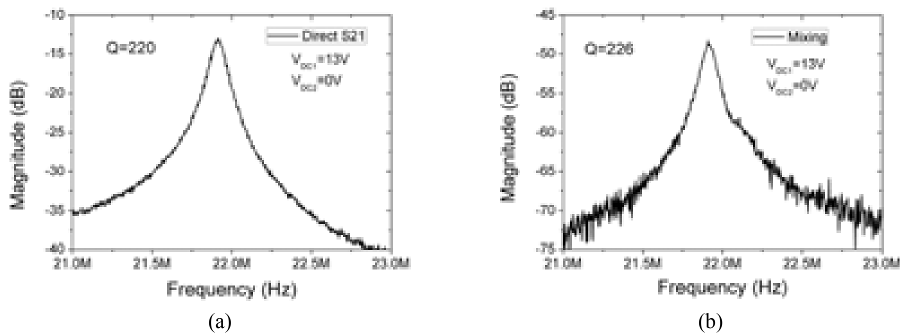

Figure 5.7: Resonator 1 measurement in air conditions. (a) Direct S21 measurement and (b) Mixing measurement for the same applied V_{DC} and P_{LO}=0dBm ,f_{LO}=5MHz and input frequency is swept from 26MHz to 28MHz. Applied input power is 0dBm.

5.1.2 COMBINED RESONATOR RESPONSE: FILTERING

By selecting the appropriate V_{DC1} and V_{DC2}, a filter with a desired bandwidth and centered around resonance frequency of the MEMS can be built. Unfortunately, the ripple limits the filter bandwidth as the resonance frequency and the motional resistance (which determines the magnitude peak) depend on the applied dc voltage. The bandwidth of the filter can be defined by the DC biasing, as it is shown in *Figure 5.6(a)*. Wide bandwidth filters require a high difference between voltages, and this will make the magnitudes of each peak to be different, as shown in *Figure 5.6(b)*, degrading the filter ripple, see *Figure 5.8*. In conclusion, to obtain a low ripple V_{DC1} and V_{DC2} values should be close, and the bandwidth of the obtained filter would be relatively narrow.

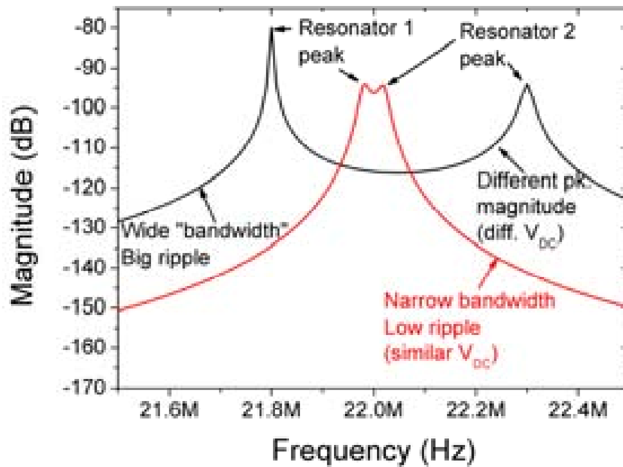

Figure 5.8: ADS simulation showing ripple-bandwidth compromise.

To alleviate the problem of the dependence of the magnitude peak with V_{DC}, an alternative amplification scheme was presented [1]. In this proposed scheme the gain of the TIA stages was made tunable with two external signals. However, even with this more complex amplifier, the maximum bandwidth would be limited by the ripple, unless termination resistors are added to flatten the response [2], as mentioned in *Chapter 2*.

Figure 5.9 shows the first measurements of the effect of biasing both resonators compared to the stand-alone resonator frequency response.

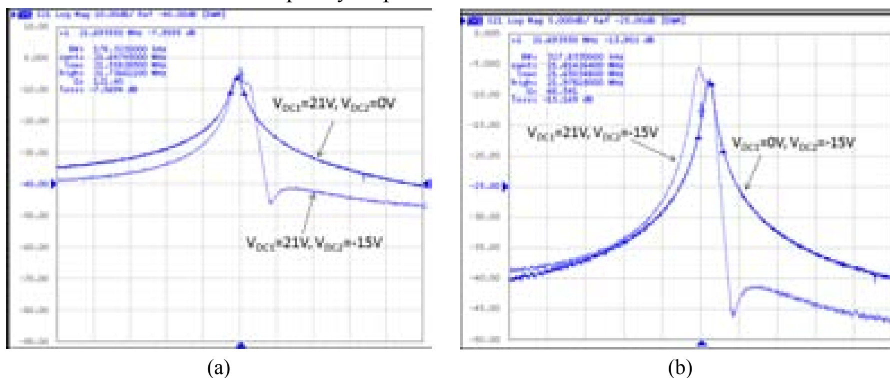

(a) (b)

Figure 5.9: Filter frequency response for V_{DC1}=21V, V_{DC2}=-15V. (a) Shows the stand-alone frequency response for resonator 1 (V_{DC1}=21V, V_{DC2}=0V) and (b) shows the response of resonator 2 (V_{DC1}=0V, V_{DC2}=-15V). The filter response is clearly obtained from the combination of both resonator peaks.

It is shown that by biasing both resonators, in addition to the bandwidth created, the out of band attenuation is also increased and a notch in the frequency response appears. This notch is caused by the removal (thanks to the differential amplifier) of two identical magnitude signals with an equal phase shift, as it is shown in the Cadence simulations, presented in *Figure 5.10*, performed with the differential amplifier and Verilog-A resonator model [3].

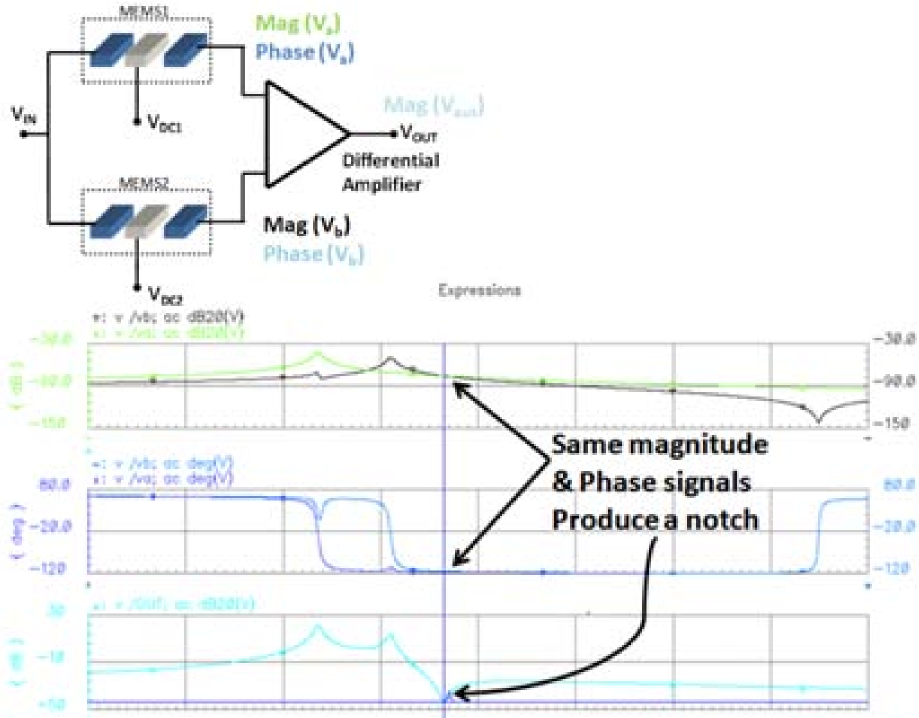

Figure 5.10: Cadence simulation using Verilog-A Clamped-Clamped beams models used to show the origin of the notch in magnitude frequency response.

Figure 5.11 shows the S21 magnitude measurements for different applied V_{DC1} and V_{DC2} values, which demonstrates the reconfigurability of the system. It can be observed that the filter measured shows a bandwidth between 100kHz and 200kHz, an insertion loss lower than 5dB, and a ripple lower than 1dB, for all the bandwidths and on air measurements.

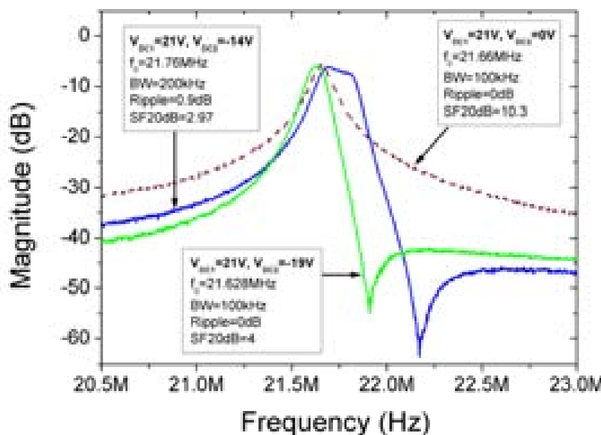

Figure 5.11: Several filters obtained with parallel filtering for different V_{DC2} voltages are performed with fixed V_{DC1}=21V and P_i=0dBm.

When magnitude S21 measurements are performed in vacuum, the combined filter bandwidth has to be much smaller to minimize the ripple, this effect is shown in *Figure 5.12*, which compares in-air and an in-vacuum measurement of the parallel filter.

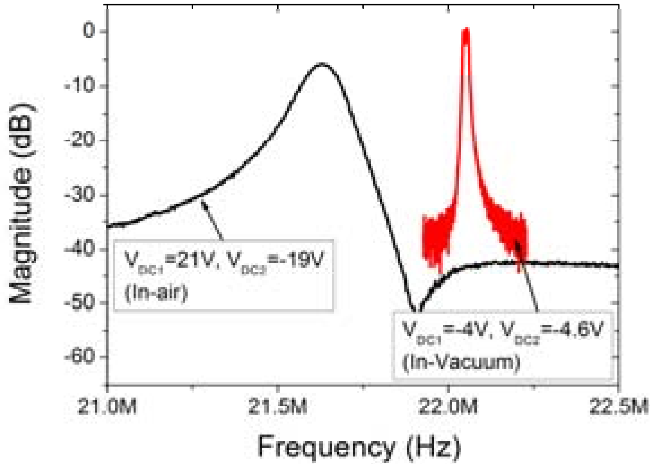

Figure 5.12: Comparison of the in-air and in-vacuum measurement of the parallel filter.

Moreover it becomes more difficult to obtain a flat bandwidth due to the increase of *Q* of the resonators. On the good side, the use of vacuum allows to reduce the DC voltages to a CMOS compatible level. *Figure 5.13* shows S21 magnitude measurements in vacuum under different applied DC voltages.

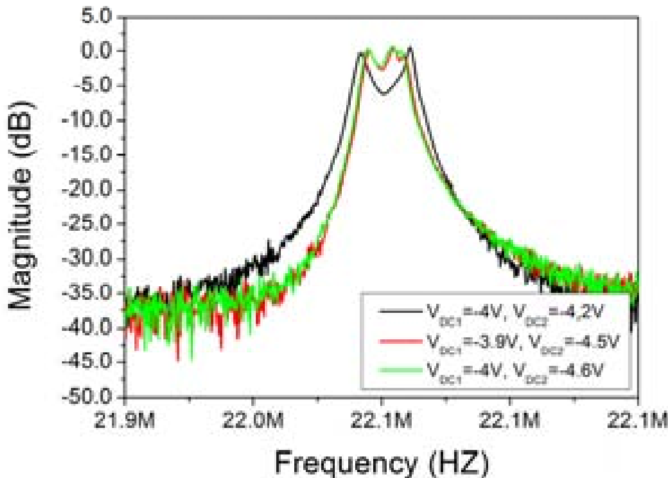

Figure 5.13: S21 Magnitude responses of the CMOS-MEMS parallel filter with different DC voltages in vacuum conditions.

Although in the figure is not evident, there is an important reduction in the obtained bandwidths of the filters when operated in vacuum. From *Figure 5.13*, a bandwidth around 20kHz

is obtained, which is at least 10 times less the bandwidth measured in atmospheric pressure. It is also worth to mention three important aspects: (1) the required DC voltage is now smaller than 5V, (2) a conversion gain is reached (although less than1dB) and (3) stop-band rejection and shape factor are improved when compared to on-air measurements, as it can be observed in *Table 5.1*. In this table a summary of filter properties for all measured filters (in air and in vacuum) is provided. Note that in this table the in-vacuum measured filters show a negative insertion loss, that is, the filter provides gain.

Table 5.1: CMOS-MEMS monolithic parallel filter performance

Reference	f_0 (MHz)	BW_{3dB} (kHz)	***IL*** dB	***Ripple*** (dB)	V_{DC} (V)	SF_{20dB} BW_{20dB}/BW_{3dB}	***SB Rejection*** (dB)
On air							
Res. alone	21.66	100	5.8	0	21/0	10.3	24
Filter 1	21.62	100	5.8	0	21/-19	4	34
Filter 2	21.73	160	6	0	21/-15	3.29	33
Filter 3	21.76	200	6	0.9	21/-14	2.97	31
In vacuum							
Res. alone	22.06	5.01	-4.13	0	5/0	8.78	28.63
Filter 1	22.05	23.4	-0.5	6.6	-4/-4.2	2.14	36
Filter 2	22.05	17	-0.26	2.8	-3.9/-4.5	2.47	35
Filter 3	22.05	17	-0.66	2.8	-4/-4.6	2.42	36

Linearity of the filter measurements was also performed to evaluate the performance of the system, for these measurements, a wide bandwidth filter (on air) was chosen. Fundamental and third order frequency component was measured. The third-order component was measured using a network analyzer with frequency offset option. *Figure 5.14* shows the results of these measurements in terms of applied input power P_{in}. The complete system shows an *IIP3*=0dBm.

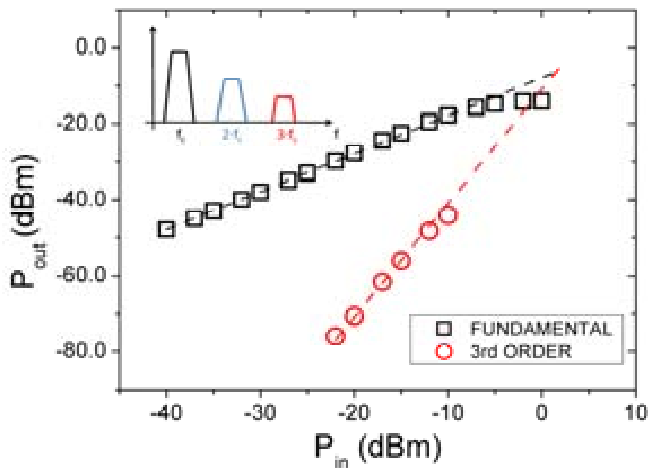

Figure 5.14. IIP3 measurement of the complete filter measured in air and with V_{DC1}=21V and V_{DC2}=-14V

5.2 SINGLE RESONATOR FILTER

A Double-ended Tuning fork (DETF) with high distance between tines was also fabricated to demonstrate the mechanical coupling of the two resonance modes. The convenient election of resonance frequencies for the in-phase (large frequency) and out-of-phase (small frequency) lateral resonant modes and the possibility to use two-port readout, provides a direct band-pass filter response. *Figure 5.15* shows the SEM image of the DETF resonator with distance between tines equal to 2μm and *s*=100nm.

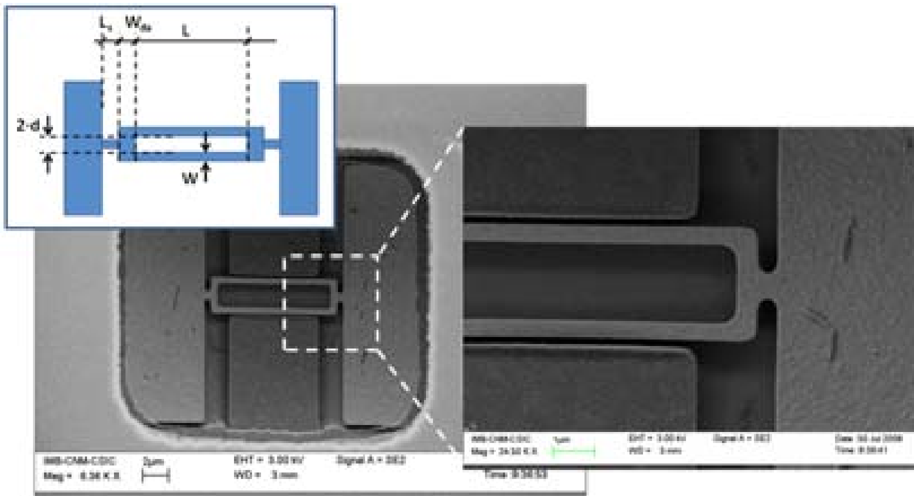

Figure 5.15: SEM image of the DETF with *d*=1μm. Inset shows the detailed dimensions on the text.

The SEM image allows us to measure the physical dimensions of the resonator, which are: L=8.7μm, W=0.47μm, W_{da}=0.4μm, L_s=0.4μm and W_s=0.7μm. Coventor FEM simulations gives a resonance frequency of 44.14MHz for the tine movement symmetric (out-of phase) mode and 44.1MHz for the antisymetric one (in-phase) (*Figure 5.16*). For this resonator then, the balanced mode is found before the symmetric mode, the opposite case than was shown in previous DETF resonators.

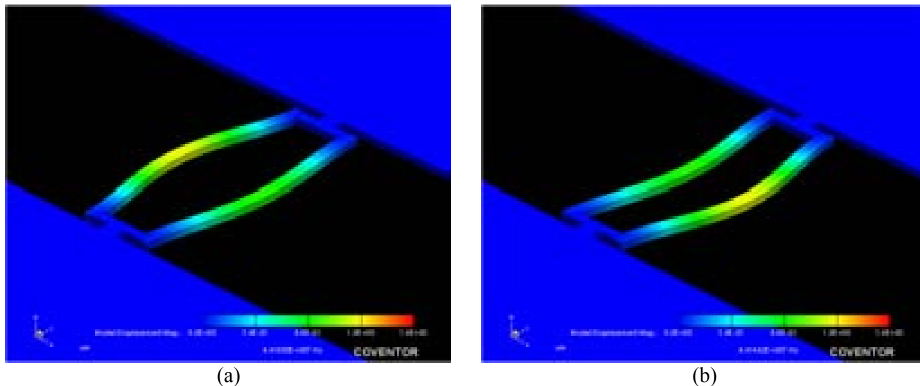

(a) (b)

Figure 5.16: DETF resonator FEM simulations. (a) Balanced frequency mode at 44.1MHz and (b) Unbalanced frequency mode at 44.14MHz.

Figure 5.17 shows the S21 measurement (magnitude and phase) for the DETF resonator once it is released.

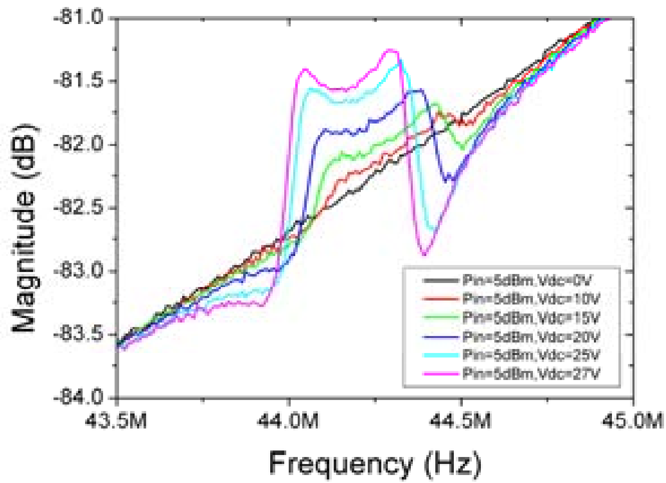

(a)

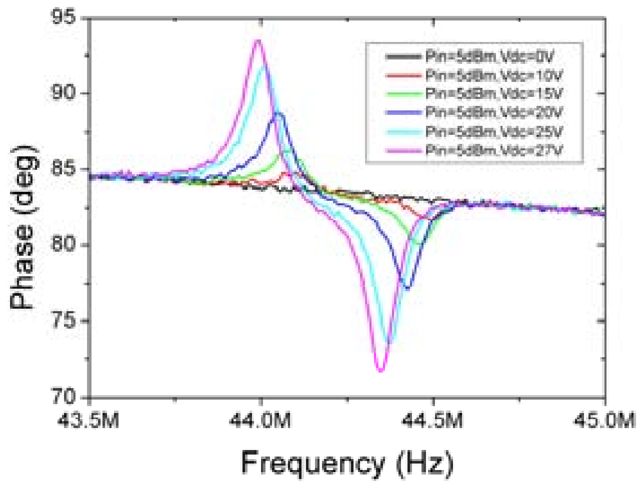

(b)

Figure 5.17: S21 magnitude (a) and phase (b) measurement for a DETF resonator and V_{DC} values from 10V and 27V.

It can be observed in the phase plots how the balanced mode (positive phase shift) is located at lower frequencies. Magnitude response shows a filter-like response (band-pass), with notching in the attenuation bands. The filter is tunable in center frequency and bandwidth with the applied DC voltage. To observe more clearly the frequency response of the DETF filter, the feedthrough current is subtracted in *Figure 5.18*.

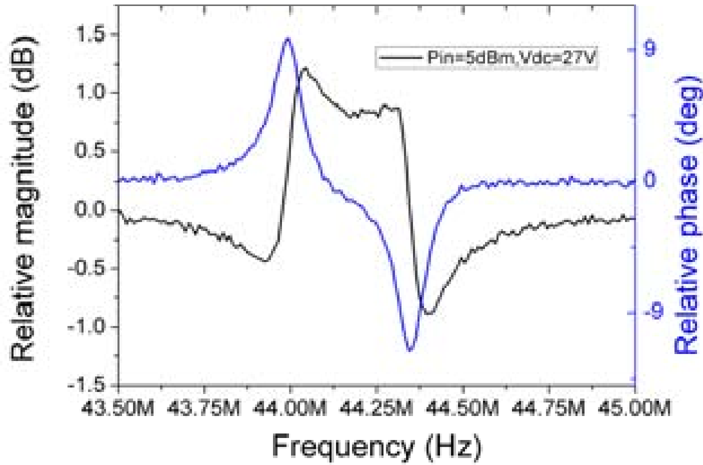

Figure 5.18: Relative magnitude and phase of the *d*=1um DEFT resonator for an applied V_{DC}=27V measured in air conditions.

On *Figure 5.18* it can be clearly observed the filter shape of the resonator response. In particular, the filter has a central frequency of 44.17MHz and a ripple of 0.43dB. Although the filter stop-band attenuation is less than 1dB, and therefore no 3dB bandwidth can be found, it demonstrates the possibility of performing filtering (in this case with a bandpass of 300kHz or the 0.68%) using a sole MEMS resonator, without using different sign biasing, as it was required in [4]. Moreover, this configuration, thanks to the presence of notching at stop-band improves the attenuation slope.

5.3 SINGLE RESONATOR MIXING

The non-linear behavior of the MEMS resonator actuated electrically that was previously used for characterization purposes, allows the use of MEMS resonators as mixers. In this section, the results of the characterization of single-resonator mixers on the HF and the VHF frequency ranges are shown. In particular, clamped-clamped beam mixers with 22MHz and 200MHz resonance frequency and a DETF resonator at 40MHz are reported.

5.3.1 HF CC-BEAM RESONATOR

The HF resonator used in this mixer is the same that was used in the differential amplification scheme: a clamped-clamped beam fabricated in polysilicon1 layer of AMS 0.35µm standard CMOS technology. Resonator dimensions are: *L*=13µm, *W*=350nm and *s*=150nm, and its resonance frequency is located around 22MHz. This resonator was integrated with a monolithic CMOS amplifier to obtain lower losses [5]. *Figure 5.9* shows the SEM images of the released resonator.

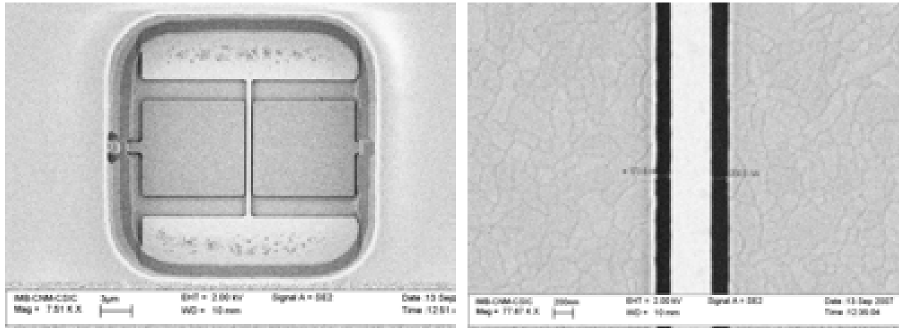

Figure 5.19: SEM images of the CC-beam resonator, a) resonator and drivers b) close view showing the gap.

Figure 5.20 shows the resonator+amplifier magnitude frequency response in mixing down-conversion operation with a f_{LO}=1GHz and P_{LO}=P_{RF}=5dBm. The RF signal is swept from 1.022GHz to 1.023GHz and is applied to the driver electrode whereas the DC plus LO signal is applied to the beam.

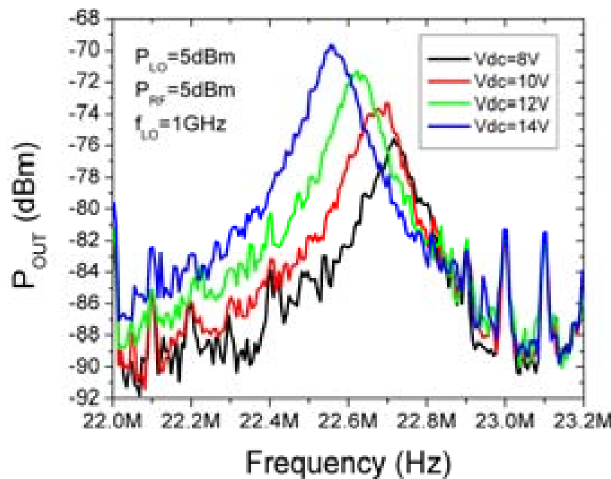

Figure 5.20: Down-conversion mixing frequency response of a 22MHz CC-beam resonator.

From these measurements a power conversion loss of 75dB is obtained (because of impedance mismatch). However, measurements of isolation show very high values: $I_{RF\text{-}IF}$=82dB and $I_{LO\text{-}IF}$=58dB [6].

In addition to down-conversion, up-conversion is also demonstrated in this device. Because of the resonance frequency is around 22MHz, mechanical mixing (the method used in previous measurements), would allow only an output signal at its resonance frequency. This limitation is broken if current mixing mechanism is used (see *Chapter 2*). For doing so, the input signal is swept around the resonance frequency of the resonator, whereas the LO signal is applied to the resonator, like in the previous technique. *Figure 5.21(a)* shows the output signal spectrum when a LO signal at 434MHz is used and *Figure 5.21(b)* shows the same signal for an applied LO signal at 1GHz.

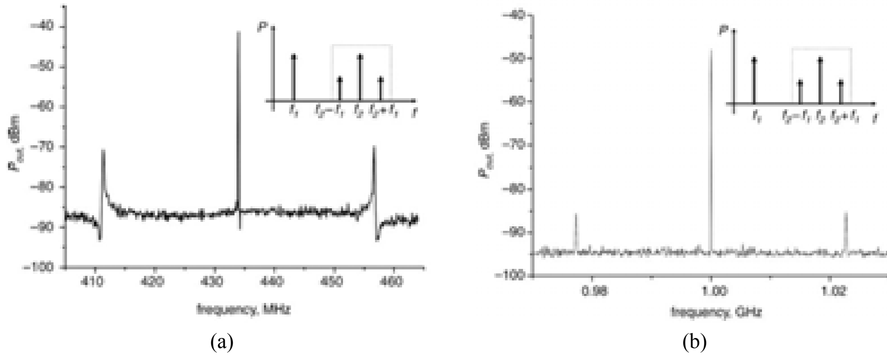

(a) (b)

Figure 5.21: HF-CC beam mixer output spectrum for upconversion. (a) f_{LO}=434MHz and (b) f_{LO}=1GHz. In the figure f_1 is the input frequency (f_{IN}) and f_2 is local oscillator frequency (f_{LO}). Applied powers are P_{LO}=P_{IN}=5dBm.

It can be observed that the carrier (f_{LO}) signal is present in both measurements, and that current mixing translates the resonator behavior to f_{LO}-f_{IN} and f_{LO}+f_{IN}, where f_{IN} is the input signal frequency. The reduction in the peak at the 1GHz measurement is caused by the limited bandwidth of the on-chip amplifier (6MHz).

The obtained results on down-conversion and up-conversion are especially relevant due to the high frequency of the input and output signals.

5.3.2 VHF Double-Ended Tuning Fork Filter-Mixer

This resonator was firstly designed as a first attempt to increase the distance between the excitation and read-out drivers and therefore reduce the parasitic feedthrough capacitor (C_p) using a simple mechanical structure. The distance between tines was chosen at 0.9 μm (d=0.45μm), which according to *Figure 10* on *Annex1* would provide a distance between the resonant modes frequency of 500kHz for the given resonator dimensions. The excitation and read-out electrodes were designed to have a T-shape to reduce the unnecessary electrode area and therefore reduce the C_p.

The SEM image of the released resonator is shown in *Figure 5.22*.

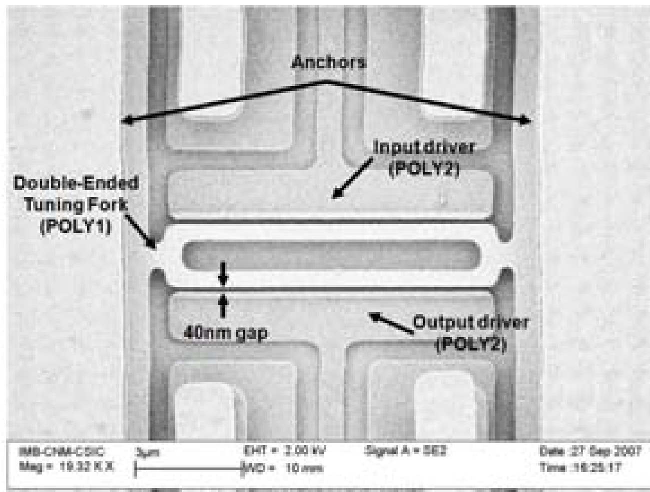

Figure 5.22: SEM image of the DETF resonator

From this SEM image the physical resonator dimensions can be obtained, and are: L_s=0.4µm, d=0.4µm and W_{da}=0.5µm and L_r=9µm. It is then expected, as d is lower than the designed, that the distance between the resonance modes will be higher than the 500kHz designed, as it was corroborated in forthcoming experimental measurements.

Figure 5.23 shows the magnitude frequency response of the DETF resonator for different DC voltage values and an applied input power P_i=10dBm.

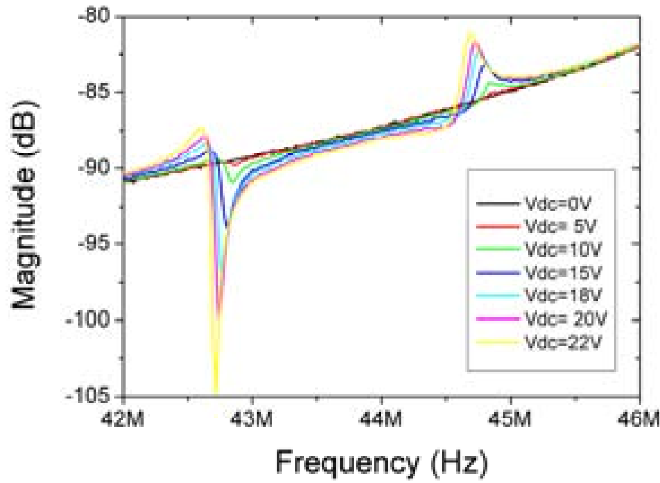

(a)

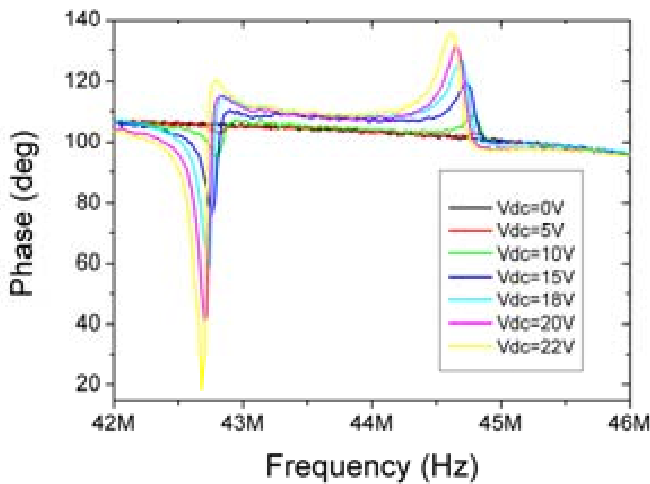

(b)

Figure 5.23: Frequency response of the released DETF. (a) Magnitude and (b) Phase

From *Figure 5.23* it can be observed that there are two peaks, each one corresponding to one resonance mode. As expected the second resonance peak is flipped compared to the first one because of the different signs of the motional current in each resonance mode. The first resonance mode on which the tuning fork tines move on phase has a resonance frequency around 42.75MHz

whereas the second resonance mode, with the tines moving out-of-phase, is around 44.75MHz. This difference between the resonance frequencies of 2MHz can be explained by the aforementioned differences between the designed and the obtained physical dimensions of the resonators.

Q values of both resonator lateral vibration modes have to be calculated from the phase measurements, as no 3dB peak is obtained in air measurements. In particular, *Q* is obtained from the measurements performed on both peaks with V_{DC}=18V (*Figure 5.24*).

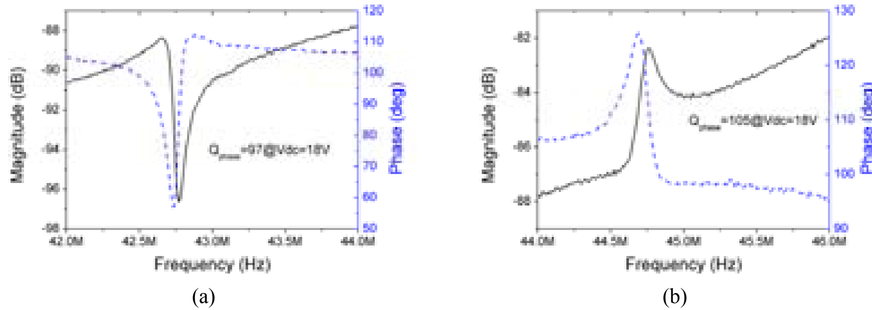

(a) (b)

Figure 5.24: Magnitude and phase measurements with V_{DC}=18V used for experimental Q measurement. (a) Resonance mode 1 (unbalanced or in-phase) and (b) Resonance mode 2 (balanced or out-of-phase)

Both quality factor values are quite similar: 97 and 105, for unbalanced and balanced modes, respectively. To obtain more accurate *Q* values for both peaks and demonstrate mixing functionality, the resonator was wire-bonded and introduced on a vacuum chamber where mixing measurements were performed under vacuum conditions (5µBar). *Figure 5.25* shows the results of these measurements for different applied DC voltages. It can be observed that no output signal is present at the output when V_{DC}=0V, i.e. the mixer-filter is switched off, as already mentioned in *Chapter 2*. Spring softening effect can also be observed from the measurements, i.e. the mixer-filter is tunable. To perform these measurements LO signal is set to f_{LO}=50MHz and P_{LO}=10dBm. The applied RF signal power is of 15dBm and is swept from 92.55MHz to 92.82MHz and from 94.6MHz to 94.85MHz for unbalanced mode and balanced resonance mode, respectively.

Although the second resonance mode is expected to have greater quality factor, the experimental *Q* of the two resonance modes are on the same magnitude order, even being the ballanced mode smaller ($Q_{UNBALANCED}$=1642 and $Q_{BALANCED}$=1637). This is caused by an improper balance of the movement in the structure (each tine has a slightly different displacement), and consequently the inertia moment at the support beam is not completely canceled, as it can be observed in *Figure 5.26* in which FEM mechanical simulation of the displacement of each tine in balanced resonance is performed.

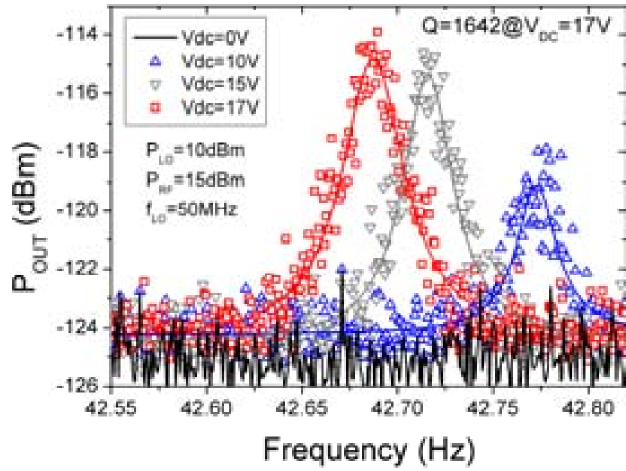

(a)

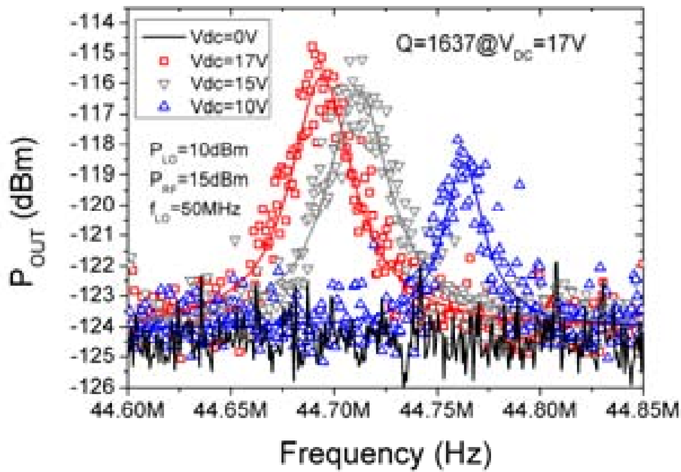

(b)

Figure 5.25: Measured output power for mixing applications under vacuum conditions (5μBar). (a) First resonance mode (unbalanced or in-phase). (b) Second resonance mode (balanced or out-of-phase).

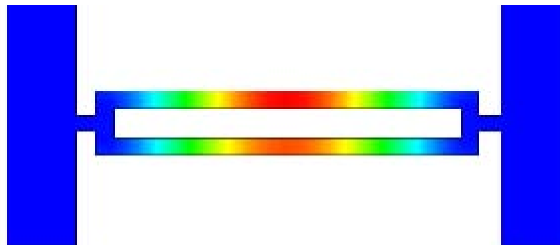

Figure 5.26: FEM displacement simulation of the balanced mode. Red area shows the maximum displacement and blue is the area without movement.

This observed unbalance into the displacement of each tine allows the support losses on the balanced operation mode. In fact, the balance of the resonator and the design methodology for the tuning forks presented in *Annex 1* was not developed until the measurement and discussion of the results of this resonator [7]. Another important fact is that in the fabrication of this particular device, no VIA openings were placed above the resonator. As a result of this, the releasing time of this resonator was increased greatly and metal paths were damaged, degrading the performance and the yield of the post-process (see *Figure 3.12* in chapter 3).

5.3.3 VHF CC-BEAM RESONATOR

The VHF resonator is a clamped-clamped beam with 200MHz resonance frequency, fabricated in polysilicon 2, whose dimensions are: L=4µm, W=500nm and s=40nm, implemented with an on-chip amplifier [8] [1]. *Figure 5.27* shows an optical photograph of the complete resonator+amplifier, as well as SEM detailed image of the resonator.

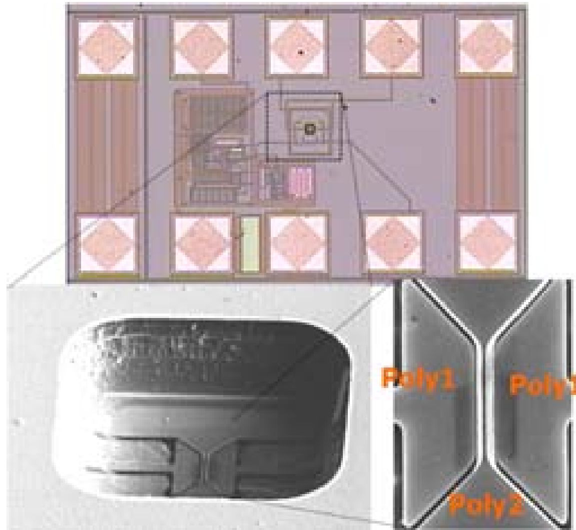

Figure 5.27: Top image: optical microscope image of the complete CC-beam+ amplifier system. Bottom images: SEM images of the CC-beam resonator, showing the etching and the resonator and drivers structure and material.

For mixing measurement the output electrode is connected to a spectrum analyzer, because input and output frequencies of the device in mixing are different. *Figure 5.28* shows the S21 measurement of the CC-beam resonator with and without mixing. As it is shown, for V_{DC}=0V, the mixer is switched off.

The power conversion loss of this resonator+amplifier is of 93dB, higher than for previous HF resonator, because of the smaller coupling area of this higher frequency device.

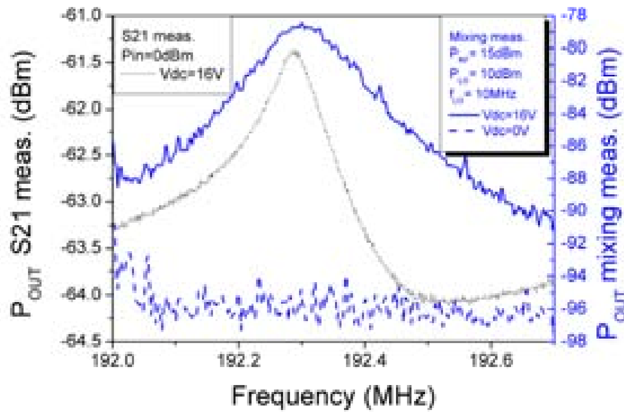

Figure 5.28: Output power for direct S21 measurement (V_{DC}=16V) and mixing measurement. The applied signals are: P_{RF}=P_{LO}=10dBm, V_{DC}=10V, f_{RF}=232MHz and f_{LO}= 10MHz, for RF signal downconversion.

The isolation between ports is also calculated by measuring the power of the output signals at the input frequency components, but this time with a similar device that shows a resonance frequency at 220MHz but without on-chip amplification. Measured frequency components at the output of this resonator are: P_{OUT}(10MHz)=-96.9dBm, P_{OUT}(232MHz)=-74dBm and P_{OUT}(222MHz)=-110dBm. Therefore, the values for this 220MHz CC-beam resonator, working as a mixer and without amplification are: CL=125dB, $I_{RF\text{-}IF}$=89dB and $I_{LO\text{-}IF}$=96.9dB. The power conversion loss of the stand alone CC-beam resonator is obviously higher than the one with on-chip amplifier.

5.4 PARALLEL MIXING

The parallel amplification scheme can be also used to perform mixing. For doing so, the LO signal is applied to the resonator beam combined with the DC voltage (*Figure 5.29*). In this configuration, input LO signal is a common-mode component and is cancelled due to the differential amplification, thus a better isolation of the LO port can be obtained.

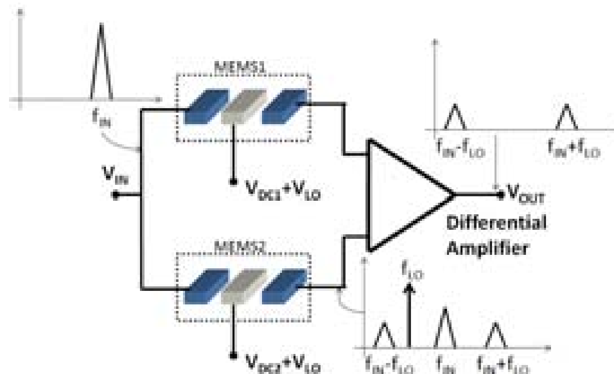

Figure 5.29: Parallel amplification scheme used as a mixer. Note that even though at the output of the differential amplifier f_{IN}-f_{LO} and f_{IN}+f_{LO} signals are shown, only one of them (the one corresponding to the natural resonance of the MEMS) will be present, whereas the other will be filtered.

Figure 5.30 shows the measured result for different V_{DC2} values whereas V_{DC1} is fixed at 20V. Applied LO signal is a 10MHz signal with P_{LO}=10dBm, and the input signal is swept from 30.5MHz to 33.5MHz, with an input power of 0dBm.

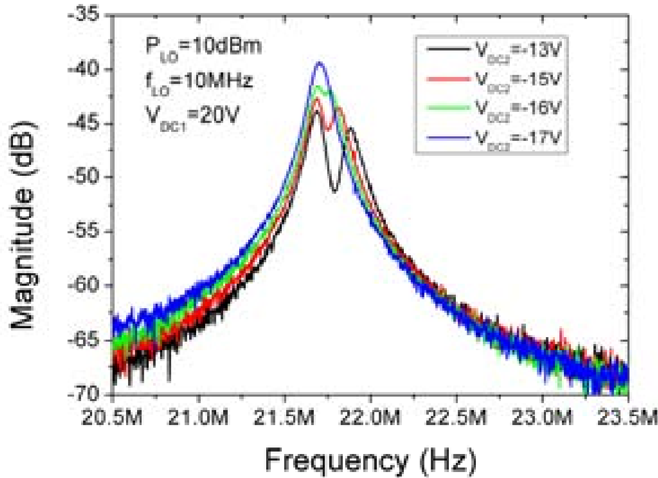

Figure 5.30: Mixing measurements for the parallel mixing using the differential amplifier. P_{IN}=0dBm.

It can be observed that in mixing operation at a DC voltage of -16V, the obtained ripple is 0.5dB, the bandwidth is 197kHz and the stop band is -65dB. The magnitude of the measured signal depends on the LO power, as it is shown in *Figure 5.31*. The higher the applied LO power is, the higher is the measured magnitude.

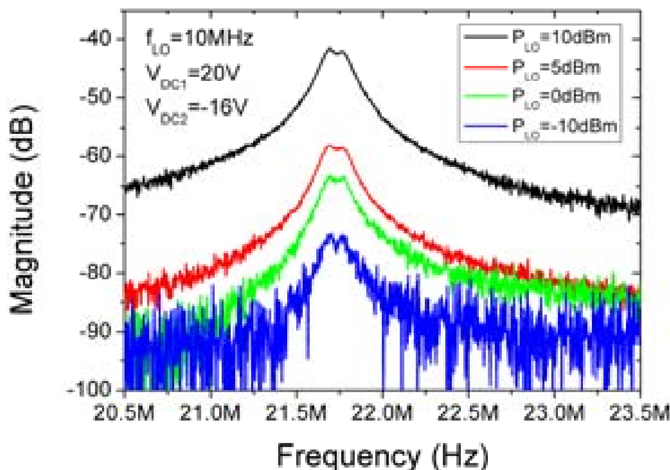

Figure 5.31: Mixing frequency response for different LO power. P_{IN}=0dBm

The low LO frequency applied (10MHz) has no use in real RF systems, where RF signals around hundreds or thousands of MHz are used. Unfortunately, the response of this system is degraded when LO (and therefore the input frequencies) are increased (*Figure 5.32*). Although the

signal frequency at the output of the resonator is the same for both cases, frequency response shows lower magnitude. It is believed that this behavior change is caused by the decrease of the CMRR of the differential amplifier as the frequency increases.

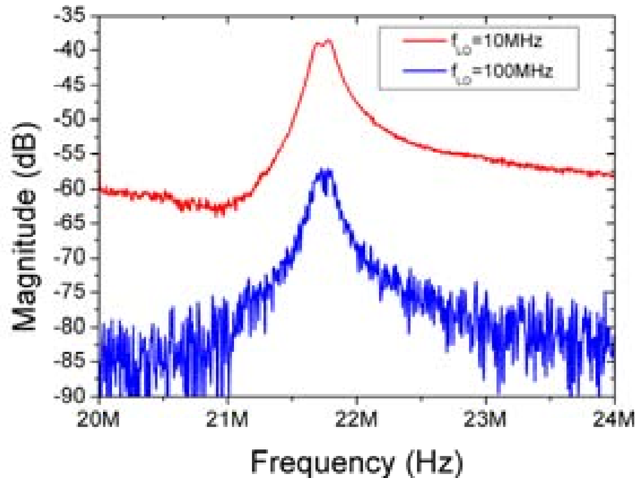

Figure 5.32: Measured frequency response for the parallel filter-mixer for two f_{LO} values (f_{LO}=10MHz and f_{LO}=100MHz)

This kind of degradation was not observed in the literature [9] for low feedthrough capacitor devices, not even on the single resonator+amplifier reported in the previous section. Therefore, additional methods to reduce C_P and increase the CMRR of the amplifier should be studied to allow operation at RF frequencies.

5.5 OSCILLATOR:

This section describes the results of the fabricated oscillators with CMOS-MEMS resonators used as frequency references. The oscillator circuit was designed by Jaume Verd for mass sensing applications [10], and has been used here to test the performance of these resonators in this kind of applications. The resonators tested are a DETF in unbalanced mode and showing a resonance frequency of 11.4MHz and a CC-beam designed for a 24MHz resonance frequency.

5.5.1 S=100NM CLAMPED-CLAMPED BEAM RESONATOR OSCILLATOR

The 24MHz clamped-clamped beam resonator with *s*=100nm is designed to be used as a frequency reference for an oscillator circuit

The oscillator topology is a Pierce oscillator, in which the active circuit generates a negative resistor that cancels the losses of the motional resistance of the MEMS resonator [10]. The oscillation builds up for V_{DC}>17V, as can be observed in the output spectrum (*Figure 5.33-a*) and oscilloscope output signal (*Figure 5.33-b*) of the oscillator.

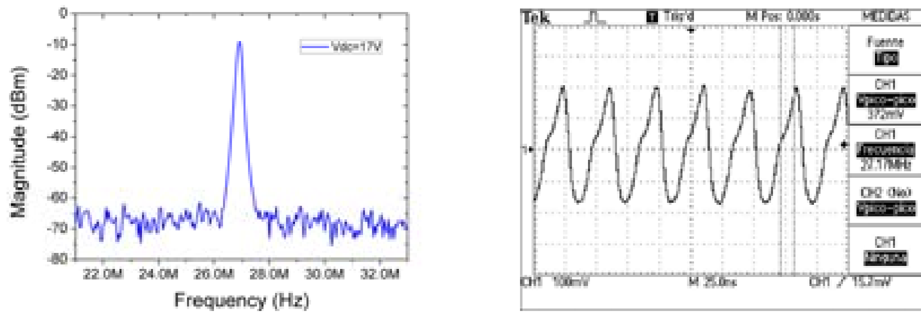

(a) (b)

Figure 5.33: Output signals of the oscillator. (a) Spectrum analyzer measurement and (b) Oscilloscope measurement for V_{DC}=17V. Peak to peak amplitude is 372mV.

The output signal of the oscilloscope has a 27.17MHz frequency and 372mV peak-to-peak amplitude (which corresponds to a -4.6dBm signal at 50Ω). Although it presents a no-sinusoidal shape, it is similar to the one obtained with metal clamped-clamped beams resonators [3].

Two important parameters to evaluate the oscillation stability are the jitter (used for reference frequencies) and phase noise (for RF oscillators). The results of these measurements (jitter and phase noise) for the clamped-clamped beam resonator are shown in *Figure 5.34*.

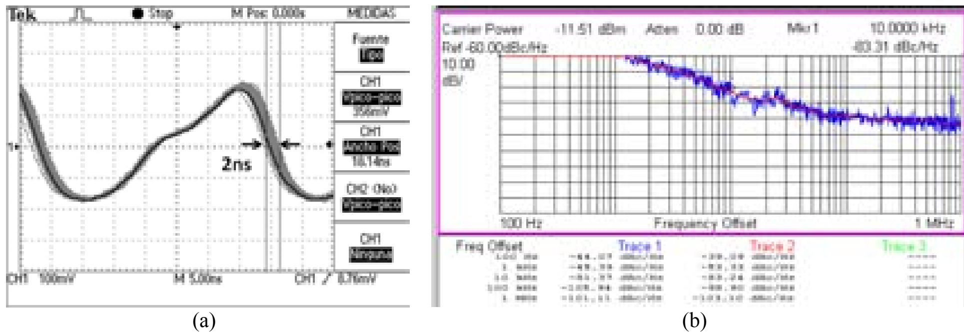

(a) (b)

Figure 5.34: Stability measurements for the CC-beam MEMS-based pierce oscillator

Jitter measurement for the oscillator with 17V applied DC voltage is of 2ns, approximately a jitter of the 5.4% (or 54000ppm), which is far from the 0.005% USB requirement over all the temperature range. Phase noise results of this oscillator are -45.33dBc/Hz@1kHz from carrier, -83.24dBc/Hz@10kHz and -98.9dBc/Hz@100kHz. Phase noise measurement shows a region of $1/f^2$ noise from 10kHz to 100kHz, where it transitions to the flat noise region, whereas the $1/f^3$ noise is found from 1kHz to 10kHz. Considering that $1/f^3$ is caused by the non linear operation of the resonator it can be stated that the distortion on the time domain (and also the jitter) is caused by this non-linear operation of the resonator. Measurements on *Chapter 4* of this device shown that the resonator is in the non-linear range for V_{DC}=17V.

The same oscillator topology was also implemented with a CC-beam of equal resonance frequency as the presented in the previous section but with the minimum achievable gap obtainable by the AMS technology used (s=40nm). *Figure 5.35* shows the oscillator output

spectrum, located at 27.6MHz , measurement of the previous resonator was also included for ease of comparison,

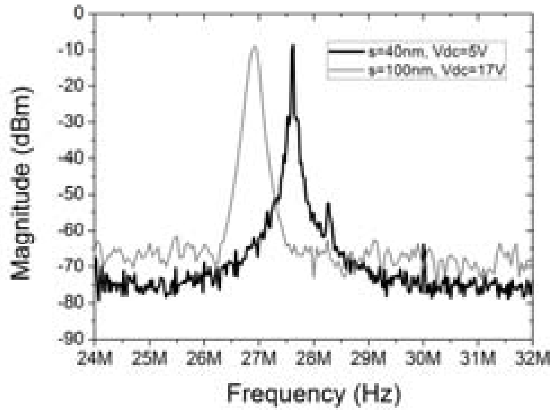

Figure 5.35: CC-Beam oscillator spectrum. In black it is shown the spectrum of the *s*=40nm resonator oscillator and in gray the measurement of the s=100nm oscillator version.

From *Figure 5.35* it can be observed that both oscillators have nearly the same output power (the narrower gap has 2dBm bigger magnitude, even though for the *s*=40nm the applied voltage is reduced to 5V, instead of the 17V applied to the *s*=100nm oscillator. It is observed that the resonance frequency is 0.5MHz (approximately) higher for the *s*=40nm although it seems to be produced by process variations described in *Chapter 3*. *s*=40nm oscillator peak seems to be narrower than the *s*=100nm oscillator, even though this effect is produced by different configuration of the spectrum analyzer used to capture these measurements: in the *s*=40nm the resolution bandwidth was set to a lower value.

Figure 5.36 shows the phase noise measurement of this resonator.

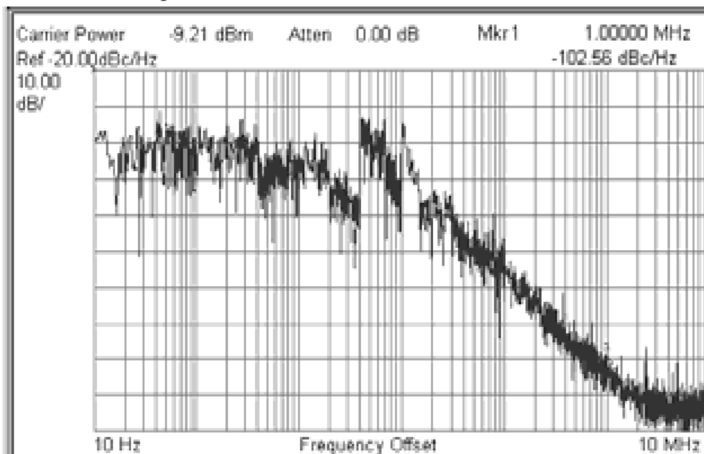

Figure 5.36: Phase noise measurement for the s=40nm clamped-clamped beam oscillator. Applied DC voltage is 5V.

It is observed no $1/f^2$ contribution on this curve, in fact, the slope of the phase noise up to the intersection with white noise floor is of -30dBc per decade, and clearly the oscillator is working

with a non-linear resonator. Moreover, the intersection occurs at f_m=2MHz, quite far from the carrier. The measured phase noise of this oscillator is: -45dBc/Hz@10kHz and -70dBc/Hz@100kHz, much higher than the one of the 100nm resonator, because of resonator no linearity. This non-linear behavior was observed in the characterization of the s=40nm CC-beam stand alone resonator from *Chapter 4*.

5.5.2 DETF OSCILLATOR

A s=40nm version of the DETF resonator with λ/4 support and second lateral mode at 24MHz is used as a reference frequency with the same oscillator circuit. *Figure 5.37* shows an optical photograph of the resonator and the monolithic CMOS oscillator.

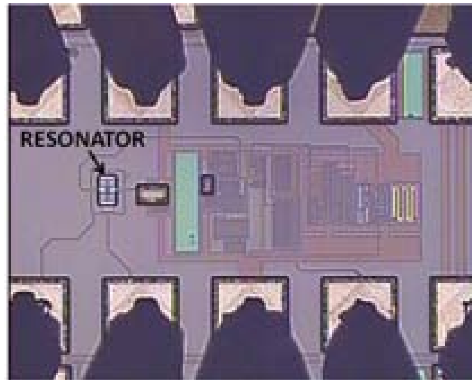

(a)

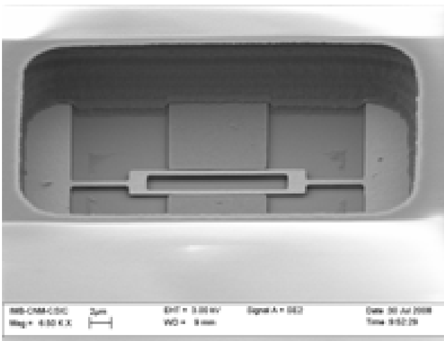

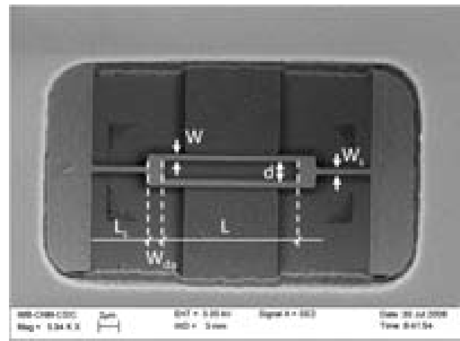

(b) (c)

Figure 5.37: DETF based monolithic oscillator. (a) Optical micrograph of the complete oscillator. DETF resonator is highlighted. (b) and (c) SEM images showing the released DETF resonator

The dimensions of this device are: L=12.8µm, W=0.5µm, W_{da}=1.2µm, d=2µm and L_s=5.3µm. This resonator was designed to show the balanced resonance at 24MHz. However, when used as a frequency reference, the oscillator has an output frequency of 11.4MHz, corresponding to the first lateral mode, as shown in the FEM simulations from *Figure 5.38*. Note that in this mode the supports are also bended, thus the DETF behaves like a simple clamped-clamped beam.

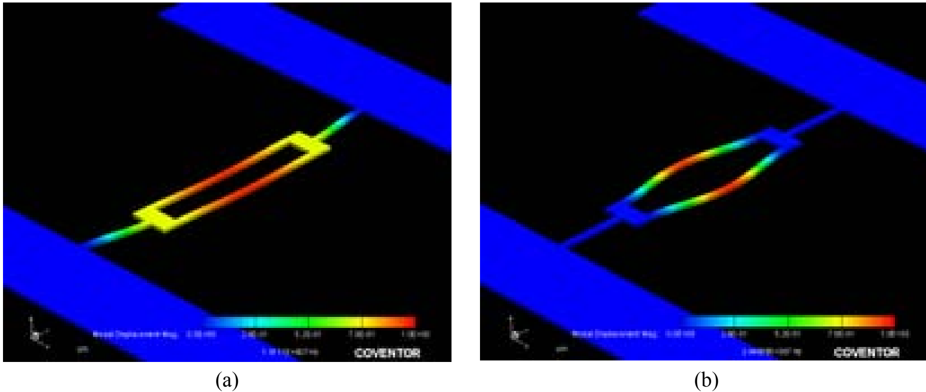

(a) (b)

Figure 5.38: FEM mechanical simulations of the Double-Ended Tuning Fork resonator. (a) First lateral mode found at 10MHz and (b) Second lateral mode at 24.48MHz.

The oscillator based on the DETF resonator, oscillates at 11.4MHz with a small bias voltage applied to the resonator (V_{DC}) of 3.8V, thanks to its tiny gap (s=40nm). *Figure 5.39* shows the time domain output of the resonator measured with an oscilloscope for different V_{DC} values.

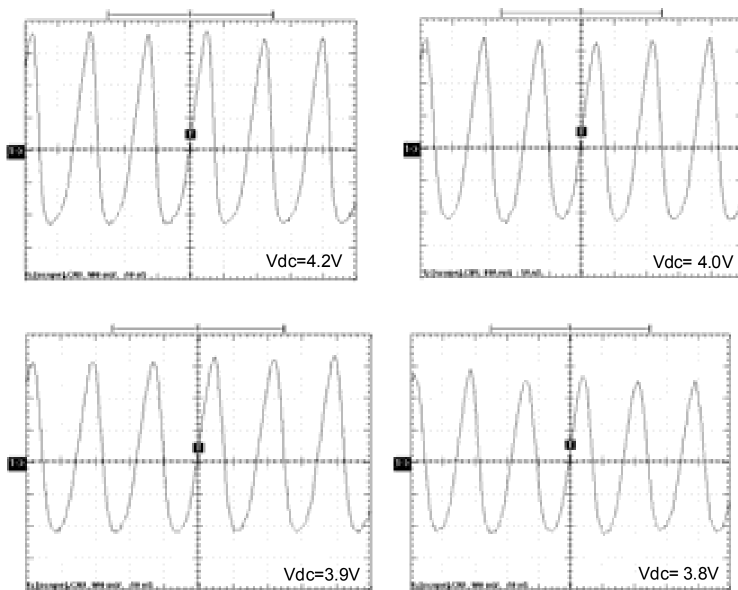

Figure 5.39: Oscillator output waveforms for different V_{DC} voltages.

The measured peak-to-peak voltage are: 600mV, 580mV, 550mV and 520mV for applied V_{DC} of 4.2V, 4V, 3.9V and 3.8V, respectively. These peak-to-peak voltages are higher (nearly twice) than the obtained in previous clamped-clamped beam oscillator for a voltage much smaller (one third or less). Frequency domain measurements (spectrum and phase noise) are shown in *Figure 5.40* for a V_{DC}=4.2V.

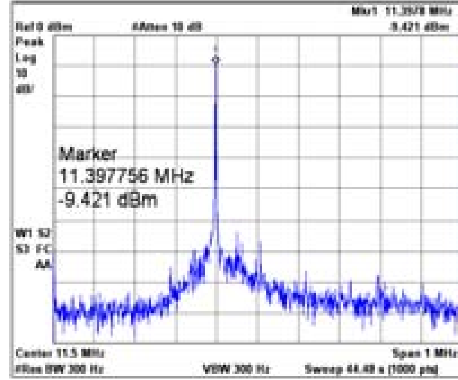

(a)

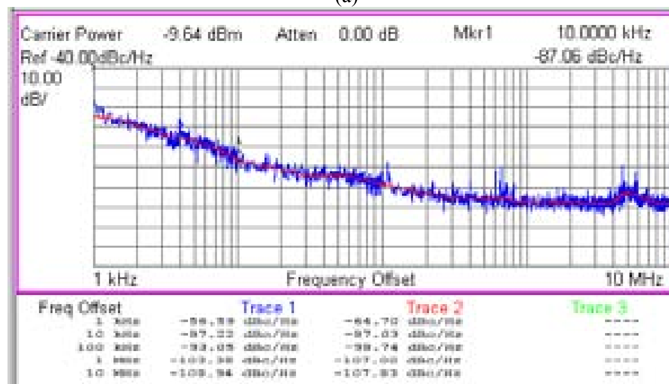

(b)

Figure 5.40: Frequency domain measurements of the DETF oscillator with V_{DC}=4.2V. (a) Spectrum and (b) phase noise measurement.

It can be observed that this resonator presents a similar spectrum magnitude than the clamped-clamped beam oscillator but, again, with a smaller applied V_{DC}. Phase noise measurements are also lower: -64.7dBc/Hz@1kHz from carrier, -87.03dBc/Hz@10kHz and -98.74dBc/Hz@100kHz. The phase noise presents -20dB/dec and -30dB/dec slopes regions, the $1/f^3$ region is from 1kHz to 10khz and the $1/f^2$ is placed from 40kHz to 400kHz, point in which intersects the white noise floor. Even though the region in this resonator starts at 400kHz, instead of the 100kHz form the s=100nm clamped-clamped beam oscillator, it is especially important the reduction of the close-to-carrier phase noise (1kHz from carrier), that indicates that this resonator is more linear than the clamped-clamped beam, as it can be also observed in the time domain waveform. In this case, the use of vacuum is expected to benefit the performance of the oscillator in two ways: 1) reduce the phase noise and 2) further decrease the DC voltage applied to the resonator.

5.6 CONCLUSIONS

In this section the presented resonators are compared between them and with some of the most relevant examples of the state-of-the-art devices mentioned in *Chapter 2*. This discussion is divided between the different applications shown in this chapter.

5.6.1 FILTERS

Table 5.2 shows a summary of the performance of the MEMS filters presented in this chapter (in bold) including the state-of-the art MEMS filters as reference.

Table 5.2: MEMS-based filter performance summary

Resonator	*f_c (MHz)*	*BW_{3dB} (kHz)*	*Ripple (dB)*	*SF_{20dB}*	*SB Rej. (dB)*	*Comments*
Parallel resonator filter						
V_{DC1}=21,V_{DC}2= -19V	21.62	100	0	4	34	Meas. in-air
V_{DC1}=21,V_{DC2}= -14V	21.76	200	0.9	2.97	31	Meas. in-air
V_{DC1}= -4V,V_{DC}2= -4.2V	22.05	23.4	6.6	2.14	36	Meas. In vacuum
V_{DC1}= -4V,V_{DC2}= -4.6V	22.05	17	2.8	2.42	36	Meas. In vacuum
DETF filter	44.17	300[a]	0.43	N.M.	1.22	Meas. in-air
Tuning fork	2.29	8.24	2.7	1.64	22	Yan'08 [4]
Coupled lame-mode square resonators	44.4	44.4[a]	0.1	N.M.	0.2	Yan'08 [11]
CC-Beam mechanical coupling	7.8	18	1.5	2.31	35	Bannon'00 [12] Meas. In vacuum
CC-Beam electrical coupling	0.810	0.54	N.R.	2.9	28	Pourkamali'05 [13] Meas. In vacuum
CC-Res.+nanowire	17.9	120	0.3	NR	6	Arellano'08 [14] Meas. In vacuum
Coupled disk	163	98.5	0.5	2.85	27.6	Li'07 [15] Meas. In vacuum
Bridged CC-beam	9	20	NR	1.95	51	Li'04 [16] Meas. In vacuum
Array composite filter	68.1	190	NR	NR	25	Demirci'05 [17] Meas. In air

(a) No 3dB attenuation is reached

The reported parallel resonator filter presents a tunable and high bandwidth (200kHz) while operated in air when compared to other MEMS-based filters whereas maintaining a low ripple (less than 1dB). It is however, worth to mention that the bandwidth measured for the parallel filter is reduced when operating in vacuum conditions. The 20dB shape factor of the parallel filter is comparable to the reported works with similar bandwidths and frequencies [15, 17]. Note that the ones with shape factor below 2, are the ones with resonance frequencies below 10 MHz and offer narrower bandwidths [4, 16].

It is also important to note that no other resonators are fabricated using CMOS technologies. In particular, the addition of monolithic differential amplification circuitry showed to be very important to obtain the competitive results reported, especially in stop-band rejection. The presented CMOS-MEMS filter, can be further improved by circuitry or by the substitution of the

clamped-clamped beams with higher Q resonators, like the FF-beams presented in the previous chapter.

Finally we want to highlight the single resonator filter based on a mechanical coupling, the double ended tuning fork. This DETF is the one that presents the higher bandwidth. We expect to improve its performance with additional CMOS circuitry..

5.6.2 MIXERS

Table 5.3 shows a summary of performance for the mixers presented in this chapter using the same performance parameters used for state of the art filters and mixers from *Chapter 2*.

Table 5.3: MEMS-based mixers performance summary

Resonator	***CL* (dB)**	**P_{LO}(dBm)/ /V_{DC}(V)**	**f_{RES}(MHz)**	***Isolation* (dB) I_{LO-IF}/I_{LO-RF}/I_{RF-IL}**	**f_{RF} (MHz)**	**Comments**
HF CC-Beam+ amplifier	75	5 / 14	22.55	58 / - / 82	1022.5	s=150nm
DETF (unbalanced) (meas. Vacuum)	129.8	10 / 17	42.7	Not measured	92.7	s=40nm
DETF (balanced) (meas. Vacuum)	130.8	10 /17	44.7	Not measured	94.7	s=40nm
VHF CC-Beam	125	10 / 10	222	96.9 / - / 89	232	s=40nm
Parallel mixer	42.3	10 / 20	21.7	Not measured	31.7	Differential amplifier
Cantilever	49.5	13.5/10	0.435	- / - /-	3200	Chen'05 [9] Meas. In vacuum
Coupled CC-Beams	72/13*	15/11	37	39 / 29.4 / 44	242	Wong'04 [18] Meas. In vacuum
Coupled rings res.	83.5	18/3	423		438	Li'05 [19] Meas. In vacuum
DETF	48	0/40	0.743	36 / 48 / -	10	Alastalo'04 [20] Meas. In vacuum
Coupled DETF	54		0.66	56 / 68 / -	10	Alastalo'04 [20] Meas. In vacuum
Coupled DETF	45	0/7	1.3	30 / 38 / -	400	Koskenv.'08 [21] Meas. In vacuum
Coupled DETF (AM modulation)	15	Not required/7	1.3		500	Koskenv.'08 [21] Meas. In vacuum

From the table several conclusions can be extracted: A) From all the state-of-the art mixers (different than ours), the only one fabricated in CMOS technology is the one from Chen et al. [9], which operates at low frequency, 435kHz. B) Our CMOS-MEMS resonators present the highest isolation between ports, validating the MEMS design for RF applications. C) The MEMS

resonators presented in this thesis show a quite high resonance frequency, especially when compared to [9] and [20], with frequencies lower than 1MHz. The main drawback of our approach is the high conversion loss (much higher than the reported mixers) which is mainly due to the lack of impedance matching between the CMOS-MEMS resonator and the characterization set-up. It is specially remarkable the low conversion loss of Koskenvuori et al. [21] of only 15dB (the lowest conversion loss of the table) obtained with AM modulation and parametric amplification. We expect to improve this conversion loss taking profit of the CMOS integration and thus the possibilities to adapt the resonator to other impedance different than the standard 50 Ohms.

5.6.3 OSCILLATORS

Table 5.4 compares the performance of the presented oscillators to selected state-of-the-art MEMS-based oscillators in terms of phase noise and applied V_{DC} to the resonator.

Table 5.4: Phase noise performance of different MEMS resonator-based oscillators

Res.	*Ref.*	f_{RES} (MHz)	V_{DC} (V)	*L* (dBc/Hz)			Comments
				1kHz	10kHz	100kHz	
CC-Beam oscillator		27.17	17	-53.3	-83.3	-98.9	s=100nm, AMS monolithic, polysilicon
DETF oscillator		11.39	4.2	-64.7	-87	-98.7	s=40nm, AMS monolithic, polysilicon
Cantilever	[10]	6.3	45	-55.6	-75.6	-91.6	Verd'08, AMS monolithic, Metal
CC-Beam	[3]	15.35	70	-53.1	-83.8	-98.1	Verd'08, AMS monolithic, Metal
Cantilever[a]	[3]	6.3	17	-68.5	-85.8	-95	Verd'08, AMS monolithic, Metal
CC-Beam[a]	[3]	15.35	30	-69.1	-88.7	-98	Verd'08, AMS monolithic, Metal
CC-Beam[a]	[22]	9.34	8	-82	-110	-116	Lin'04, TSMC integrated oscillator, wire-bonded, ALC
CC-Beam 2 (wide)[a]	[22]	8.61	15	-80	-106	-120	Lin'04, TSMC integrated oscillator, wire-bonded, ALC
Wine-glass Dsk[a]	[22]	61.2	12	-110	-128	-132	Lin'04, TSMC integrated oscillator, wire-bonded, ALC
Square BAW[a]	[23]	12.9	20	-130	NR	-147	Rantakari'05, AMS 0.35um, wire-bonded
Wine-glass array[a]	[24]	10.9	5	-80	-95	NR	Huang'08, TSCM integrated + CMOS comp nickel resonator,

[a]Measurement in vacuum

When the reported CC-beam oscillator is compared to previous oscillators also fabricated using AMS 0.35µm CMOS technology and the release process described in Chapter 3 [3, 10] the presented oscillator shows similar phase noise performance than the other resonators, but also with a smaller V_{DC} and better low frequency phase noise (for a f_m=100Hz phase noise the reported resonator shows -39.1dBc/Hz, whereas the best result for metal resonators measured in air is of -32dBc/Hz). This improvement in close-to carrier phase noise shows that the presented resonator is more linear than the metal resonators, even though the smaller gap of 100nm. The DETF oscillator presents an important breakthrough when compared to previous implementations as the phase noise obtained is similar to the measured even with measurements in vacuum and with a much smaller DC voltage. Moreover, these results should take advantage of in-vacuum measurements which should reduce the phase noise, and decrease the V_{DC} as it happened in metal resonator

oscillators, in this way the DETF oscillator would reduce more the required DC voltage, surely below 3.3V.

When compared to other solutions, the presented oscillator (together with the aforementioned metal resonators) and [24] are the only one fabricated monolithically in a CMOS technology, although the one step mask-less etching used to fabricate the presented resonator is simpler than the fabrication of the disks of [24]. Performance of the CC-beam prototype oscillator must be improved to face the superior phase-noise characteristics of the other resonators [22-24].

In particular, the most important milestones are on-vacuum encapsulation, introduction of ALC in the oscillator and arraying of several resonators to reduce R_m and improve the linearity [24].

Although the target in terms of phase noise and jitter are obviously far away, the oscillators reported show the possibility to integrate simply the resonator and the oscillator in the same wafer. Obviously, to reach the high stability required in a wide range of temperature, temperature compensation on the oscillator (and in a future in the resonator itself) has to be implemented. Moreover, although the applied signal power at the input of the resonator (-5dBm) seems low enough to drive the resonator in linear operation, automatic level control (ALC) circuitry improves the linearity of the resonator [25]. Furthermore, the necessary V_{DC} has to be reduced to 3.3V (maximum) in order to implement a commercial product. For doing so, vacuum encapsulation and reduction of the gap are the most straightforward ways to reach this objective,as it has been demonstrated with the DETF oscillator which has a low bias voltage.

REFERENCES

[1] J. L. Lopez, J. Teva, A. Uranga, F. Torres, J. Verd, G. Abadal, N. Barniol, J. Esteve, and F. Perez-Murano, "Mixing in a 220MHz CMOS-MEMS," in *Circuits and Systems, 2007. ISCAS 2007. IEEE International Symposium on*, 2007, pp. 2630-2633.

[2] C. T. C. Nguyen, "MEMS for Frequency and Timing References," 2005.

[3] J. Verd, "Monolithic CMOS-MEMS Resonant Beams for Ultrasensitive Mass Detection." vol. Ph.D Bellaterra: Universitat Autònoma de Barcelona, 2008.

[4] J. Yan, A. A. Seshia, K. L. Phan, and J. T. M. van Beek, "Internal electrical phase inversion for FF-beam resonator arrays and tuning fork filters," in *Micro Electro Mechanical Systems, 2008. MEMS 2008. IEEE 21st International Conference on*, 2008, pp. 1028-1031.

[5] J. Verd, A. Uranga, J. Teva, J. L. Lopez, F. Torres, J. Esteve, G. Abadal, F. Perez-Murano, and N. Barniol, "Integrated CMOS-MEMS with on-chip readout electronics for high-frequency applications," *Electron Device Letters, IEEE,* vol. 27, pp. 495-497, 2006.

[6] A. Uranga, J. Verd, J. L. Lopez, J. Teva, G. Abadal, F. Torres, J. Esteve, F. Perez-Murano, and N. Barniol, "Fully integrated MIXLER based on VHF CMOS-MEMS clamped-clamped beam resonator," *Electronics Letters,* vol. 43, pp. 452-454, 2007.

[7] J. L. Lopez, F. Torres, G. Murillo, J. Giner, J. Teva, J. Verd, A. Uranga, G. Abadal, and N. Barniol, "Double-ended tuning fork resonator in 0.35um CMOS technology for RF applications," in *Research in Microelectronics and Electronics, 2008. PRIME 2008. Ph.D.*, 2008, pp. 89-92.

[8] J. Teva, G. Abadal, A. Uranga, J. Verd, F. Torres, J. L. Lopez, J. Esteve, F. Perez-Murano, and N. Barniol, "VHF CMOS-MEMS resonator monolithically integrated in a standard 0.35μm CMOS technology," in *Micro Electro Mechanical Systems, 2007. MEMS. IEEE 20th International Conference on*, 2007, pp. 779-782.

[9] F. Chen, J. Brotz, U. Arslan, C.-C. Lo, T. Mukherjee, and G. K. Fedder, "CMOS-MEMS resonant RF mixer-filters," in *Micro Electro Mechanical Systems, 2005. MEMS 2005. 18th IEEE International Conference on*, 2005, pp. 24-27.

[10] J. Verd, A. Uranga, G. Abadal, J. L. Teva, F. Torres, J. L. Lopez, E. Perez-Murano, J. Esteve, and N. Barniol, "Monolithic CMOS MEMS Oscillator Circuit for Sensing in the Attogram Range," *Electron Device Letters, IEEE,* vol. 29, pp. 146-148, 2008.

[11] J. Yan, A. A. Seshia, K. L. Phan, and J. T. M. van Beek, "Mechanical phase inversion for coupled lamé mode resonator array filters," in *Micro Electro Mechanical Systems, 2008. MEMS 2008. IEEE 21st International Conference on*, 2008, pp. 1024-1027.

[12] F. D. Bannon, J. R. Clark, and C. T. C. Nguyen, "High-Q HF microelectromechanical filters," *Solid-State Circuits, IEEE Journal of,* vol. 35, pp. 512-526, 2000.

[13] S. Pourkamali and F. Ayazi, "Electrically coupled MEMS bandpass filters - Part 1: With coupling element," *Sensors and Actuators a-Physical,* vol. 122, pp. 307-316, Aug 2005.

[14] N. Arellano, E. P. Quevy, J. Provine, R. Maboudian, and R. T. Howe, "Silicon nanowire coupled micro-resonators," in *Micro Electro Mechanical Systems, 2008. MEMS 2008. IEEE 21st International Conference on*, 2008, pp. 721-724.

[15] S.-S. Li, Y.-W. Lin, Z. Ren, and C. T. C. Nguyen, "An MSI Micromechanical Differential Disk-Array Filter," in *Solid-State Sensors, Actuators and Microsystems Conference, 2007. TRANSDUCERS 2007. International*, 2007, pp. 307-311.

[16] S.-S. Li, M. U. Demirci, Y.-W. Lin, Z. Ren, and C. T. C. Nguyen, "Bridged micromechanical filters," in *Frequency Control Symposium and Exposition, 2004. Proceedings of the 2004 IEEE International*, 2004, pp. 280-286.

[17] M. U. Demirci and C. T. C. Nguyen, "A low impedance VHF micromechanical filter using coupled-array composite resonators," in *Solid-State Sensors, Actuators and Microsystems, 2005. Digest of Technical Papers. TRANSDUCERS '05. The 13th International Conference on*, 2005, pp. 2131-2134 Vol. 2.

[18] A.-C. Wong and C. T. C. Nguyen, "Micromechanical mixer-filters ("mixlers")," *Microelectromechanical Systems, Journal of,* vol. 13, pp. 100-112, 2004.

[19] S.-S. Li, Y.-W. Lin, Y. Xie, Z. Ren, and C. T. C. Nguyen, "Small percent bandwidth design of a 423-MHz notch-coupled micromechanical mixler," in *Ultrasonics Symposium, 2005 IEEE*, 2005, pp. 1295-1298.

[20] A. T. Alastalo, M. Koskenvuori, H. Seppa, and J. Dekker, "A micromechanical resonating RF mixer," in *Microwave Conference, 2004. 34th European*, 2004, pp. 1297-1300.

[21] M. Koskenvuori and I. Tittonen, "Towards Micromechanical Radio: Overtone Excitations of a Microresonator Through the Nonlinearities of the Second and Third Order," *Microelectromechanical Systems, Journal of,* vol. 17, pp. 363-369, 2008.

[22] Y.-W. Lin, S. Lee, S.-S. Li, Y. Xie, Z. Ren, and C. T. C. Nguyen, "Series-resonant VHF micromechanical resonator reference oscillators," *Solid-State Circuits, IEEE Journal of,* vol. 39, pp. 2477-2491, 2004.

[23] P. Rantakari, V. Kaajakari, T. Mattila, J. Kiihamaki, A. Oja, I. Tittonen, and H. Seppa, "Low noise, low power micromechanical oscillator," in *Solid-State Sensors, Actuators and Microsystems, 2005. Digest of Technical Papers. TRANSDUCERS '05. The 13th International Conference on*, 2005, pp. 2135-2138 Vol. 2.

[24] W.-L. Huang, Z. Ren, Y.-W. Lin, H.-Y. Chen, J. Lahann, and C. T. C. Nguyen, "Fully monolithic CMOS nickel micromechanical resonator oscillator," in *Micro Electro Mechanical Systems, 2008. MEMS 2008. IEEE 21st International Conference on*, 2008, pp. 10-13.

[25] L. Seungbae and C. T. C. Nguyen, "Influence of automatic level control on micromechanical resonator oscillator phase noise," in *Frequency control symposium and pda exhibition jointly with the 17th european frequency and time forum, 2003. proceedings of the 2003 ieee international*, 2003, pp. 341-349.

6 CONCLUSIONS

The main contributions of this thesis are in the field of CMOS-MEMS for RF applications and can be summarized in the following items:

1. It presents the design considerations for MEMS resonators to be carried out and the constrains for main RF applications. These considerations are derived from a careful study of the state-of-the art
2. Describes the MEMS fabrication process using CMOS technologies from a design point of view. In this topic different solutions to solve problems with etching related to the design and technology (e.g. falling via squares) were provided.
3. Demonstrates the validity for the MEMS fabrication approach in CMOS with the successful fabrication of RF MEMS in deep submicrometric CMOS technologies (specifically 0.18 um) from a complete different foundry that the first prototypes. This process validation open new possibilities using other CMOS technologies with smaller dimensions and in this way opens the possibilities for smaller (nanoelectromechanical systems, NEMS) and higher frequency devices.
4. Different resonator topologies to enhance mechanical resonant behavior were fabricated and tested. In addition to the CC beam, lateral free-free beams (in first and third resonance mode) and double ended tuning forks were measured and compared to determine the best resonator topology for monolithically integrated oscillators.
5. RF signal processing applications (filtering and mixing) of MEMS resonators were explored and prototypes were designed and carefully tested, giving state-of-the art performances as will be detailed in next section.
6. Oscillators using the CC-beam and Double-ended tuning fork frequency references with gap of 40nm showed an important breakthrough in the CMOS-MEMS resonators, with resonator biasing below 5V.
7. The thesis also provides a detailed description of the design process for MEMS fabrication in CMOS and highlights several points to take care when design rules are broken.
8. Some experimental methods used to obtain more accurate measurements for electrostatically excited and capacitively transduced MEMS resonators are also described and tested.

Next sections describe in detail the major advances for the presented devices.

MEMS RESONATORS

As resonator the most relevant structure due to its higher Q is the 24MHz free-free beam. This resonator presents a Qxf value of 8.48GHz in air using mixing measurements. Extrapolating the increase of Q when using vacuum measurements (a x20 factor) this figure of merit would reach 169.7GHz showing a quite competitive value when compared to other CMOS-MEMS resonators, as shown in *Figure 6.1*, although this value is far than the obtained in discrete resonators 9.98THz

[1]. The CC beam with differential amplifier is demonstrated as a powerful system to accurately characterize MEMS due to an increase with previously measures of Q for the same resonators: the measured Q using the differential amplifier in vacuum conditions is 4400, whereas for the single amplifier of [2] is 2600 on the same conditions.

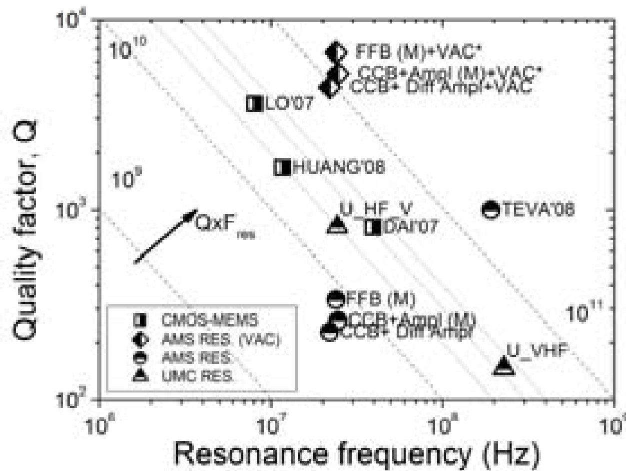

Figure 6.1: Q vs. f_{RES} plot for selected resonators on this thesis. (M) Depicts the Q factor measurement with mixing. U_HF_V depicts the HF UMC cc-beam resonator from Chapter 3 and measured in vacuum. U_VHF designates the VHF resonator fabricated on UMC technology and measured in air conditions.

The state of the art resonators selected for comparison are: Dai'07 [3], Lo'07 [4], Huang'08 [5] and Teva'08 [6]. All these resonators are flexural but [6], which was moreover fabricated with the same technology and fabrication technique, and is a disk with bulk mode. On this figure the resonators labeled with an asterisk (*) represent the expected Q value when measured in vacuum and not measurement values.

The results presented for resonators with monolithic amplification demonstrate the advantage and the convenience of using CMOS technology to fabricate on-chip MEMS devices.

MEMS RF SIGNAL PROCESSORS

Among the MEMS applications it is especially relevant the parallel tunable CMOS-MEMS filter-mixer. With this topology, an active filter (with gain) was measured using voltages below 5V under vacuum conditions whereas in in-air operation the filter had a bandwidth of 200kHz suitable for applications like GSM.

The thesis also reports a 24MHz cc-beam based mixer which uses force mixing to downconvert RF signals of frequencies up to 1GHz (being this limit was set by the setup employed at that moment) and uses current mixing to up convert the input signal (AM modulation) to the GHz range.

In this range of RF signals processors, the application of the DETF tuning fork was also relevant: this resonator is a potential filter (and also mixer) as long as the two resonance modes are designed adequately. In this sense we have been capable to obtain a band-pass filter with

mechanical coupling with a single DETF resonator. Considering all this, these structures show a high versatility as signal processors.

Finally and due to the different layouts of the excitations and read-out drivers with the resonator, phase inversion circuits are also possible, as was demonstrated with the third order beam resonator.

To enhance the performance of these last functional resonators, and thanks to the monolithical fabrication with CMOS, additional CMOS circuit for amplification and for reducing the impedance mismatch can be added. In this sense this thesis can be thought as the first step to new mechanical signal processors.

CMOS-MEMS OSCILLATORS

This thesis faced the challenge of obtaining low bias voltage oscillators. For doing so the gap of the electrode to resonator was reduced to the minimum achievable distance by the technology (40nm). Measurements demonstrate the ability of these oscillators to operate with voltages below 5V, however jeopardizing the phase noise, as it was observed in the CC-beam oscillators. The DETF oscillator overcomes this limitation obtaining a reasonable phase noise whereas operated at voltages below zero. This better stability however is far than the reported in {Rantakari, 2005 #121}, although this is not monolithically integrated. This oscillator, even though not presenting a competitive performance allows the implementation of oscillators monolithically with a low cost solution when compared to more complex fabrication process. Moreover, because oscillation is reached in air conditions, it is expected operation in vacuum with very low biasing voltage (by using the gate bias voltage of the CMOS circuitry). Further improvements to guarantee a linear behavior of the MEMS resonator and studies on stability (including long term and temperature and biasing drifts) are needed for obtaining final prototypes to really compete with crystal quartz based oscillators.

FINAL CONCLUSIONS

The presented results on this thesis has demonstrated the feasibility and the potential of CMOS-MEMS integration in RF applications, there are however some challenges to overcome. One of the most important problems is the development of a zero-level vacuum packaging for these resonators. The success in this issue would infer a leap in the performance of these devices, that is expected to be closer to the nowadays superior discrete MEMS fabrication.

REFERENCES

[1] M. A. Abdelmoneum, M. U. Demirci, and C. T. C. Nguyen, "Stemless wine-glass-mode disk micromechanical resonators," in *Micro Electro Mechanical Systems, 2003. MEMS-03 Kyoto. IEEE The Sixteenth Annual International Conference on*, 2003, pp. 698-701.

[2] J. Verd, "Monolithic CMOS-MEMS Resonant Beams for Ultrasensitive Mass Detection." vol. Ph.D Bellaterra: Universitat Autònoma de Barcelona, 2008.

[3] C.-L. Dai, C.-H. Kuo, and M.-C. Chiang, "Microelectromechanical resonator manufactured using CMOS-MEMS technique," *Microelectronics Journal,* vol. 38, pp. 672-677, 2007.

[4] C. C. Lo and G. K. Fedder, "On-Chip High Quality Factor CMOS-MEMS Silicon-Fin Resonators," in *Solid-State Sensors, Actuators and Microsystems Conference, 2007. TRANSDUCERS 2007. International*, 2007, pp. 2449-2452.

[5] W.-L. Huang, Z. Ren, Y.-W. Lin, H.-Y. Chen, J. Lahann, and C. T. C. Nguyen, "Fully monolithic CMOS nickel micromechanical resonator oscillator," in *Micro Electro Mechanical Systems, 2008. MEMS 2008. IEEE 21st International Conference on*, 2008, pp. 10-13.

[6] J. Teva, G. Abadal, A. Uranga, J. Verd, F. Torres, J. L. Lopez, J. Esteve, F. Perez-Murano, and N. Barniol, "From VHF to UHF CMOS-MEMS monolithically integrated resonators," in *Micro Electro Mechanical Systems, 2008. MEMS 2008. IEEE 21st International Conference on*, 2008, pp. 82-85.

PUBLICATION LIST

JOURNALS

Lopez J L, Verd J, Teva J, Murillo G, Giner J, Torres F, Uranga A, Abadal G and Barniol N 2009 Integration of RF-MEMS resonators on submicrometric commercial CMOS technologies *Journal of Micromechanics and Microengineering* **19**

Lopez J L, Verd J, Uranga A, Giner J, Murillo G, Torres F, Abadal G and Barniol N 2009 A CMOS-MEMS RF-Tunable Bandpass Filter Based on Two High-Q 22-MHz Polysilicon Clapmed-Clamped Beam Resonators *Electron Device Letters, IEEE* **30** 718-20

Torres F, Teva J, **Lopez J L**, Uranga A, Abadal G, Barniol N, Sanchez-Amores A, Montserrat J, Perez-Murano F and Esteve J 2007 Nanometer scale gaps for capacitive transduction improvement on RF-MEMS resonators *Microelectronic Engineering* **84** 1384-7

Uranga A, Teva J, Verd J, **Lopez J L**, Torres E, Esteve J, Abadal G, Perez-Murano E and Barniol N 2005 Fully CMOS integrated low voltage 100 MHz MEMS resonator *Electronics Letters* **41** 1327-8

Uranga A, Verd J, **Lopez J L**, Teva J, Abadal G, Torres F, Esteve J, Perez-Murano F and Barniol N 2007 Fully integrated MIXLER based on VHFCMOS-MEMS clamped-clamped beam resonator *Electronics Letters* **43** 452-4

Uranga A, Verd J, Torres F, Teva J, **Lopez J L**, Abadal G, Esteve J, Perez-Murano F and Barniol N 2007 Electrical detection of multiple resonant modes in a CMOS-MEMS cantilever *Microelectronic Engineering* **84** 1374-8

Verd J, Uranga A, Abadal G, Teva J L, Torres F, **Lopez J L**, Perez-Murano E, Esteve J and Barniol N 2008 Monolithic CMOS MEMS Oscillator Circuit for Sensing in the Attogram Range *Electron Device Letters, IEEE* **29** 146-8

Verd J, Uranga A, Teva J, **Lopez J L**, Torres F, Esteve J, Abadal G, Perez-Murano F and Barniol N 2006 Integrated CMOS-MEMS with on-chip readout electronics for high-frequency applications *Ieee Electron Device Letters* **27** 495-7

CONFERENCES

Lopez J L, Verd J, Marigo E, Murillo G, Giner J, Torres F, Abadal G and Barniol N 2009 Monolithically Integrated Double-Ended Tuning Fork- Based Oscillator with Low Bias Voltage in Air Conditions. In: *Eurosensors' 2009 (ACCEPTED),*

Lopez J L, Verd J, Uranga A, Murillo G, Giner J, Marigo E, Torres F, Abadal G and Barniol N 2009 VHF band-pass filter based on a single CMOS-MEMS double-ended tuning fork resonator. In: *Eurosensors' 2009 (ACCEPTED),*

Lopez J L, Verd J, Giner J, Uranga A, Murillo G, Marigo E, Torres E, Abadal G and Barniol N 2009 HIGH Q CMOS-MEMS RESONATORS AND ITS APPLICATIONS AS A RF TUNABLE BAND-PASS FILTERS. In: *Transducers' 2009,*

Lopez J L, Murillo G, Giner J, Uranga A, Torres F, Abadal G, Esteve J, Perez-Murano E and Barniol N 2008 HF and VHF Nanoresonators Fabricated in a Commercial 0.18mm CMOS technology. In: *Micro and Nano Engineering (MNE),*

Lopez J L, Murillo G, Giner J, Uranga A, Abadal G, and Barniol N 2008 Fabrication of MEMS resonators in the HF and the VHF range on a 0.18um CMOS comercial technology. In: *DCIS,*

Lopez J L, Torres F, Murillo G, Giner J, Teva J, Verd J, Uranga A, Abadal G and Barniol N 2008 Double-ended tuning fork resonator in 0.35um CMOS technology for RF applications *Prime: 2008 Phd Research in Microelectronics and Electronics, Proceedings* 89-92

Teva J, Abadal G, Uranga A, Verd J, Torres F, **Lopez J L**, Esteve J, Perez-Murano F and Barniol N 2008 From VHF to UHFCMOS-MEMS monolithically integrated resonators *Mems 2008: 21st Ieee International Conference on Micro Electro Mechanical Systems, Technical Digest* 82-5

Lopez J L, Teva J, Uranga A, Torres F, Verd J, Abadal G, Barniol N, Esteve J and Perez-Murano F 2007 Mixing in a 220MHz CMOS-MEMS. In: *Circuits and Systems, 2007. ISCAS 2007. IEEE International Symposium on,* ed J Teva pp 2630-3

Teva J, Abadal G, Uranga A, Verd J, Torres F, **Lopez J L**, Esteve J, Perez-Murano F and Barniol N 2007 VHF CMOS-MEMS resonator monolithically integrated in a standard 0.35μm CMOS technology. In: *Micro Electro Mechanical Systems, 2007. MEMS. IEEE 20th International Conference on,* pp 779-82

Uranga A, Teva J, Verd J, **Lopez J L**, Torres F, Abadal G, Barniol N, Esteve J and Perez-Murano F 2006 CMOS integrated MEMS resonator for RF applications *2006 Ieee International Symposium on Circuits and Systems, Vols 1-11, Proceedings* 2301-4

Lopez J L, Teva J, Torres E, Abadal G, Uranga A and Barniol N 2005 Frequency Synthesis using on-chip Micromechanical Resonators. In: *PRIME' 2005,*

ANNEX 1: MEMS design equations

In this section, the design equations and methodology for each resonator is described. All implementations are based on three-port devices, due to the reduced feed-through capacitance that these devices offer when compared to the two-port counterparts. The lateral vibration mode is selected in order to make resonance frequency independent from layer thickness (*h*), which is established by the CMOS technology used.

FLEXURAL MODES IN BEAMS

In this section the natural free vibration modes for beams, like the shown in *Figure A1.1*, are derived. These equations will be solved for the clamped-clamped beam (fixed ends) and for the free-free beam boundary conditions. Most relevant dimensions of the beam are shown in Figure A1.1.

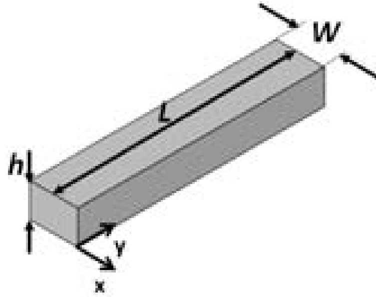

Figure A1.1: Important dimensions of a beam: thickness (*h*), width (*W*) and length (*L*). The axis definition is also shown.

The free resonance modes are given by the Euler-Bernoulli equation. Neglecting the external force term and damping and beam's own loading (gravitational force), this equation is written as as (7.1) [1].

$$E \cdot I \cdot \frac{\partial^4 x(y,t)}{\partial y^4} + \rho \cdot h \cdot W \cdot \frac{\partial^2 x(y,t)}{\partial t^2} = 0 \tag{7.1}$$

The variable *x(y,t)* states the deflection of the beam as a function of the position along the beam axis (*y*) and time (*t*). The constants *E* and ρ are the Young modulus and mass density of the beam material, respectively, and *I* is the moment of inertia of the beam. This moment of inertia can be written for a beam in lateral deflection as (7.2).

$$I = \frac{h \cdot W^3}{12} \tag{7.2}$$

The solution of (7.1) can be expressed as a product of two functions: one independent from the time and the other independent of beam position (7.3).

$$x(y,t) = x(y) \cdot \cos\left(\omega_n \cdot t + \theta\right) \tag{7.3}$$

Where *n* denotes the n-vibration mode of the resonator. Substituting (7.3) into (7.1) leads to:

$$\frac{\partial^4 x(y)}{\partial y^4} = \omega_n^2 \cdot \frac{\rho \cdot h \cdot W}{E \cdot I} \cdot x(y) \tag{7.4}$$

The variable κ_n can be defined as:

$$\kappa_n^4 = \omega_n^2 \cdot \frac{\rho \cdot h \cdot W}{E \cdot I} \tag{7.5}$$

And therefore the n-mode oscillation frequency can be expressed like:

$$\omega_n = \kappa_n^2 \cdot \sqrt{\frac{E \cdot I}{\rho \cdot h \cdot W}} \tag{7.6}$$

Substituting (7.2) into (7.6), the expression of the angular frequency of the n-mode as a function of material physical properties (E and ρ), beam dimensions (W and L) is found (7.7).

$$\omega_n = \kappa_n^2 \cdot \sqrt{\frac{E \cdot W^2}{12 \cdot \rho}} = \frac{\left(\kappa_n \cdot L\right)^2}{\sqrt{12}} \cdot \sqrt{\frac{E}{\rho}} \cdot \frac{W}{L^2} \tag{7.7}$$

κ_n is a parameter that depends on the n-mode of oscillation and the boundary conditions of the beam. It is important to note that (7.7) is independent of the beam thickness, as it was desired.

Rewriting (7.4) leads to:

$$\frac{\partial^4 x(y)}{\partial y^4} = \kappa_n^4 \cdot x(y) \tag{7.8}$$

A general solution of (7.8) can be written as (7.9).

$$x(y) = A_n \cdot \sin(\kappa_n \cdot y) + B_n \cdot \cos(\kappa_n \cdot y) + C_n \cdot \sinh(\kappa_n \cdot y) + D_n \cdot \cosh(\kappa_n \cdot y) \tag{7.9}$$

Where A_n, B_n, C_n and D_n are integration constants which value is determined by the boundary conditions. Once found these values, equation (7.9) will determine the profile of the deflection of the beam.

It is important to note that (7.7) is the general expression for the resonance frequency of lateral beams. The only difference between the beams considered in this thesis (clamped-clamped and free-free beams) is found in the value of $\kappa_n \cdot L$ constant, which is determined according to the boundary conditions of each resonator.

CLAMPED-CLAMPED BEAMS

As their name indicates these beams are fixed at both resonator ends (*Figure A1.2*)

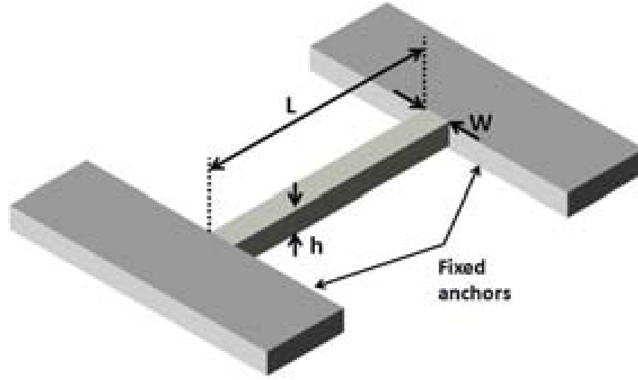

Figure A1.2: Clamped-Clamped beam diagram

The elastic constant for the lateral clamped-clamped beam is:

$$k = 16 \cdot \frac{E \cdot h \cdot W^3}{L^3} \tag{7.10}$$

It can be useful to know how the resonance frequency expression from *Chapter 2*, $\omega_n=(k/m_n)^{1/2}$ is related to (1.7). For doing so, we'll start with expression (1.7):

$$\omega_n = \frac{(\kappa_n \cdot L)^2}{\sqrt{12}} \cdot \sqrt{\frac{E \cdot W^2}{\rho \cdot L^4}} = \frac{(\kappa_n \cdot L)^2}{\sqrt{12}} \cdot \sqrt{\frac{E \cdot h \cdot W \cdot W^2}{\rho \cdot h \cdot W \cdot L \cdot L^3}} \tag{7.11}$$

If we substitute $m = \rho \cdot t \cdot W \cdot L$ in (7.11) the following expression is obtained:

$$\omega_n = \frac{(\kappa_n \cdot L)^2}{\sqrt{12}} \cdot \sqrt{\frac{E \cdot h \cdot W^3}{m \cdot L^3}} \tag{7.12}$$

And substituting (7.10) into (7.12) and arranging the expression:

$$\omega_n = \frac{(\kappa_n \cdot L)^2}{\sqrt{12}} \cdot \sqrt{\frac{k}{16 \cdot m}} \tag{7.13}$$

Comparing the equation of Chapter 2 and (7.13), it can be observed that both expressions are the same if the effective mass for the clamped-clamped beam is defined as:

$$m_n = \frac{192}{(\kappa_n \cdot L)^4} \cdot m \tag{7.14}$$

The boundary conditions for this kind of resonator are: both ends fixed (displacement at ends equal to zero) and the first derivative of the displacement also zero at both ends (y=0 and y=L), these conditions can be written as:

$$x(y=0)=0; \quad x(y=L)=0; \quad \left.\frac{\partial x}{\partial y}\right|_{y=0} = 0; \quad \left.\frac{\partial x}{\partial y}\right|_{y=L} = 0 \tag{7.15}$$

Applying the first and third boundary conditions on (7.9), the following relationships between the integration constants are obtained:

$$A_n = -C_n$$
$$B_n = -D_n \tag{7.16}$$

Equations (7.17) and (7.18) show the result of applying the second and fourth boundary conditions on (7.9), respectively.

$$C_n \cdot [\sinh(\kappa_n \cdot L) - \sin(\kappa_n \cdot L)] + D_n \cdot [\cosh(\kappa_n \cdot L) - \cos(\kappa_n \cdot L)] = 0 \tag{7.17}$$

$$C_n \cdot [\cosh(\kappa_n \cdot L) - \cos(\kappa_n \cdot L)] + D_n \cdot [\sinh(\kappa_n \cdot L) + \sin(\kappa_n \cdot L)] = 0 \tag{7.18}$$

The following relationship between C_n and D_n constants can be obtained from (7.17) and (7.18):

$$\frac{D_n}{C_n} = \frac{\sin(\kappa_n \cdot L) - \sinh(\kappa_n \cdot L)}{\cosh(\kappa_n \cdot L) - \cos(\kappa_n \cdot L)} \tag{7.19}$$

$$\frac{D_n}{C_n} = \frac{\cos(\kappa_n \cdot L) - \cosh(\kappa_n \cdot L)}{\sinh(\kappa_n \cdot L) + \sin(\kappa_n \cdot L)} \tag{7.20}$$

Combining (7.18) and (7.19) and rearranging the results, the equation to obtain $\kappa_n \cdot L$ nodal parameter is obtained for a clamped-clamped beam:

$$\cosh(\kappa_n \cdot L) \cdot \cos(\kappa_n \cdot L) = 1 \tag{7.21}$$

Graphically solving expression (7.21), (*Figure A1.3*),the values of this parameter, $\kappa_n \cdot L$, can be found and are: 4.73, 7.853, 11 and 14.14 for the first, second, third and fourth lateral oscillation modes for a clamped-clamped beam.

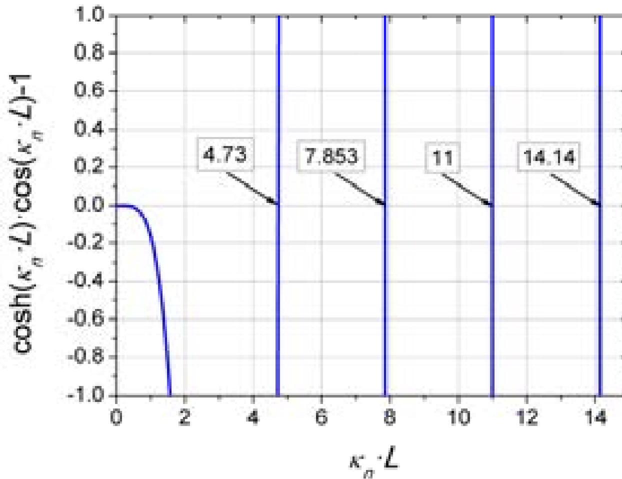

Figure A1.3: Plot of function (7.21) equal to zero. The plot shows the crosses of the function with zero axis, where $\kappa_n \cdot L$ values are found.

The profile of the displacement of the beam can be found by substituting (7.16) and (7.19) into (7.9) and setting one the free variable C_n value equal to 1. By doing so, the deflection profile follows equation (7.22).

$$x(y) = \cosh(\kappa_n \cdot x) - \cos(\kappa_n \cdot x) - \xi \cdot [\sinh(\kappa_n \cdot x) - \sin(\kappa_n \cdot x)] \tag{7.22}$$

Where ξ is defined in (7.23):

$$\xi \equiv \frac{\cosh(\kappa_n \cdot L) - \cos(\kappa_n \cdot L)}{\sinh(\kappa_n \cdot L) - \sin(\kappa_n \cdot L)} \quad (7.23)$$

Figure A1.4 shows the deflection profile for a clamped-clamped beam for the first two lateral resonance modes. The corresponding resonance frequencies for these two first lateral modes are (from eq 1.7):

$$\omega_{CC-BEAM,1st\,\mathrm{mod}} = \frac{(4.73)^2}{\sqrt{12}} \cdot \sqrt{\frac{E}{\rho}} \cdot \frac{W}{L^2} \quad (7.24)$$

$$\omega_{CC-BEAM,2nd\,\mathrm{mod}} = \frac{(7.853)^2}{\sqrt{12}} \cdot \sqrt{\frac{E}{\rho}} \cdot \frac{W}{L^2} \quad (7.25)$$

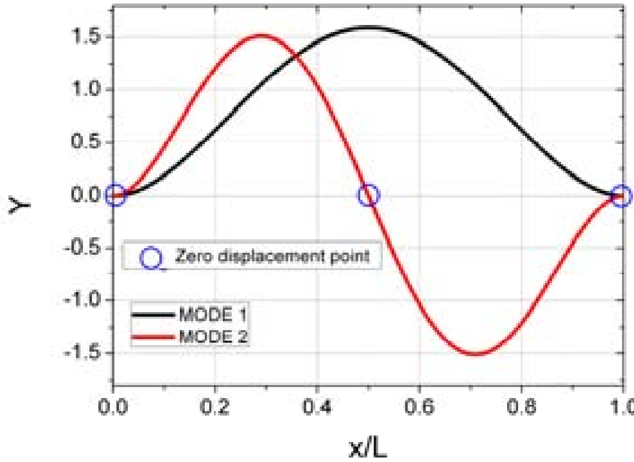

Figure A1.4: Lateral deflection profile of the first two resonance modes for a clamped-clamped beam.

FREE-FREE BEAMS

In this kind of beams, both ends are not anchored, and they can move freely. Therefore the boundary conditions for the ends of this kind of resonators are related to the second and third derivative of the displacement:

$$\left.\frac{\partial^2 x}{\partial y^2}\right|_{y=0} = 0; \quad \left.\frac{\partial^3 x}{\partial y^3}\right|_{y=0} = 0; \quad \left.\frac{\partial^2 x}{\partial y^2}\right|_{y=L} = 0; \quad \left.\frac{\partial^3 x}{\partial y^3}\right|_{y=L} = 0 \quad (7.26)$$

When the first and second boundary conditions are applied to (7.9), the following relationships are found:

$$\begin{aligned} A_n &= C_n \\ B_n &= D_n \end{aligned} \quad (7.27)$$

Whereas the third and fourth boundary conditions lead to:

$$C_n \cdot \left[\sinh(\kappa_n \cdot L) - \sin(\kappa_n \cdot L)\right] + D_n \cdot \left[\cosh(\kappa_n \cdot L) - \cos(\kappa_n \cdot L)\right] = 0 \quad (7.28)$$

$$C_n \cdot \left[\cosh(\kappa_n \cdot L) - \cos(\kappa_n \cdot L)\right] + D_n \cdot \left[\sinh(\kappa_n \cdot L) + \sin(\kappa_n \cdot L)\right] = 0 \quad (7.29)$$

And the conditions between the coefficients are:

$$\frac{D_n}{C_n} = \frac{\sin(\kappa_n \cdot L) - \sinh(\kappa_n \cdot L)}{\cosh(\kappa_n \cdot L) - \cos(\kappa_n \cdot L)} \quad (7.30)$$

$$\frac{D_n}{C_n} = \frac{\cos(\kappa_n \cdot L) - \cosh(\kappa_n \cdot L)}{\sinh(\kappa_n \cdot L) + \sin(\kappa_n \cdot L)} \quad (7.31)$$

The same relationships of (7.19) and (7.20). Combining (7.30) and (7.29), the equation to calculate $\kappa_n \cdot L$ parameter for a free-free beam is obtained:

$$\cosh(\kappa_n \cdot L) \cdot \cos(\kappa_n \cdot L) = 1 \quad (7.32)$$

Note that (7.32), formula for free-free beams, is the same expression that (7.21), for clamped-clamped beams, and therefore the values of $\kappa_n \cdot L$ are: 4.73, 7.853, 11 and 14.14 for the first four vibration modes.

Consequently, the resonance frequencies for the first three oscillation modes are:

$$\omega_{FF-BEAM,1st\,\mathrm{mod}} = \frac{(4.73)^2}{\sqrt{12}} \cdot \sqrt{\frac{E}{\rho}} \cdot \frac{W}{L^2} \quad (7.33)$$

$$\omega_{FF-BEAM,2nd\,\mathrm{mod}} = \frac{(7.853)^2}{\sqrt{12}} \cdot \sqrt{\frac{E}{\rho}} \cdot \frac{W}{L^2} \quad (7.34)$$

$$\omega_{FF-BEAM,3d\,\mathrm{mod}} = \frac{(11)^2}{\sqrt{12}} \cdot \sqrt{\frac{E}{\rho}} \cdot \frac{W}{L^2} \quad (7.35)$$

The bending profile can be obtained by combining (7.9) with (7.27) and (7.30):

$$x(y) = \cosh(\kappa_n \cdot x) + \cos(\kappa_n \cdot x) - \xi \cdot \left[\sinh(\kappa_n \cdot x) + \sin(\kappa_n \cdot x)\right] \quad (7.36)$$

Where ξ is the same coefficient found in the CC-beam (7.23).

$$\xi \equiv \frac{\cosh(\kappa_n \cdot L) - \cos(\kappa_n \cdot L)}{\sinh(\kappa_n \cdot L) - \sin(\kappa_n \cdot L)} \quad (7.37)$$

Whereas for clamped-clamped beams bending profile offers little information, it has to be calculated for free-free beams to determine the zero displacement points (nodal points) that will be used to anchor the structure. The bending profile for first and third lateral mode free-free beams is shown in *Figure A1.5*. In this figure the nodes (zero displacement points) of the beam are highlighted.

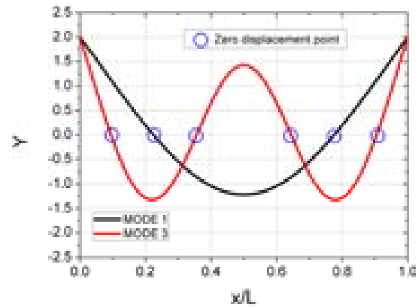

Figure A1.5: Diagram of the bending profile of a free-free beam for the first and third lateral resonance modes.

The anchoring of these structures in lateral mode is done by using two clamped-clamped beams orthogonal to the free-free beam connected through its nodal points. The key point of the design is the use of second-mode clamped-clamped beams so that the nodal point of the CC-beams ,located in the middle of the support beam (*Figure A1.4*) corresponds to the nodal points of these free-free beam, and therefore the support beam movement does not affect the free-free beam resonance [2].

Figure A1.6(a) shows the complete free-free beam structure with clamped-clamped beam anchoring, whereas *Figure A1.6(b)* shows the FEM simulation of a free-free beam with second mode clamped-clamped beam support.

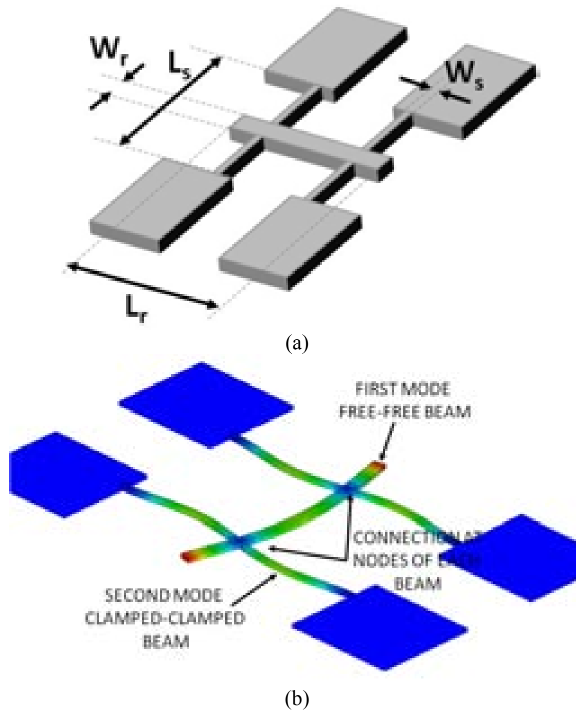

(b)

Figure A1.6: (a) Design variables of the lateral free-free beam. W_r: resonator width; L_r=resonator length; W_s: support width and L_s: support length. (b) FEM simulation of the complete Free-Free beam showing the displacement of the whole resonator, red colored parts present the maximum displacement whereas and blue colored areas displacement is zero.

DOUBLE-ENDED TUNING FORKS (DETF)

These resonators are basically two coupled clamped-clamped beams *Figure A1.7(a)*. Each beam is named tine and are mechanically coupled between them by means of the decoupling area. Some part of the movement of one tine (the one which is AC excited) is translated to the other through the decoupling area. The DETF used in this work presents stubs (or supports) to join the decoupling area with the anchor to minimize the support area and therefore reduce anchor losses, as shown in *Figure A1.7(b)*. Unfortunatelly, the use of these stubs allows additional resonance modes (torsional) which transfer lateral displacement to higher harmonics.

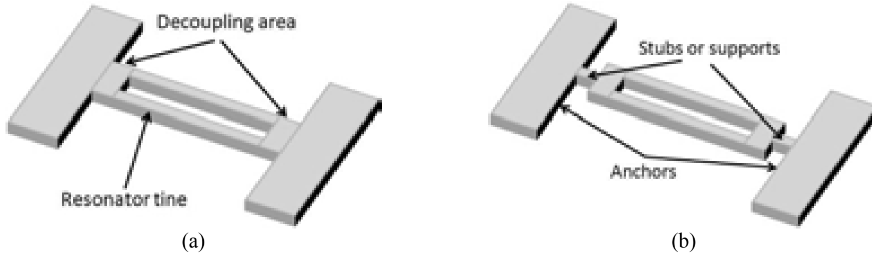

Figure A1.7: (a) Double-ended tuning fork. (b) Modified DETF resonator with stubs to reduce anchor losses

Figure A1.8 shows the relevant dimensions of the DETF: *W* and *L* are the width and length of the beam, respectively, $2 \cdot d$ is the distance between the tines, W_{da} is the width of the decoupling area and L_s is the length of the support beams.

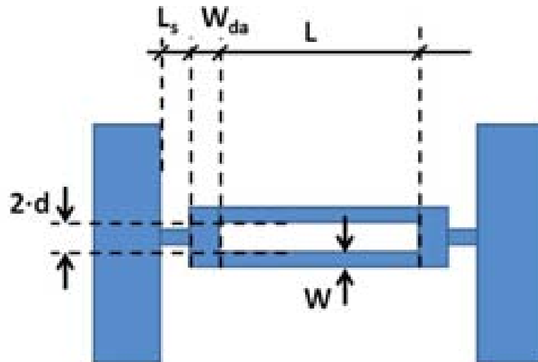

Figure A1.8: Design variables of the double-ended tuning fork.

One of the most important characteristic of this kind of resonators is that they present two lateral oscillation modes, in the first one the two tines move in phase (*Figure A1.9-a*) whereas on the second one the tines move out of phase (*Figure A1.9-b*).

Figure A1.9: DETF lateral oscillation modes: (a) First lateral mode, unbalanced operation and (b) second lateral mode or balanced operation.

This can be used for example to create a bandwidth for filtering applications using a stand-alone resonator[3, 4], given that for fixed dimensions, the distance between the two resonant frequencies is determined by the distance between tines as is obtained using FEM simulations (Figure A1.10).

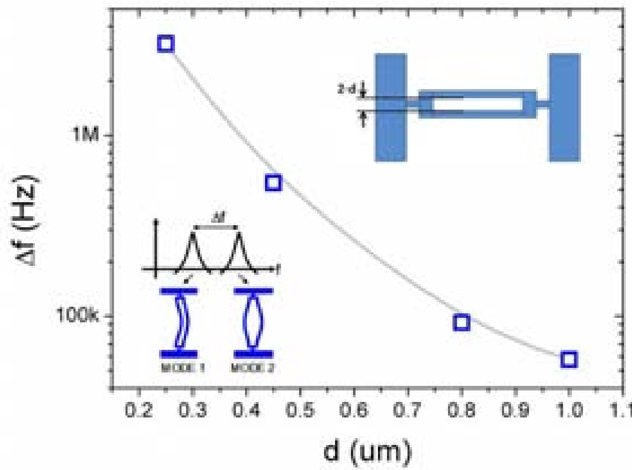

Figure A1.10: FEM simulation using Coventor of the lateral modes frequency distance as a function of the separation of the tines.

Another important issue about these resonators is that second oscillation mode is balanced, i.e. the forces applied to the tines into the decoupling region are cancelled and therefore the anchor losses are reduced, obtaining a higher Q. As a consequence of this, the resonance frequency is independent of d, W_{da} and L_s. This mode has been widely used for force sensors. However, to obtain a completely balanced resonator, the decoupling region has to be accurately dimensioned. The analytic expression for the resonance frequency at this balanced mode can be written as [5, 6]. Where β=4.73 for the balanced mode.

$$f_0 = \frac{\beta^2}{4 \cdot \pi \cdot \sqrt{3}} \cdot \sqrt{\frac{E}{\rho} \cdot \frac{W}{L^2}} \quad (7.38)$$

Analytic expression for the unbalanced mode is more difficult to obtain as it is modified by the decoupling area and support beams dimensioning. The design aspects for the first lateral resonance mode are complex and rely mainly in FEM simulations.

Therefore the design workflow shown in *Figure A1.11* was used to perform the design of these resonators. The resonator is dimensioned according to (7.38), setting the desired second mode resonance frequency, and obtaining an initial set of dimensions. In this early stage, the width of the decoupling area is selected to have the same width of the beams. Once the resonance frequency is obtained from mechanical simulations, the resonator is redimensioned (using W and L) following relationship (7.38) to fine tuning the resonance frequency.

When the target resonance frequency is obtained, d is varied to obtain the desired bandwidth or frequency separation. Special attention must be taken in this phase, because enlarging the stubs adds a mass on the unbalanced resonance mode (reducing its resonance frequency). Therefore it is considered a good tip to dimension d to obtain a lower bandwidth than the desired, in case L_s is expected to be increased.

The fourth stage of the design determines the balance of the second resonance mode. *Figure A1.12* shows the effect of proper decoupling area dimensioning on a DETF resonator obtained from FEM simulations.

Finally the length of the stubs is also dimensioned. This length can be set to be a quarter of length of the flexural movement for the frequency of operation to further reduce losses [7]. However the use of long supports should be avoided to prevent sticking of the resonators with the substrate. In the last step, the global performance (resonance frequencies and balancing) is analyzed and the design dimensions are fine-tuned.

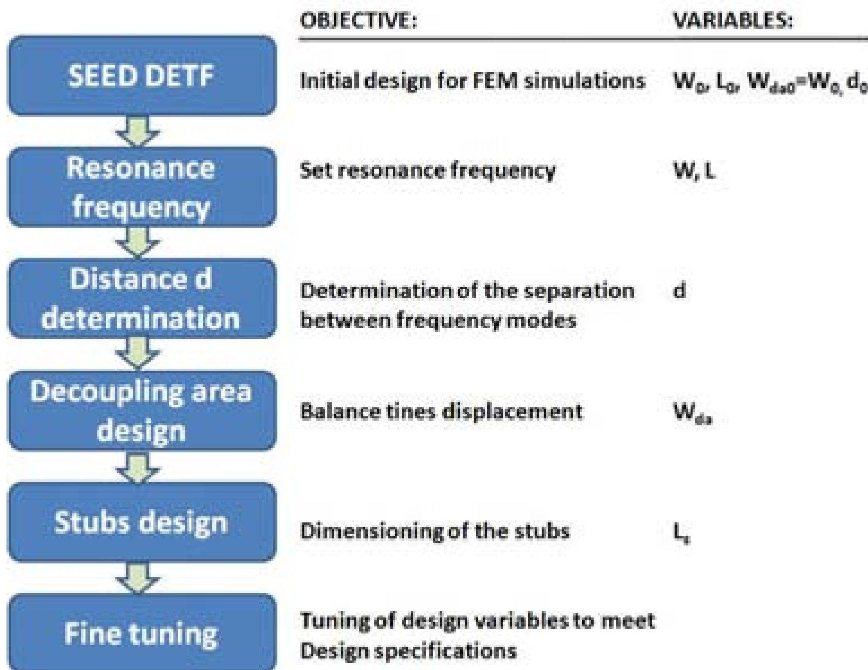

Figure A1.11: Developed DETF resonators design workflow

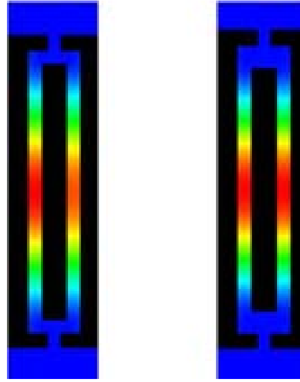

Figure A1.12: Modal displacement simulation for the second lateral frequency mode of a double ended tuning fork. The resonator at the right (with a wider decoupling area) shows close displacement in both tines, compared to the left one.

REFERENCES

[1] M. Bao, *Micro mechanical transducers : pressure sensors, accelerometers, and gyroscopes*. Amsterdam New York: Elsevier, 2000.

[2] W. T. Hsu, Clark J R, and C. T. C. Nguyen, "Q-optimized lateral free-free beam micromechanical resonators," in *Int. Conf. on Solid-State Sensors & Actuators (Transducers'01)*, Munich, Germany, 2001, pp. 1110-1113.

[3] J. Yan, A. A. Seshia, K. L. Phan, and J. T. M. van Beek, "Internal electrical phase inversion for FF-beam resonator arrays and tuning fork filters," in *Micro Electro Mechanical Systems, 2008. MEMS 2008. IEEE 21st International Conference on*, 2008, pp. 1028-1031.

[4] J. Yan, A. A. Seshia, K. L. Phan, P. G. Steeneken, and J. T. M. van Beek, "Narrow Bandwidth Single-Resonator MEMS Tuning Fork Filter," in *Frequency Control Symposium, 2007 Joint with the 21st European Frequency and Time Forum. IEEE International*, 2007, pp. 1366-1369.

[5] R. A. Buser and N. F. de Rooij, "Tuning forks in silicon," in *Micro Electro Mechanical Systems, 1989, Proceedings, An Investigation of Micro Structures, Sensors, Actuators, Machines and Robots. IEEE*, 1989, pp. 94-95.

[6] M. Agarwal, K. K. Park, M. Hopcroft, S. Chandorkar, R. N. Candler, B. Kim, R. Melamud, G. Yama, B. Murmann, and T. W. Kenny, "Effects of Mechanical Vibrations and Bias Voltage Noise on Phase Noise of MEMS Resonator Based Oscillators," in *Micro Electro Mechanical Systems, 2006. MEMS 2006 Istanbul. 19th IEEE International Conference on*, 2006, pp. 154-157.

[7] S. P. Beeby, G. Ensell, and N. M. White, "Microengineered silicon double-ended tuning fork resonators," *Engineering Science and Education Journal,* vol. 9, pp. 265-271, 2000.

ANNEX2: MEMS Characterization Equipment and Techniques

In this annex the different measurement equipment used to carry out the measurements is described. The fundamental measurements techniques and the fitting process of the experimental curves with ADS for an electrical equivalent models are also provided.

MEASUREMENT TEST SETUP

Figure A2.1 shows a photograph of the main parts of the measurement equipment. The test setup is formed by a manual probe table Süs Microtech PM-8, equipped with a CCD camera and optical microscope, and RF probes (from Cascade Microtech and Süs) for direct on-chip measurement.

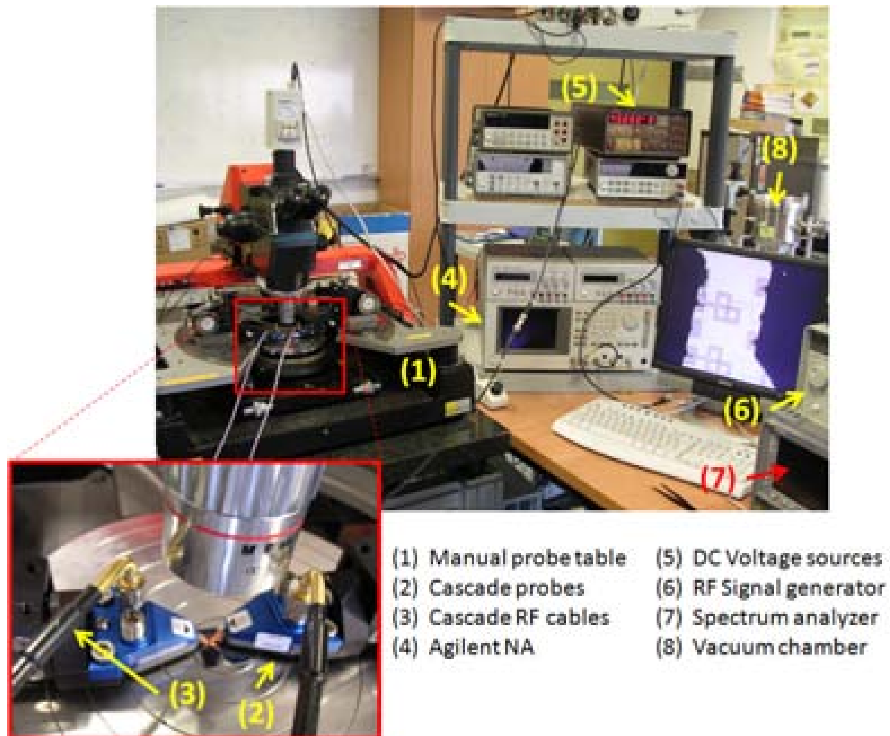

Figure A2.1: Photograph of the measurement facilities and measurement test setup.

Table A2.1 shows a list of the used equipment, as well as its main characteristics.

Table A2.1: List of the measurement equipment used for MEMS characterization

Manufacturer	*Model*	*Characteristics*
Süs Microtech	PM-8	Manual probe table
	[1]	GSGSG Probe tips (150µm pitch)
Cascade Microtech	Infitity probe holder	
	Infinity probe	GSGSG probe tips (150um pitch)
	RF cable 101-162	40 GHz flexible K-connector cable
Agilent technologies	Agilent E5100A	Network Analyzer, f=10kHz-300kHz
	Agilent E5070	4-port network analyzer f=300kHz-3GHz Frequency offset option
	E3611A DC	DC source
	81150A	Dual channel signal generator
	HP-8647A	RF signal generator f=250kHz-1GHz
	E4404B	Spectrum analyzer f=100Hz-6.7GHz Phase noise measurement
	E5052A	Signal Analyzer
Keithley	230 DC	DC voltage source 100V, 2mA
Microcircuits	ZFBT-6GW+	Bias-T

MEASUREMENT TECHNIQUES

In this section the basic measurement techniques are explained. These techniques are based on the working principles presented in Chapter 2.

DIRECT S21 MEASUREMENTS

S21 parameter is the forward gain for a two-port device, where port 1 is the input port and 2 is the output port, when using the scattering (S) parameters. It is understood as the coefficient between the voltage wave going out the port 2 and the voltage wave injected to port1. Other S parameters like reflections on both ports (S11 and S22) or reverse gain (S12) have been not considered in this thesis. Additional information about the scattering parameters can be found in [2].

S21 measurement is the simplest measurement technique. It involves the use of a network analyzer and a DC source to bias the MEMS resonator (*Figure A2.2*). The output of the network analyzer is connected to the excitation electrode and the input is connected to the read-out

electrode, whereas the DC voltage source is connected to the resonator. To prevent damage to the network analyzer (and depending on the model of the analyzer and the DC voltage level used), a bias-T or a decoupling capacitor is added before the input of the network analyzer. This decoupling element is always added to the measurements with on-chip amplification, as the amplifiers are designed to have a DC-uncoupled output.

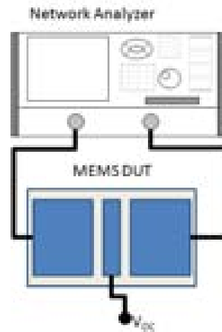

Figure A2.2: Direct S21 measurement connection

MIXING MEASUREMENTS

In this second technique, the frequency of the excitation signal and the read-out frequency are different, and therefore a test setup to measure different frequency signals and relate them must be used. Even though this measurement can be performed using a single network analyzer, by introducing an additional mixing stage [3], it is preferred not to use this technique as the addition of this mixing stage can alter the MEMS resonator characterization. In these measurements, a LO signal is applied to the resonator, using a Bias-T to combine the DC voltage and this LO signal. To generate this LO signal a signal source or a RF signal source is used (depending on the required frequency). *Figure A2.3* shows the two mixing measurement test setup used for MEMS measurement.

In the first test setup, *Figure A2.3(a)*, the output signal is measured using a spectrum analyzer, centered at the output frequency, whereas the input signal is swept from the network analyzer. The MEMS resonator translates this input signal in frequency, and this modified signal is captured by the spectrum analyzer, using the MAXHOLD function to store the measurement. In this measurement several considerations must be taken into account: in spectrum analyzers, to measure low power signal measurements, like the output of MEMS, the acquisition time must be increased, furthermore, the sweep time of the network analyzer must be slow enough to allow the spectrum analyzer to measure 200 frequency points during each input signal sweep. This makes this king of measurements quite slow.

Figure A2.3(b) shows the test setup with the Agilent E5070 network analyzer, that by being provided with the frequency offset measurement, is able to excite and read at different frequencies, therefore simplifying the test setup, and without the measurement time constrain imposed by the use of the network analyzer. It is worth to mention that the results obtained by the two test setup from *Figure A2.3* are equivalent, because the working principle of both schemes is the same. However there is a difference: whereas the network analyzer with frequency offset provides directly the mixing “S21” (the coefficient between output and input powers), the spectrum analyzer provides the power of the output, and therefore the measurement is not directly the “S21”, although it can be easily calculated knowing the input signal power.

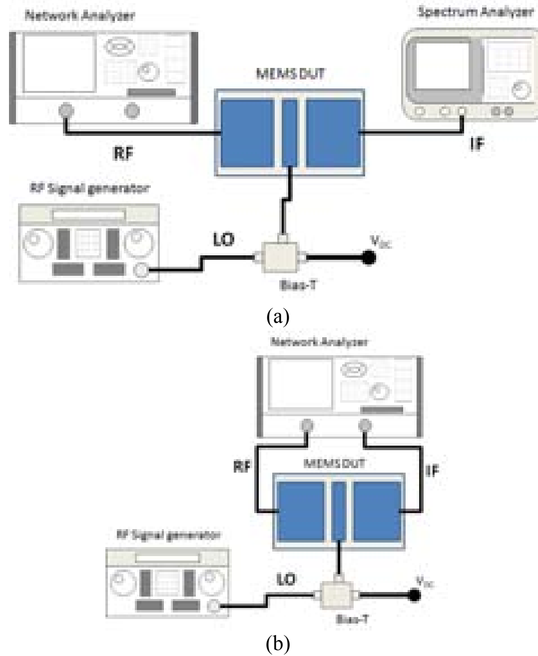

(a)

(b)

Figure A2.3: Mixing measurement test setups. (a) Mixing measurement with spectrum analyzer and (b) Mixing measurement with frequency offset network analyzer.

Q MEASUREMENT TECHNIQUES

From the S21 measurements, there are two ways to calculate this quality factor:

1. From magnitude measurements, the quality factor can be obtained using $Q_{3dB} = f_0 / BW_{3dB}$, where f_0 is the resonance frequency and BW_{3dB} is the 3dB bandwidth of the resonance peak. Therefore this calculus requires a resonance peak higher than 3dB.
2. From phase measurements, Q can be computed using the following formula [4]:

$$Q_{phase} = f_0 \cdot \frac{\pi}{360} \cdot \frac{d\theta}{df} \quad (8.1)$$

Where $d\theta / df$ is the slope of the phase curve corresponding to the phase variation due to the resonance peak. This expression is useful to calculate the quality factor when no magnitude resonance peak higher than 3dB is measured.

MOTIONAL RESISTANCE EXTRACTION

There are several ways to calculate the motional resistance of a stand-alone MEMS resonator once the frequency response is obtained. A simple method to calculate this parameter (and the most widely used in the literature) is by using the formula [5].

$$R_m = R_L \cdot \left(10^{-(A/20)} - 1\right) - R_p \quad (8.2)$$

Where R_L is the load resistor (typically 50Ω), A is the magnitude in dB of the resonance peak and R_p is the parasitic resistor caused by signal paths and electrical contacts. Note that for high loss-devices, the influence of R_p can be neglected, obtaining the R_m expression (8.3) [6].

$$R_m = 50 \cdot 10^{-(A/20)} \qquad (8.3)$$

Although this expression is very simple, is not at all accurate as it neglects the effect of the parasitic parallel capacitor. This parasitic capacitor raises the level of the measurements, and therefore, this formula produces an underestimation of the motional resistance value. Another method that is more accurate is the use of an RLC//Cp model to fit the frequency response, which includes the effect of the parasitic capacitor, a detailed explanation of this method can be found in Annex 2. For fair comparison between the MEMS of this thesis and reported resonators, both R_m values (using electrical fit and analytic formulas) will be provided (if possible).

ADVANCED MEASUREMENT TECHNIQUES

In this section, more advanced techniques are explained. In particular, the obtention of the RLC model parameters and the effect of the 50Ω termination of the instrumentation on the experimental measurement.

CALIBRATION

Even though calibration of the test setup does not show relevant improvement on conventional measurements, because of the big impedance mismatch, it is important to be performed when RLC model fitting is used and termination load is changed. Calibration was found necessary for RLC fitting for resonators above 100MHz, however it is mandatory when the impedance of the network analyzer are changed.

This calibration is performed up to the probe tips thanks to special calibration substrates provided by probe manufacturers. This calibration allows an accurate characterization of the resonator, as it corrects the effects of the measurement cables.

ADS FITTING

The RLC model fitting is performed using the Advanced Design System (ADS) CAD software from Agilent because its easy interconnection with experimental measurements. In particular the Agilent E5070 network analyzer allows saving measurement data as a touchstone file, that can be incorporated as an element in ADS simulations. Moreover, ADS allows the quick fitting thanks to additional tools like disable component and parameter tuning. As it was previously mentioned, the RLC model used was shown in *Figure 1.6.*.

This model consists on two shunt capacitors (C_{pad}) that models the parasitic capacitor to the substrate of the electric pads. These capacitors have the values C_{pad}=1pF and C_{pad}= 31.36fF for AMS and UMC technologies, respectively. The value of these capacitors can be found from the extracted layout netlist from Cadence. Other elements of this model are the resonator branch (R_m, L_m and C_m) and the parasitic parallel capacitance (C_p). The step-by-step procedure for model fitting is the following:

1. Calibration and measurement of the MEMS resonator. The measurement data is saved as touchstone file (S2P). It is preferred to obtain two measurements, one with a typical DC value and other with V_{DC}=0V.
2. Include the touchstone measurement file in ADS using a S2P element.

3. Fitting of C_p. The resonance branch (R_m,C_m and L_m) is disabled using the "Activate and deactivate" utility. The value of C_p is adjusted considering V_{DC}=0V resonator frequency response or the feedthrough signal level *(Figure A2.4)*.

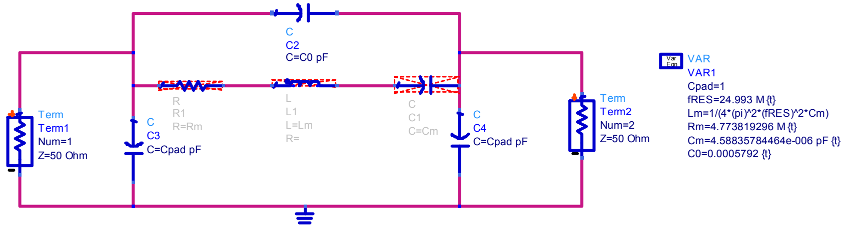

(a)

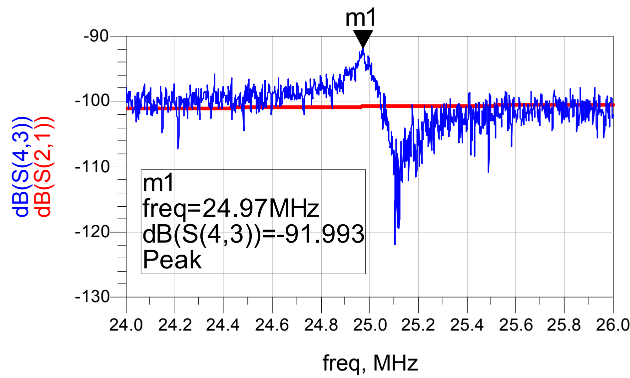

(b)

Figure A2.4: Feedthrough signal level fitting. Kindly note that although the shown marker is placed in the peak the C_p value is adjusted in the flat response region.

4. Adjust of Rm. The C_m and L_m are bypassed using a wire, and R_m resistor is enabled and tuned to fit the measured peak magnitude *(Figure A2.5)*.

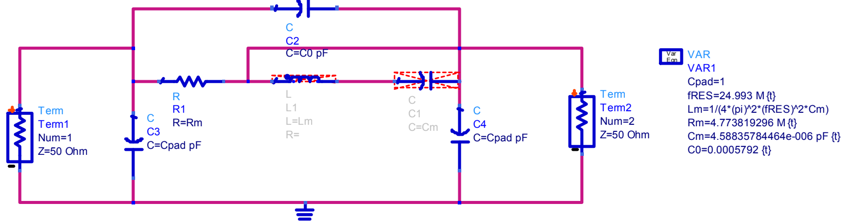

(a)

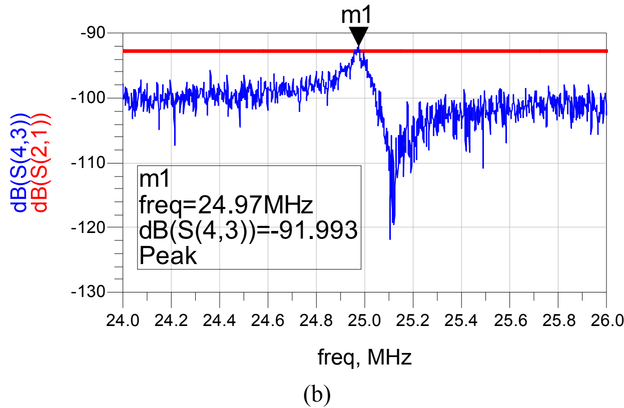

(b)

Figure A2.5: Peak level fitting

5. Finally, C_m and L_m elements are enabled. The value of Lm is fixed and equal to L_m=1/C_m*(2*pi*fres)^2, where fres is the peak frequency. And doing so, only the C_m value has to be fitted *(Figure A2.6)*.

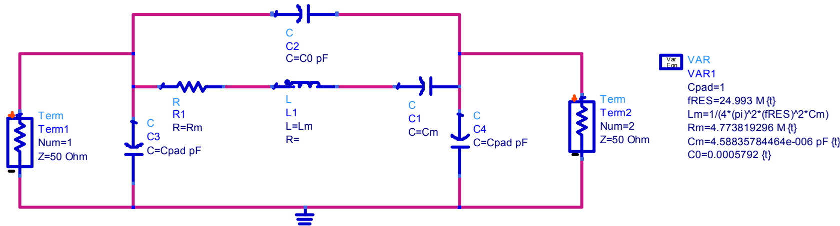

(a)

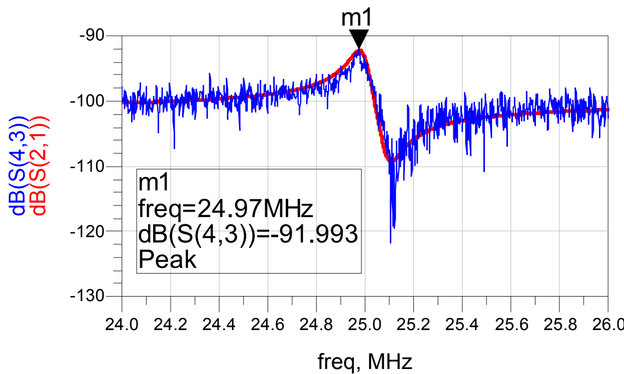

(b)

Figure A2.6: Motional capacitor and inductance fitting

6. Fine tuning. Once all parameters have been fitted, additional tuning (with small variations) on R_m, C_m and C_p can be used to improve the fitting of the electrical model with the measurements.

TERMINATION

The Agilent E5070 network analyzer has a novel function named fixture simulator, which allows the simulation of different circuits to adapt the impedances. In particular, the network analyzer is capable to simulate the behavior of the device under test for different termination impedances instead of the typical 50Ω from measurement instrumentation. To use all the potential of this test fixture simulation, the test setup should be previously calibrated up to the probe tips, if this is not done the measurements would show no improvement (but degradation). *Figure A2.7* shows the magnitude frequency response for a clamped-clamped beam resonator with different termination resistances.

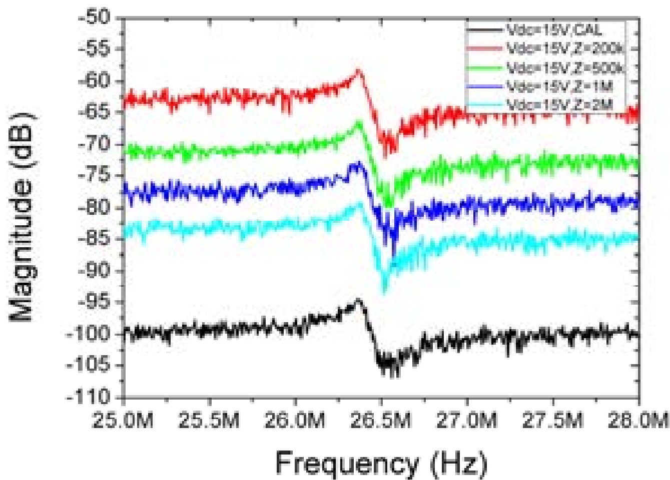

Figure A2.7: Effect of change the termination impedance using test fixture simulator. Black curve is the calibrated measurement with 50Ω termination impedance.

From *Figure A2.7* it can be observed how an increase of the termination resistance reduces the magnitude losses, provoked as aforementioned by the impedance mismatch. The minimum losses are obtained for termination resistances of 200kΩ, whereas for higher impedance values, the losses increases again, as it can be observed in *Figure A2.7.* This effect is caused by the influence of the parasitic pad capacitors.

The foreseen termination effect corroborates the fact that the losses measured are mainly provoked by the impedance mismatch between the resonator and the measurement test setup. It also indicates that pad capacitors play an important role into the measurement. The impedance change technique can be used to extrapolate the performance of the resonator in completely monolytic systems when no on-chip amplifier is implemented.

REFERENCES

[1] F. D. Bannon, J. R. Clark, and C. T. C. Nguyen, "High-Q HF microelectromechanical filters," *Solid-State Circuits, IEEE Journal of,* vol. 35, pp. 512-526, 2000.

[2] HP, "S-Parameter techniques," *Test and Measurement Application Note 95-1 (Available on-line at http://contact.tm.agilent.com/Agilent/tmo/an-95-1/index.html)*.

[3] J. R. Clark, W. T. Hsu, and C. T. C. Nguyen, "Measurement Techniques for Capacitively-Transduced VHF-to-UHF Micromechanical Resonators," in *Transducers'01*, Munich, Germany, 2001, pp. 1118-1121.

[4] B. Razavi, "A study of phase noise in CMOS oscillators," *Solid-State Circuits, IEEE Journal of,* vol. 31, pp. 331-343, 1996.

[5] K. Wang, A.-C. Wong, and C. T. C. Nguyen, "VHF free-free beam high-Q micromechanical resonators," *Microelectromechanical Systems, Journal of,* vol. 9, pp. 347-360, 2000.

[6] S. Pourkamali, H. Zhili, and F. Ayazi, "VHF single crystal silicon capacitive elliptic bulk-mode disk resonators-part II: implementation and characterization," *Microelectromechanical Systems, Journal of,* vol. 13, pp. 1054-1062, 2004.

ANNEX 3: run Description

In this annex, all the runs containing the MEMS resonators reported along this thesis are described.

AMS RUN 1

RUN code:	10941-009	**Technology:**	AMS C35B4C3
Date:	June 2007	**Funding**	TIC2003-07237-C03-02
Complete chip area	3690 × 2721 μm^2 (mini@sic)		
RUN description	Several MEMS for RF applications with and without on-chip amplification. MEMS with integrated on-chip oscillator for mass sensing applications and massive cantilevers for energy scavenging. All the devices except the scavenger were fabricated in polysilicon layers.		
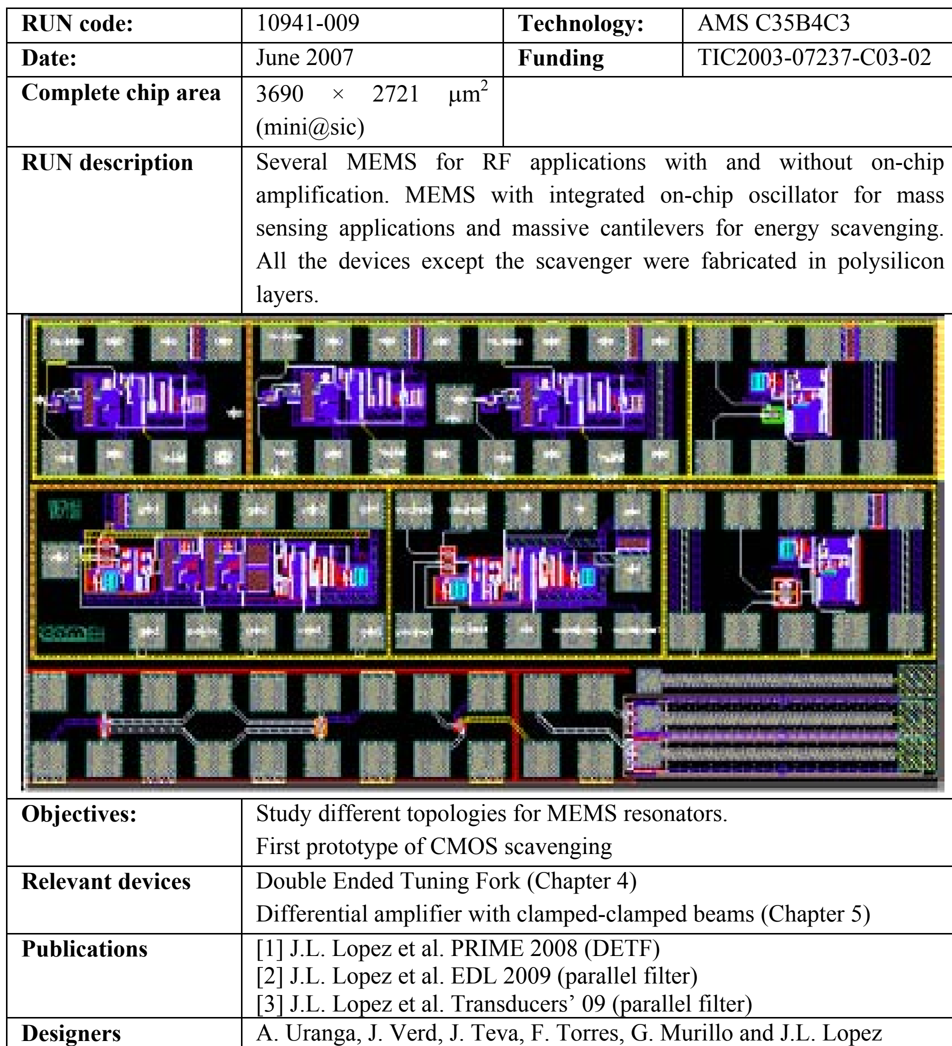			
Objectives:	Study different topologies for MEMS resonators. First prototype of CMOS scavenging		
Relevant devices	Double Ended Tuning Fork (Chapter 4) Differential amplifier with clamped-clamped beams (Chapter 5)		
Publications	[1] J.L. Lopez et al. PRIME 2008 (DETF) [2] J.L. Lopez et al. EDL 2009 (parallel filter) [3] J.L. Lopez et al. Transducers' 09 (parallel filter)		
Designers	A. Uranga, J. Verd, J. Teva, F. Torres, G. Murillo and J.L. Lopez		

UMC RUN

RUN code:	12187	**Technology:**	UMCL180
Date:	June 2007	**Funding**	TIC2003-07237-C03-02
Complete chip area	1500 x 1500 μm^2		
RUN description	Clamped-clamped beams in different configurations fabricated in M5 layer. Oscillators for discrete FBAR resonators		
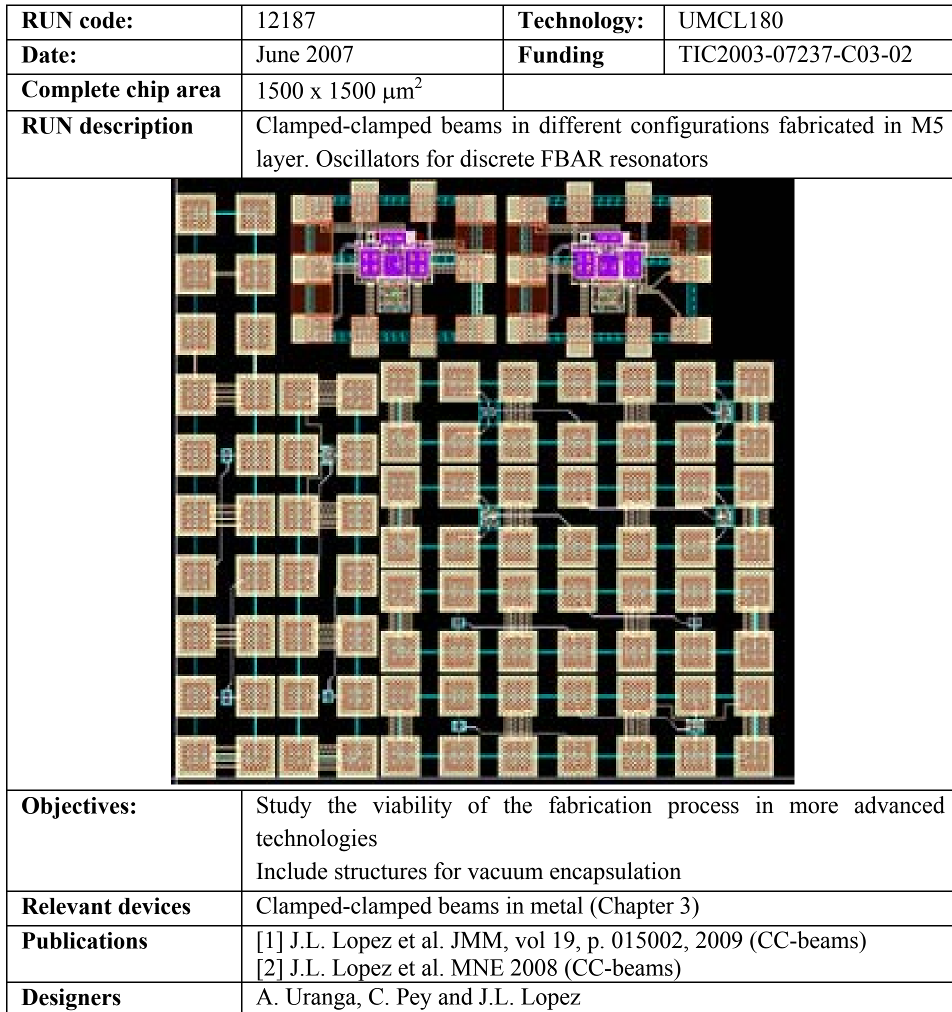			
Objectives:	Study the viability of the fabrication process in more advanced technologies Include structures for vacuum encapsulation		
Relevant devices	Clamped-clamped beams in metal (Chapter 3)		
Publications	[1] J.L. Lopez et al. JMM, vol 19, p. 015002, 2009 (CC-beams) [2] J.L. Lopez et al. MNE 2008 (CC-beams)		
Designers	A. Uranga, C. Pey and J.L. Lopez		

AMS RUN 2

RUN code:	12187-010	**Technology:**	AMS C35B4C3
Date:	April 2008	**Funding**	TEC2006-03698/MIC
Complete chip area	3610 x 2850 μm^2		
RUN description	RF MEMS fabricated in polysilicon, with and without on-chip amplification. MEMS based oscillators for RF applications. Vacuum encapsulation devices. "Scavenger on-chip" prototype		
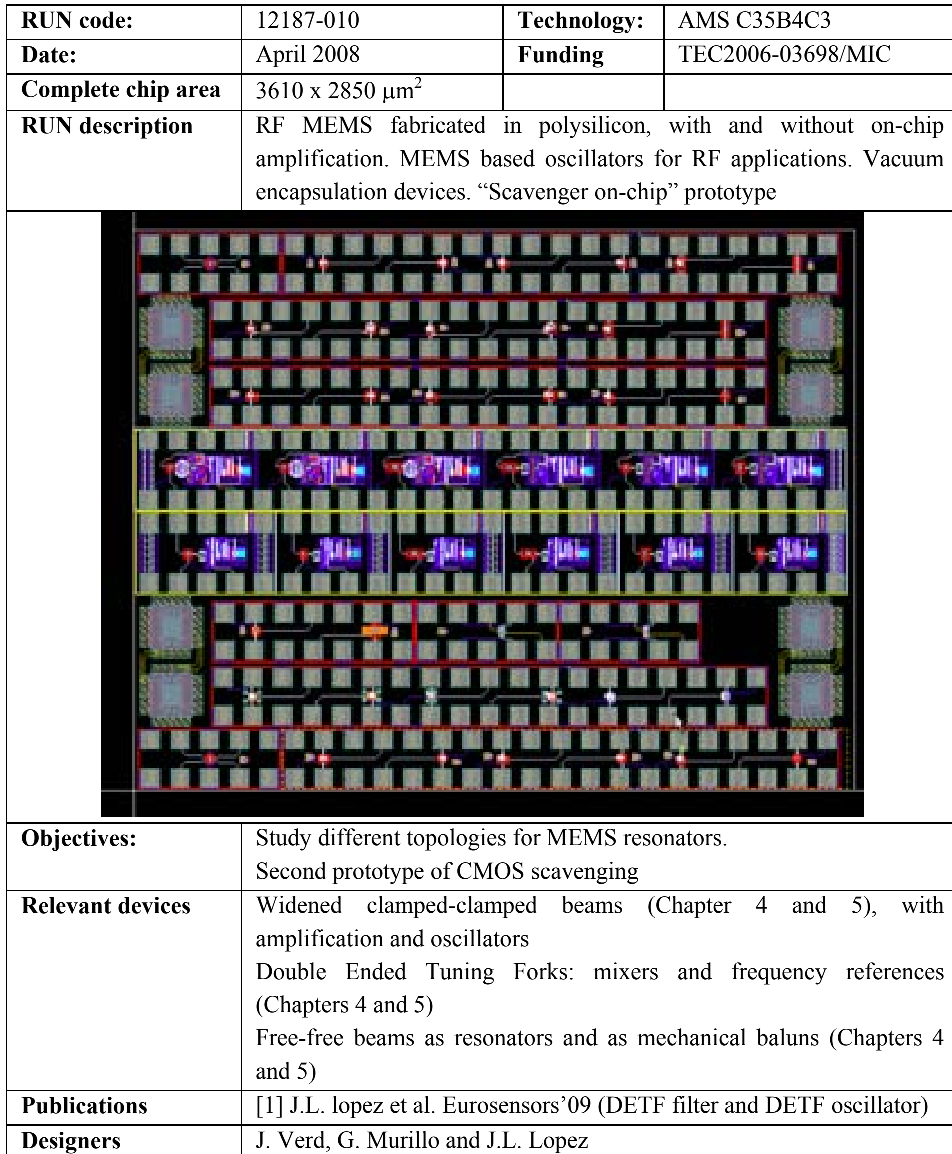			
Objectives:	Study different topologies for MEMS resonators. Second prototype of CMOS scavenging		
Relevant devices	Widened clamped-clamped beams (Chapter 4 and 5), with amplification and oscillators Double Ended Tuning Forks: mixers and frequency references (Chapters 4 and 5) Free-free beams as resonators and as mechanical baluns (Chapters 4 and 5)		
Publications	[1] J.L. lopez et al. Eurosensors'09 (DETF filter and DETF oscillator)		
Designers	J. Verd, G. Murillo and J.L. Lopez		